UNIVERSITÀ DI PARMA

UNIVERSITÀ DEGLI STUDI DI PARMA

DOTTORATO DI RICERCA IN SCIENZE CHIMICHE

XXXVII CICLO

Spectroscopy and Chirality in Supramolecular Aggregates: A Joint Experimental and Theoretical Study

Coordinatore
Prof.ssa Alessia Bacchi

Relatori
Prof.ssa Francesca Terenziani
Prof. Andrea Lapini

Dottorando
Francesco Bertocchi

Anni accademici 2021/22 - 2023/2024

Contents

Nomenclature

α	Optical rotatory power
ϵ	Molar extinction coefficient
η	Refractive index
Φ_f	Quantum yield
θ	Ellipticity
$\vec{\mu}$	Electric dipole moment
$\vec{m}$	Magnetic dipole moment
c	Speed of light in a vacuum inertial frame
g_{abs}	Dissymmetry factor in absorption
g_{lum}	Dissymmetry factor in emission
h	Planck constant
k_r	Radiative decay constant
R	Rotational strength
BTW	Biological transparency window
C8O3	3,3′-bis(3-carboxy-n-propyl)-3,3′-di-n-octyl-5,5′,6,6′-tetrachlorobenzimidacarbocyanine
CD	Circular dichroism
CPL	Circularly polarized luminescence
CT	Charge transfer
DCM	Dichloromethane
DFT	Density functional theory
DiD	1,1-dioctadecyl-3,3,3,3-tetramethylindodicarbocyanine perchlorate
DiR	1,1′-dioctadecyl-3,3,3′,3′-tetramethylindotricarbocyanine iodide
DMSO	Dimethylsufoxyde
ED	Electron diffraction
ESM	Essential-state models
FE	Frenkel exciton

HOMO Highest occupied molecular orbital

IR Infrared

LH Left-handed

LUMO Lowest unoccupied molecular orbital

MD Molecular dynamics

NIR Near Infrared

NMR Nuclear magnetic resonance

ODA Oscillating dipole approach

ODIN -(7-oxo-7,8-dihydro-1,8-naphthyridin-2-yl)urea

ONP Organic nanoparticle

OPA One-photon absorption

ORD Optical rotatory dispersion

POA Polarizable object approach

PTM perchlorotriphenylmethyl

RH Right-handed

rPET Reductive photoelectron transfer

SE Simulated emission

TAS Transient absorption spectroscopy

TD-DFT Time dependent-density functional theory

THF Tetrahydrofurane

TPA Two-photon absorption

TPEF Two-photon excited fluorescence

TRIR Time resolved infrared spectroscopy

TTM Tris(2,4,6-trichlorophenyl)methyl

List of Publications

- F. Bertocchi, et al. Aggregates of Cyanine Dyes: When Molecular Vibrations and Electrostatic Screening Make the Difference. The Journal of Physical Chemistry C, 2023, 127(21), 10185–10196;
- F. Bertocchi et al. "Circular dichroism of molecular aggregates: A tutorial." Chirality 35.10 (2023): 681-691.;
- F. Bertocchi et al. "Tuning the Optical Properties Through Hydrogen Bond-assisted H-aggregate Formation: The ODIN Case" Chemistry–A European Journal 30 (1), e202302619;
- F. Bertocchi et al. "Chiroptical properties of cyanine aggregates: hierarchical modelling from monomers to bundles" Chemical Science (2024);
- N. Gonzalez-Pato et al., "Nanothermometer Based on Polychlorinated Trityl Radicals Showing Two-Photon Excitation and Emission in the Biological Transparency Window: Temperature Monitoring of Biological Tissues" Small methods 8 (3), 2301060;
- F. Di Maiolo et al., "How nitro group position determines the emission properties of diketopyrrolopyrroles", submitted manuscript;
- D. Kusy et al., "Synthesis and chiral optical activity of π-expanded electron-rich heterohelicenes based on the 1,4-dihydropyrrolo[3,2-b]pyrrole core", submitted manuscript;

Introduction 1

1.1 Supramolecular aggregation

A supramolecular aggregate, or supramolecular assembly, is a chemical structure composed of molecules held together by noncovalent bonds.[1] These aggregates often form through the self-assembly of molecules, which spontaneously organize via non-covalent interactions.[2, 3] Due to the weak nature of non-covalent interactions, self-assembled aggregation is often a reversible process, and aggregates are in equilibrium with the monomeric species.[4] For homoaggregates, this equilibrium can be described by the following chemical equation:

$$\mathrm{nM} \rightleftharpoons \mathrm{M}_n \tag{1.1}$$

where n indicates the number of molecules within the aggregate and M is the monomer. The equilibrium 1.1 is characterized by the equilibrium constant

$$K = \frac{[M_n]}{[M]^n} \tag{1.2}$$

It can be inferred from Eq. 1.2 that high concentrations of monomer favour aggregation, according to Le Chatelier principle.[5] The variation in standard Gibbs free energy associated with the aggregation process is:

$$\Delta G^0 = \Delta H^0 - T\Delta S^0 = -RTlnK \tag{1.3}$$

To shift the equilibrium towards the assembly ($K >> 1$) ΔG^0 must be negative. Aggregation typically involves a decrease in both enthalpy ($\Delta H^0 < 0$) and entropy ($\Delta S^0 < 0$). This occurs because new non-covalent bonds are formed, but n individual molecules combine into a single aggregate, significantly reducing their degrees of freedom.[6]Therefore, the interactions between molecules must be strong enough to compensate the loss in entropy. High temperatures tend to favor endoergonic processes, which can lead to the disruption of supramolecular assemblies.[7]

Non-covalent interactions are crucial in shaping the geometry of a supramolecular assembly. These interactions can be classified as nonspecific, when their formation doesn't depend on the presence of specific functional groups, or specific, when it does.[8] Additionally, they can be categorized as either directional or non-directional. A common feature of all these interactions is that their strength decreases as the distance between molecules increases.

1.2 Nonspecific interactions

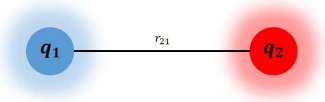

Figure 1.1: Scheme of interaction between two ions.

1.2.1 Ion-ion interaction

The electrostatic interaction between net charges, or monopoles, (Fig. 1.1) is isotropic. The interaction energy E depends on the magnitude of charges and the distance between them, as:

$$E = \frac{1}{4\pi\epsilon_0\epsilon_r}\frac{q_1 q_2}{r_{21}}$$

where ϵ_0 is the dielectric constant in vacuum, ϵ_r is the relative dielectric constant of the medium, $q_{1/2}$ are the net charges of the ions, including the sign, and r_{21} is the distance between them. The interaction is attractive (repulsive) when charges have opposite (same) sign.[9]

Ion-ion interaction strongly depends on the medium and is suppressed in polar media (e.g. in water ϵ_r=78, meaning the interactions between two charges is 78 times weaker than in vacuum). The dependence on r^{-1} makes it a long-range interaction. The common energies for a ionic bond (like in NaCl) are in the range of 100-300 kJ/mol.[10]

Electrostatic interactions between charged molecules, and their screening by the medium, will be the central subject of chapter 2.

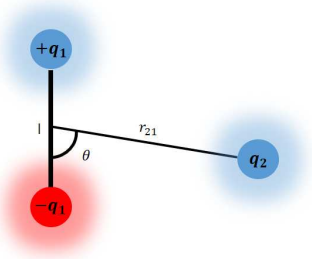

Figure 1.2: Scheme of interaction between a dipole and a monopole.

1.2.2 Ion-dipole interaction

A neutral molecule possesses an electric dipole moment when its positive and negative charges are unevenly distributed, meaning the center of the negative charges does not coincide with the center of the positive charges. Electric dipoles can interact with ions or other dipoles.

With reference to Fig. 1.2, in the limit of $r_{21} >> l$, l being the dipole length, the interaction energy between an ion and a dipole can be written as:

$$E = -\frac{1}{4\pi\epsilon_0\epsilon_r}\frac{q_2\mu cos(\theta)}{r_{21}^2}$$

where $\mu = lq_1$ is the dipole moment amplitude, and q_2 is the ion charge.[11]

The interaction is slightly directional (Fig. 1.2) and can be attractive or repulsive depending on the geometry and sign of the q_2 charge. It is in general weaker than ion-ion interaction (in molecular systems ranges from 50 to 200 kJ/mol) and decreases more sharply with distance.[8]

1.2.3 Dipole-dipole interaction

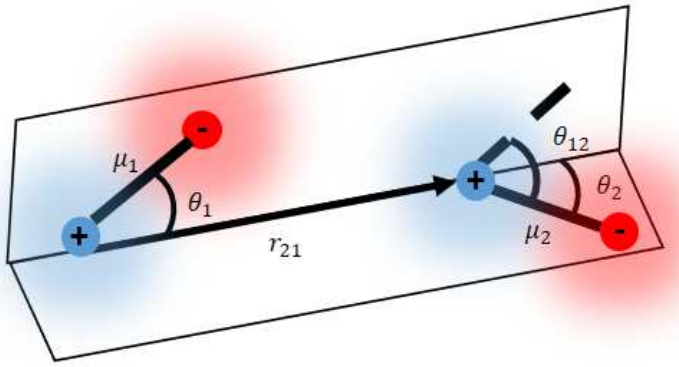

Figure 1.3: Scheme of interaction between two dipoles

Dipole-dipole interaction (also called dipolar interaction)[12, 13] is highly directional. In the limit of $r_{21} >> l$, l being the dipoles' length, it is associated with an interaction energy given by:

$$E = \frac{1}{4\pi\epsilon_0\epsilon_r}\frac{\vec{\mu}_1\cdot\vec{\mu}_2 - 3(\hat{r}_{12}\cdot\vec{\mu}_1)(\hat{r}_{12}\cdot\vec{\mu}_2)}{r_{21}^3} = \frac{1}{4\pi\epsilon_0\epsilon_r}\frac{\mu_1\mu_2(cos(\theta_{12}) - 3cos(\theta_1)cos(\theta_2))}{r_{21}^3}$$

where the relevant angles and distances are represented in Fig. 1.3. The energy range for dipolar interaction in organic systems is 5-50 kJ/mol, making it weaker in respect to interactions involving ionic species. The dipolar interaction can be attractive or repulsive depending on the geometrical parameters, and rapidly decays with interdipolar distance, from which it holds a cubic dependence.[14]

Van der Waals interactions

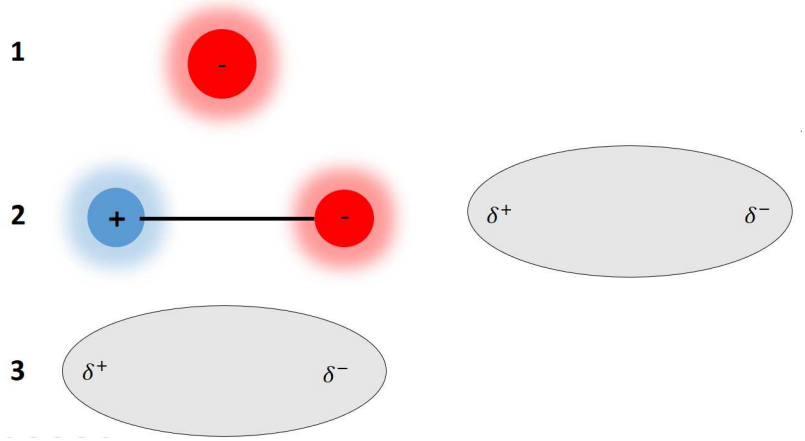

Figure 1.4: Summary diagram of Van der Waals interactions. 1: ion-induced dipole interaction. 2: dipole-induced dipole interaction. 3: London forces.

Molecules, even if non polar, can alter their charge distribution when exposed to an external electric field, which can be generated by a point charge or a dipole. The external electric field induces a dipole moment within the molecule. The induced dipole moment is proportional to

the molecular static polarizability, $\alpha = \frac{d\mu}{dE}$ where E is the amplitude of the external electric field. α is in general a tensor, and the induced dipole moment depends on the directions along which the electric field is applied.[15]

Van der Waals interactions are always attractive, as molecules redistribute their charge density in order to minimize the overall energy.[16] The interaction energy between an ion and an induced dipole (**1** in Fig. 1.4) is given by:

$$E = -\frac{1}{4\pi\epsilon_0\epsilon_r}\frac{q^2\alpha}{r_{21}^4}$$

A permanent dipole can also induce a dipole moment in a non polar molecule (**2** in Fig. 1.4). If the permanent and induced dipoles are aligned, the interaction energy is given by:

$$E = -\frac{1}{4\pi\epsilon_0\epsilon_r}\frac{2\mu^2\alpha}{r_{21}^6}$$

Both interaction energies are linearly proportional to the polarizability of the molecule in which the dipole is induced, and decrease rapidly with increasing intermolecular distance. The weakest kind of Van der Waals interaction is represented by London dispersion forces (**3** in Fig. 1.4). These forces arise when random fluctuations in the electron density of a nonpolar molecule create an instantaneous dipole, which in turn induces a dipole in a nearby nonpolar molecule.[17] The energy of London forces goes with $\frac{1}{r_{21}^6}$ and linearly depends on the polarizability of both the involved molecules. Though London forces are individually weak, they are usually cooperative interactions meaning that the presence of an interaction greatly favours the formation of other analogous interactions.[18]

In general individual energies of van der Waals interaction are under 5 kJ/mol.[19]

1.2.4 Hydrophobic effect

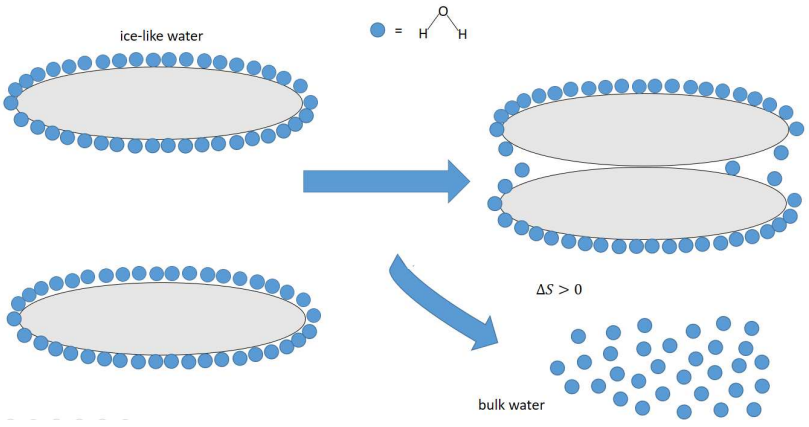

Figure 1.5: Illustration of entropy driven hydrophobic effect: water solvating non polar solutes (left panel) is released into liquid bulk upon solute aggregation (right panel), thus increasing the system entropy.

Hydrophobic effect consists in the aggregation of lipophilic solutes in aqueous environment. The aggregation is due to the repulsion between the solutes and water rather than the affinity of the solutes for each other.

Water is unable to efficiently solvate a lipophilic solute, therefore water molecules maximize the interactions with other water molecules in proximity of the solute. Around a nonpolar solute, the first solvation layer consists of ice-like water, forming the most stable hydrogen bond network possible.[20] The molar entropy of ice-like water is much lower than the molar entropy of bulk water (in general entropy of ordered solids is lower than entropy of liquids). When two solutes aggregate, the exposed lipophilic surface decreases (Fig. 1.5), releasing ice-like water back into the bulk. This process is associated with positive ΔH^0 (bulk water forms a less efficient net of hydrogen bonds) and positive ΔS^0. The positive variation in enthalpy associated with solvent disorganization is typically balanced by the Van der Waals interactions between aggregated solutes. The net contribution is the positive ΔS^0 generated by the solvent release into the bulk, reason why this effect is termed "entropy driven hydrophobic effect".[21–23]

Entropy driven hydrophobic effect is not the only kind of possible hydrophobic effect. In the case of encapsulation of a lipophilic guest by a macrocicle in water, hydrophobic effect is instead enthalpy driven. The solute, once encapsulated in the macrocycle, is blocked into a rigid environment. This causes a loss in entropy ($\Delta S^0 < 0$), which is balanced by the entropy-increasing release of water into the bulk. The solute can interact with the cavity of the macrocycle much better than water, leading to a net negative variation of ΔH^0, which represents the driving force of encapsulation.[24]

Hydrophobic effect has foremost importance in the formation of organic nanoparticles and micelles[25]. The role of hydrophobic effect will be fundamental in Chapters 2, 5 and 10 of this thesis.

1.3 Specific interactions

1.3.1 $\pi - \pi$ stacking

$\pi - \pi$ stacking involves molecules with aromatic systems, i.e. π electrons delocalized over cyclic structures. Symmetric aromatic hydrocarbons (e.g. benzene) typically possess a quadrupole moment, due to the different electronegativity between hydrogens and sp^2 carbons.[26] The electrostatic potential is negative in the internal part of the ring while it is positive for the outer crown of hydrogens (left panel of Fig. 1.6). The situation is different if hydrogens are replaced with very electronegative atoms such as fluorines. In that case the quadrupole itself is reversed (right panel of 1.6).

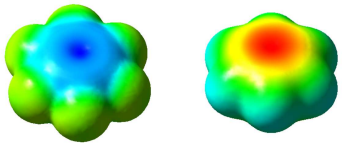

Figure 1.6: Electrostatic potential of benzene (left) and hexafluorobenzene (right) molecules (blue positive, red negative).

The electrostatic interaction between quadrupoles is the leading term in $\pi - \pi$ stacking. Three geometries are possible for a dimer of aromatic molecules (Fig. 1.7): face-to-face, offset parallel and edge-to-face.[27, 28]

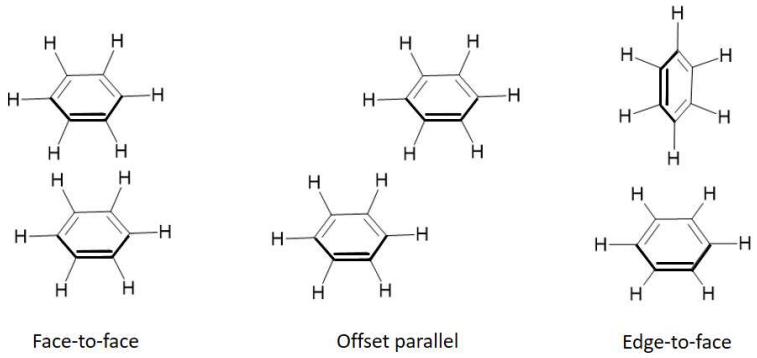

Figure 1.7: Possible geometries of $\pi - \pi$ stacking.

The face-to-face geometry is repulsive and cannot occurr for identical rings, due to the perfect superimposition between quadrupoles.[28] Face-to-face stacking can occurr if the quadrupoles have opposite charge distribution, e.g. benzene interacting with hexafluorobenzene. The offset parallel and edge-to-face geometries overlap the positive part of one ring's quadrupole with the negative region of the other ring's quadrupole, resulting in attractive interaction (ΔH ~ -2 to -8 kJ/mol).[29] $\pi - \pi$ interactions play a pivotal role in charge transport within organic materials.[30]

Other kind of electrostatic interactions involving aromatic rings are cation-π[31] (anion-π for electronpoor aromatic systems)[32] and C-H-π interactions.[33]

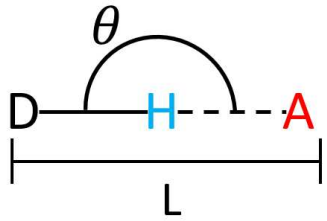

Figure 1.8: Scheme of hydrogen bond interaction, with relevant geometrical parameters described in the text.

1.3.2 Hydrogen bond

Hydrogen bond (HB, Fig. 1.8) is a specific interaction wherein a hydrogen atom linked to an electronegative atom or group (the HB donor) accepts electron density from the lone pairs of another electronegative atom (the HB acceptor).[34, 35] Common donors and acceptors include nitrogen and oxygen, while fluorine is an excellent donor but a poor acceptor. The nature of HB is primarily electrostatic,[36] so that cationic donors and anionic acceptors form stronger HBs.[37] To determine the presence of HB in a supramolecular aggregate or a crystal, the distance between the donor atom D and acceptor atom A (L in Fig. 1.8) should be smaller than the sum of their Van der Waals radii.[38] The D—A distances for HB typically fall in the 2.5-3 Å range. Another important geometrical parameter is the θ angle defined by the positions of donor, hydrogen and acceptor atoms. θ should be close to 180° in order to have a strong HB.[38] This characteristic makes the HB interaction strongly directional and an apt candidate to build a variety of supramolecular architectures.[39]

HB is deeply affected by the specific microenvironment in which it is formed.[40] The solvent can compete with the formation on HBs both with a nonspecific mechanism, linked to polarity, and a specific mechanism, linked to the solvent possibility to donate or accept HB.[41] HBs are nonspecifically screened by the static dielectric constant of the medium, due to their electrostatic nature. Moreover, if the solvent can donate or accept HB, the molecules are much likely to interact with the solvent than with each other, as the solvent is in large excess.[42]

For instance, amides form HB dimers in non polar solvent CCl_4, but are in their monomeric form in dioxane, which is polar and a moderate HB acceptor.[43]

HB strength is greatly increased if a resonance structure either brings a negative charge on the acceptor or a positive charge on the donor (resonance assisted hydrogen bonding, RAHB). A classic example is the aforementioned intermolecular HB between amides (Fig. 1.9).[44, 45]

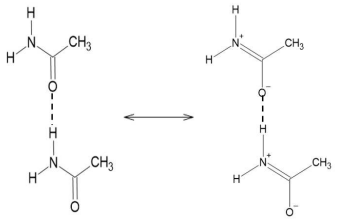

Figure 1.9: HB between two molecules of acetilamide, in their neutral (left panel) and ionic (right panel) resonance structures.

RAHB is also a stabilizing force of the double helix of DNA, wherein donors and acceptors are organized on arrays in complementary strands.[46] When HB donors and acceptors form an array of bonds, secondary interactions come into play. If donors are disposed on a row, opposite to a row of acceptors, secondary interactions are not favourable, whereas they reinforce the array if donors an acceptors alternate within the same row (Fig. 1.10).[47]

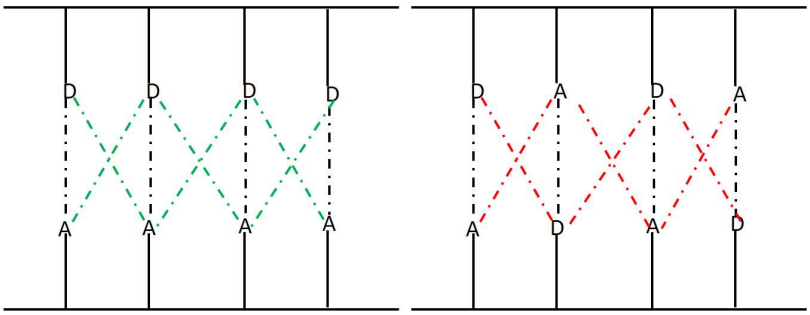

Figure 1.10: Scheme of positive (left panel, favourable secondary interactions are represented as green dashed lines) and negative (right panel, unfavourable secondary interactions are represented as red dashed lines) secondary interactions in an array of HBs.

Chapter 3 will focus on a molecule capable of assembling into dimers by forming an array of hydrogen bonds. Both resonance effects and secondary interactions will come into play to determine the dimer geometry.

1.3.3 Halogen bond

When a halogen atom is bound to an electronwithdrawing group, a positive region of electrostatic potential is formed on the halogen atom, along the axis joining it with the electrowithdrawing group.[48, 49] This region of positive potential is called σ-hole, and is prone to accept electron density from a Lewis base, forming a halogen bond (Fig. 1.11).[50] Being an electrostatic interaction, halogen bond is nonspecifically screened by polar solvents. The strength of halogen bonding mainly depends on the σ-hole size, which in turn is linked to the polarizability of the halogen atom. Fluorine is the worst halogen bonding acceptor, and iodine is the best (Fig. 1.12).[51]

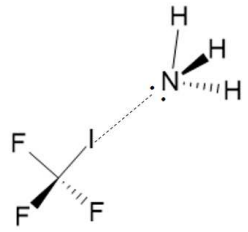

Figure 1.11: Halogen bond between trifluoroiodometane and ammonia.

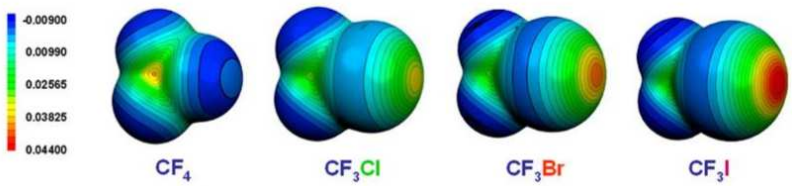

Figure 1.12: Electrostatic potential (ESP) of a series of trifluorohalogens. The magnitude of σ-hole increases with halogen polarizability from fluorine to iodine.

Halogen bond often competes with S_N2 reaction mechanism, wherein the halogen bond acceptor acts as a nucleophile rather than a base. S_N2 is disfavoured by sterically hindered electrophilic centers, which therefore favour halogen bond formation.[52]

1.4 Excited state interactions

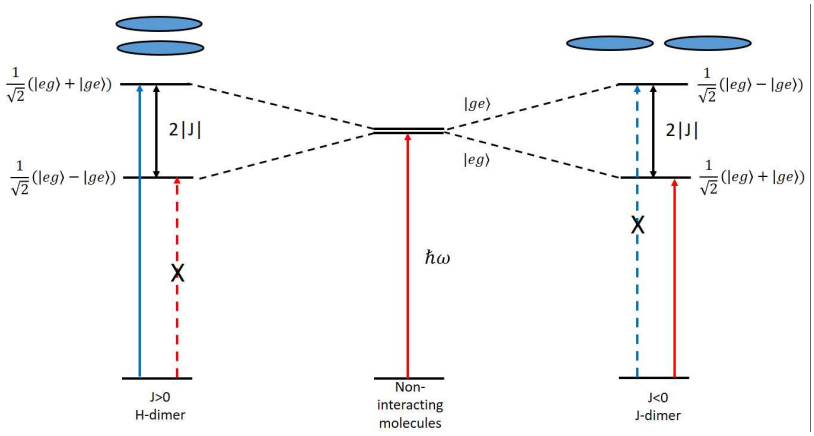

Figure 1.13: Scheme of levels involved in exciton interaction between two molecules. H-dimer (left panel), non interacting molecules (center panel) and J-dimer (right panel).

While the geometry of a molecular aggregate is determined by ground state interactions (see previous sections), excited state interactions (often termed excitonic interactions) determine its spectroscopic properties, making the aggregate a distinct spectroscopic entity with respect to the monomer.[53]

Let's consider a dimer of identical molecules. We assume each molecule can be either in the ground state $|g\rangle$ or in an excited state $|e\rangle$, in the hypothesis all other excited states fall outside the spectral window of interest (we usually refer to UV-Vis wavelengths, 300-800 nm). If the two molecules are not interacting, we can write the system electronic states as the direct product between the monomer states. Therefore we have four states: $|gg\rangle$, the degenerate $|ge\rangle$ and $|eg\rangle$, and the doubly excited state $|ee\rangle$. The exciton approximation neglects the role of the doubly excited state in defining the spectroscopic properties of the system.[54, 55]

As the single excitations, $|ge\rangle$ and $|eg\rangle$, are degenerate, a small perturbation is enough to split them in a symmetric and an antisymmetric combination, thus lifting their degeneracy. The splitting is a consequence of the electrostatic interaction between transition dipole moments of the monomers. This electrostatic interaction is usually termed J. In a point-dipole approximation J can be expressed as:

$$J = \frac{1}{4\pi\epsilon_0\epsilon_r} \frac{\vec{\mu}_1 \cdot \vec{\mu}_2 - 3(\hat{r}_{12} \cdot \vec{\mu}_1)(\hat{r}_{12} \cdot \vec{\mu}_2)}{r_{21}^3}$$

where $\vec{\mu}_{1/2}$ are the transition electric dipole moments of the molecules, $\hat{r}_{21}$ is the unit vector which joins them and r_{21} the distance between them.

The resulting splitting between the two states, often referred to as the exciton gap,[53] is $2J$. If the excited state $|e\rangle$ is dipole forbidden in the monomer, meaning that $|\vec{\mu}_{1/2}| \sim 0$, the exciton gap is very low or null.

This is the case of triplet states, which are left unscathed by exciton interactions.

The splitting of single excitation gives rise to an in-phase combination and an out-of-phase combination of $|ge\rangle$ and $|eg\rangle$ (Fig. 1.13). The in-phase combination is optically allowed, with twice the oscillator strength of the monomer, while the out-of-phase combination is forbidden.[55] The relative energy of the two combinations depends on the sign of J: if $J > 0$ (repulsive interaction) the in-phase combination lies at higher energy, while it is at lower energy if $J < 0$ (attractive interactions). Repulsive interactions happen for cofacial dipoles, while attractive interactions happen for head-to-tail oriented dipoles. The aggregates are respectively defined H and J aggregates. As a consequence of Kasha state being bright (dark) J(H)-aggregates are emissive (not emissive).[53]

Interestingly, exciton interaction vanishes when transition dipoles are orthogonal. In this case no splitting is observed and optical properties are identical to the monomer (Fig. 1.14).[56]

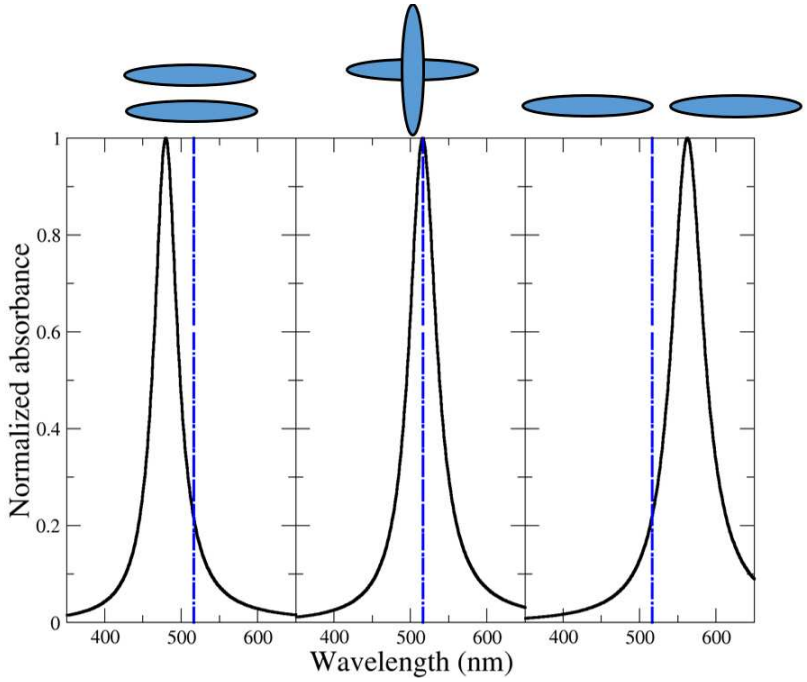

Figure 1.14: Normalized absorption spectra of a cofacial H-dimer (left panel), a dimer of orthogonal molecules (middle panel) and a head-to-tail J-dimer (right panel). The monomer absorption wavelength is marked by a dashed blue line.

For dipoles forming an angle between 0° and 180°, both exciton states become partially allowed, and the system acquires supramolecular chirality.[57] This will be discussed in detail in Chapter 6.

Excitonic interactions and their effect on spectroscopic properties will be the centerfold of chapters 2, 3 and 4.

1.5 Excimers

Organic excimers are a special kind of supramolecular aggregate, typically formed between one molecule in its ground state and another in its excited state.[58] When both molecules are in their ground state, the interaction between them is weak, and they behave independently. However, upon

photoexcitation of one molecule, its charge distribution changes, making interaction with another ground-state molecule more favorable. If the distance between the two molecules is suitable (3-4 Å)[59] they can associate, forming an excimer (Fig. 1.15).

Absorption spectra are the same as the monomer, since excimers only form after photoexcitation, but emission properties are usually different, both in terms of emission energy and lifetime of the excited state.[60] The emission of the excimer is usually red shifted with respect to the monomer, and the fluorescence lifetime revealed on it is longer due to the time taken by geometrical rearrangement to form the excimer. In some cases the distance and relative orientation of the two molecules is already ideal to form the excimer. As a consequence, no geometrical rearrangement is required, thus making fluorescence lifetime shorter. This kind of excimer is referred to as a "preformed excimer".[61]

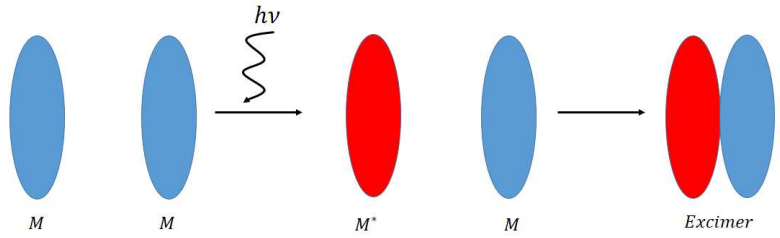

Figure 1.15: Three stages of excimer formation. From left to right: non interacting molecules, both in the ground state; one molecule is photoexcited, the other is not; the excited state molecule interacts with the ground state molecule forming the excimer.

The formation of excimers is strongly temperature-dependent, with several possible regimes.[62] When two molecules associate, both entropy and enthalpy decrease ($\Delta S^0 < 0$, $\Delta H^0 < 0$), making the process exothermic and more favorable at low temperatures. However, the process can also be diffusion-limited, as the monomers must come close enough to interact. In such cases, an increase in temperature can facilitate excimer formation by enhancing molecular diffusion.[63]

Chapter 5 will follow the variation of excimer to monomer ratio as a function of temperature, choosing fluorescence spectroscopy as probing technique.

1.6 Outline

This outline refers to the first part of the thesis, focused on supramolecular aggregation and its spectroscopic effects. The second part of the thesis (from Chapter 6 onwards) will instead address chirality, both at the molecular and supramolecular level.

Chapter 2 concerns the preparation, linear and non linear optical characterization, and theoretical modelling of aggregates of charged cyanine dyes. The different screening of ground state and excitonic interactions by a polar medium is discussed in detail. Chapter 3 presents an extensive characterization of a molecule that forms arrays of hydrogen bonds in non polar solvents. Molecular dynamics and *ab initio* calculations are performed to explain the ground state and the spectroscopic properties of the molecule and its aggregates. Chapter 4 focuses on a a series of BODIPY J-aggregates, where exciton coupling and reductive photoinduced

electron transfer (rPET) compete to determine the fluorescence spectroscopy of the aggregates. The role of temperature and environmental polarity on the emission properties is carefully evaluated. At last, Chapter 5 describes the formation of excimers by organic radicals encapsulated in organic nanoparticles, and how their fluorescence properties vary with temperature, which makes them suitable nanothermometers for biological tissues.

Aggregates of Cyanine Dyes: Molecular Vibrations and Electrostatic Screening

2

2.1 Introduction

Cyanines are a widespread family of dyes, constituted by heterocyclic electron donors or acceptor groups linked through a polymethinic bridge.[64, 65] Cyanines are of interest for several applications, including photovoltaics,[66] bioimaging,[67–70] phototherapy,[71–73] optical devices,[74, 75] sensors [76] etc. The tendency of cyanines to self-organize in aggregates is known since 1937 when Jelley and Scheibe first described the formation of cyanine aggregates in solution.[77, 78] The photophysics of cyanine aggregates strongly depends on the details of the molecular packing, which, in turn, are affected by several factors, including the length of the polymethinic bridge, the presence of non conjugated alkyl chains and their length, the environment (including the presence of additives) etc.[79–84] The possibility to widely tune the material properties makes cyanine aggregates extremely promising for applications in photonics, electronics, imaging, etc.[85–89] A robust theoretical approach must therefore be developed to relate the intriguing properties of cyanine aggregates to their supramolecular structure.

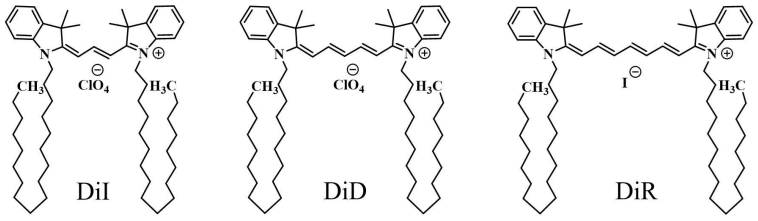

Figure 2.1: Molecular structures of the three cyanine dyes studied in this work.

Here, we present a joint experimental and theoretical work on self-assembled aggregates of DiI, DiD and DiR (Fig. 2.1), a family of cyanine dyes commercialized for fluorescence microscopy applications. The three molecules only differ in the length of the π-conjugated chain. An extensive spectroscopic study is carried out on the solvated dyes and on the aggregates in liquid suspension as well as embedded in a jelly matrix. In water/ethanol mixtures the dyes aggregate with important effects on linear (absorption and emission) and nonlinear (two-photon absorption) spectra. Specifically, we recognize the formation of J-aggregates for the shorter molecule DiI, and of H-aggregates for DiD and DiR. This study offers a solid basis for a detailed theoretical analysis shedding light on the intertwined role of intermolecular interactions, molecular polarizability, vibronic effects and environmental screening on the rich spectral properties of cyanine aggregates.

As for the theoretical modelling, we adopt a bottom-up strategy that relies on a comparatively simple and reliable model for the isolated dye in solution. An accurate description of low-energy excitations of cyanine dyes is challenging and this class of molecules is often adopted to test the validity of theoretical approaches.[90–93] Here we work in the spirit of essential-state models (ESM) and describe the low-energy physics of cyanine dyes in terms of few electronic basis (diabatic) states coupled to few effective molecular vibrations. The model, parameterized against experimental data, was successfully adopted to describe the photophysics of linear symmetric dyes [94, 95], including cyanines [96, 97]. The model accounts for the non-trivial evolution of linear and nonlinear spectra with

the solvent polarity, driven in cyanine dyes with long polymethinic chains by symmetry-breaking phenomena occurring in the ground state.

Once the ESM for the molecular unit is defined and accurately parameterized against experimental data, we build the aggregate model, introducing intermolecular electrostatic interactions. ESMs have been successfully applied to several types of molecular aggregates [98–103] and have been recently adopted to investigate the reliability of the exciton approximation in aggregates of polarizable dyes with either a non-polar or polar structure.[104, 105]

Since cyanine aggregates are formed in highly polar environments (like, e.g. water/alcohols mixtures), special care is needed to properly address the screening of electrostatic intermolecular interactions. Polar solvents are characterized by high dielectric constants, that effectively screen the interactions between static charges. On the other hand, excitonic interactions are related to transition dipole moments (or more generally to transition charge distributions) that oscillate at optical frequencies. Accordingly, these latter interactions must be screened by the dielectric constant at optical frequency, i.e. the squared refractive index. Two different screening regimes must therefore be considered, as already discussed in a previous work on dimers of quadrupolar dyes bearing positive charges.[106] Here, in an effort to also address nonlinear optical spectra of aggregates of cyanine dyes, we extend the model to account for molecular vibrations.

In the present work, the detailed spectroscopic characterization of DiI, DiD and DiR in solution is described, with a discussion of UV-Vis, fluorescence and two-photon absorption spectra. The preparation procedure and the linear and nonlinear spectroscopic characterization of the aggregates are addressed. A detailed theoretical investigation of monomers and aggregates is presented, based on essential-state models. Finally, the results of modelling are compared with experimental data, emphasizing the non-trivial role played by molecular vibrations and electrostatic screening effects.

2.2 Experimental Methods

A general description of the employed methods (linear and non linear spectroscopic measurements, and dynamic light scattering) is reported in the Experimental section. Here we report the details strictly relevant to the present chapter.

2.2.1 Materials

1,10-dioctadecyl-3,3,30,30-tetramethyl-indocarbocyanine perchlorate (DiI), 1,10-dioctadecyl-3,3,30,30-tetramethyl-indodicarbocyanine perchlorate (DiD) and 1,1′-dioctadecyl-3,3,3′,3′-tetramethyl-indotricarbocyanine iodide (DiR) were purchased from ThermoFisher (Invitrogen). Agarose (low electroendosmosis, EEO $\leq$ 0.1) was obtained from Acros Organics. All chemicals were used without further purification. Spectra grade or HPLC solvents were used to prepare solutions. Bi-distilled water was used to prepare aggregates.

2.2.2 Linear spectroscopic characterization

Fluorescence quantum yields and lifetimes for DiI and DiD in EtOH were taken from Ref [107]. In the case of DiR in EtOH, the fluorescence quantum yield was estimated using HITC in EtOH as a reference ($\Phi_f = 0.28$ from Ref [108]).

Lifetime decay of DiR in ethanol has been collected exciting the sample with a 405 nm pulsed diode laser (pulse duration < 200 ps) at a repetition rate of 1 MHz, collecting the emission at 780 nm.

2.2.3 Nonlinear spectroscopic characterization

The two-photon absorption (TPA) cross section σ_2, which expresses the probability of the TPA process, can be measured using a relative method. Fluorescein in NaOH 0.1 M was used as a reference ($\Phi_{f,ref} = 0.9$), considering the absolute values of cross section reported in the literature.[109] The following equation was used to estimate the sample's cross section as a function of the incoming wavelength λ:[110]

$$\sigma_2(\lambda) = \sigma_{2,ref}(\lambda)\frac{\Phi_{f,ref}}{\Phi_f}\frac{C_{ref}}{C}\frac{P^2_{ref}(\lambda)}{P^2(\lambda)}\frac{F(\lambda)}{F_{ref}(\lambda)}\frac{\eta_{ref}}{\eta} \tag{2.1}$$

where Φ_f is the fluorescence quantum yield, C the solution concentration, F the integrated two-photon excited fluorescence (TPEF) spectrum, P the laser power and η the refractive index of the solvent. The subscript "ref" indicates the properties of the reference, while all the others terms refer to the sample. All measurements were carried out employing a Two-Photon Microscope Nikon A1R MP+ Upright, described in more detail in the 10.4 section. The reliable comparison of the integrated TPEF spectra of sample (F) and reference (F_{ref}) requires to collect the major part of the TPEF spectra and correct them for the wavelength-dependent sensitivity of the employed detector. This is possible only for the spectral detector coupled to the microscope, so only for samples whose emission band mainly falls inside its sensitivity region (400-650 nm). Unfortunately, NDDs do not allow to correct the TPEF intensity (the signal collected by the NDDs is relevant to the whole bandwidth of the corresponding bandpass filter). The TPEF signal was measured with NDDs and/or with the spectral detector, according to the excitation and fluorescence spectral ranges of the sample. More specifically, in the case of DiI and DiD, for excitation between 700 nm and 1080 nm, the TPEF is detected using the spectral detector (for DiD only a tiny portion of the emission spectrum falls inside the 400-650 region, so that a TPEF signal could be measured with the spectral detector but a scale factor accounting for the missing part of the emission spectrum, needed to estimate the cross section, could not be reliably guessed). For excitation above 820 nm, TPEF is detected using the green (for DiI) and the red (for DiD) NDDs. The overlapping excitation region (820-1080 nm) was used to merge the two parts of the excitation spectra acquired with different detectors. For DiR in solution, only the far-red NDD is suitable for the detection of its TPEF signal and the sample was excited in the 900-1300 nm spectral region. For the explained reasons, the TPA cross section could not be quantified for DiD and DiR, whose fluorescence (or most of it) falls outside the

region covered by the spectral detector: for these compounds, only the bandshapes of the corresponding TPA spectra are available. TPEF of DiI, instead, could be (almost entirely) measured with the spectral detector, so that the TPA cross section could be retrieved for this sample. As TPA involves the simultaneous absorption of two photons, its probability should be quadratic with the excitation power. For TPA spectra collected in solution, deviation from quadraticity resulted below ±15% repeating the measurements with three different laser powers. For aggregates in suspension, the deviation from quadraticity resulted to be more critical (up to ±25% in a few points) due to the intrinsic non-homogeneity of the sample. For TPA spectra of aggregates in the gel, the quadraticity was not tested to prevent photobleaching of the sample.

Liquid samples (solutions and suspensions) were analyzed in quartz cuvettes placed horizontally under the microscope objective. Each cuvette was completely filled with the liquid sample to avoid the presence of air between the upper wall and the solution. Distilled water was employed to ensure the contact between the objective and the cuvette. Each measurement has been conducted focusing the excitation beam as near as possible to the cuvette upper wall, to avoid artifacts due to the different refractive index of the solvent and inner-filter effects.

2.2.4 Preparation of aggregates

Aggregates in water/ethanol suspension

DiI aggregates. 65 mg of a previously sonicated 1220 μM stock solution of DiI in ethanol are put into a dark vial. Ethanol is added until reaching 1.5 g of mass, followed by bi-distilled water, rapidly added at room temperature until the mixture is 5 g in weight, in order to obtain a 70/30 m/m mixture of water/ethanol. The resulting mixture is homogenized at the vortex for 40 seconds.

DiD aggregates. 149 mg of a previously sonicated 530 μM stock solution of DiD in ethanol are put into a dark vial. Ethanol until reaching 0.5 g of mass and then bi-distilled water are rapidly added until the mixture is 5 g in weight, in order to obtain a 90/10 m/m solution of water/ethanol. The resulting mixture is homogenized at the vortex for 40 seconds.

DiR aggregates. 40.82 mg of a a previously sonicated 1970 μM stock solution of DiR in ethanol are put into a dark vial. Ethanol until reaching 0.5 g of mass and then bi-distilled water are rapidly added until the mixture is 5 g in weight, to obtain a 90/10 m/m solution of water/ethanol. The resulting mixture is homogenized at the vortex for 40 seconds.

Aggregates in the gel. 0.5 g of agarose powder are weighed in a 50 mL beaker and 25 mL of bi-distilled water are added, forming a white suspension. The suspension is heated up to its boiling point. After boiling for 20 minutes, the agarose powder is completely dissolved and a water-clear solution is obtained. The agarose solution is cooled down until it reaches 40 °C, then 1 mL of aggregates suspension in water/ethanol mixture is added. The resulting suspension, containing the agarose and the aggregates, is poured in a plastic cuvette to register UV-Vis absorption and in a small circular plastic holder for linear fluorescence and two-photon excited microspectroscopy. We point out that at 40°C

the suspension is still liquid and the hydrogel is then obtained after cooling down at room temperature. The temperature at which aggregates is added is crucial: if it is too high aggregates could break or modify, if it is too low they wouldn't diffuse homogeneously into the bulk due to its high viscosity. In order to verify that aggregates are not significantly damaged in the process, absorption and emission of the dye-containing gel were acquired (Fig. 2.8).

2.3 Results and discussion

2.3.1 Spectroscopic characterization

Cyanine dyes in solution

One-Photon Absorption (OPA), emission and Two-Photon Absorption (TPA) spectra of DiI, DiD and DiR dissolved in ethanol (a good solvent for cyanine dyes[25]) are reported in Fig. 2.2. All spectra move to the red upon increasing the length of the polymethinic bridge, in line with the increased delocalization length. At the same time, the relative intensity of the 0-1 vibronic transition progressively decreases as the length of the molecule increases, both in absorption and in emission, an indication that the equilibrium geometries of the ground and first excited state become more similar for longer cyanines. The large molar extinction coefficients (Table 2.2) are typical of cyanine dyes, and are related again to the delocalization of electrons involved in the transition. Fluorescence quantum yields are high, particularly with reference to the emission spectral region which goes from yellow (DiI) to red (DiD) to far-red (DiR). Fluorescence lifetimes are in the nanosecond range, as reported in Tab. 2.1.

Table 2.1: Fluorescence average lifetimes of cyanine monomers in ethanol. [a] From Ref [107].

Cyanine	$\langle\tau\rangle$ (ns)
DiI	0.40[a]
DiD	1.31[a]
DiR	1.22

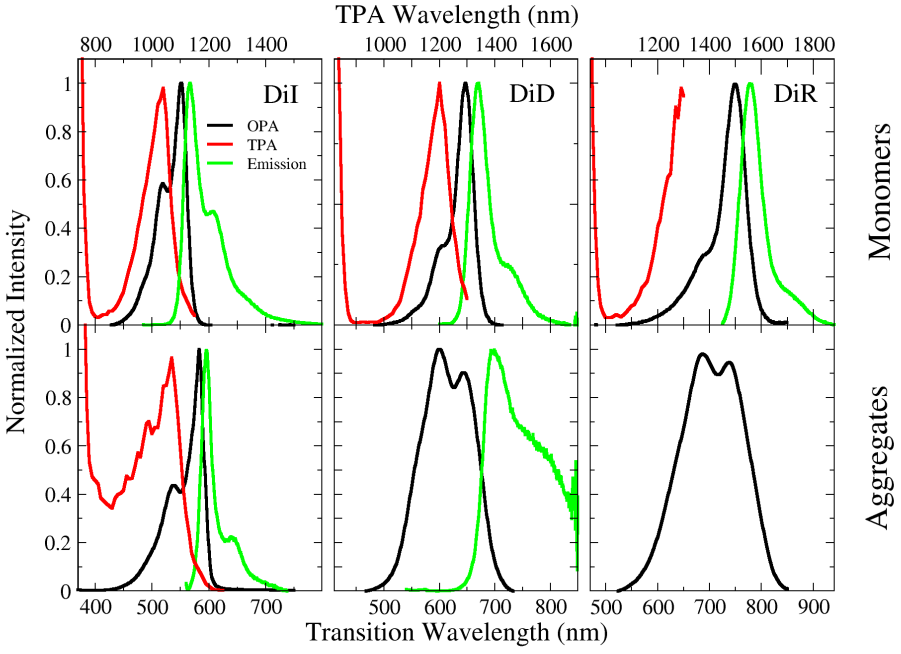

Figure 2.2: OPA (black lines), TPA (red lines) and emission (green lines) spectra of DiI, DiD and DiR monomers in ethanol (top panels) and aggregates in water/ethanol mixtures (bottom panels).

	λ^{abs}_{max} (nm)	λ^{em}_{max} (nm)	ϵ_{max} (L mol^{-1} cm^{-1})	Φ_f	Stokes shift (cm^{-1})
DiI	550	567	140.000[a]	0.1[a]	487
DiD	647	670	246.000[a]	0.37[a]	511
DiR	750	780	305.000	0.37	513

Table 2.2: Spectroscopic data of cyanine dyes dissolved in ethanol. Φ_f indicates the fluorescence quantum yield. [a] from Ref [107]

OPA and emission spectra are mirror images and the Stokes shifts are negligible (Tab. 2.2), suggesting minor structural and solvent reorganization after excitation. Accordingly, marginal effects of polar solvation are expected, as confirmed by the negligible dependence of absorption and emission spectra on the solvent polarity (Fig. 2.3).

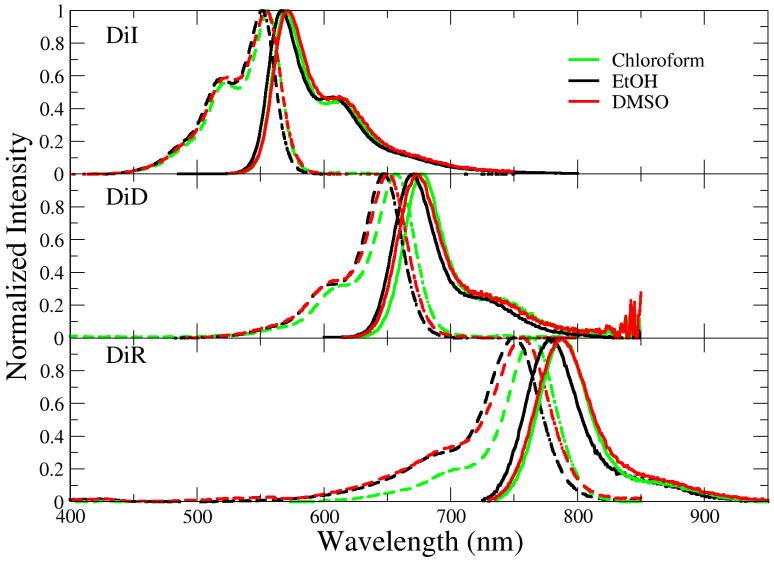

Figure 2.3: Normalized absorption (dashed lines) and emission (continuous lines) spectra of DiI, DiD and DiR in solvents of different polarity.

TPA spectra of the three dyes in ethanol solution (Fig. 2.2) were collected with a multiphoton microscope, measuring the two-photon excited fluorescence (TPEF, technical details are reported in the section 2.2). TPA has different selection rules with respect to OPA, and specifically, symmetric (*gerade*) states, that are OPA forbidden, are bright in TPA.

The TPA spectra of the three dyes show the tail of an intense band (350-450 nm transition wavelength) whose maximum is not accessible with our experimental setup. In this spectral region, the OPA intensity is negligible, suggesting that this state is described by a symmetric (*gerade*) wavefunction. However, in the region where the OPA band is observed, a weak TPA signal is collected, whose maximum is located at the same frequency as the 0-1 vibronic transition of OPA (due to the setup limitation, the maximum of this TPA band is not accessible for DiR).

The TPA cross section was measured only for DiI (Fig. 2.4), amounting to σ_2 = 46 GM (Goeppert-Mayer, 1 GM = 10^{-50} cm^4 s photon^{-1}) at 520 nm. The experimental setup for measuring TPA spectra is not suitable for the measurement of the cross section of DiD and DiR (more details are reported in the Experimental Methods section).

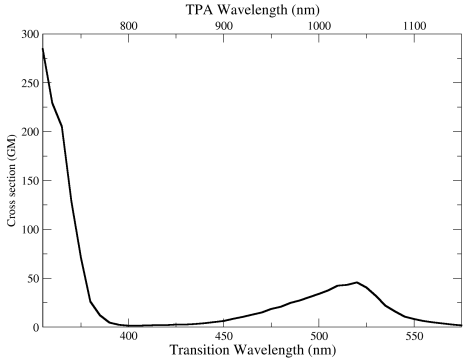

Figure 2.4: TPA cross section of DiI in ethanol as a function of wavelength, expressed in Goeppert-Mayer (GM) units.

Cyanine aggregates

Aggregates of the three dyes were prepared in water/ethanol mixtures, as described in the section 2.2. Aggregation is confirmed by dynamic light scattering (DLS) measurements, as reported in Tab. 2.3. The suspensions of DiI and DiR aggregates show a bimodal size distribution, with average dimensions of ~ 73 nm and ~ 83 nm, respectively (additional details about DLS are reported in Table 2.3 and Fig. 2.5). A single population of nanoparticles is detected for DiD, with an average hydrodynamic diameter of ~ 38 nm.

Table 2.3: DLS data relative to DiI aggregates in water/ethanol 70/30 (m/m) and DiD, DiR aggregates in water/ethanol 90/10 (m/m). PdI indicates the polidispersity index of the suspension. The mean sizes of the peaks refer to the intensity distributions. Data were collected three hours after preparation, at 25°C and averaged over 3 measurements.

Aggregates	Z-average (nm)	PdI	Peak 1 mean size (nm)	Peak 1 intensity area %	Peak 1 volume area %	Peak 2 mean size (nm)	Peak 2 intensity area %	Peak 2 volume area %
DiI 70-30	83.1	0.461	120	89.6	6.1	14.1	6.8	93.4
St. Dev %	2.73	4.48	13.5	2.42	30.5	11.4	14	1.76
DiD 90-10	37.8	0.234	42.2	96.6	99.2	/	/	/
St. Dev %	6.32	11.2	10.6	3.1	0.7	/	/	/
DiR 90-10	72.8	0.327	85.7	93.2	22.4	18.8	6.8	77.6
St. Dev %	1.54	5.83	3.17	1.16	12.5	3.76	15.9	3.61

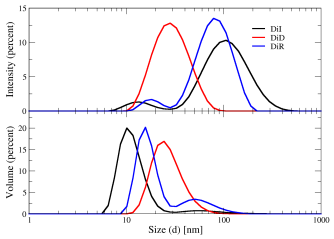

Figure 2.5: Size distributions by intensity (top panel) and by volume (bottom panel) of DiI, DiD and DiR aggregates obtained three hours after preparation as the average of three measurements each. Measurements were performed at 25°C.

Hydrodynamic diameters expressed as average size values (Z-averages) or as the mean values of each peak were evaluated from intensity size distributions. Since the intensity distributions amplify the amount of larger particles, volume distributions have been reported to better appreciate the presence of smaller aggregates in the DiI and DiR suspensions (Fig. 2.5). The relative areas of the two peaks in the volume distributions clearly show that most of the aggregates belongs to the population with smaller size. More details about DLS measurements are reported in the 10.4 section.

OPA, emission and TPA spectra of aggregates are shown in the bottom panels of Fig. 2.2 and spectroscopic data are summarized in Tab. 2.4. OPA and emission spectra of DiI are clearly consistent with J-aggregation: both bands are shifted to the red if compared to the monomer, the Stokes shift is marginal, and the ratio of the 0-1 vs the 0-0 vibronic band decreases, pointing to an exciton delocalization length ~ 2.[111, 112] On the opposite, DiD and DiR spectra suggest H-aggregation: the OPA band is broader and blue-shifted vs the monomer band and fluorescence is suppressed. Indeed DiR fluorescence was not detected, while a weak emission is observed for DiD, largely red-shifted with respect to OPA. This behavior is consistent with the observation of a vibronically-induced fluorescence from H-aggregates.[53, 104] The TPEF technique used to collect TPA spectra only works for emissive species, so we were able to obtain data only for DiI aggregates (DiD aggregates emission is too weak). Much as with monomers, TPA spectra of DiI aggregates are blue-shifted compared to the OPA, with the TPA maximum located at the frequency of the 0-1 vibronic band of the OPA spectrum of the aggregates.

Table 2.4: Spectroscopic and DLS data of cyanine aggregates in water/ethanol mixtures. Z-average is the average hydrodynamic diametre of the nanoparticles.

Aggregates	λ^{abs}_{max} (nm)	λ^{em}_{max} (nm)	Stokes shift (cm^{-1})	Z-average (nm)
DiI	586	596	278	83.1
DiD	600	700	2381	37.8
DiR	690	n.d.	n.d.	72.8

Absorption spectra of DiI aggregates were collected as a function of temperature (Fig. 2.6). After the first temperature cycle, absorption changes significantly with respect to spectra collected just after preparation, suggesting that the prompt formation of aggregates is kinetically-driven, while thermal treatment allows for the formation of thermodynamically-favored aggregates. This is supported by the observation that absorption does not vary after a second temperature ramp. For DiD aggregates, variations after heating are smaller and could be due to partial breaking of aggregates (Fig. 2.7).

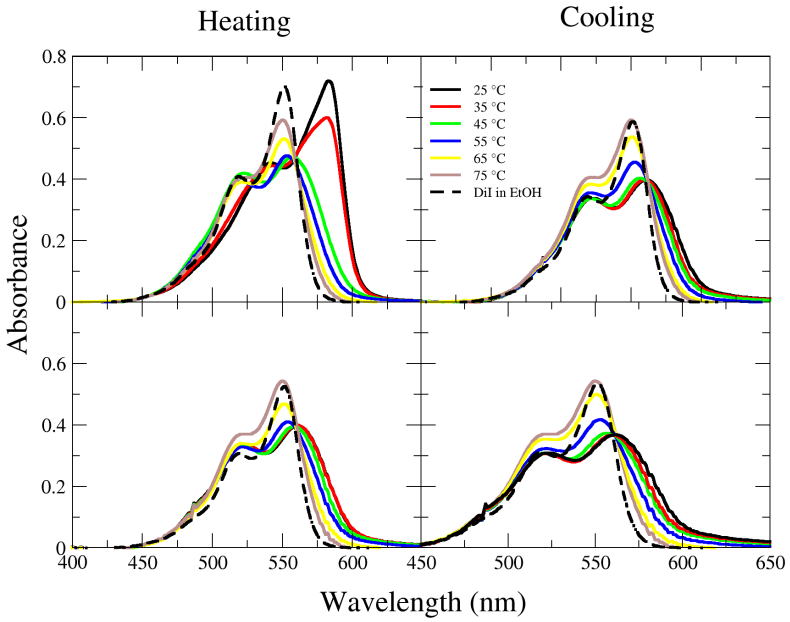

Figure 2.6: Upper panel: first cycle of heating (left) and cooling (right) of DiI aggregates in water/ethanol 70/30 (m/m). Lower panel: second cycle of heating (left) and cooling (right) of DiI aggregates in water/ethanol 70/30 (m/m).

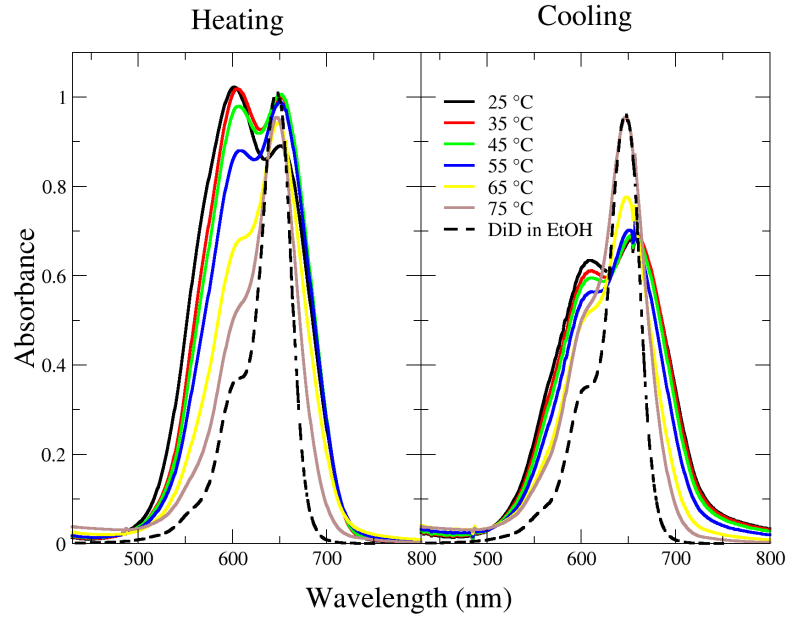

Figure 2.7: Left: heating of DiD aggregates in water/ethanol 90/10 (m/m). Right: cooling of DiD water/ethanol 90/10 m/m aggregates

The good fluorescence of DiI allows for the microscopic characterization of aggregates with the two-photon microscope. To such an aim, DiI aggregates were dispersed in an agarose hydrogel (see the Experimental Methods section for the preparation procedure), a highly viscous medium that hinders the diffusion of nanoparticles during the measurement. In this way, the fluorescence collected from immobilized aggregates allows to obtain images and spectra from single aggregates. Firstly, we verified that OPA, emission and TPA spectra collected from the hydrogel coincide with the ones collected in suspension (Fig. 2.8), thus confirming that the hydrogel environment does not significantly affect the aggregate spectroscopic behavior.

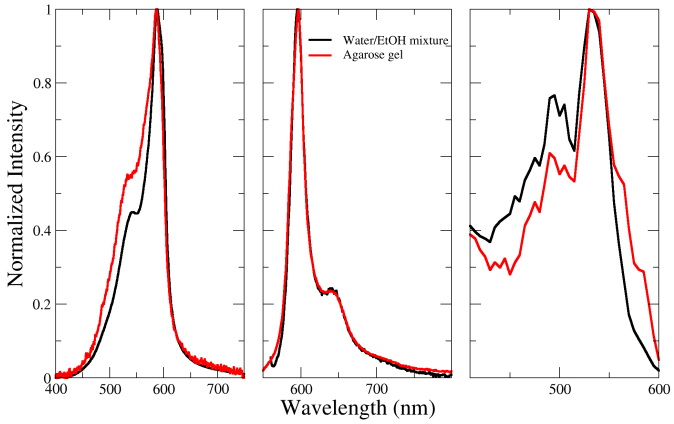

Figure 2.8: From right to left OPA, emission and TPA spectra of DiI aggregates suspended in the water/ethanol mixture (black line) and in the agarose gel (red line).

Fig. 2.9 shows a TPEF image of DiI aggregates collected with the two-photon microscope. Aggregates of different sizes and different colors are imaged, in line with DLS data that point to polydisperse suspensions. The two bigger aggregates, labelled as "G" and "R" in Fig. 2.9, were selected to collect single-aggregate fluorescence and TPA spectra, shown in the left panel of Fig. 2.9. Aggregate "G" is greenish, with an emission spectrum peaked at 585 nm, almost overlapping the spectrum collected on the bulk hydrogel or equivalently the spectrum collected from the liquid suspension. Aggregate "R" shows weak red fluorescence, as typical of H-aggregates,[104] with a broad spectrum, extending from ~600 nm downwards, outside of the region accessible with the spectral detector coupled to the microscope. The TPA bandshapes of the two aggregates are very similar, at least within the 10-nm spectral resolution of the setup. The TPA spectrum of the "R" aggregate is slightly red-shifted with respect to the green aggregate and the total TPA spectrum of the hydrogel is intermediate between them. We conclude that DiI forms both H and J-aggregates with distinctively different fluorescence spectra, and the overall emission of the suspension and of the gel is largely dominated by the fluorescence of J-aggregates, which is much more intense than the emission from H-aggregates.

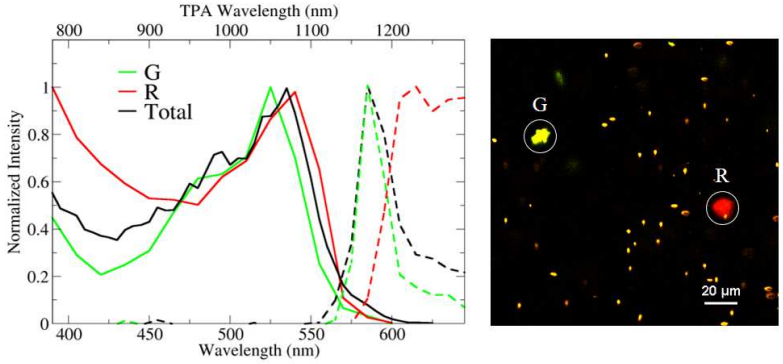

Figure 2.9: Left panel: two photon excited emissions (dashed lines) and excitation (continuous lines) spectra of single nanoparticles in the gel. Right panel: two-photon excited fluorescence images of the aggregates chosen for single aggregate spectra.

2.3.2 Essential-state models for monomers and aggregates

The three-state model for monomers

To describe the low-energy physics of the three cyanine dyes of interest, we adopt a three-state model originally developed for linear quadrupolar dyes,[94] and then extended to cyanine dyes.[96, 97] For the sake of clarity, here we just outline the model, but more details can be found in the original papers.[94, 96, 97]

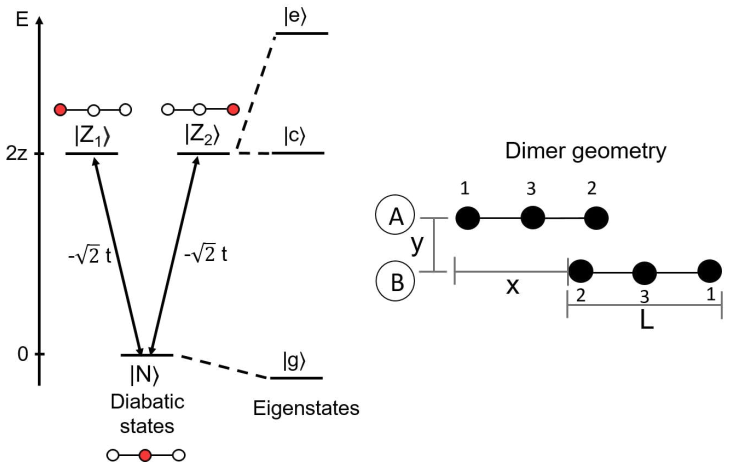

Figure 2.10: Left: scheme of diabatic basis states $|N\rangle, |Z_1\rangle, |Z_2\rangle$ and of the eigenstates $|g\rangle, |c\rangle, |e\rangle$ of a cyanine monomer. The red filled circles show where the net charge is located in the basis states. Right: schematic representation of a cyanine dimer. The black filled circles represent the three sites, numbered as 1, 2 and 3, of the two molecules, labeled as A and B. L, x and y are the geometrical parameters that define the arrangement of the two molecules in the dimer.

As sketched in Fig 2.10, we consider three molecular sites, 1 and 2 corresponding to the two terminal electron donor (D) sites and 3 corresponding to the polymethinic bridge, π. The electronic structure is then minimally described by three basis states, corresponding to the three main resonance structures: $|N\rangle$ representing the state D-π^+-D while $|Z_1\rangle$ and $|Z_2\rangle$ represent D$^+$-π-D and D-π-D$^+$, respectively. The energy of the $|N\rangle$ state is set to 0, while the two degenerate states $|Z_1\rangle$ and $|Z_2\rangle$ have energy $2z$. Charge hopping is allowed from the central bridge to the lateral groups, with $-\sqrt{2}t$ measuring the matrix element mixing both $|Z_1\rangle$ and $|Z_2\rangle$ with $|N\rangle$. The electronic Hamiltonian written on the diabatic basis ($|N\rangle, |Z_1\rangle, |Z_2\rangle$) for a cyanine reads:

$$\hat{H}_{el} = \begin{pmatrix} 0 & -\sqrt{2}t & -\sqrt{2}t \\ -\sqrt{2}t & 2z & 0 \\ -\sqrt{2}t & 0 & 2z \end{pmatrix} \tag{2.2}$$

Introducing the auxiliary operators:

$$\hat{\sigma} = \begin{pmatrix} 0 & 1 & 1 \\ 1 & 0 & 0 \\ 1 & 0 & 0 \end{pmatrix} \tag{2.3}$$

$$\hat{\rho}_1 = \begin{pmatrix} 0 & 0 & 0 \\ 0 & 1 & 0 \\ 0 & 0 & 0 \end{pmatrix} \tag{2.4}$$

$$\hat{\rho}_2 = \begin{pmatrix} 0 & 0 & 0 \\ 0 & 0 & 0 \\ 0 & 0 & 1 \end{pmatrix} \tag{2.5}$$

the Hamiltonian may be written as:

$$\hat{H}_{el} = 2z(\hat{\rho}_1 + \hat{\rho}_2) - \sqrt{2}t\hat{\sigma} \tag{2.6}$$

where $\hat{\rho}_1$ and $\hat{\rho}_2$ measure the charge on sites 1 and 2 of the cyanine dye (see Fig. 2.10). For a symmetric molecule, the expectation values of $\hat{\rho}_1$ and $\hat{\rho}_2$ are the same, so that it is convenient to define the operator $\hat{\rho} = \hat{\rho}_1 + \hat{\rho}_2$, which quantifies the charge displacement from the central site to each lateral unit.

In symmetric dyes, the two degenerate basis states $|Z_1\rangle$ and $|Z_2\rangle$ are conveniently combined in symmetric and antisymmetric states: $|Z_\pm\rangle = (|Z_1\rangle \pm |Z_2\rangle)/\sqrt{2}$. The symmetric $|N\rangle$ and $|Z_+\rangle$ states mix to give the two symmetric eigenstates: the ground state $|g\rangle$ and the excited state $|e\rangle$. The antisymmetric $|Z_-\rangle$ state stays unmixed and coincides with the $|c\rangle$ eigenstate.

$$\begin{aligned} |g\rangle &= \sqrt{1-\rho}\,|N\rangle + \sqrt{\rho}\,|Z_+\rangle \\ |c\rangle &= |Z_-\rangle \\ |e\rangle &= \sqrt{\rho}\,|N\rangle - \sqrt{1-\rho}\,|Z_+\rangle \end{aligned} \tag{2.7}$$

Due to the mixing between $|N\rangle$ and $|Z_+\rangle$, in the ground state the charge distribution on the three sites of the molecule can be described in terms of the parameter ρ, which is the expectation value of the previously defined $\hat{\rho}$ operator. ρ can be expressed as a function of model parameters z and t:

$$\rho = \frac{1}{2}\left(1 - \frac{z}{\sqrt{z^2 + 4t^2}}\right) \tag{2.8}$$

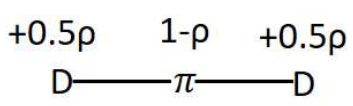

Figure 2.11: Charge distribution of the ground state.

Since the total charge is +1, the central site (corresponding to the π bridge) bears a positive charge of $+(1-\rho)$. The overall charge distribution in the ground state is $D^{+\rho/2}\pi^{+(1-\rho)}D^{+\rho/2}$ (Fig. 2.11).

The symmetric $|e\rangle$ state, forbidden in OPA, is responsible for the intense TPA band observed at transition wavelengths shorter than 500 nm, as shown in Fig. 2.2 (the maximum of these bands are not accessible by our experimental setup). The dipole moment of a charged object is not defined

but, to address spectral properties, we define an effective dipole moment operator, measuring the charge unbalance of $|Z_1\rangle$ and $|Z_2\rangle$ with respect to $|N\rangle$. Accordingly, the non-vanishing matrix elements of the dipole moment operator in the chosen diabatic basis are $\langle Z_1|\,\hat{\mu}\,|Z_1\rangle = -\mu_0$ and $\langle Z_2|\,\hat{\mu}\,|Z_2\rangle = \mu_0$ (the relevant component of the dipole moment is parallel to the main molecular axis).

To address spectral bandshapes and, when relevant, symmetry-breaking phenomena, the model was extended to account for electron-vibration coupling.[94, 97] To such an aim, two effective harmonic vibrational coordinates, q_1 and q_2, are introduced to describe the rearrangements of the molecular geometry upon charge redistribution from $|N\rangle$ to $|Z_1\rangle$ and $|Z_2\rangle$, respectively. The two vibrational modes are equivalent, with harmonic frequency ω_v and relaxation energy ϵ_v. The vibronic Hamiltonian for the monomer reads:

$$\hat{H} = \hat{H}_{el} - \sqrt{2\epsilon_v\omega_v}\hat{q}_1\hat{\rho}_1 - \sqrt{2\epsilon_v\omega_v}\hat{q}_2\hat{\rho}_2 + \frac{1}{2}(\omega_v^2\hat{q}_1^2+\hat{p}_1^2) + \frac{1}{2}(\omega_v^2\hat{q}_2^2+\hat{p}_2^2) \quad (2.9)$$

where $\hat{H}_{el}$ is the three-state electronic Hamiltonian described above (see also Eq. 2.6), $\hat{\rho}_1 = |Z_1\rangle\langle Z_1|$ and $\hat{\rho}_2 = |Z_2\rangle\langle Z_2|$ are the operators that measure the charge on the two lateral sites in the cyanine. The Hamiltonian is diagonalized on the basis obtained from the direct product of the 3 electronic diabatic states and the first N eigenstates of each harmonic oscillator. The dimension of the problem is $3N^2$, since we consider two effective vibrational coordinates. N is set to a large enough value to guarantee convergence; in our case $N = 10$ is a good choice.

The diagonalization of the Hamiltonian gives $3N^2$ numerically exact vibronic eigenstates. OPA spectra are calculated assigning a Gaussian bandshape to each vibronic transition (where the model parameter γ is the half width at half maximum of the Gaussian). The intensity of each vibronic transition is proportional to the squared transition dipole moment between the ground state and the relevant excited state. The spectrum is calculated summing up all the contributions of each vibronic transition. Emission spectra are calculated in the same way, but the transition dipole moments are calculated between the emissive state and all states having lower energy. The emissive state is chosen as the lowest-energy state having a sizable transition dipole moment from the ground state. For TPA spectra, the sum-over-state expression of third-order polarizability by Orr & Ward[113] is adopted. The detailed expressions for the calculation of spectra are reported in Ref [114]. Polar solvation has marginal effects in these cyanine dyes, as demonstrated by negligible absorption and emission solvatochromism (Fig. 2.3), and will be disregarded in the following.

The proposed model is semiempirical in nature and model parameters in Tab. 2.5 are selected to best reproduce experimental spectra. It is worth mentioning that, for each dye, only six molecular parameters are required to describe the position and bandshapes of OPA, TPA and emission spectra. Indeed μ_0 does not affect spectral bandshapes but only their intensity, so that for each dye μ_0 was set to the value needed to reproduce the molar extinction coefficient. With this choice, the TPA cross section of DiI is estimated as 47 GM at 520 nm, in very good agreement with the experimental data. Overall, calculated spectra in Fig. 2.12 reproduce well experimental data in Fig. 2.2, in terms of spectral

position and bandshapes, including the vibronic progression. This result confirms that the three-state model captures the most important spectral features of the cyanine molecules under investigation.

Table 2.5: Set of parameters used to fit cyanine monomer spectra.

Cyanine	z (eV)	$\sqrt{2}t$ (eV)	ω_v (eV)	ϵ_v (eV)	γ (eV)	μ_0 (D)
DiI	0.105	1.689	0.15	0.745	0.06	19.1
DiD	0.11	1.4	0.15	0.4	0.06	26.4
DiR	0.15	1.15	0.15	0.32	0.06	33.0

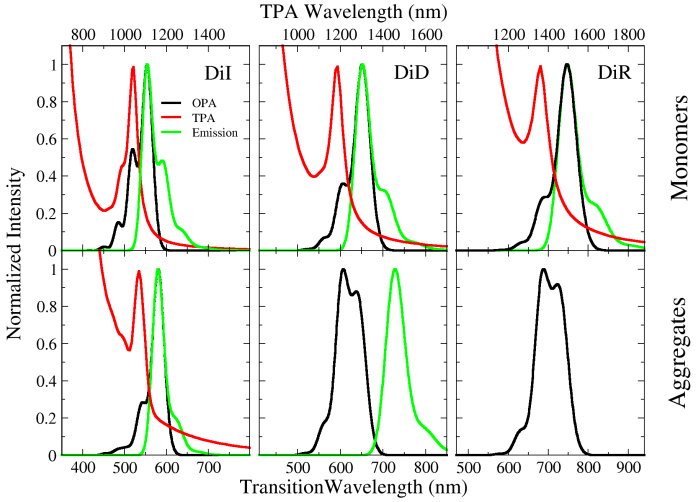

Figure 2.12: Calculated OPA (black lines), TPA (red lines) and emission (green lines) spectra of DiI, DiD and DiR monomers (top panels) and dimers (bottom panels). Geometrical parameters for the dimers: L=7 Å, x=7 Å, y=3 Å for DiI; L=8 Å, x=3 Å, y=6.8 Å for DiD; L=9 Å, x=4 Å, y=4 Å for DiR (the definition of geometrical parameters is reported in Fig. 2.10). Calculations are performed adopting static (ϵ) and optical (η^2) dielectric constants of water, ϵ=78 and η^2=1.8 respectively.

Looking at the spectra in more detail, the TPA transition towards the lowest state (state "0") of the vibrational manifold relevant to the lowest excited electronic state is forbidden, while the transition towards the successive vibrational state (state "1") acquires sizeable intensity, in agreement with experimental data. In centrosymmetric molecules, allowed TPA states must be symmetric. In our model, the lowest electronic excited state, $|c\rangle$, is antisymmetric and, as a consequence, the electronic contribution to the TPA intensity is vanishing (in other words, the $|c\rangle$ state is forbidden in TPA). The TPA intensity becomes sizeable thanks to the coupling with antisymmetric vibrations (Herzberg-Teller effect). For the sake of clarity, in the framework of this discussion it is useful to adopt the Born-Oppenheimer (or adiabatic) approximation: the vibronic wavefunction is the product between an electronic and a vibrational function. In our model, the two molecular vibrations (q_1 and q_2) recombine in a symmetric and an antisymmetric mode, $q_\pm = (q_1 \pm q_2)/\sqrt{2}$. For an electronic antisymmetric state ($|c\rangle$), the total vibronic wavefunction is overall symmetric only if the vibrational part of the wavefunction is antisymmetric: this only occurs for the odd vibrational states related to the antisymmetric coordinate q_-. In summary, the formally TPA forbidden transition towards the $|c\rangle$ state acquires intensity thanks to the coupling with the antisymmetric vibrational coordinate. In particular, while the 0-0 TPA transition is symmetry-forbidden, the 0-1 transition

is symmetry-allowed (its intensity is low because it is related to small vibrational displacements around the equilibrium geometry).

Modelling cyanine aggregates

Modelling aggregates is a complex issue in several respects. First of all, it is hard to obtain reliable information on the precise supramolecular arrangement of the dyes in the aggregate. Moreover, molecular vibrations enter the problem non-adiabatically,[104] so that addressing large aggregates becomes extremely demanding, because very large basis are required. In the following, we will limit our discussion to cyanine dimers, as to maintain a reasonable dimension of the problem, while acquiring a good understanding of the complex physics of the aggregates. Experimental spectroscopic data on DiI aggregates show that the 0-0 vibronic transition, allowed in OPA, is forbidden in TPA, much as observed for the DiI monomer in ethanol. This suggests that the aggregate maintains a centrosymmetric structure as to support the mutual exclusion rule. Therefore, we will consider simple centrosymmetric cyanine dimers as illustrated in the right panel of Fig. 2.10. The geometry of the dimer is defined by the intermolecular distance, y in the figure, and by the offset, x. The effective length of the chromophoric core L is set to 7, 8 and 9 Å for DiI, DiD and DiR, respectively.

The physics of aggregates is driven by intermolecular electrostatic interactions. As discussed in recent literature,[99–101, 105, 106, 115–118] essential-state models lend themselves quite naturally to introduce intermolecular interactions. The diabatic basis set for the dimer is the direct product of electronic basis states $|N\rangle$, $|Z_1\rangle$ and $|Z_2\rangle$ of the monomer (see Table 2.6).

Table 2.6: Diagonal energies associated to each diabatic basis state for the dimeric structures.

Basis states	Diagonal energies
$\|\Phi_1\rangle$ ($\|NN\rangle$)	0
$\|\Phi_2\rangle$ ($\|NZ_1\rangle$)	$2z$
$\|\Phi_3\rangle$ ($\|NZ_2\rangle$)	$2z$
$\|\Phi_4\rangle$ ($\|Z_1N\rangle$)	$2z$
$\|\Phi_5\rangle$ ($\|Z_1Z_1\rangle$)	$4z$
$\|\Phi_6\rangle$ ($\|Z_1Z_2\rangle$)	$4z$
$\|\Phi_7\rangle$ ($\|Z_2N\rangle$)	$2z$
$\|\Phi_8\rangle$ ($\|Z_2Z_1\rangle$)	$4z$
$\|\Phi_9\rangle$ ($\|Z_2Z_2\rangle$)	$4z$

On this basis, intermolecular electrostatic interactions are diagonal and can be easily estimated from the aggregate geometry. Specifically, the dimer Hamiltonian reads:

$$\hat{H} = \hat{H}_A + \hat{H}_B + \sum_{i,j}^{3} V_{ij}\hat{\rho}_{A,i}\hat{\rho}_{B,j} \tag{2.10}$$

where $\hat{H}_{A/B}$ are the molecular Hamiltonians for the two isolated dyes, labelled as in Fig. 2.10. The third term accounts for intermolecular interactions, with $\hat{\rho}_{A/B,i}$ measuring the amount of charge on the i-th site of molecule A/B (3 being the central site, $\hat{\rho}_3 = |N\rangle\langle N|$), while V_{ij} measures the repulsion energy between two unit charges on sites i and j located on different molecules (explicit expressions for V_{ij} are reported in Eqs 2.11).

$$
\begin{aligned}
V_{11} &= \frac{1}{4\pi\epsilon_0}\frac{1}{\sqrt{(x+L)^2+y^2}} \\
V_{12} = V_{21} &= \frac{1}{4\pi\epsilon_0}\frac{1}{\sqrt{x^2+y^2}} \\
V_{13} = V_{31} &= \frac{1}{4\pi\epsilon_0}\frac{1}{\sqrt{(x+\frac{L}{2})^2+y^2}} \\
V_{22} &= \frac{1}{4\pi\epsilon_0}\frac{1}{\sqrt{(L-x)^2+y^2}} \\
V_{23} = V_{32} &= \frac{1}{4\pi\epsilon_0}\frac{1}{\sqrt{(x-\frac{L}{2})^2+y^2}} \\
V_{33} &= \frac{1}{4\pi\epsilon_0}\frac{1}{\sqrt{x^2+y^2}}
\end{aligned}
\tag{2.11}
$$

There is however an issue, related to the screening of the interactions. In our case, aggregates are formed in water/ethanol mixtures. The two solvents are highly polar (static dielectric constants are 80 and 24.5 for water and ethanol, respectively). The mixture then constitutes a highly polar environment: the large dielectric constants of both solvents (and hence of their mixture) produces a large screening of static interactions. On the opposite, the dielectric screening at optical frequencies, as measured by the squared refractive index, amounts to ~ 1.8, a typical value for common organic solvents (water and ethanol refractive indices are 1.33 and 1.36, respectively). Therefore interactions between static charges should be largely screened by the static dielectric constant, while the screening related to oscillating dipoles should be much smaller, being related to the squared refractive index. The delicate issue is how to discriminate the two kinds of interactions. Indeed this is not possible adopting the diabatic basis, since the third term of Eq. 2.10 accounts for static and dynamical interactions at the same time.[105, 106, 115, 118]

Following an approach developed some years ago for aggregates of quadrupolar dyes,[106] a step-by-step procedure is adopted. First, a mean-field Hamiltonian is defined to accurately describe the ground-state properties of the dyes inside the aggregate. At the mean-field level, only static (ground state) properties are addressed and intermolecular electrostatic interactions are screened by the static dielectric constant, ϵ. In the second step, the eigenstates of the molecular mean-field Hamiltonian are used to rotate the Hamiltonian in the adiabatic (or exciton) basis, where the states are classified according to the number and type of excitation. Once the Hamiltonian is written on this basis, it is easy to single out excitonic interactions, i.e. interactions that only account for exciton migration.[115] In line with the exciton model, we only consider interactions between degenerate states: these interactions are screened by the squared refractive index at optical frequency, η^2.

In the mean field approach, the Hamiltonian of a single molecule is diagonalized accounting for the presence of the electrostatic potential generated by the other molecule(s). Indeed, positive charges on the sites of molecule B affect the energy required to locate charges in the different sites of molecule A, an effect that reflects on the renormalization of the z

parameter. In turn, the renormalized z leads to a variation of the charge distribution in the molecule. Since the two molecules are equivalent, we force the same charge distribution in corresponding molecular sites (see Fig. 2.10), leading to a self-consistent problem, that is numerically solved as schematically shown in Fig. 2.13. We notice that in dimers with a finite offset ($x \neq 0$ in Fig. 2.10) the sites 1 and 2 in each molecule are no more equivalent, so that the two diabatic states $|Z_1\rangle$ and $|Z_2\rangle$ are no more degenerate.

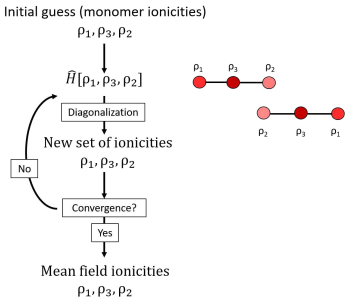

Figure 2.13: Self-consistent mean-field calculation scheme.

We consider centrosymmetric dimers, so that the two monomers in each dimer are equivalent. For aligned dimers ($x = 0$) the inversion center is conserved on each molecule, so that $\rho_1 = \rho_2$; but for staggered dimers ($x \neq 0$) the inversion symmetry of each dye is lost and $\rho_1 \neq \rho_2$. ρ_3 measures the amount of charge on the central site and of course $\rho_3 = 1 - \rho_1 - \rho_2$. The energies of diabatic states are renormalized by the interaction with the other cyanine.

The mean-field energies of the diabatic states of each molecule depend on the charge on the sites of the other molecule, but, since the dimer is symmetric, we enforce equal charge distributions in the two molecules, ending up with a self-consistent problem. Specifically, the energies of the basis states of each dye in the mean field approximation read:

$$\langle N|\,\hat{H}_{el}\,|N\rangle = \frac{1}{4\pi\epsilon_0\epsilon}\left(\frac{\rho_2}{\sqrt{(x-\frac{L}{2})^2+y^2}}+\frac{\rho_3}{\sqrt{x^2+y^2}}+\frac{\rho_1}{\sqrt{(x+\frac{L}{2})^2+y^2}}\right) \quad (2.12)$$

$$\langle Z_1|\,\hat{H}_{el}\,|Z_1\rangle = 2z+\frac{1}{4\pi\epsilon_0\epsilon}\left(\frac{\rho_2}{\sqrt{x^2+y^2}}+\frac{\rho_3}{\sqrt{(x+\frac{L}{2})^2+y^2}}+\frac{\rho_1}{\sqrt{(x+L)^2+y^2}}\right)$$

$$\langle Z_2|\,\hat{H}_{el}\,|Z_2\rangle = 2z+\frac{1}{4\pi\epsilon_0\epsilon}\left(\frac{\rho_2}{\sqrt{(L-x)^2+y^2}}+\frac{\rho_3}{\sqrt{(x+\frac{L}{2})^2+y^2}}+\frac{\rho_1}{\sqrt{x^2+y^2}}\right)$$

We address the self-consistent problem by solving first the electronic problem for an isolated monomer, in order to get three initial values for the ground state ionicities ρ_1, ρ_2, ρ_3 (of course, $\rho_1 + \rho_2 + \rho_3 = 1$). These values are then inserted in a molecular Hamiltonian where the diagonal energies are corrected as in Eq. 2.12. The diagonalization of this Hamiltonian leads to new eigenvectors and hence to new ionicities, that are again inserted in Eqs. 2.12 to define a novel (improved) mean-field Hamiltonian. The cycle is repeated until ionicities at the n-th iteration differ from ionicities at the $(n-1)$-th iteration by the seventh decimal digit. We discuss mean field effects considering two dimers with interplanar distance y= 4 Å, one in aligned geometry ($x = 0$) and one in staggered geometry x=6 Å. Resulting mean field charges on the molecular sites are reported in Tab. 2.7. We notice that, as schematically illustrated in Fig. 2.14, in the aligned dimer, the charge flows from the bridge to the lateral sites as to minimize electrostatic repulsion. For the same reason, in the staggered dimer the charge moves towards the outer sides.

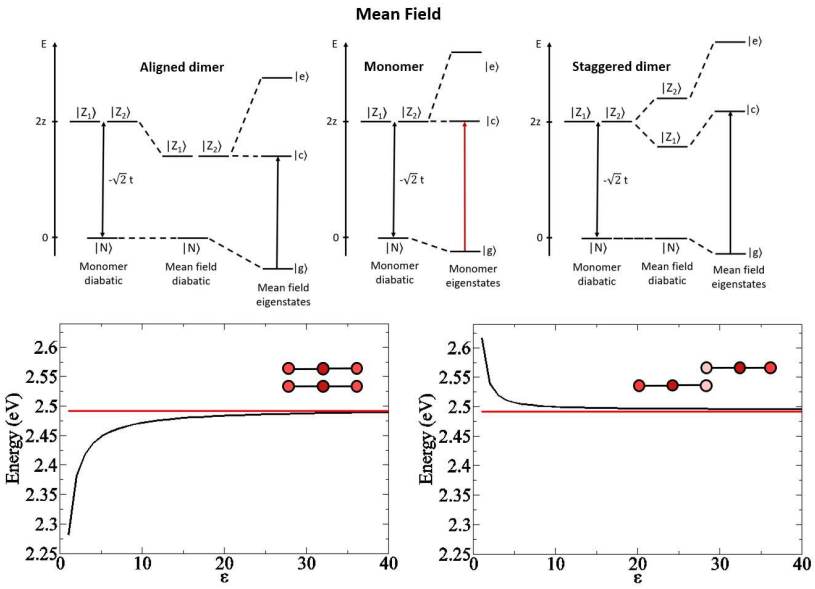

Figure 2.14: Top panels: schematic representation of mean field approach to the dimers. The central panel refers to the isolated monomer (same information as in Fig. 2.10). Left and right panels (referring to the aligned and staggered dimers, respectively) show how the energy of diabatic states is affected by the mean field potential. In the lower panels, in a schematic representation of the two dimers, the intensity of the red color assigned to each site gives a qualitative representation of the amount of charge on the corresponding site, as calculated in mean field approximation for the ground state. In the two graphs, the red line shows the OPA transition energy of the monomer, while the black line shows the lowest OPA transition energy of the dimer calculated as a function of the medium dielectric constant in the mean field approximation.

Bottom panels of Figure 2.14 show the OPA transition energies calculated in the mean field approach for aligned (left) and staggered (right) DiI dimers as a function of the static dielectric constant. Mean field effects are sizeable in low-polarity environments (see also Table 2.8 where results on the mean field charge distribution are listed for a system with $\epsilon = 5$), while they become negligible in medium/high polarity environments. In our case, in water/ethanol mixtures with $\epsilon \sim$ 60-70, mean-field effects are negligible for both geometries. We notice, however, that the aligned geometry (left-bottom panel of Figure 2.14) corresponds to an H-aggregate, where the exciton model predicts a blue-shift of the absorption band. However, mean-field effects lead to an opposite effect: a red-shift of the lowest transition with respect to the monomer is observed (for small values of the dielectric constant).[100, 105, 117, 119–121]

Table 2.7: Ground state charge distribution resulting from mean-field calculations on cyanine dimers setting the dielectric constant to the pure water value $\epsilon = 78$ (results are unaffected for smaller values down to $\sim$ 40). Results refer to aligned ($x = 0$) or staggered (x=6 Å) geometries for intermolecular distance y=4 Å. The chromophore length is set to L= 7, 8 and 9 Å for DiI, DiD and DiR, respectively.

		ρ_1	ρ_3	ρ_2
DiI	Monomer	0.239	0.522	0.239
	aligned	0.239	0.521	0.239
	staggered	0.241	0.522	0.237
DiD	Monomer	0.236	0.529	0.236
	aligned	0.237	0.527	0.237
	staggered	0.238	0.528	0.234
DiR	Monomer	0.227	0.546	0.227
	aligned	0.228	0.545	0.228
	staggered	0.230	0.546	0.225

Table 2.8 reports the values of ground-state charge distributions for a medium- polarity environment ($\epsilon = 5$). Lowering the screening constant, leads to sizable mean-field effects, as expected.

		ρ_1	ρ_3	ρ_2
DiI	Monomer	0.239	0.522	0.239
	aligned	0.244	0.512	0.244
	staggered	0.266	0.524	0.210
DiD	Monomer	0.236	0.528	0.236
	aligned	0.243	0.514	0.243
	staggered	0.270	0.527	0.203
DiR	Monomer	0.227	0.546	0.227
	aligned	0.237	0.526	0.237
	staggered	0.268	0.543	0.189

Table 2.8: Ground state charge distribution resulting from mean field calculations on cyanine dimers setting the dielectric constant to $\epsilon = 5$. Results refer to aligned ($x = 0$) or staggered (x=6 Å) geometries for intermolecular distance y= 4 Å. The chromophore length is set to L= 7, 8 and 9 Å for DiI, DiD and DiR, respectively.

Table 2.9: Energies associated to the excitonic basis states.

Wave functions	mean-field energies
$\|\Psi_1\rangle$ ($\left\|gg\right\rangle$)	0
$\|\Psi_2\rangle$ ($\left\|gc\right\rangle$)	E_c
$\|\Psi_3\rangle$ ($\left\|ge\right\rangle$)	E_e
$\|\Psi_4\rangle$ ($\left\|cg\right\rangle$)	E_c
$\|\Psi_5\rangle$ ($\|cc\rangle$)	$2E_c$
$\|\Psi_6\rangle$ ($\|ce\rangle$)	$E_c + E_e$
$\|\Psi_7\rangle$ ($\left\|eg\right\rangle$)	E_e
$\|\Psi_8\rangle$ ($\|ec\rangle$)	E_c+E_e
$\|\Psi_9\rangle$ ($\|ee\rangle$)	$2E_e$

The Hamiltonian in Eq. 2.10 includes both ground-state and excited-states interactions. Since ground-state interactions, screened by ϵ, are accounted for in the mean-field part, we now introduce interactions between excited states, and we screen them with η^2. To tackle this issue, we must rotate the basis from the initial diabatic basis to the excitonic basis (Tab. 2.9), i.e. the basis of the states derived as direct product of the three eigenstates, $\left|g\right\rangle$, $|c\rangle$ and $|e\rangle$ obtained for each dye in the mean field approximation. On this new basis, exciton interactions enter as off-diagonal elements between states having the same energy, and it is easy to single them out.

The eigenstates matrix ($\hat{U}$) of an interacting dimer at the mean field level is the rotation matrix which rotates the diabatic basis into the exciton basis. The matrix $\hat{U}$ is exploited to numerically rotate the basis and to rewrite relevant operators.

In the framework of the exciton approximation, we consider, out of the rotated interaction matrix, only the interaction terms that mix degenerate states, and specifically: $\left\langle gc\right|\hat{H}\left|cg\right\rangle$, $\left\langle ge\right|\hat{H}\left|eg\right\rangle$ and $\langle ce|\,\hat{H}\,|ec\rangle$.

From a purely electronic point of view, these matrix elements represent the interactions between transition charge densities: the $\left\langle ge\right|\hat{H}\left|eg\right\rangle$ element would be zero in the point dipole approximation, and it is small (but finite) in the extended dipole approach we adopted.

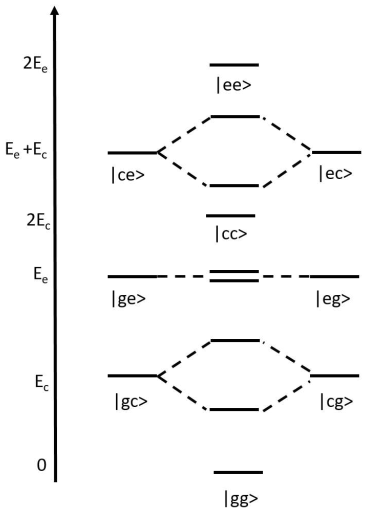

Figure 2.15: A schematic view of the exciton basis states and of their mixing as due to the interactions between degenerate states (the only interactions retained in the exciton approximation). The mixing matrix elements between $|ge\rangle$ and $|eg\rangle$ is very small leading to a small splitting.

We can validate the exciton approximation repeating the calculation for a dimer in a non-polar environment ($\epsilon = \eta^2 = 1.8$). In this case, the diagonalization of the full Hamiltonian in Eq. 2.10 leads to nominally exact results that can be compared with those obtained in the exciton approximation. Results in Fig. 2.16 show marginal differences, that are ascribed to ultraexcitonic interaction terms (which are disregarded in the excitonic approximation, but enter the full Hamiltonian, written on the diabatic basis): the result confirms that ultraexcitonic terms are small, and they can be safely disregarded.

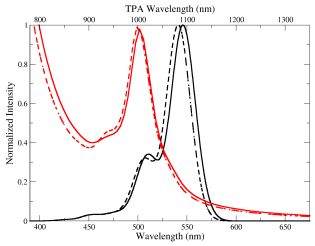

Figure 2.16: Continuous lines: OPA (black) and TPA (red) spectra calculated for the geometry chosen for the DiI dimer ($x = 7$ Å, $y = 3$ Å), using a diabatic basis in which all the interactions are screened by $\eta^2 = 1.8$. Dashed lines: OPA (black) and TPA (red) spectra calculated for the same geometry, considering a mean-field problem and exciton interactions screened by $\epsilon = \eta^2 = 1.8$. Calculations are performed accounting for electron-vibration couplings. The difference between dashed and continuous lines is due to the electronic ultraexcitonic terms, that are accounted for in continuous line spectra and are disregarded in dashed line spectra. The results confirm that ultraexcitonic terms have small contributions.

Finally, two effective vibrational coordinates are introduced for each dye, for a grand total of four vibrational coordinates, $q_{A,1}, q_{A,2}, q_{B,1}, q_{B,2}$. The vibronic Hamiltonian for the dimer in the exciton approximation reads:

$$\hat{H} = \hat{H}_{el}^{dimer} + \sum_{k=1}^{2} \frac{1}{2}(\omega_v^2 \hat{q}_{A,k}^2 + \hat{p}_{A,k}^2) - \sqrt{2\epsilon_v}\omega_v \hat{q}_{A,k}\hat{\rho}_{A,k} + \sum_{k=1}^{2} \frac{1}{2}(\omega_v^2 \hat{q}_{B,k}^2 + \hat{p}_{B,k}^2) - \sqrt{2\epsilon_v}\omega_v \hat{q}_{B,k}\hat{\rho}_{B,k} \quad (2.13)$$

where $\hat{H}_{el}^{dimer}$ is the Hamiltonian electronic part comprising mean field and excitonic interaction terms with the respective screenings, k runs on the two molecular arms of each dye, A and B refer to the first and second cyanine dye in Fig. 2.10. The ionicity operators, $\hat{\rho}_{A/B,k}$, are diagonal on the diabatic basis, but they have off-diagonal elements on the exciton basis. Accordingly, vibronic couplings enter the picture mixing up degenerate and non-degenerate states.

Calculated spectra in Fig. 2.12 are obtained with the same model parameters adopted to describe the monomer spectra (Tab. 2.5) and adjusting geometrical structure (caption of Fig. 2.12) to best reproduce the OPA spectra. TPA spectra calculated with the same geometrical parameters are well in line with available experimental data.

Quite interestingly, the same model with the same model parameters reproduces well also the spectra collected in the hydrogel (Fig. 2.17). The spectra of the green aggregate "G" in Fig. 2.9 are reproduced adopting

exactly the same model parameters adopted for DiI in Fig. 2.12, while for the red aggregate "R", the offset is set $x = 0$ and the interplanar distance y is increased, keeping all other parameters unaffected.

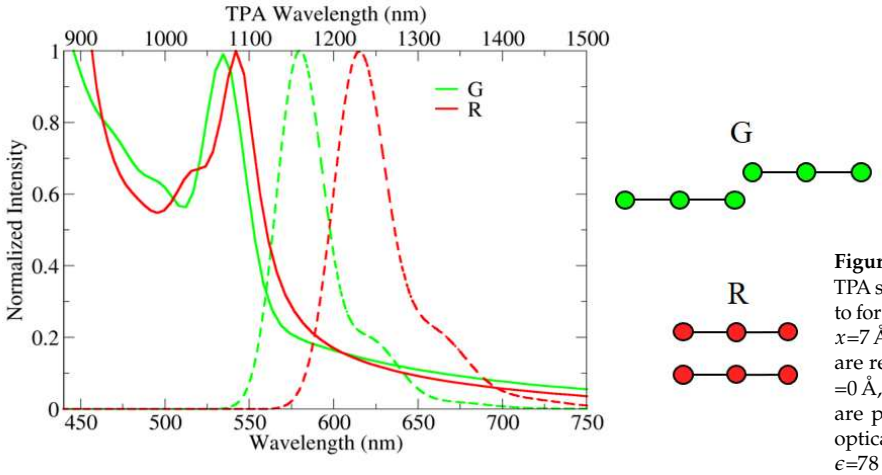

Figure 2.17: Emission (dashed lines) and TPA spectra (continuous lines) calculated to for two DiI dimers. Green spectra have x=7 Å, y=3 Å , L=7 Å, while red spectra are relative to a cofacial dimer with x= =0 Å, y= =6.3 Å, L==7 Å. Calculations are performed adopting static (ϵ) and optical (η^2) dielectric constants of water, ϵ=78 and η^2=1.8 respectively.

2.3.3 Conclusion

In this work, a joint experimental and theoretical study of the optical properties of a family of commercial cyanine dyes (DiI, DiD and DiR) and their aggregates in polar suspension is presented. The cyanine dyes under investigation differ only for the polymethinic bridge length, i.e. for the delocalization length. The bridge length affects the spectral position of OPA, emission and TPA spectra of monomers in solution: the spectra move to the red if the length of the π-conjugated structure is increased. DiI, DiD and DiR are good candidates as fluorescent probes for two-photon imaging, since TPA shows reasonable intensity in the OPA region. This band is nominally forbidden by symmetry, but it acquires intensity thanks to electron-vibration coupling. Experimental spectra of dyes in solution are fully rationalized by adopting the ESM approach developed some years ago for quadrupolar dyes.[94, 96, 97]

The tendency of cyanines to form aggregates is well known. [77, 78] In the present work, aggregates of DiI, DiD and DiR are prepared in water/ethanol mixtures, and show different optical properties depending on the monomer. DiI clearly forms J-aggregates: the aggregates are emissive, their absorption spectrum is red-shifted compared to the monomer, the Stokes shift is negligible and the ratio between the intensities of the 0-0 and 0-1 vibronic transitions both in absorption and in emission is increased with respect to the monomer. For DiI aggregates, we were able to collect TPA spectra, that, being slightly blue-shifted with respect to OPA, suggest a centrosymmetric structure for the aggregate. On the opposite, DiD and DiR form H aggregates, with a broad OPA band, slightly blue-shifted compared to the monomer, while the emission (not detectable for DiR aggregates) is very weak and red-shifted.[104]

The formation of different types (H or J) of aggregates for the different dyes can be ascribed to a delicate balance between the Coulomb repulsion of positively charged molecules and the hydrophobic effect. If we consider a dimer, only accounting for the hydrophobic effect, the favoured geometry

would be a cofacial stacking in order to form the most extended possible hydrophobic pocket. In this geometry, however, positive charges would be perfectly superimposed, leading to large Coulomb repulsions. As a consequence, the dyes arrange themselves in a staggered geometry, the mutual shift being larger for shorter cyanines, where electrostatic repulsions are larger. This leads to the formation of almost cofacial H-aggregates for long cyanines such as DiD and DiR,[82] and to J-aggregates for the shorter DiI.

The proposed theoretical approach, based on essential-state models and accounting for molecular vibrations, allows to rationalize in an excellent way the spectral properties of aggregates. To the best of our knowledge, this work is the first attempt to calculate nonlinear optical spectra of dimers of cyanines, accounting for molecular vibrations. Molecular vibrations play a crucial role on the spectral properties of centrosymmetric dyes where forbidden transitions acquire intensity as a result of Herzberg-Teller vibronic coupling.[122]

The effects of intermolecular interactions on the spectral properties of aggregates are particularly interesting. Accounting for intermolecular interactions is a critical issue, as two different screening regimes must be considered, one governed by the static dielectric constant and one governed by the dielectric constant at optical frequencies, i.e. the squared refractive index. This delicate conundrum is faced here based on the separation of the interaction occurring in the ground state (mean-field approach) and in the excited states (excitonic model). This issue is particularly relevant for polar solvents, in which these two numbers are considerably different.

To conclude, DiI, DiD and DiR show very interesting linear and nonlinear spectral properties both in the monomeric form and in their aggregate form. The adopted theoretical approach, based on essential-state models, accounting for vibrational coupling, and for a detailed description of screening effects of intermolecular interactions, allows to effectively reproduce linear and nonlinear optical spectra of aggregates of charged centrosymmetric dyes. The approach can be extended to supramolecular assemblies of polar or multipolar chromophores.

Hydrogen Bond-assisted H-aggregate Formation: The ODIN Case

3

3.1 Introduction

The manipulation of intermolecular interactions represents a widely explored strategy for tuning the optical properties of supramolecular structures formed by independent molecular units.[123, 124] Various approaches have been employed in this endeavor, including the introduction of suitable substituents to optimize steric hindrance[125, 126] and the precise control of the distance and positioning of the molecular units.[127] Chromophore aggregation is a well-known approach to adjust the optical properties of materials, particularly when medium-strong intermolecular dipole-dipole coupling is involved.[128–130] Such coupling gives rise to the formation of exciton molecular aggregates. However, while exciton molecular aggregates are easily formed through weak intermolecular interactions between molecules possessing an extended distribution of π-electrons, such as Van der Waals and stacking interactions,[131–135] they provide limited control over the conformational geometry of the aggregate. To gain precise control over the coupling between chromophores and manipulate their absorption and fluorescence properties, it is essential to control the geometry of the aggregate. This can be achieved using a wide palette of directional weak interactions, among which H-bonding is one of the preferred options.[131, 136] Hydrogen bonds offer the advantage of maximizing interactions in specific directions while minimizing them in other directions.[129, 137] Furthermore, hydrogen bonds can be exploited in a multiple bonding strategy to leverage the chelate cooperative effect,[138] leading to a preferential network formation among certain hydrogen interactions over others.[139, 140] The precise arrangement of donors (D) and acceptors (A) in complementary units can further increase the strength of the resulting H-bond pattern,[141] according to the Jorgensen rules.[142] In general, the formation of a new molecular aggregate, composed of two or more coupled molecules, results in the emergence of new electronic states that are delocalized across all the involved molecules. These states arise from the in-phase or anti-phase combination of the excited states of the individual molecules. Depending on the sign of the coupling constant J, aggregates can be classified as H-aggregates ($J > 0$) or J-aggregates ($J < 0$).[131] As explained in chapter 1, H and J-aggregates have substantially different optical properties. In a previous work, Tellers et al. reported the design and synthesis of a functionalized naphthyridine unit, named ODIN, which possesses the ability to self-dimerize through six intermolecular hydrogen bonds, forming a DDADA bonding motif, in which two H-bonds are bifurcated.[143] The self-dimerization of ODIN in the solid state was demonstarted through X-ray crystal structure analysis, providing insights into its supramolecular arrangement. Furthermore, the authors successfully incorporated ODIN into a polyolefin matrix to create a dynamic cross-linked polyethylene material, where ODIN acts as a physical cross-linker.[143] Subsequent investigations focused on studying the tendency of ODIN to tautomerize, self-dimerize, or form intramolecular hydrogen bonding, and the role played by solvents in favoring inter- or intra-hydrogen bond formation.[144] However, a comprehensive rationalization of the interplay between the structural and optical properties, with a clear reference to the intermolecular interactions, is still missing. Therefore, the objective of the present work is to shed light on the correlation between the structure and light-matter response of ODIN molecules, with particular attention to the

influence of the polarity of the surrounding environment. To accomplish this, various characterization techniques were used, including X-ray crystallography 3D electron diffraction[145, 146], UV-vis spectroscopy, fluorescence spectroscopy, time resolved fluorescence spectroscopy and Ultrafast pump-probe spectroscopy. X-ray and electron crystallography allowed us to obtain precise structural information, highlighting the supramolecular arrangement and hydrogen bonding interactions of ODIN molecules, while the spectroscopic analyses let us to elucidate the type of aggregates present in different solvents and the corresponding optical properties.

3.2 Results and discussion

Two different ODIN derivatives, namely ODIN-EtPh and ODIN-But, were synthesized.[143] ODIN-EtPh features a butyl chain attached to the naphthyridine ring and a 4-ethylphenyl unit directly linked to the urea group (Fig. 3.1, left), while ODIN-But is characterized by a butyl chain attached to the urea group (Fig. 3.1, right). These derivatives were specifically designed to investigate the structural and optical properties of ODIN molecules under different solvent environments, thereby providing valuable insights into the influence of environment polarity on the hydrogen bond-assisted H-aggregate formation of ODIN.

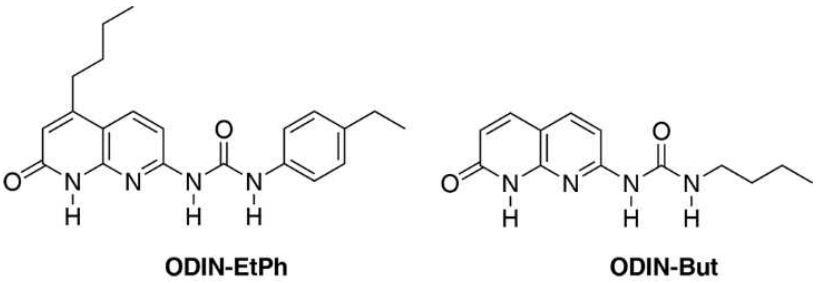

Figure 3.1: Molecular structures of ODIN-EtPh and ODIN-But, both based on the 1-(7-oxo-7,8-dihydro-1,8-naphthyridin-2-yl)urea (ODIN) scaffold.

In particular, we focused attention on the effect of the substituent linked to the ureidic group on the stability of the intermolecular interactions. We decided to insert in one derivative a rigid group (4-Ethylphenyl group) to limit the number of conformational degrees of freedom of the system and, possibly, to stabilize the formation of aggregates, and in the other one a small aliphatic chain, to simulate a condition very similar to that found when ODIN is linked to polymeric systems. The presence of the aliphatic chain linked to naphthyridine has the purpose of increasing the solubility of the system, quite low in the case of ODIN-EtPh. The effect of such chain related to the electronic properties of the monomer molecular system is negligible, and we also verified that the behavior of ODIN-EtPh in absence and in presence of the aliphatic side chain is identical in terms of aggregates optical properties and stability (Fig. 3.2).

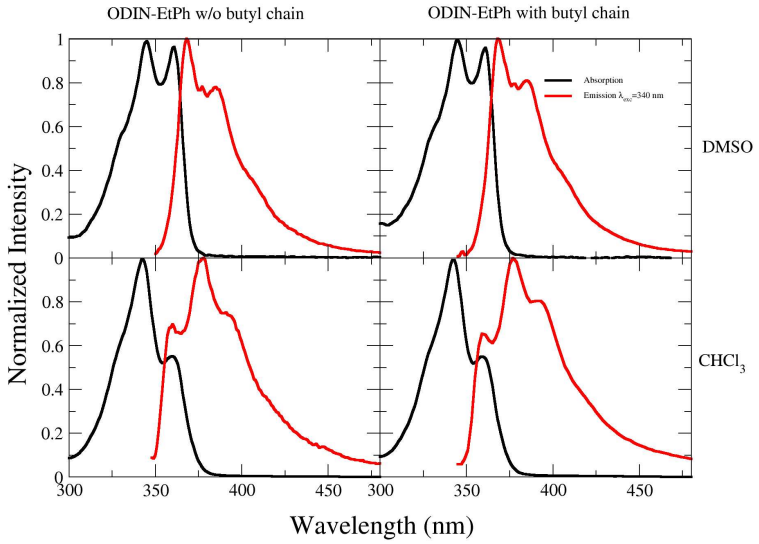

Figure 3.2: Comparison between absorption, and emission spectra of ODIN-EtPh with (righ panels) and without (left panels) lateral butyl chain. Concentration for both samples is close to 4 μM.

3.2.1 Synthesis

All syntheses were carried out in the laboratory of Prof. Enrico Dalcanale, and are reported here for completeness. ODIN-EtPh was obtained following a previous work,[143] while ODIN-But was synthetized by reacting 7-Amino-1,8-naphthyridin-2(1H)-one, prepared according to the literature,[143] with butyl isocyanate in DMF, in presence of dibutyltin dilaurate (DBTDL) as catalyst, and pyridine as base. The mixture was stirred overnight at 80°C, then cooled to room temperature and the product precipitated with hexane. The crude was filtered, washed with hexane and the final product recovered with 75% yield. ODIN-But was characterized via 1H NMR, 13C NMR and HR-ESI MS spectroscopy, and 3D electron diffraction (3D ED) analysis.

3.2.2 Crystallographic Analysis

The electron diffraction experiments were carried out by Dr. Danilo Marchetti and Prof. Mauro Gemmi.

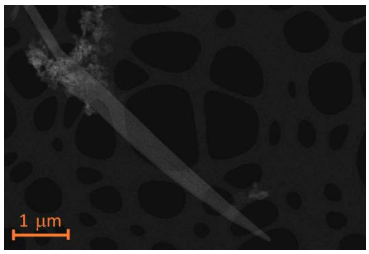

Figure 3.3: HAADF STEM-Image of the ODIN-But microcrystals used for the 3D ED data collection

The solid-state characterization was carried out to investigate ODIN H-bond pattern in crystals grown from polar and non-polar solvents. The ODIN-But crystallized from a chloroform solution exhibits thin micrometric rod-shaped crystals (Fig. 3.3).

The small crystalline domains hamper its structural analysis by single-crystal X-ray diffraction, requiring the use of 3D electron diffraction (3D ED)[145, 147]. Due to the sensitivity of the ODIN-But crystals to the electron beam, diffraction data were collected from three separate crystal areas using a special low-dose setup, in which the electron dose is below 0.05 el s^{-1} Å^{-2}. The diffraction patterns were recorded using a Timepix single electron detector[146] and for each crystal region, a full 3D ED experiment was performed without partial amorphization of the sample or considerable loss in diffraction data resolution. In order to track the

crystal position, while the sample is rotating, the 3D ED data have been collected in nano-diffraction mode with a particular continuous rotation (cRED) protocol, in which the parallel electron beam is not fixed in one point, but it is scanning a square area of 200 x 200 nm^2.[148] During the crystal rotation, the diffracted electrons pass through the central hole of the high-angle annular dark field (HAADF) STEM detector and are collected by the Timepix below, while the HAADF records real-time images of the scanned area, allowing live-tracking of the crystal position. The small size of the imaged area guarantees that the diffraction signal comes from a coherent domain. To our knowledge, this is the first time that this combined STEM-cRED data collection protocol has been successfully applied to a fully organic system. The collected diffraction data were merged, allowing for the ab-initio structure determination and kinematical refinement of the ODIN-But crystal structure. The ODIN-EtPh crystal structure, obtained in the same crystallization conditions of ODIN-But, was previously published proving that in the solid state the ODIN molecules form a dimer via a sextuple H-bonding network in a DDADA fashion (CCDC Ref Code: PIWVEZ).[143] The molecular arrangements of ODIN-But and ODIN-EtPh, in crystals produced from chloroform solution, exhibit the same propensity to produce linear DDADA dimers (Fig. 3.4). In agreement with the computational calculations, in both dimers, the ureic groups are involved in an intermolecular bifurcated N-H—O contact with the lactam C=O while the N-H of the latter in an NH—N interaction with the pyridyl ring. Since ODIN-But and ODIN-EtPh crystal structures present an inversion centre in the middle of the ODIN dimer, three of the six hydrogen bonds are symmetrical equivalent.

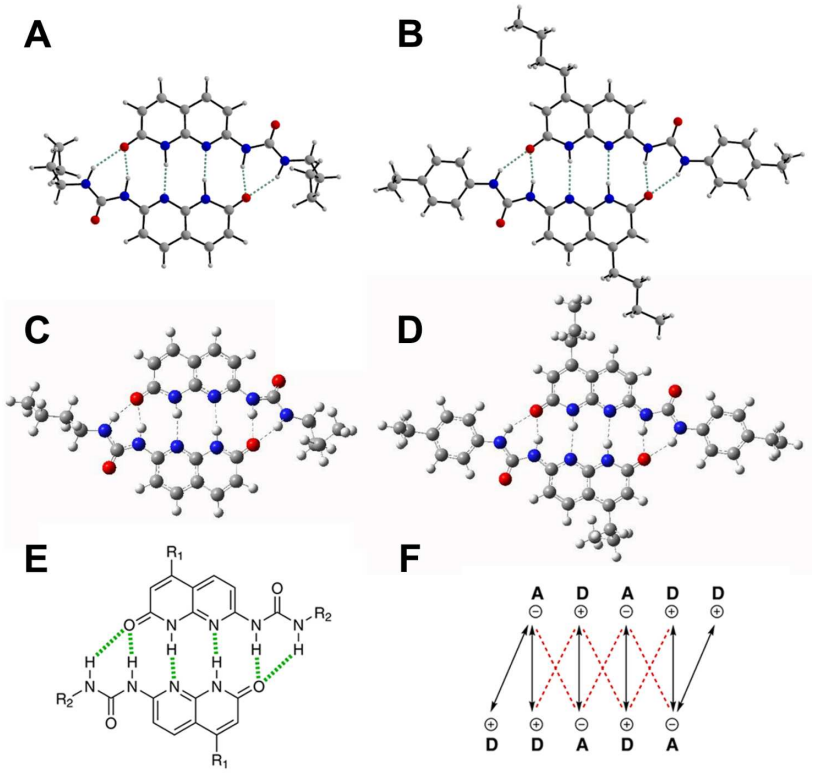

Figure 3.4: Dimeric assembly of ODIN-But (A) and ODIN-EtPh (B) in crystals grown from a $CHCl_3$ solution and obtained by Molecular Dynamics simulation ODIN-But (C) and ODIN-EtPh (D) performed in chloroform (See Computational Section). The hydrogen bonds are highlighted with dashed lines. Oxygen atoms are represented in red, nitrogen in blue, carbon in light grey and hydrogen in white. (E) Representation of the H-bonded dimeric assembly of ODIN molecules in a DDADA arrangement. The hydrogen bonds are represented as dotted lines (intramolecular, green; intermolecular, orange). (F) The schematization of hydrogen bond donor, D, and acceptor, A, in which the secondary repulsive electrostatic interactions are illustrated as red dashed lines.

In order to elucidate the influence of a strong H-bond acceptor solvent on the ODIN molecule conformation and its dimeric aggregation in the solid

state, crystals of ODIN-EtPh were grown from a DMSO solution and characterized by single crystal X-ray diffraction (Fig. 3.5). The structural model shows in the asymmetric unit a DA dimer composed by two bent ODIN isomers respectively interacting by two intermolecular hydrogen bonds (Fig. 3.5B,C). The bent form of ODIN-EtPh also presents an intramolecular N-H—N hydrogen bond between the ureic and pyridyl functions. The bent ODIN dimers interact in the solid state through contacts between their ureic groups, interactions that are responsible for a linear hydrogen bond network (Fig. 3.5A). The reported crystal structure confirms that the bent ODIN isomers, also hypothesized by Loos et.al.,[144] could be generated from a polar and strong H-bond acceptor solvent such as DMSO. Attempts to growth crystals from a DMSO solution of ODIN-But unfortunately failed.

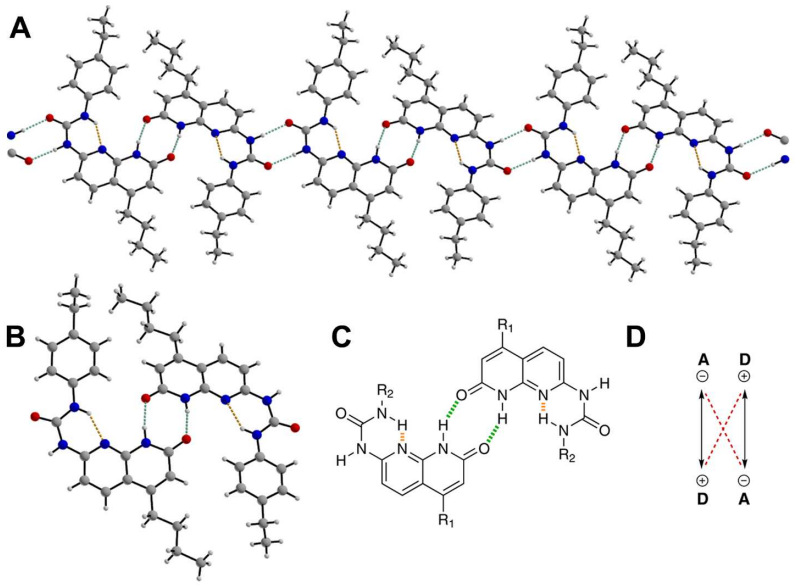

Figure 3.5: Dimeric assembly of ODIN-EtPh (A, B) in crystals grown from a DMSO solution. The intramolecular and intermolecular hydrogen bonds are respectively highlighted with orange and green dashed lines. Oxygen atoms are represented in red, nitrogen in blue, carbon in light grey and hydrogen in white. (C) Representation of the H-bonded dimeric assembly of ODIN molecules in a DA arrangement. The hydrogen bonds are represented as dotted lines (intramolecular, green; intermolecular, orange). (D) The schematization of hydrogen bond donor, D, and acceptor, A, in which the secondary repulsive electrostatic interactions are illustrated as red dashed lines.

3.2.3 Effects of solvent on ODIN aggregation

The optical properties of ODIN-But and -EtPh have been investigated via the help of UV-Vis absorption, steady-state fluorescence, time-resolved fluorescence, femtosecond transient absorption both in the visible and in the infrared spectral range. As already reported,[143] ODIN has a well-documented tendency to establish intermolecular hydrogen bonds giving rise to a maximum of 6 intermolecular hydrogen bond interactions in a bi-molecular structure (Fig. 3.4E).[143] Here, our attention is focused on how the solvent polarity and capability to donate or accept hydrogen bonds influences the aggregation status and, consequently, ODIN's spectroscopic properties. Absorption and emission spectra are expected to be very sensible probes of intermolecular interactions,[25, 55] but to fulfill a complete understanding of the aggregation status and its consequences on photo-physics, ultrafast transient absorption spectroscopy, transient infrared spectroscopy and quantum Chemical Calculations (Density functional level of theory, DFT) have been used. DMSO and $CHCl_3$ have been chosen as solvents, respectively representing a polar and highly prone to accept hydrogen bonds environment and a scarcely polar and poorly capable of forming hydrogen bonds environment.

3.2.4 UV-Vis spectroscopy and DFT calculations

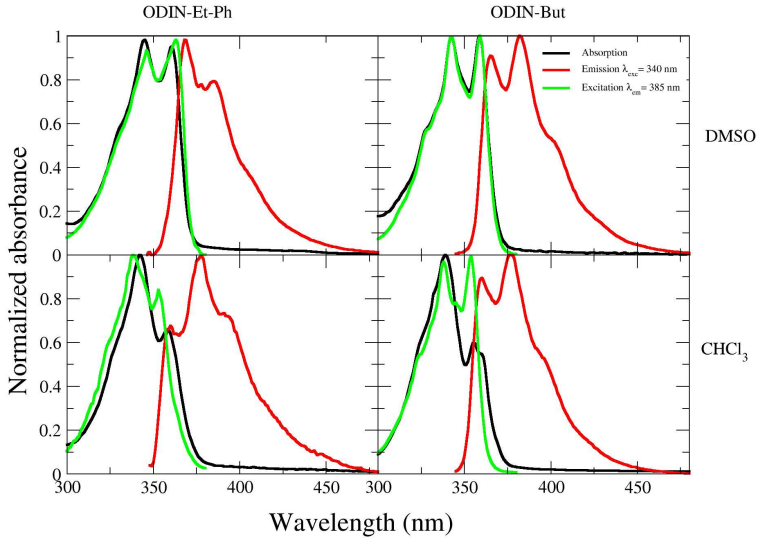

Figure 3.6: Absorption (black), emission (red) and fluorescence excitation (green) spectra of ODIN-EtPh (left) and ODIN-But (right) in DMSO (upper panels) and $CHCl_3$ (lower panels). Concentration of the solution are: ODIN-EtPh (DMSO)= $2.84 * 10^{-6}M$, ODIN-But (DMSO)=$3.13 * 10^{-6}M$. The concentration for Chloroform solution represent the nominal concentration and it is: ODIN-EtPh ($CHCl_3$)= $3.55 * 10^{-}5M$, ODIN-But ($CHCl_3$)~ 10^{-4} M

Absorption, steady state and time resolved emission spectra of ODIN-EtPh and ODIN-But have been recorded in DMSO and $CHCl_3$ and are reported in Fig. 3.6 and summarized in Table 3.1. Absorption and emission spectra in DMSO of both compounds (top panels) show well-resolved vibronic structure and a weak Stokes shift. The excitation spectrum is almost perfectly superimposed with the absorption band, an indication that in solution only one emissive specie is present. The striking difference between ODIN-EtPh and ODIN-But regards the fluorescence quantum yield: ODIN-EtPh is a weak emitter, having $\Phi_f \sim 0.06$, while ODIN-But is a very good emitter with $\Phi_f \sim 0.78$. However, the variation of fluorescence lifetime (time constant reported in Tab. 3.1) in DMSO between ODIN-But and ODIN-EtPh is negligible, translating into a 15-fold factor decrease of k_r in DMSO between ODIN-EtPh to ODIN-But, suggesting a sizeable decrease of the transition dipole moment. DFT and TD-DFT calculations were carried out in order to rationalize this difference.

Molecule	Solvent	λ^{abs}_{max} (nm)	$\epsilon_{(\lambda_{max})}$ (L/M*cm)	λ^{em}_{max} (nm)	Φ_f	τ (ns)	k_r (ns^{-1})
ODIN-EtPh	DMSO	363	28153	368	0.06	2.5	0.024
	Chloroform	338	-	377	0.02	1.7	0.012
ODIN-But	DMSO	359	22368	383	0.78	2.1	0.37
	Chloroform	339	-	377	0.47[a]	1.9	0.25

Table 3.1: Spectroscopic data relative to ODIN-EtPh and ODIN-But in DMSO and Chloroform. a Referred to diluted spectrum reported in Fig. 3.10.

For both ODIN-But and ODIN-EtPh, ground state geometries were optimized to a minimum in the gas phase using DFT, with B3LYP as a functional and 6-31G(d) as basis set. The optimization is performed for both the linear form and a bent one,[144] which is stabilized by an intramolecular hydrogen bond leading to the formation of a 6-term ring (Fig. 3.4). The relative energy is similar for the two forms, but the bent form is 9.5 kJ/mol more stable than the linear one for ODIN-But, and 14 kJ/mol more stable for ODIN-EtPh, due to the presence of intramolecular hydrogen bond. Since the doublet of phenylurea moiety

is partially delocalized on the phenyl group in ODIN-EtPh, we can infer the hydrogen involved in the intramolecular bond should be more acidic, leading to a bigger stabilization. The difference in relative energies means that 85 % of ODIN-EtPh and 80 % of ODIN-But molecules are bent at thermodynamic equilibrium at 298 K. Equilibrium constant has been estimated by equation 3.1

$$K = e^{\frac{-\Delta E}{RT}} = \frac{[Bent]_{eq}}{[Linear]_{eq}} \tag{3.1}$$

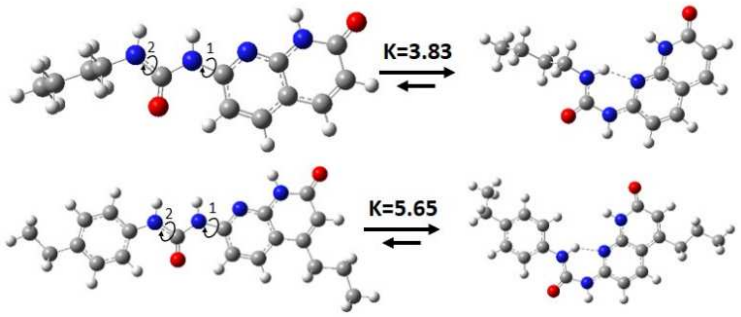

Figure 3.7: Straight (left panel) and bent (right panel) conformations of ODIN-But (upper panel) and ODIN-EtPh (lower panel). 1 and 2 indicate the bonds around which groups must rotate to convert the molecule from a linear to a bent conformation. K is the thermodynamic equilibrium constant defined by equation 3.1

The geometrical rearrangement from linear to bent structure involves rotations around two dihedrals (1 and 2, as shown in Fig. 3.7) and requires very similar activation energy for ODIN-EtPh and ODIN-But. The rate determining step (RDS) of the rearrangement, which is the rotation around the dihedral 2, requires 39 kJ/mol activation energy for ODIN-EtPh and 42 kJ/mol for ODIN-But. This barrier is intermediate between the rotation around a single C-C bond ($\sim 10 kJ/mol$) and a double C=C bond ($\sim 80 kJ/mol$). A plot of molecular energy as a function of dihedrals 1 and 2 is reported in Figure 3.8. The slight difference in the rotational barrier around dihedral 2 of 3.8 can be rationalized assuming that the bond around which the groups rotate has less double bond character in ODIN-EtPh, due to the fact the urea nitrogen doublet is partially delocalized on the terminal phenyl group rather than on the carbonyl group. We can conclude that isomerization between linear and bent structures is possible for both compounds, with a prevalence of the bent conformation.

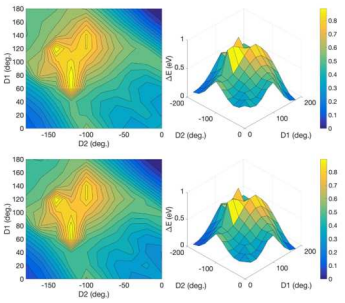

Figure 3.8: Energy as a function of dihedral angles 1 and 2. The scans are very similar for ODIN-EtPh (upper panel) and ODIN-But (lower panel), indicating a similar interconversion barrier from linear (lower right angle) to bent (upper left angle) conformations.

TD-DFT calculations were run to investigate the different spectroscopic properties of the two compounds, in their different conformations. In ODIN-But, bent and linear conformations have very similar spectroscopic properties: the first transition has a sizeable oscillator strength, and is dominated by a HOMO-LUMO transition, mostly localized on the naphtyridine moiety (Figure 3.9).

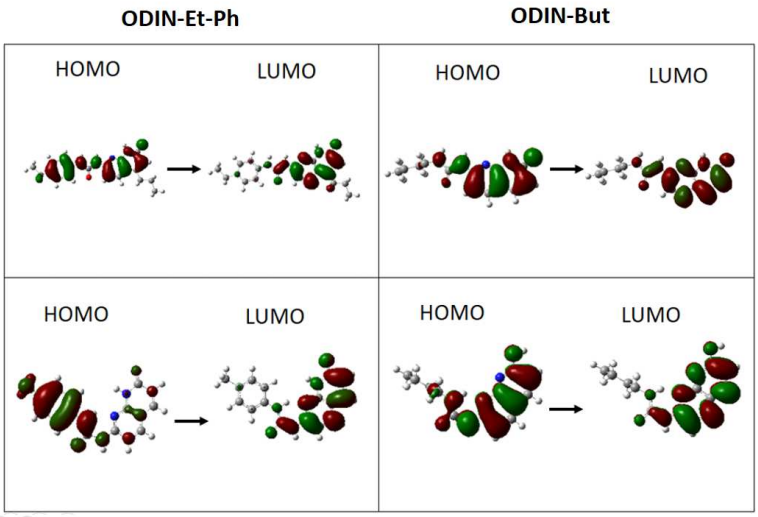

Figure 3.9: orbitals involved in the transition to the first excited state (HOMO-LUMO) of linear (upper panel) and bent (lower panel) ODIN-EtPH and ODIN-But.

The excited state landscape is different for the two conformations of ODIN-EtPh: in the linear conformation the first excited state has a sizeable oscillator strength (0.63), while in the bent conformation the oscillator strength decreases by a six-fold factor. Furthermore, the transition energy shifts to the red and the second excited state acquires a relevant oscillator strength. Looking at the molecular orbital contributions to the first excited state of the linear conformation of ODIN-EtPh, we notice a sizeable charge transfer (CT) from the phenyl-urea to the naphtyridine unit (Fig. 3.9), that is almost absent in ODIN-But. More interestingly, in the bent form of ODIN-EtPh the first excited state still has HOMO-LUMO character, but now the HOMO is localized mostly on the phenylurea moiety, while the LUMO is still on the naphtyridine moiety, conferring an almost pure CT character to the transition, with consequent decrease of the oscillator strength (from 0.63 in the linear form to 0.11 upon bending). The different nature of low energy excited states of bent ODIN-EtPh and ODIN-But is the key to rationalize the difference in quantum yields and the radiative constant k_r (Tab. 3.1).

Absorption spectra of ODIN-EtPh and ODIN-But collected in $CHCl_3$ (Figure 3.6, bottom panels) show different band-shapes with respect to absorption spectra in DMSO. The two peaks at $\sim 340nm$ and $\sim 360nm$ do not resemble a vibronic structure. The marked differences observed between absorption and excitation spectra (black and green lines) points to the presence of different species in solution, that can be reasonably attributed to the formation of aggregates. In fact, as shown in Fig. 3.10, the absorption spectrum of ODIN-But changes in shape upon dilution, and the absorption spectrum of the diluted solution compares better with the spectral shape in DMSO. No significant spectroscopic effects are observed for ODIN-EtPh upon dilution, suggesting that intermolecular interactions are stronger in aggregates of ODIN-EtPh than ODIN-But.

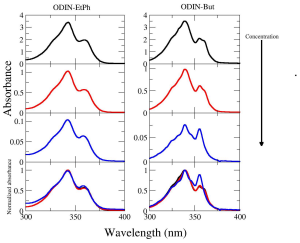

Figure 3.10: Absorption spectra of ODIN-EtPh (left panel) and ODIN-But (right panel) as a function of the nominal concentration. Concentration for ODIN-EtPh are: 110 μM 37 μM 3.5 μM from top to bottom. Concentration for ODIN-But are: 105 μM 35 μM 4.5 μM from top to bottom. Effects on spectral band-shape are negligible for ODIN-EtPh and significant for ODIN-But.

3.2.5 Aggregation MD simulations

Aggregation in $CHCl_3$ is also confirmed by molecular dynamics (MD) simulations. MD calculations show that both ODIN-EtPh and ODIN-But in chloroform tend to aggregate in stable dimers showing a well-defined

scheme of hydrogen bonding similar to that found in the crystal obtained from the same solvent (Fig. 3.5). On the other hand, MD simulations confirm both ODIN-But and ODIN-EtPh remain in monomeric form in DMSO, starting either from a bent or linear conformation. Dimer stability is evidenced by the evolution of the inter-chromophores distance as a function of the simulation time reported in Fig. 3.12 for ODIN-EtPh. Exploiting a counterpoise calculation, we obtained the stabilization energy of the array of hydrogen bonds formed in the dimer (6 hydrogen bonds, four being bifurcate) as $\Delta E_{stab} = E_{dimer} - 2E_{monomer}$, finding 192 kJ/mol stabilization for the dimer of ODIN-EtPh and 179.5 kJ/mol stabilization for ODIN-But. Calculations seem to qualitatively corroborate the experimental observation that ODIN-EtPh aggregates are more strongly bound which makes them less sensitive to dilution (Fig. 3.10). The reason resides in the higher acidity of ureidic NH protons which form stronger HB with the lactam C=O. In fact, bifurcate HBs formed by ODIN-EtPh are shorter and closer to linearity of the D-H—A angle.

Aggregates formed by ODIN-EtPh and ODIN-But should be similar from a UV-Vis spectroscopy point of view. Molecules are linear and co-facial in both dimers. Since transition dipole moments of the first excited states of linear monomers are polarized along the long axis of napthyridine their interactions should be repulsive, therefore classifying the dimer as a H-dimer. The UV-Vis absorption is consequently shifted to the blue with respect to the monomer and fluorescence is suppressed, indeed the low energy state (Kasha-state) coming from the out-of phase combination of monomer transition dipole moments is virtually dark (Figure 3.11).

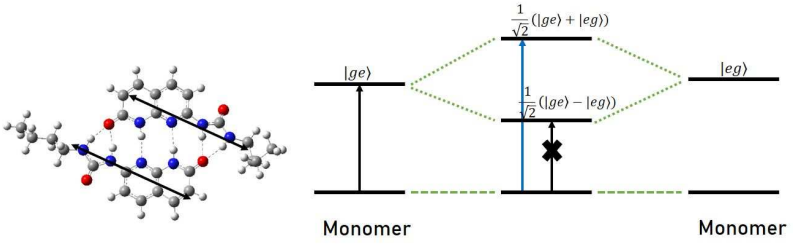

Figure 3.11: Scheme of transition dipole moments arrangement within ODIN dimers (left panel, double arrows indicate transition dipole moments) and scheme of involved electronic levels (right panel).

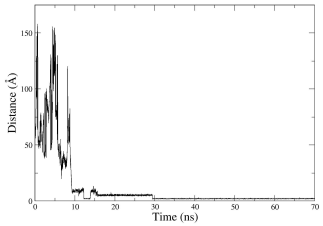

Figure 3.12: Distance between the pyridine nitrogen of one molecule and the lactame hydrogen of the other molecule forming a dimer in $CHCl_3$. Apart from minor rearrangements, the dimer is stable from 10 to 70 ns.

While the decrease in quantum yield due to H-aggregation is apparent for ODIN-But when moving from DMSO to $CHCl_3$, ODIN-EtPh has low quantum yields both in DMSO and chloroform, for different reasons.

In DMSO, ODIN-EtPh exists prevalently in its bent conformation, which is scarcely emissive due to the presence of a low lying CT state, while in chloroform the emission is quenched by H-aggregation, despite the monomer itself is in a linear conformation (and hence potentially emissive), forming the largest possible numbers of intermolecular hydrogen bonds. It is possible to obtain stable dimers of both bent ODINs (right panels of Figure 3.7) if MD simulations in chloroform are run starting from the bent conformation. These dimers form just two intermolecular hydrogen bonds, while maintaining the intramolecular bonds typical of the bent structures. Of course, the stabilization energy is smaller than for the dimers in Figure 3.4 and equilibrium may progressively shift towards the more stable dimers. Moreover, the dimers of Figure 3.5 have a head-to-tail arrangement of transition dipole moments so, at least for ODIN-But (the lowest excited state of bent ODIN-EtPh is dark, so

would not give rise to Davydov splitting), they would be J-dimers with red-shifted absorption and enhanced emission (see chapter 1), features which we did not experimentally observe. The marginal presence of these kind of aggregates, especially at high concentrations and in the first phases of aggregation, cannot however be excluded.

3.2.6 Steady state IR spectoscopy

The scheme of hydrogen bonding is coherent with the shift of C=O and C=N stretching in steady state IR upon moving from DMSO to chloroform (Figure 3.13). In particular the C=O of lactam shifts at lower frequencies (1664 cm^{-1} to 1658 cm^{-1}) as a consequence of forming two hydrogen bonds (HBs) in the dimer configuration, while the C=O of urea is mostly unaffected and the C=N of pyridine visibly shifts at lower frequencies (1609 cm^{-1} in DMSO to 1590 cm^{-1} in chloroform). No shifts are expected for N-H stretching as they act as HB donors in both solvents, with (i) the solvent itself as the acceptor in the case of DMSO, or (ii) another ODIN molecule in the case of chloroform.

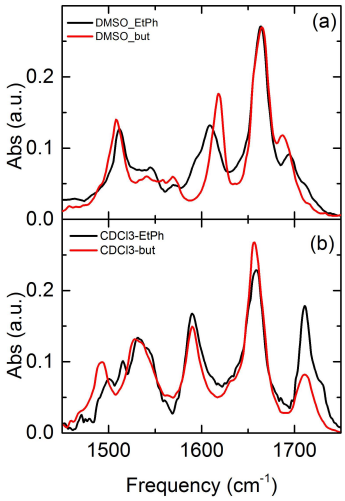

Figure 3.13: TSteady state Infrared Spectra of ODIN-EtPh and ODIN-but in DMSO (upper panel), and CDCl3 (lower panel).

3.2.7 Ultrafast Spectroscopy

Excited state evolution has been characterized by ultrafast UV-Vis transient absorption spectroscopy (TAS) and ultrafast visible pump-Infrared probe spectroscopy (TRIR).

Transient Absorption Pump-probe transient absorption data have been analyzed with a target analysis procedure, selecting for each measurement a kinetic scheme taking into account the presence of different conformers and aggregate in solution. The analysis results with the main spectral components are reported in Fig. 3.14. The transient absorption spectra of ODIN-But in DMSO are characterized by a bleaching plus Stimulated Emission (SE) signal on the low-wavelength side of the spectrum and by a broad absorption band that covers the entire range between 450 nm and 750 nm. Measurements have been performed with 340 nm and 350 nm excitation wavelength and the results obtained are almost superimposable. The temporal evolution has been fitted by using the dedicated target kinetic model reported in Figure 3.14a. We assumed, as it was evidenced by the calculations, that the solution is formed by a mixture of bent (70-80%) and linear (30-20%) monomer molecules in the ground state. Both bent and linear species contribute to the black spectral component of Figure 3.14a. Such spectrum evolves with a time constant of 8 ps in the red spectrum. The time scale and the spectral changes (slight narrowing) are fully compatible with a vibrational cooling. At this point we consider a branched evolution, giving rise to the green and the magenta spectral components. Such bifurcated evolution is related to a) the linearization of a small fraction of bent molecules (inducing a slight increase of the stimulated emission signal (green spectral component) and b) to the population of the magenta long living excited state (possibly a triplet state). Finally, the green component relaxes back to the ground state through fluorescence emission.

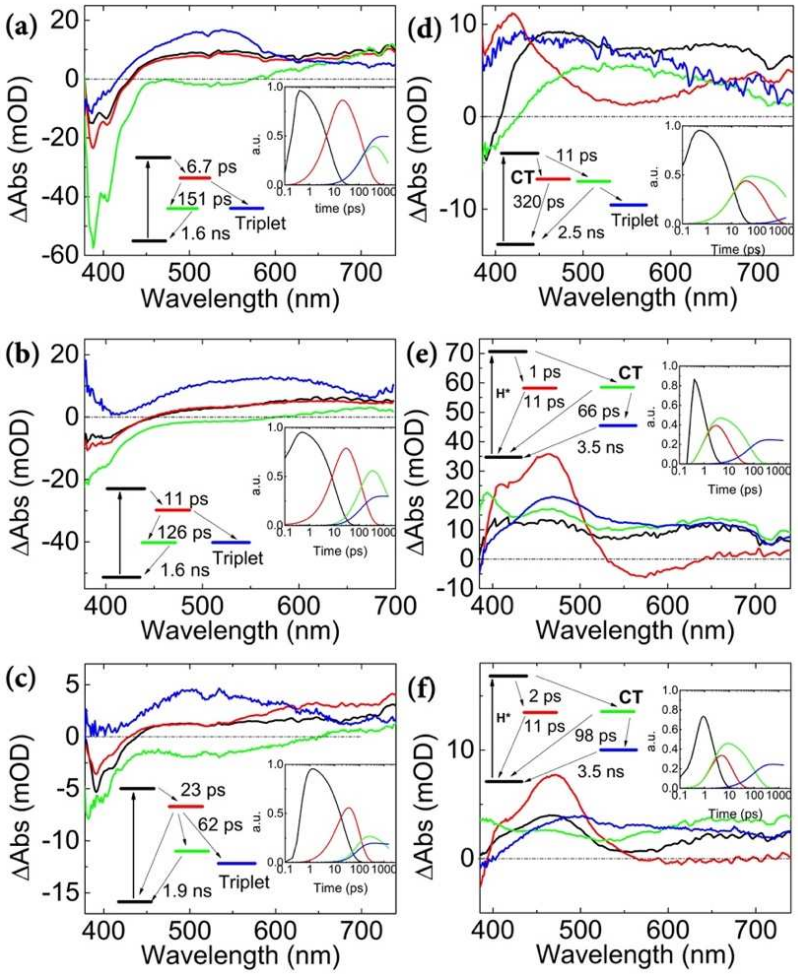

Figure 3.14: Target Analysis of transient absorption spectra; ODIN-But (a,b,c) and ODIN-Et-Phen (d,e,f) in: DMSO following 350 nm excitation (a,d), in chloroform following 350 nm excitation (b,e) and 340 nm excitation (c,f). The kinetic models adopted are schematically represented inside the graph. Spectral components are reported in the main graphs; temporal evolution of each spectral component is reported in the inset.

Concerning ODIN-EtPh in DMSO, the most significant feature is a recurrence in the intensity of the bleaching plus stimulated emission signal on the hundreds picoseconds time scale. This recurrence is due to the superimposition of an excited state absorption, that decays in the hundred picoseconds time scale, on the stimulated emission. Target kinetic model is reported in Figure 4d and is based, as for ODIN-But on the results of computations, indicating the species present at the ground state. The first spectral component (black Figure 3.14d) is ascribed to the presence of two excited species: bent molecules (80-90%) and a small fraction of linear molecules (20-10%). On the picosecond time scale, the excited bent molecules undergo relaxation towards an excited state showing the transient absorption depicted in red in Figure 3.14d. Based again on the results of computations, this state is been assigned to the Charge-Transfer and not emissive state (CT). On the same time scale, linear molecules cool down giving rise to the green spectrum (in ODIN-But the cooling process was observed on the 8 ps time scale). The CT relaxes back to the ground state with a time constant of 302 ps while the emissive state of linear molecules undergoes a partial population transfer to a long-living state (possibly a triplet state) and the back relaxation to the ground state. The excited state evolution of ODIN-But in $CHCl_3$ excited at 350 nm (Figure 3.14b) very well traces the trend observed for the ODIN-But in DMSO and the target analysis follows the same kinetic model. On the contrary the excitation at 340 nm

(Figure 3.14c) shows a different excited state absorption pathway. When ODIN-But is pumped at 340 nm, it is preferentially excited the dimeric form. The bright excitonic state of the dimer highly contributes to the black spectral component in Figure 3.14c. The red spectral component is assigned in terms of different contributions: broad absorption and stimulated emission from the monomer species and an excited state absorption from the dark excitonic state (H*) of dimers. The state H* than relaxes back to the ground state on several tens of picoseconds timescale ($\tau = 62ps$), leaving the residual spectral contribute from the monomeric species (green and blue spectral components in Figure 3.14c), similar to the monomer species in DMSO (green and magenta spectral component in Figure 3.14a). Excited state absorption spectra of ODIN-EtPh in $CHCl_3$ evidence a different pattern, independently from the excitation wavelength. The main spectral feature is a well-structured excited state absorption spanning the 400-500 nm spectral range (red spectral component Figure 3.14e-f). It is formed with a time constant of roughly 1-2 ps, and decays to the ground state with a time constant of 10-11 ps. It has been assigned to the transient absorption from the dark exciton state (H*) of the dimer. The time scale for the formation, as well as its decay time are in reasonable agreement with the excited state evolution observed for the excitonic states of some Perylene-dicarboximide (PDI) derivatives.[149–151] A small percentage of monomers in the ground state cannot be excluded, giving rise to the characteristic CT excited state absorption (green spectral component in 3.14e-f) that relaxes back to the ground state with time constants ranging from several tens of picoseconds (λ_{exc} = 350 nm) to a hundred of picoseconds (λ_{exc} = 340 nm) in very good agreement with the time scales observed in DMSO. Furthermore, it is worth mentioning that a residual signal, not fully recovering on our accessible maximum temporal delay time (1.5-1.6 ns), is observed. Careful target analysis allowed us to disentangle two different contributions: namely the blue and the magenta spectral component reported in 3.14e-f. The spectral shape (Figure 3.14e-f) of blue component very well matches, spectrally and temporally, the green nanoseconds decaying component observed in DMSO (Figure 3.14d), leading us to assign such component as the emissive one. The long living component, represented by the magenta spectra in Figure 3.14e-f and that do not decay on our accessible time scale, very well resemble the magenta spectrum obtained from the target analysis of for ODIN-But in Chloroform after 340 nm excitation, strongly suggesting the population of a triplet state also for ODIN-EtPh. Further information of the excited state dynamics is obtained from the analysis of transient absorption data in the infrared. These data confirm the dynamic evolution observed in the visible for both molecules, and further suggest that the systems do not undergo any conformational change, supporting the observation that the different conformations-aggregate in solution do not interconvert between each other, but decay following independent pathways.

3.3 Conclusions

We studied ODIN, a functionalized naphthyridine unit, designed to self-dimerize through intermolecular hydrogen bonds as demonstrated in the solid state through X-ray crystal structure analysis. Crystals of

ODIN-EtPh were obtained from $CHCl_3$ and DMSO. The crystals obtained from $CHCl_3$ evidenced dimerization by linear conformers of ODIN-EtPh with the formation of six intermolecular hydrogen bonds (Figure 3.4A,B), on the contrary the crystals obtained from DMSO showed bent ODIN-EtPh conformers forming dimers with only two intermolecular and one intramolecular hydrogen bond (Figure 3.5A,B). Such experimental evidence is related to the strong hydrogen-bond acceptor properties of DMSO with respect to chloroform. MD simulation performed in chloroform strongly support the X-Ray evidence for both compounds, as showed in Figure 3.4C,D. In DMSO, ODIN-EtPh and ODIN-But exhibit distinct absorption and emission spectra, with ODIN-But showing high fluorescence ($\Phi_f \sim 0.78$) and ODIN-EtPh being nearly non-emissive ($\Phi_f < 0.06$). MD simulations showed that ODIN-But and ODIN-EtPh are stable as monomer in DMSO. The fluorescence quenching in ODIN-EtPh is attributed to an intramolecular distortion leading to the population transfer towards a non-emissive state during the relaxation process. Computational analysis reveals that ODIN-EtPh possesses an excited state, lower in energy than the bright state, with pronounced charge transfer character and a very low transition dipole. Transient absorption spectroscopy confirms these results, showing the presence of an excited electronic state that decays with a time constant of 320 ps. Finally, our data strongly indicate that both ODIN-EtPh and ODIN-But are present as monomer species in DMSO In $CHCl_3$, both ODIN-EtPh and ODIN-But display optical properties indicating intermolecular interactions. The absorption spectra for both compounds suggest the formation of H-type intermolecular aggregates. MD simulations support this evidence, indicating that ODIN-But and ODIN-EtPh form stable dimers in chloroform with the hydrogen bond pattern DDADA. However, the excitation spectra of ODIN-But are strongly concentration-dependent, while ODIN-EtPh shows little dependence, suggesting that ODIN-EtPh form more stable intermolecular interactions. On the other hand, for ODIN-EtPh we have evidence of formation of dark excitonic state on a timescale of 1-2 picoseconds, followed by decay back to the ground state on a timescale of 10-11 picoseconds, furtherly contributing to the quenching of fluorescence emission. This study highlights the selective effect of multiple hydrogen bonds on dimer formation and the influence of the substituent attached to the ureidic group. The presence of a phenyl group stabilizes the aggregates, as seen in the strong dependence of ODIN-But's excitation spectra on concentration compared to ODIN-EtPh. Additionally, the introduction of a phenyl group leads to the formation of charge transfer excited states, altering the distribution of excited electronic states in the molecules.

Emission of BODIPY Oligomers: Tuning by Polarity and Temperature

4

4.1 Introduction

J-aggregates were first discovered by Jelley in 1937 while studying PIC cyanine in water.[77] J-aggregation is associated with red-shifted absorption, narrow bandwidth and enhanced emission properties[53, 152], which make J-aggregates appealing for applications in biosensing and microscopy[102]. In recent work by Patalag et al.,[153] J-aggregation was employed to enhance fluorescence in BODIPY dyes by suppressing non-radiative decay pathways such as intersystem crossing (ISC),[154] internal conversion (IC), and reductive photoelectron transfer (rPET).[155, 156] The covalent linking of substituted BODIPY units through ethylene bridges efficiently coupled their transition dipole moments to form intramolecular J-aggregates. As a result of J-aggregation, Kasha state becomes optically allowed and quantum yield Φ_f increases, for some BODIPY series, from 0.04-0.05 in the monomer to 0.7-0.8 in the oligomers.[153]

Here, we focus on the competition between rPET and radiative decay shown by homologous series 7 from Ref. [153]. In the rPET process, an electron acceptor unit is initially photoexcited, prompting an electron transfer from a neighboring unit to the excited acceptor, which is therefore reduced. This transfer creates a new excited state, often characterized as a charge transfer (CT) or $n \rightarrow \pi^*$ state, which typically leads to quenching of radiative emission.[157] Series 7 was obtained by Dr. L. Patalag in the group of Prof. D. Werz (University of Freiburg) from the oligomerization of BODIPY **1** (left panel of Fig. 4.1), to yield dimer, tetramer, hexamer and octamer. The rPET mechanism involves the transfer of an electron from the lateral alkylaniline unit (the charged donor) to the electron-poor BODIPY core (the charge acceptor).

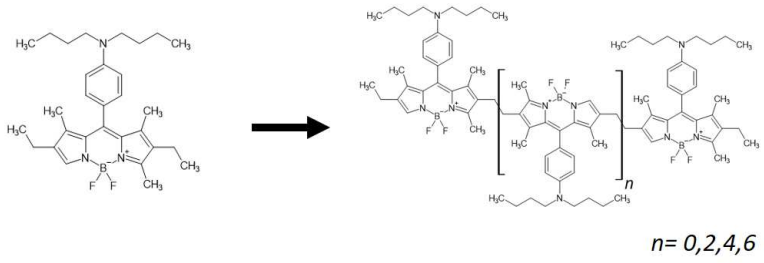

Figure 4.1: Monomer (left panel) and oligomers (right panel) of the functionalized BODIPY **1** studied in the following chapter.

rPET leads to the formation of an almost perfectly dark charge transfer (CT) excited state, whose energy is highly sensitive to the polarity of the surrounding environment. The relative energy of the CT and the bright $\pi \rightarrow \pi^*$ transitions localized on the BODIPY core differs between non-polar solvent toluene and polar solvent THF.

As a consequence, the nature of Kasha state, hence the fluorescence properties, change with the solvent polarity. BODIPY **1** is fluorescent in non polar solvents like toluene, while it is not in polar solvents like

THF. In fact the Φ_f of **1** is 0.03 in THF and 0.55 in toluene. When various units of **1** are covalently linked to form a J-aggregate (Fig. 4.1), the exciton coupling stabilizes the $\pi \rightarrow \pi^*$ state, making the oligomers fluorescent even in polar solvents. For an instance, Φ_f in THF steadily increases from the 0.05 of the dimer to the 0.39 of the octamer.[153]

The polarity of the environment can change in response to external stimuli. Here, we focus on the role of temperature. Since the nature of Kasha state of BODIPY **1** and its oligomers depends on solvent polarity and, in turn, solvent polarity depends on temperature[158], we expect the fluorescence properties of BODIPYs to drastically vary with temperature, making them potential probes for temperature variations.

4.2 Results and discussion

4.2.1 DFT and TD-DFT calculations

The structure of BODIPY **1** (left panel Fig. 4.1) was optimized in gas-phase using DFT, with CAM-B3LYP as functional and 6-31G(d,p) as basis set. The minimum is characterized by a 90° dihedral between the aniline electrondonor group and the BODIPY core (Fig. 4.2). This geometry stems from steric repulsion between hydrogens of the aniline and the methyl groups of the BODIPY, similarly to what happens in biaryls.[159]

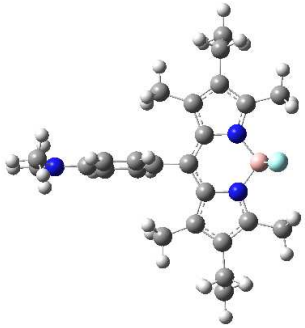

Figure 4.2: Ground state equilibrium geometry of BODIPY **1**.

A TD-DFT calculation (CAM-B3LYP,6-31G(d,p)) was performed on the optimized structure. The first excited state is a bright HOMO→LUMO transition, with $\pi \rightarrow \pi^*$ character, entirely localized on the BODIPY unit; the second excited state is instead a pure CT with the aniline as donor and the BODIPY core as the acceptor. Since the two units are orthogonal the electric transition dipole to this state vanishes.[160] TD-DFT data for the monomer are summarized in Fig. 4.3.

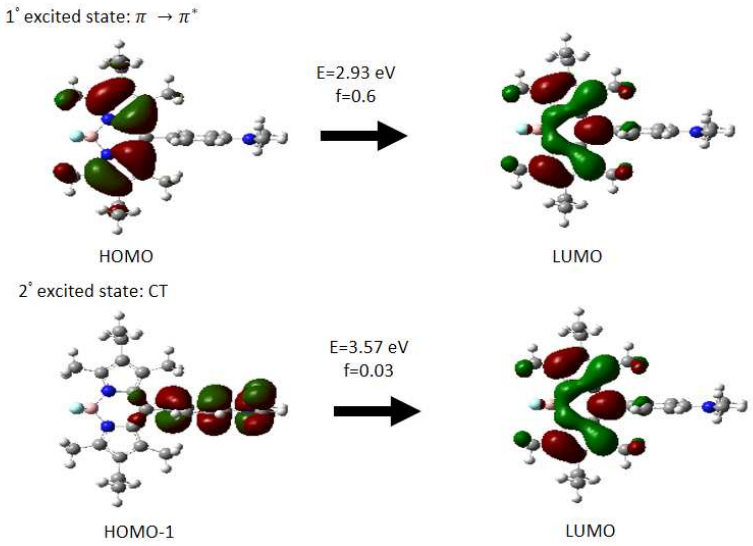

Figure 4.3: First and second excited states of BODIPY **1** from TD-DFT (CAM-B3LYP,6-31G(d,p)). E and f indicate respectively the transition energy and oscillator strength.

Taking the geometry from Ref. [153], we performed TD-DFT calculations on the most stable conformation for the dimer (SC-trans-saddle1). Results in Table 4.1 are in agreement with exciton theory and clearly identify the

dimer as a J-dimer. The bright $\pi \rightarrow \pi^*$ states split into a lower energy in-phase combination, with twice the monomer oscillator strength, and a high energy out-of-phase and dipole forbidden combination. On the other hand, the CT states remain almost degenerate with the monomer CT, due to their negligible transition dipole moments[54]. The characteristics of the first four excited states for the dimer (CAM-B3LYP,6-31G(d,p)) are summarized in Tab. 4.1.

Excited state	Nature	Energy (eV)	f
1	$\pi \rightarrow \pi^*$ (in phase)	2.82	1.28
2	$\pi \rightarrow \pi^*$ (out of phase)	2.97	0.00
3	CT	3.57	0.07
4	CT	3.58	0.08

Table 4.1: Characteristics of the first four excited states of the BODIPY dimer in gas phase. f indicates the oscillator strength.

Oligomers of **1** are hence characterized by a low lying optically allowed exciton state, which potentially makes them strongly emissive (left panel of 4.4).

However, CT states can be largely stabilized by polar solvents[161], especially if donor and acceptor are weakly conjugated[160]. CT stabilization by the solvent and J-exciton coupling between BODIPY-localized states compete to determine the nature of Kasha state. If exciton coupling prevails over CT stabilization by the solvent the dimer will be fluorescent (right panel of 4.4), but for high polarities the CT state could be Kasha state, therefore quenching the emission.

If the energy difference between the CT states and the emissive exciton state is reasonably low, it is possible to tune it by varying environmental polarity with external stimuli, giving therefore the opportunity to control the emission properties.

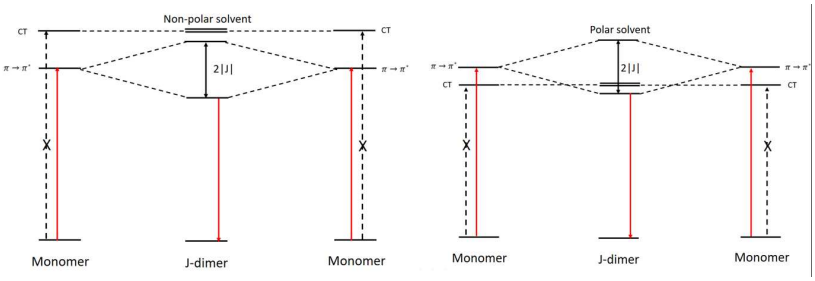

Figure 4.4: Energy levels in a non polar solvent (left panel) and a polar solvent (right panel).

4.2.2 UV-Vis spectroscopy

Monomer

The spectroscopic characterization of the monomer, BODIPY **1**, is a fundamental step in order to study aggregates.

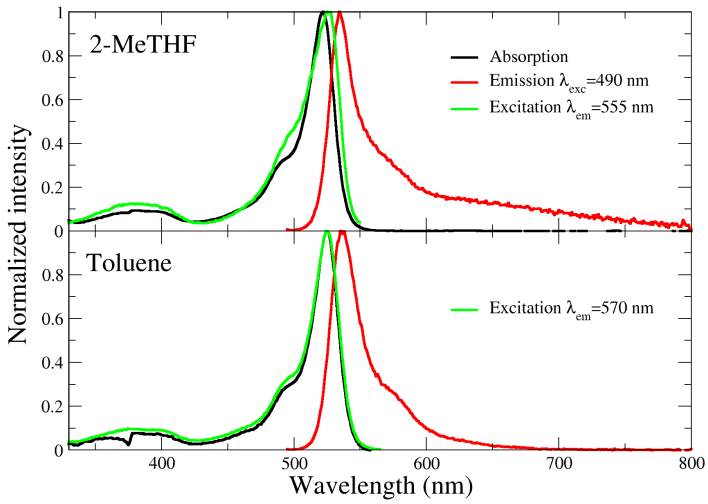

Figure 4.5: Absorption, emission and excitation spectra of BODIPY **1** in 2-MeTHF (upper panel) and toluene (lower panel).

There are some notable differences between the emission spectra of BODIPY **1** in 2-MeTHF and toluene of Fig. 4.5. Both spectra show the sharp emission characteristic of BODIPYs, but the spectrum in 2-MeTHF features a long red-shifted tail which is absent in toluene. The red-shifted tail hints at a double emission in 2-MeTHF, due to the presence of a low lying CT state, stabilized by solvent polarity. The sensitivity of CT transitions to the surrounding often reflects in large inhomogeneous broadening[160, 161], explaining why the CT emission of Fig. 4.5 is so broad. Fluorescence excitation spectrum is superimposable to absorption in toluene, while it is slightly different in 2-MeTHF, offering another hint of anti-Kasha behaviour. As reported by Patalag et al.[153], the quantum yield of BODIPY **1** in toluene is 0.76, while it is 0.03 in THF (eith similar polarity as 2-MeTHF), pointing at a different nature of Kasha state in the two solvents.

The solvent polarity generally increases with lowering temperature, and the dependence of the dielectric constant on temperature is well known for THF[158]. Measurements in 2-MeTHF were performed between 77 and 298 K. Below 100-120 K the solvent is vitrified, which heavily affects properties of the embedded chromophores[162]. On the other hand, toluene crystallizes at 178 K, making a fluorescence measurements not viable due to scattering, so the measurements could be performed between 180 and 298 K (Fig. 4.6). All experimental conditions were kept constant throughout the measurements at different temperatures, in order to have comparable absolute intensities.

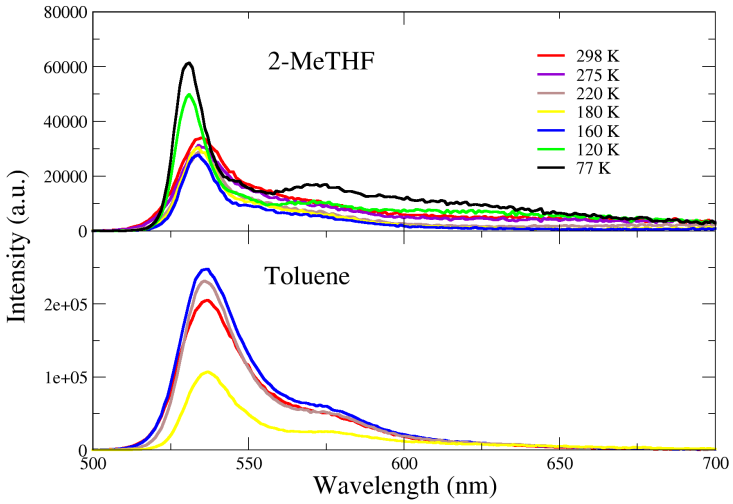

Figure 4.6: Emission spectra as a function of temperature in 2-MeTHF (upper panel) and toluene (lower panel). λ_{exc} = 525 nm for all spectra.

Emissions in 2-MeTHF are noisy and weak[153] and do not vary appreciably with temperature, except when the solvent is vitrified, as the enhanced rigidity of the matrix suppresses non-radiative decays.[160] The CT emission appears as a red-shifted broad tail from 298 to 120 K, but it is a defined peak at 573 nm at 77 K, when the matrix is vitrified. Blue shift and sharpening of CT emission are common effects of increased matrix rigidity[160]. A liquid solvent usually reorganizes around the excited CT state, leading to its stabilization and a red-shifted emission. Since many solvent configurations around the solute are thermally accessible, inhomogeneous broadening is also observed.[161] All of this is not possible when the solvent is a glassy matrix, hence the CT state gets very little stabilization and inhomogeneous broadening is drastically reduced[162].

In toluene (lower panel of Fig. 4.6) the Kasha state is bright and localized on the BODIPY, therefore emission is stronger, and the red shifted tail is not observed. Emission intensity decreases at 180 K, indicating that the CT may come close to the localized state, due to the increased polarity of the solvent. This is reflected in the fluorescence lifetime, as a relatively fast decay component (τ=1.31 ns) appears at 180 K, while the decay is monoexponential (τ=3.79 ns) at room temperature (Fig. 4.7). For reference, lifetimes of **1** in 2-MeTHF are constant with temperature and around 5.3 ns.

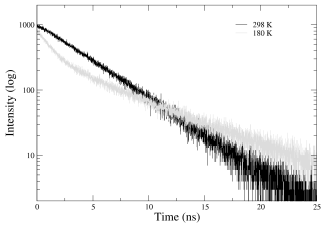

Figure 4.7: Fluorescence lifetimes of BODIPY **1** in toluene at 298 and 180 K.

Oligomers

Having characterized the monomer in a polar (2-MeTHF) and a non-polar (toluene) solvents, we proceed to study the oligomers in the same solvents. Exciton coupling comes into play in oligomers, competing with the rPET process. We will evaluate the effect of temperature, and in turn solvent polarity, on this delicate equilibrium.

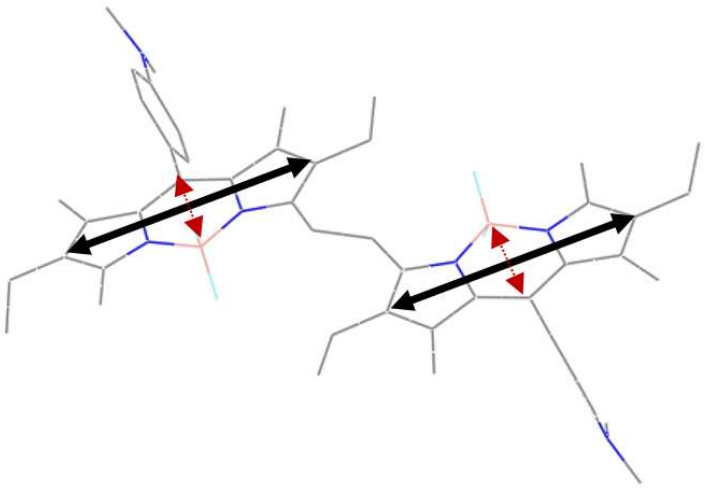

Figure 4.8: The most stable conformation of BODIPY dimers.[153] Transition dipole moments of the monomer are represented as a double headed black arrow for the $\pi \rightarrow \pi^*$ excited state and as a double headed red arrow for the CT state.

Oligomers The most stable conformation adopted by a dimer of BODIPY **1** was reported in Ref. [153] and is sketched in Fig. 4.8. From Fig. 4.8 it is apparent the transition dipole moments of BODIPY localized states are arranged in head to tail fashion, forming a J-aggregate. CT transitions are also in head to tail fashion, but due to their low transition dipole moments the exciton coupling is much weaker.

Fig. 4.9 shows absorption, emission and fluorescence excitation spectra of the homologous series synthesized from BODIPY **1** at room temperature. In these conditions oligomers are emissive as exciton coupling makes sure the lowest excited state has dipole-allowed $\pi \rightarrow \pi^*$ nature, and no CT features (such as the red shifted tail of Fig. 4.5) appear in emission. Moreover, excitation coincides with absorption, indicating Kasha's rule is respected.

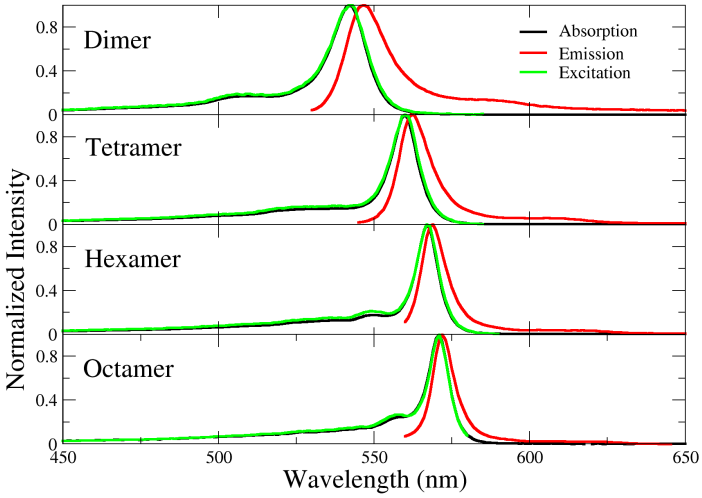

Figure 4.9: Absorption, emission and excitation spectra of the BODIPY homologous series at 298 K.

Fig. 4.9 shows how the relative intensity of the 0-1 vibronic transition decreases with increasing delocalization length, an expected effect due

to the progressive decrease of Huang-Rhys factors.[53] The shoulder at about 550 nm for the hexamer and the octamer is not linked to vibronic coupling, but to higher energy excited states becoming partially allowed due to finite chain length.

The shape and intensity of emission drastically changes upon decreasing temperature (Fig. 4.10 and 4.11). The intensity decreases by a factor of three already at 275 K, and a red shifted tail appears in emission.

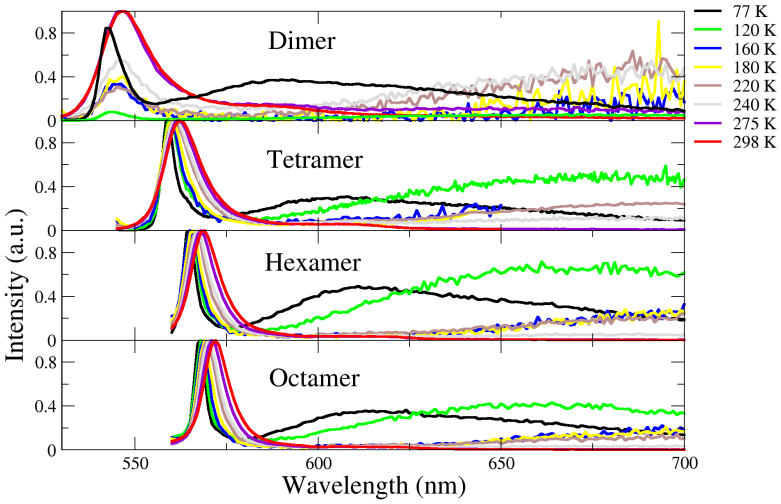

Figure 4.10: Normalized shape of emission spectra of BODIPY oligomers in 2-MeTHF at varying temperatures.

The relative intensity of CT emission increases at low temperatures (Fig. 4.10). Below 120 K the matrix is vitrified and the CT undergoes the expected blue shift. A plot of the intensities integrated all over the emission spectrum versus temperature for each member of the series is reported in Fig. 4.11.

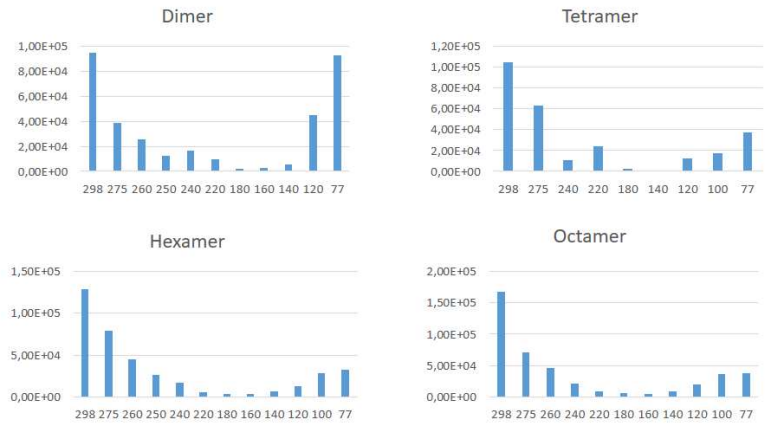

Figure 4.11: Histograms of integrated intensities vs temperature for the homologous series of BODIPY **1** in 2-MeTHF.

The trend is similar for all the series members: intensity drastically decreases between 298 and 140 K, then increases when the matrix undergoes the transition to glass. This behaviour is fully consistent with CT stabilization due to increased solvent polarity, which leads to a scarcely emissive Kasha state at low temperature.

Fluorescence lifetimes at room temperature are monoexponential and decrease from τ=4.01 ns of the dimer to τ=1.81 ns of the octamer, as the radiative decay rate increases with the length of delocalization. For all oligomers a fast component ($\tau \sim 0.4ns$) appears at low temperatures, making the decays biexponential. The relative weight of the fast component grows at low temperatures (Fig. 4.12), but the fast component disappears when the matrix is vitrified, with lifetime considerably increasing ($\tau \sim 5$ ns for all members). We suggest that the fast component is linked to the rPET process, which transfer population from the $\pi \longrightarrow \pi^*$ manifold to the CT manifold. This decay may involve conformational degrees of freedom which are hampered in a rigid environment, hence the increase of emission intensity and lifetime when the matrix is glass.

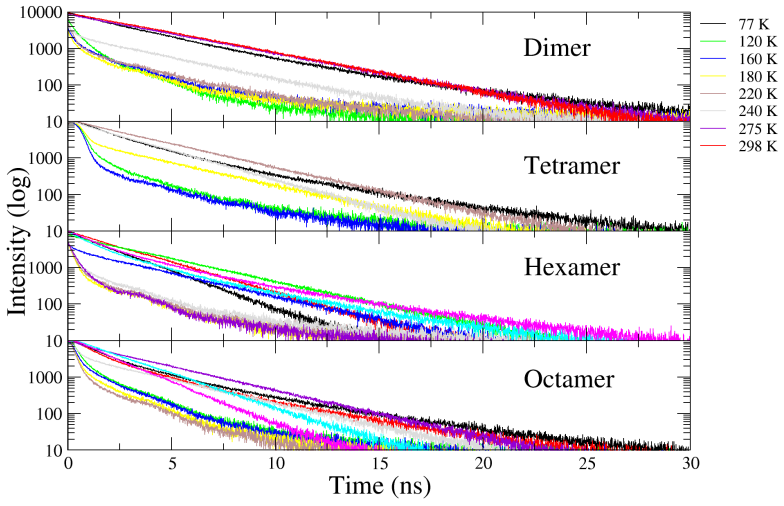

Figure 4.12: Fluorescence lifetime decays of BODIPY oligomers in 2-MeTHF at varying temperatures.

In order to confirm that the observed effects are due to variation in polarity, and not directly to variation of temperature, we repeated the variable temperature measurements in toluene. Absorption, emission and excitation spectra of the series in toluene at 298 K do not look significantly different from Fig. 4.1, but emission does not show any CT features upon decreasing temperature (Fig. 4.9), suggesting CT state is always at higher energy than BODIPY localized state.

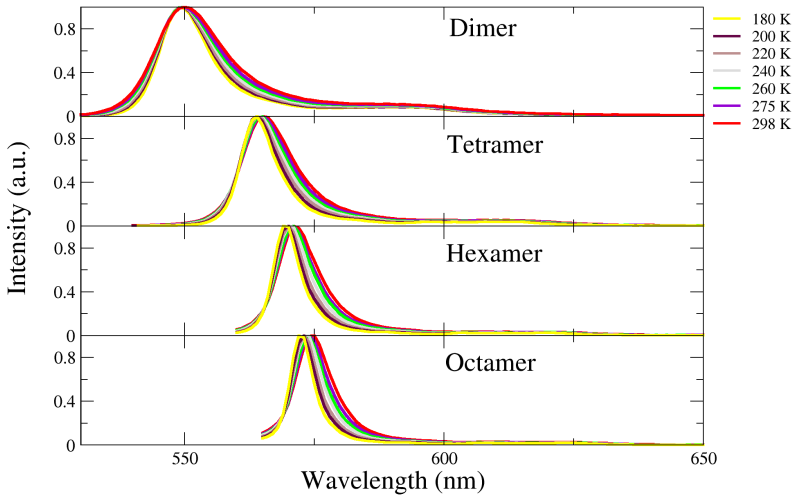

Figure 4.13: Normalized shape of emission spectra of BODIPY oligomers in toluene at varying temperatures.

Consistently, the integrated emission intensities in toluene are almost constant with varying temperature (Fig. 4.14).

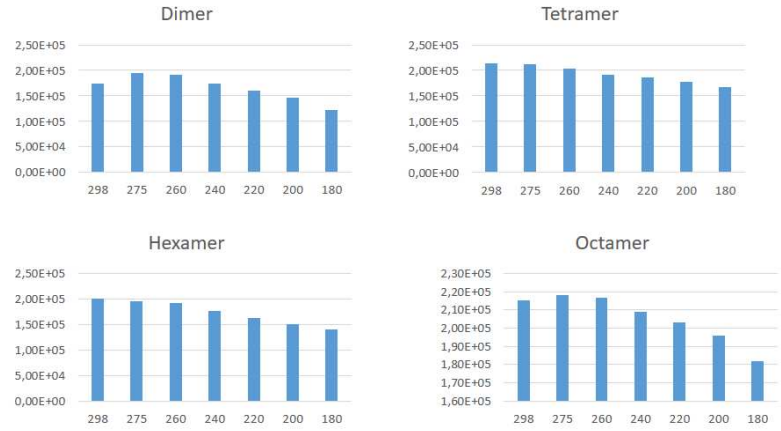

Figure 4.14: Histograms of integrated intensities vs temperature for the homologous series of BODIPY **1** in toluene.

Lifetime decays of the homologous series in toluene (from τ=3 ns for the dimer to τ=1.54 ns for the octamer) do not significantly vary with temperature either (Fig. 4.15).

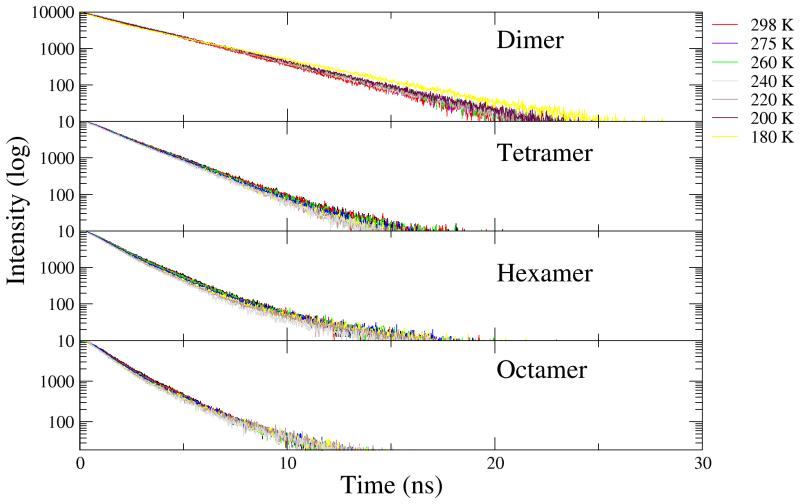

Figure 4.15: Fluorescence lifetime decays of BODIPY **1** homologous series at varying temperature in toluene.

Overall the results confirm that the T-dependence of the spectra observed in 2-MeTHF is due to the variation of the solvent dielectric constant.

4.3 Conclusions

We performed an accurate spectroscopic study on a homologous series derived from the oligomerization of a substituted donor-acceptor BODIPY dye. The competition between a fluorescence-quenching rPET process and fluorescence-inducing J-exciton coupling was analyzed as a function of temperature.

We showed that emission properties in 2-MeTHF change with temperature, with absolute intensities and fluorescence lifetimes drastically decreasing at low temperature. We disentangled the effects of temperature and polarity by performing analogous measurements in non polar solvent toluene. We could conclude the nature of Kasha state, and hence the emissivity, strongly depends on environmental polarity, which, for 2-MeTHF, increases at low temperatures. The analysis of emission spectral shape, absolute intensities and fluorescence lifetimes reveal that in 2-MeTHF CT state becomes Kasha state at low temperatures, largely suppressing emission. These findings highlight the potential of BODIPY aggregates as efficient probes for environmental polarity and, indirectly, local temperature.

Organic Radicals as Nanothermometers for Biological Tissues

5

5.1 Introduction

During the last years, we have assisted to a rising interest in the implementation of substituted trityl radicals as emitting species in electroluminescent devices.[163, 164] Owing to their doublet electronic configuration, such trityl radicals allow overcoming the problems associated to the exciton statistics in OLEDs,[165, 166] without the need of using expensive phosphorescent emitters.[167, 168] This is not the only interesting aspect of this class of open-shell molecules, since their unique absorption and emission properties can be proficiently employed in other photoluminescence applications, especially in bioimaging[169, 170]. Indeed, many substituted trityl radicals present a strong absorption in the near-UV region (~380 nm), and a weak absorption transition ($D_0 \rightarrow D_1$) close to 550 nm.[171] Such radicals are usually low emitting species in solution, with values of Φ_f of about 0.02, caused by the associated low oscillator strength, associated to the relevant transition from the Kasha's state (the lowest excited electronic state) to the ground state, and the consequent prolonged radiative lifetime, (~ 400 ns at room temperature and ~ 300 ns at 77 K).[60, 172–175]that makes the internal conversion (IC) mechanisms favored. Quantum yield is proportional to the radiative decay constant k_r, which in turns depends on the oscillator strength. Once immobilized in diluted frozen solutions at 77 K, such trityl radicals, and in a more general way carbon-centred free radicals, exhibit values of Φ_f up to 0.7-0.8.[60, 175] Nevertheless, in the condensed solid-state they are strongly affected by the aggregation-caused quenching (ACQ) phenomenon that decreases the fluorescence quantum yield.[60, 163]

Recently, Blasi et al. demonstrated that dilution of the tris(2,4,6-trichlorophenyl)methyl radical (TTM, Fig. 5.1 middle panel) into optically-neutral organic rigid matrices, like in polymers or nanoparticles, improves the luminescence properties, the photostability, and promotes the formation of red/NIR-emitting excimers.[60] In addition, the authors demonstrated that nanoparticles made of the optically neutral tris(2,4,6-trichlorophenyl)methane (TTM-αH, Figure 5.1 left panel) and doped with TTM can be used as ratiometric nanothermometers for bio applications.[176]These nanoparticles (TTMd-ONPs), when excited at 377 nm, exhibit a dual emission due to the presence of the radical monomer and excimer species. The monomer emission appears at 572 nm with an almost temperature-independent intensity, while the excimer emission appears around 665 nm and its intensity decreases with the temperature raising. TTMd-ONPs show an excellent thermal absolute sensitivity (S_a) of 0.6–3.7 % K^{-1} in a wide temperature range (from 278 to 328 K). The absolute percent sensitivity is estimated according to Equation 5.1:

$$S_a = |\frac{\Delta Q}{\Delta T}| \times 100 \tag{5.1}$$

where $\Delta Q = \Delta[I_M/I_E]$ is the variation of the monomer/excimer intensity ratio for a given temperature change (ΔT), being I_M and I_E the intensity maxima of the monomer and excimer species, respectively. TTMd-ONPs also display an excellent temperature-sensitive emission reversibility and a temperature resolution reaching 0.3 °. Moreover, TTMd-ONPs are not cytotoxic and their ratiometric output, defined as the ratio

between the emission intensities of monomer and excimer, I_M/I_E, is not affected by different aggregation levels of the nanoparticles nor by changes of pH and ionic strength that may occur under physiological conditions. S is not affected either by different aggregation levels of the nanoparticles or by changes on pH and ionic strength that may occur under physiological conditions. Such nanoparticles are therefore able to measure temperature changes at the nanoscale by the ratiometric output of each individual particle or their small aggregates. Finally, in vivo thermometry experiments made with Caenorhabditis elegans worms indicated that TTMd-ONPs can be used as fluorescence imaging probes and to monitor the temperature changes inside the worms from 278 to 313 K with a high sensitivity. All such results indicate the considerable potential applications of polychlorinated trityl radical-based ONPs in biological nanothermometry. However, to expand this application it is convenient to shift the excitation wavelength of radical doped ONPs to the first biological transparency window (BTW) at the NIR region (650–950 nm), allowing to decrease the cytotoxicity of UV excitation light and at the same time to achieve a higher penetration-depth inside biological tissues for possible in vivo investigations with such ONPs.[177, 178] In this context, it should be mentioned that open-shell fluorophores based on push-pull trityl radical derivatives have shown outstanding two-photon absorption cross sections,[179, 180] while no studies have been reported on isolated and excimeric forming polyhalogenated trityl radicals.

Here we investigate if aqueous suspensions of doped organic nanoparticles (ONPs) with two polychlorinated trityl radicals, TTM and PTM (perchlorotriphenylmethyl; Fig. 5.1), can be two-photon excited in the NIR region yielding the concurrent emission in the first BTW region region as well. Thus, we prepared and investigated the optical properties and behavior of such doped ONPs, namely TTMd-ONPs and PTMd-ONPs, as nanoprobes for NIR thermometry since the use of light in the range of the first BTW could provide the above-mentioned advantages for their use as nanothermometers in tissues studies.[179] The choice of PTM radical as possible fluorescent probe for two-photon nanothermometry was suggested by the fact that the PTM radical in solution exhibits a more red-shifted absorption and emission compared to the less chlorinated TTM species. TTM-αH ONPs showed spherical morphology and high colloidal stability even at high temperature with an impressive biocompatibility. The resulting photoluminescence properties of PTMd-ONPs were compared with those of our previous reported TTM-based nanoparticles, TTMd-ONPs.

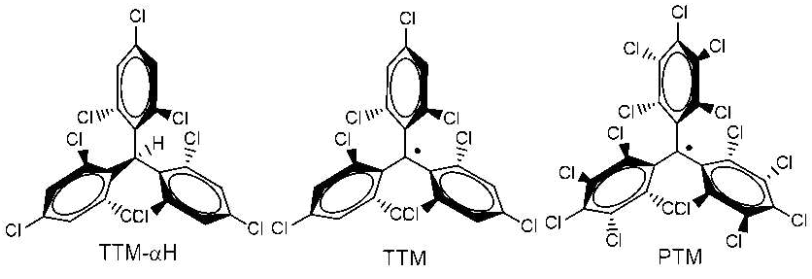

Figure 5.1: Molecular structures of TTM-α H, and of TTM and PTM radicals.

Solvent	THF	2-MeTHF (77 K)
λ_{abs}^{max} (nm)	385	387
λ_{em}^{max} (nm)	610	589
Stokes Shift (cm^{-1})	9581	8861
ϵ ($cm^{-1}M^{-1}$)	38450	-
Φ_f	0.02	0.54
τ (s)	9.7×10^{-9}[a]	2.5×10^{-7}[b]
k_r (10^{-6} s^{-1})	2.1	2.1[a]
k_{nr} (10^{-6} s^{-1})	102.9	1.8[b]

Table 5.1: Optical properties of PTM radical in THF at room temperature and in glassy 2-MeTHF at 77 K. [a] Excited-state lifetimes were estimated through mono-exponential reconvolution fit analysis of the fluorescence decay, and the fitting results were judged by the reduced χ^2 value (χ^2 < 1.2); [b] It was assumed that the radiative rate constant is independent of the temperature, so using the relation $\Phi_f = \frac{k_r}{k_r+k_{nr}} = k_r\tau$, the non-radiative rate constant and the excited-state lifetime were determined.

5.2 Results and discussion

5.2.1 Optical properties of isolated TTM and PTM radicals

Before studying the photoluminescence properties of PTM and TTM radical-doped ONPs, the absorption and emission of isolated PTM radical molecules in THF at room temperature (r.t.) and in 2-MeTHF at 77 K (Figure 5.2 and Table 5.1) were revisited. PTM radical in THF solution at r.t. presents a maximum of absorption at 385 nm, a maximum of emission at 610 nm (16.393 cm^{-1}, with λ_{exc} = 377 nm), a Φ_f of 0.02, and an average excited-state lifetime of about 9 ns. Using the simple relation $\Phi_f = \frac{k_r}{k_r+k_{nr}}$, where k_r is the radiative rate constant, k_{nr} the non-radiative rate constant and τ the excited-state lifetime, we obtain $k_r = 2 \times 10^6$ s^{-1} and $k_{nr} = 1 \times 10^8$ s^{-1}. In the glassy 2-MeTHF solution at 77 K, the PTM radical shows a strong improvement of Φ_f, achieving a value of 0.54, and a maximum of absorption at 387 nm together with a blue-shift of the emission of 605 cm^{-1}, with a maximum at 589 nm (16.998 cm^{-1}) and two vibronic peaks at 640 nm (15.625 cm^{-1}) and 703 nm (14.225 cm^{-1}). By contrast, in absorption only minor variations occur with respect to room temperature, namely a narrowing of the vibronic bands due to the decrease of the inhomogeneous broadening. Assuming that k_r is not sensitively affected by changes in temperature and viscosity,[179, 181] the excited-state lifetime at 77 K amounts to 250 ns, more than one order of magnitude longer than in solution, which is consistent with values reported for other trityl radicals in frozen matrices.[173, 174]

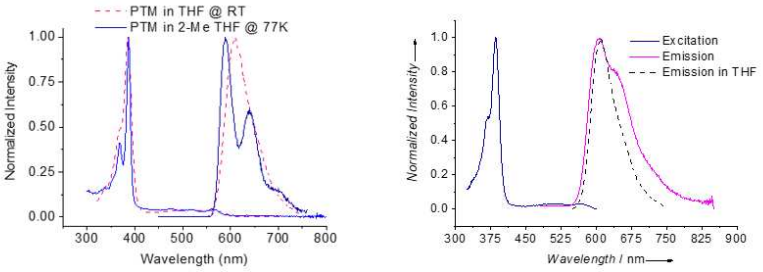

Figure 5.2: Normalized emission and excitation spectra of PTM radical. Left) in THF and 2-MeTHF at r.t. and at 77K. Right) in a PMMA film with the emission spectrum of PTM in THF solution (dashed line) for comparison.

A similar considerable enhancement of Φ_f was also obtained dispersing PTM in poly(methylmethacrylate) (PMMA) films, achieving a Φ_f of 0.19 and an average lifetime of 100 ns.[60, 175]

5.2.2 Characterization of PTM-doped organic nanoparticles

These results suggested the possibility to obtain good luminescence properties using PTM radical as a dopant of ONPs, i.e. in PTMd-ONPs. Hence, PTMd-ONPs, using TTM-αH as the inert matrix and containing different amounts of PTM radical (0.5, 3, 6.5, 13, 26, 50 % in mol.), were prepared using the re-precipitation method, similar to what was done for TTMd-ONPs.[60] TTM-αH, the hydrogenated analogue of the TTM radical, was chosen as the host because it allows generating ONPs with good colloidal properties, and offers, due to its structure, a receptive environment to the highly chlorinated radical guest molecules.[60]

Dynamic light scattering (DLS) analysis of the resulting PTMd-ONPs aqueous suspensions gave average hydrodynamic diameters in the 50–90 nm range with polydispersity indexes (PDI) < 0.16, and Z-potentials of about -42 mV for all the samples, indicative of good colloidal stability. Transmission electron microscopy (TEM) images confirmed the DLS measurements revealing the spherical morphology of the ONPs and their monomodal size distribution. Absorption spectra of PTMd-ONPs suspensions in water are affected by light scattering due to their nanoscopic sizes, especially in the near-UV region where the radical-doped ONPs present the maximum of absorption (Figure 5.3). In order to correct the scattering component, the absorption spectra of suspensions of ONPs made by pure TTM-αH with comparable sizes and size distributions were used as a reference to determine the scattering-correction functions (Figure 5.3), since TTM-αH is completely transparent in the 300–800 nm range.[60, 182]

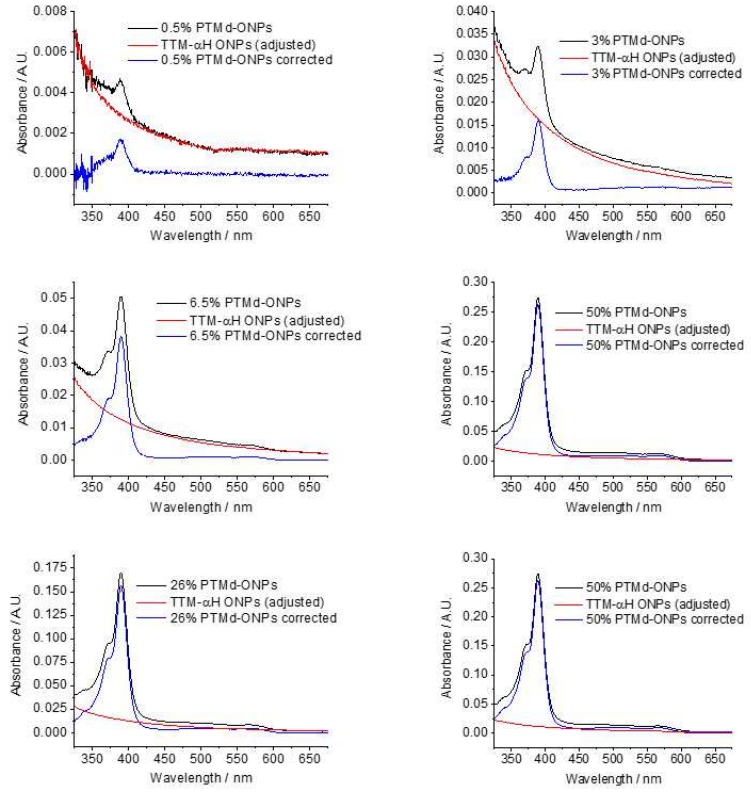

Figure 5.3: Scattering corrections of absorption spectra of suspensions of PTMd-ONPs with different doping levels in water.

The scattering-corrected absorption spectra of the PTMd-ONP suspensions (Figure 5.4) are quite similar to the spectrum of PTM in THF, confirming the good quality of the correction method.

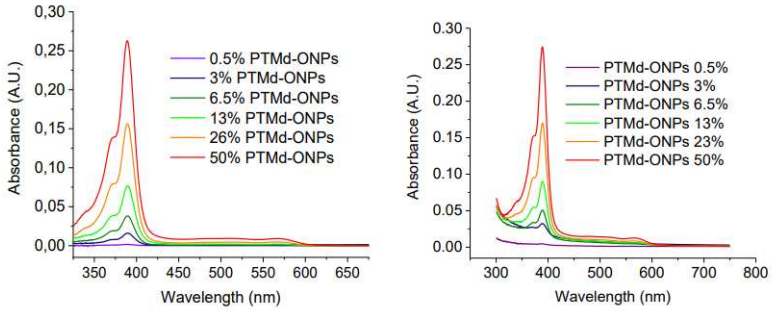

Figure 5.4: Scattering corrections of absorption spectra of suspensions of PTMd-ONPs with different doping levels in water.

The absorbance values of PTMd-ONP suspensions after the scattering correction were used for the evaluation of Φ_f. The confinement of the PTM radical in a rigid environment, like the ONPs, leads to a significant enhancement of Φ_f, due to the reduction of radiationless mechanisms of excited states decay. Indeed, the luminescence quantum yield amounts to $\Phi_f = 0.40$ in the case of the 0.5% PTMd-ONPs and to 0.15 for the 3% PTMd-ONPs, corresponding to enhancements of the luminescence of a factor of about 10 with respect to the THF solution at r.t. ($\Phi_f = 0.02$). When increasing further the amount of radical doping, an efficient ACQ is observed, leading to a halving of the luminescence efficiency when doubling the radical concentration, with an almost complete emission quenching in the case of the 50% PTMd-ONPs (Figure 5.5) affecting also the fluorescence lifetimes (Figure 5.6 and Table 5.2).

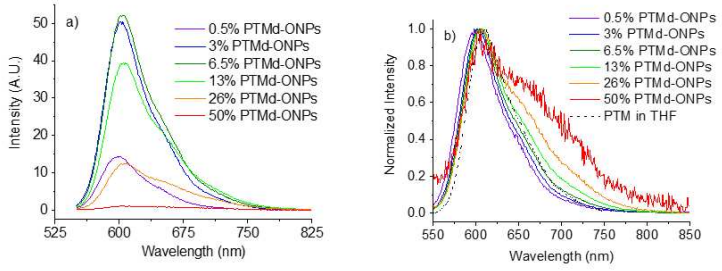

Figure 5.5: a) Emission spectra of water suspensions of PTMd-ONPs with different radical doping levels under excitation at the maximum of absorption; b) Normalized spectra of such PTMd-ONP suspensions compared with the normalized emission spectrum of PTM in THF (dashed black line).

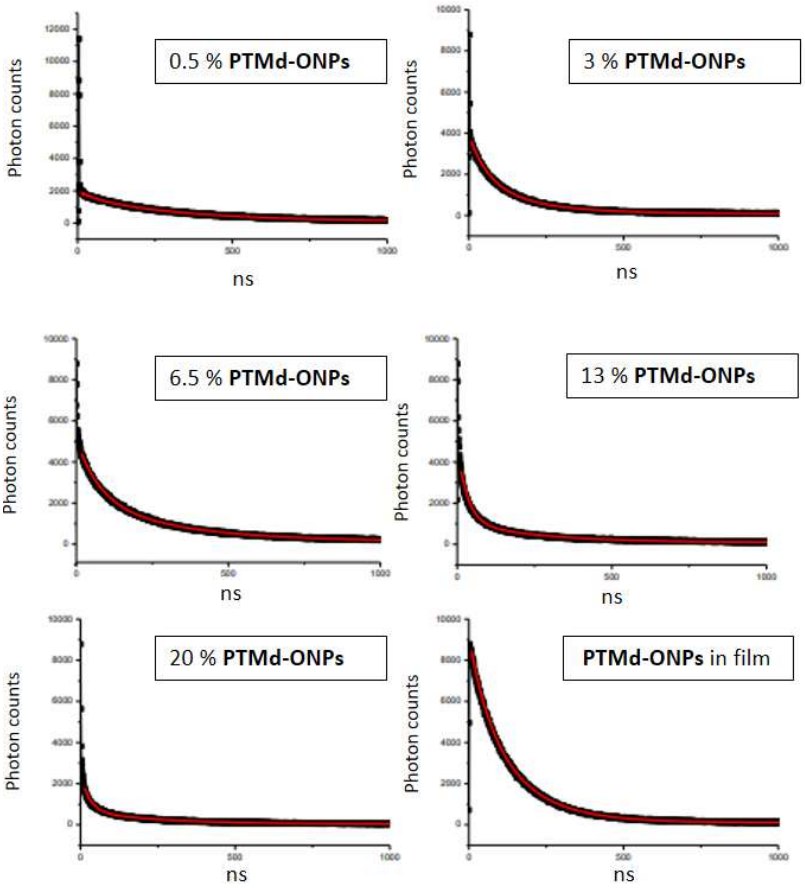

Figure 5.6: Fluorescence decays of PTMd-ONPs and of PTM radical in a polymer film

		Bi-exponential fit			Stretched exponential	
PTMD-ONPs w/w	A_1 (%)	τ_1 (ns)	A_2 (%)	τ_2 (ns)	τ_0 (ns)	β
0.5	18.7	66	81.3	334	272	0.85
3	60.9	63	39.1	195	94	0.78
6.5	57.1	74	42.9	304	120	0.67
13	79	31	21	260	24	0.44
26	73.4	27	26.6	236	18	0.4
PTM radical (film)	40.1	72	59.9	154	112	0.89

Table 5.2: Fluorescent Lifetime of PTMd-ONPs and PTM radical (film) obtained by fitting curves reported in figure 5.6.

Stretched exponential function used to fit the data is defined as follow:

$$I(t) = I_0 e^{[-(\frac{\tau}{\tau_0})^{\beta}]}$$

with $\tau = \tau_0 \Gamma(1 + \frac{1}{\beta})$, where Γ indicates the so-called Gamma function:

$$\Gamma(z) = \int_0^{\infty} x^{z-1} e^x dx$$

Emission spectra of low-doped (0.5% to 6.5%) PTMd-ONPs are very similar to the emission spectrum of PTM radical in THF solution (Figure 5.5), while for higher concentrations the band broadens on the long-wavelength side, with the appearance of a shoulder whose intensity increases with the radical doping level (Figure 5.7). Based on the results obtained for TTM-doped ONPs,[60] this red-shifted shoulder is attributed to the formation of a very weak excimeric band close to 700 nm (Figure 5.7).

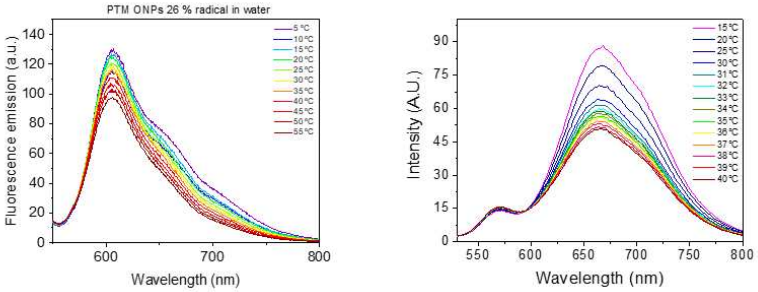

Figure 5.7: Emission spectra at different temperatures of water suspensions of ONPs containing 26 % of radical: a) PTMd-ONPs and b) TTMd-ONP. Excitation wavelengths were set to the maximum of absorption.

The much lower intensity of the excimeric band in the case of PTMd-ONPs with respect to what was observed for TTMd-ONPs (where, for the 26% doped sample, the emission is almost purely excimeric)[60] suggests that the presence of bulky chlorine atoms at the meta positions of trityl radicals may be responsible for this difference. In fact, X-ray data of single crystals of TTM and PTM radicals[182, 183] reveal the presence of dimers with minimum distances among two neighboring molecules between the two aromatic carbon atoms at the meta positions of parallel phenyl rings (Figure 5.8). While this distance is of 3.854 Å for the TTM radical, it is larger in the case of PTM, amounting to 4.237 Å because of the presence of chlorine atoms in meta positions hindering a closer approach. This fact observed at the condensed solid state could explain the lower tendency of PTM molecules to form excimeric species in radical doped ONPs.

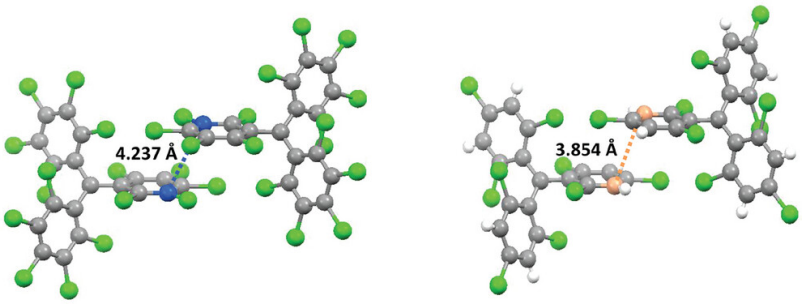

Figure 5.8: Left) Crystallographic structure of the PTM radical with a symmetry C2/c;[182]Right) crystallographic structure of TTM radical with a symmetry C2/c.[183] For both radicals the minimum distance between two neighbouring molecules is along meta carbon positions.

5.2.3 Theoretical modelling of excimers properties and temperature dependence in TTM and PTM ONPs

In order to explain the temperature dependence of the excimeric bands of both ONPs, we simulated the emission properties of the monomers and dimers of PTM and TTM species. Theoretical modelling was carried out by Dr. Jesús Cerdá and Prof. Juan Aragó.

In first place, we notice that excimeric states in molecular dimers generally imply an important mixing between Frenkel (FE) and charge-transfer (CT) excited states, together with a significant structural relaxation (mostly intermolecular motions).[184–186] The FE-CT mixing is proportional to the hole and electron transfer integrals and the energy position of the FE and CT excited states. While FE states are less sensitive to intermolecular motions, the energy position of CT states can considerably vary by intermolecular vibrations due to the relevance of the electrostatic contribution in these CT states. On the other hand, transfer integrals are also very sensitive to intermolecular arrangement because they strongly

depend on the orbital overlap. Hence, thermal intermolecular motions around the crystal structure may induce an important fluctuation of the transfer integrals and an energy (de)stabilization of the CT states. This effect would be expected to be stronger for TTM compared to PTM, since crystal dimers in TTM exhibit shorter intermolecular contacts than PTM.

We have performed time-dependent density functional theory (TDDFT) calculations for the radical monomers and dimers of PTM and TTM species using the optimally-tuned ωB97X-D/6-31G** level of theory. As structural relaxations for both PTM and TTM dimers within their corresponding ONPs (i.e., PTMd-ONPs and TTMd-ONPs) are hindered in some degree, we have started analyzing the nature of the lowest-energy excited states for PTM and TTM monomers and dimers at the crystal structures. For both PTM and TTM dimers, the first two singlet electronic transitions are predicted energetically close to the first electronic transition ($D_0 \rightarrow D_1$) of the monomers (447 and 443 nm, for PTM and TTM radicals, respectively). Therefore, the first two singlet excited states of PTM and TTM dimers are of FE-type and can be mainly described as the symmetric and antisymmetric interaction of the first doublet excited state of the radical monomers. The small energy difference between these two singlet excited states, both for PTM and TTM dimers, comes from the small excitonic coupling (-1.2 and 0.5 meV for PTM and TTM dimers, respectively). The first CT excited states are found to be higher in energy compared to the lowest-energy FE-type states for PTM and TTM (0.64 and 0.39 eV, respectively). That is in line with the shorter intermolecular distance found for TTM compared to PTM (d(Cmeta-Cmeta) 3.854 Å and 4.237 Å, respectively, Fig. 5.8) that would promote a more favorable electrostatic interaction and, thus, an energy stabilization of the CT states. These findings already suggest that TTM dimers may exhibit, upon relaxation, an excited state with a significant FE-CT mixing (excimeric state) and, consequently, TTM would display an enhanced excimeric emission band compared to PTM, as experimentally observed (Figure 5.7). To investigate further the effect that small intermolecular motions cause in the excited states energies, we have computed energy difference maps (i.e., ΔE_{CT-FE}) for PTM and TTM dimers as a function of small intermolecular displacements (Figures 5.9 and 5.10).

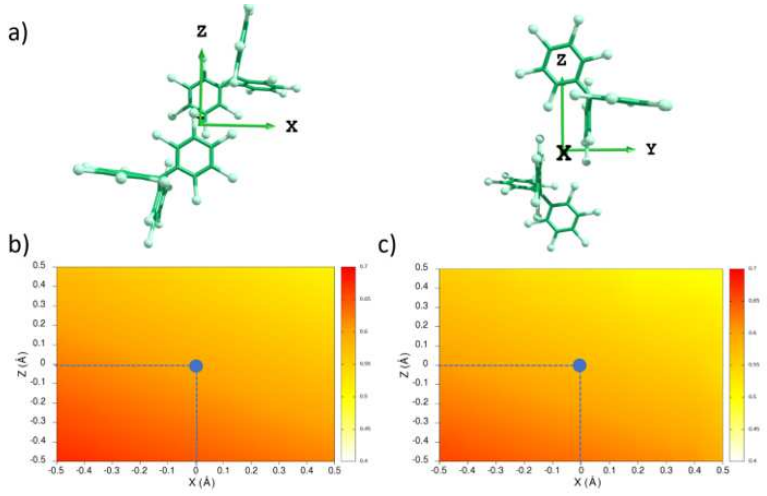

Figure 5.9: a) Different views of the crystal dimer of PTM. Energy difference (ΔE_{CT-FE}) maps in eV for the PTM crystal dimer as a function of x and z displacements computed at OT-ωB97X-D(ω=0.10)/6-31G**. b) ΔE_{CT-FE} map maintaining constant the crystal intermolecular separation between the xz planes (y direction) of the closest interacting aromatic rings (~ 3.44 Å). c) ΔE_{CT-FE} map where the crystal intermolecular separation between the xz planes has been decreased by 0.25 Å (i.e., interplanar distance along y direction of ~ 3.19 Å). Red arrows in panel a indicate the molecule that has been displaced. Blue points in the 2D ΔE_{CT-FE} maps indicate the crystal structure.

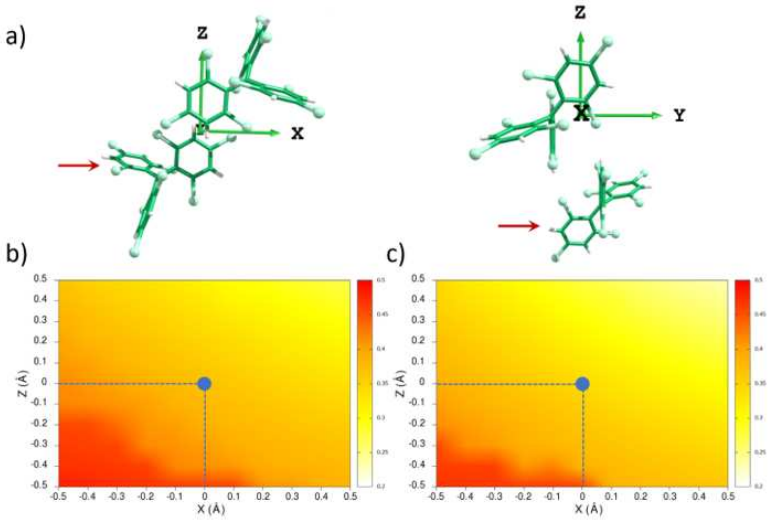

Figure 5.10: a) Different views of the crystal dimer of TTM. Energy difference (ΔE_{CT-FE}) maps in eV for the TTM crystal dimer as a function of x and z displacements computed at OT-ωB97X-D(ω=0.11)/6-31G**. b)ΔE_{CT-FE} map maintaining constant the crystal intermolecular separation between the xz planes (y direction) of the closest interacting aromatic rings (~ 3.44 Å). c) ΔE_{FE-CT} map where the crystal intermolecular separation between the xz planes has been decreased by 0.25 Å (i.e., interplanar distance along y direction of~ 3.18 Å). Red arrows in panel a indicate the molecule that has been displaced. Blue points in the 2D ΔE_{CT-FE} maps indicate the crystal structure.

Figure 5.10 shows that, for TTM, relatively small intermolecular displacements along the z and x directions starting from the crystal geometry, where the two aromatic rings are interacting more strongly (e.g., in the positive 0.3 – 0.5 Å range), are enough to stabilize the CT states with respect to the lowest-energy FE-type states by 0.1 – 0.15 eV. This effect is even stronger at larger displacements in the x-z bisector by 0.75 and 1.0 Å (ΔE_{CT-FE} of 0.19 and 0.24 eV, respectively). A similar effect has been predicted for PTM although the energy ΔE_{CT-FE} values are higher (> 0.5 eV) than those obtained for TTM. These outcomes therefore support that TTM is more prone to display an excimeric emission compared to PTM. Based on the above electronic structure calculations for PTM and TTM monomers and dimers, we have also parameterized a vibronic Hamiltonian similar to the one recently proposed by Spano and co-workers[186] to simulate the emission spectra of PTM and TTM monomers and dimers. For both PTM and TTM radical monomers (Figure 5.11), the simulated emission spectra are almost insensitive to temperature variations in the 5 – 55 °C range and exhibit structured emission bands with vibronic peaks at 448, 467 and 493 nm (461, 479 and 511 nm) for PTM (TTM).

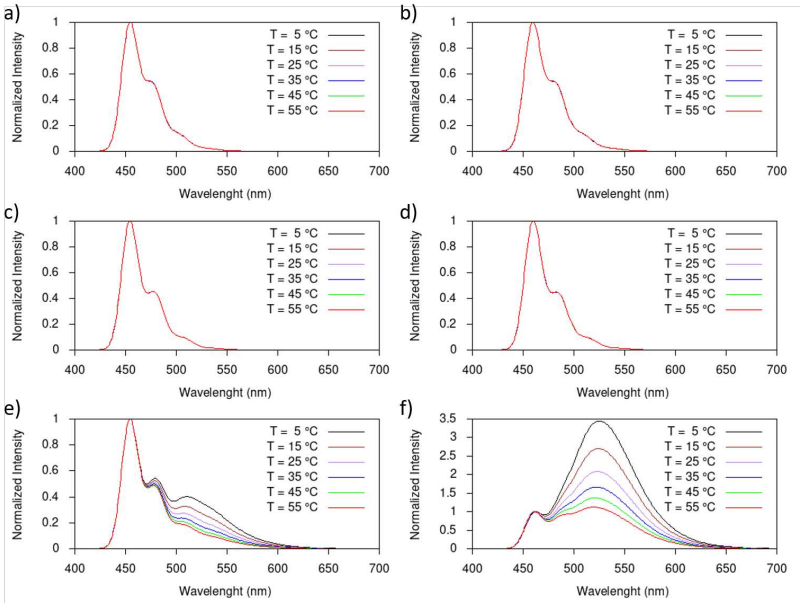

Figure 5.11: Simulated emission spectra for the radical monomers of PTM (a) and TTM (b), and PTM and TTM dimers at different energy offsets: ΔE_{CT-FE} of 0 (c and d) and -0.20 eV (e and f) in the 5 – 55 °C temperature range.

For PTM and TTM dimers, we have simulated emission spectra at different temperatures (5 – 55 °C) and with two different ΔE_{CT-FE} conditions (ΔE_{CT-FE} = 0.0 eV and ΔE_{CT-FE} = -0.20 eV). For the first resonance condition (ΔE_{CT-FE} = 0.0 eV), the simulated emission spectra for both PTM and TTM dimers are still similar to those predicted for the monomers and hardly temperature-dependent. That situation significantly changes at the ΔE_{CT-FE} = -0.20 eV condition, where the CT state is energetically below the FE-like state. The emission bands are now highly sensitive to temperature (Figure 5.11). For PTM, at high temperatures, the monomer-like emission band (at 454 nm) is the most intense one, accompanied by a shoulder at 523 nm. This shoulder progressively gains intensity when lowering the temperature, finally becoming a prominent unstructured band (excimeric band, located at 529 nm), but always stays weaker than the monomer band. The simulated emission spectra are in reasonable agreement with the experimental ones obtained for the ONPs doped with a 26% PTM (Figure 5.7a and 5.11), which exhibit an extended emission band, but the intensity of the excimeric band only slightly changes with temperature. For TTM dimer, the calculated emission spectrum at high temperatures already shows a strong excimer component, which rapidly becomes dominant when lowering the temperature. These results are in line with the experimentally observed emission spectra of TTM (Figure 5.7b and 5.11).[60] Therefore, our theoretical model can satisfactory explain the experimental changes of emission spectra at different temperatures.

5.2.4 TTM ONPs as NIR to NIR nanotherometers: temperature sensing in suspension and animal tissues

As already mentioned before, a relevant drawback of polychlorinated trityl radical-based ONPs for their use as nanothermometers is the need of using near-UV light to efficiently excite them. Near-UV light is potentially cytotoxic and also poorly penetrates into biological tissues. In order to overcome both issues, we tested the two-photon excitation of TTM and PTM radicals in THF solution. Figure 5.12 shows the normalized one-photon absorption and emission spectra (black, with λ_{exc} =380 nm) and the absolute two-photon absorption spectra (Red lines, expressed in Goeppert-Mayer (GM) units) of TTM and PTM radicals in THF solution. Such spectra indicate that TTM and PTM can be excited via two-photon absorption (TPA) at NIR wavelengths (810 and 860 nm, respectively), with TPA cross-sections (σ_2) of 17 and 6 GM, respectively. The emission spectra of TTM and PTM obtained upon two-photon excitation are superimposable to the corresponding one-photon-excited emission spectra . Although the properties mentioned above are relevant for bio-imaging applications of both radical-based ONPs, the weakness of the excimer band of PTMd-ONPs, as well as their lower TPA cross-section, in comparison with that of TTMd-ONPs, limit their use as efficient ratiometric TPA nanothermometers. This limitation made us focus on the study of TPA nanothermometers based on TTMd-ONPs.

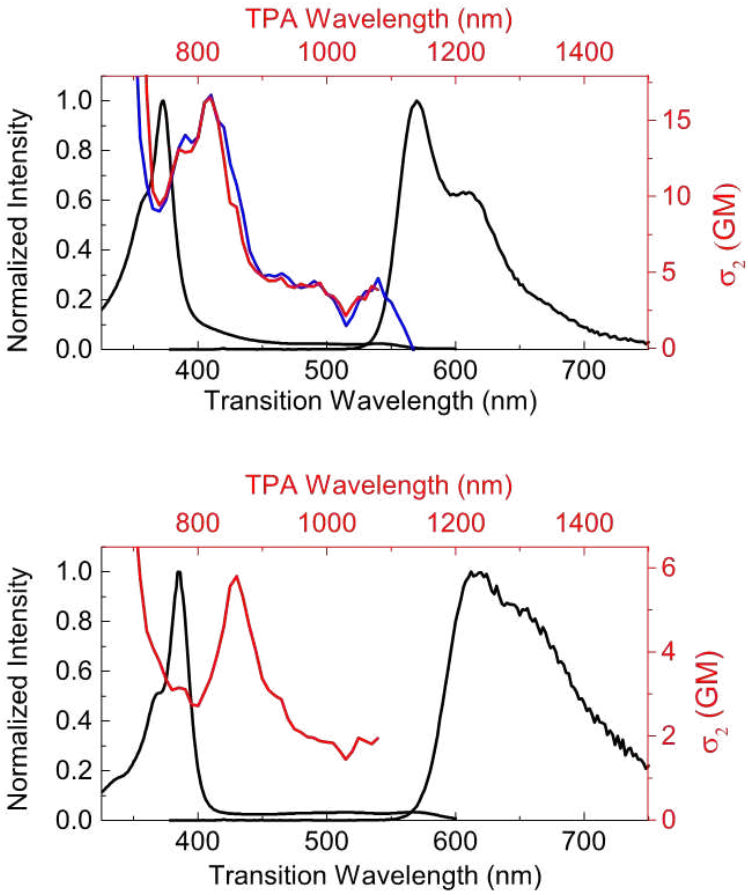

Figure 5.12: One-photon absorption and emission spectra (normalized, black lines) and two-photon absorption spectrum (red line, right and top scale) of TTM (top panel) and PTM (bottom panel) in THF. Blue line (top panel): normalized two-photon excitation spectrum of TTM-ONPs.

The efficiency of TTMd-ONP as an effective NIR-to-NIR nanoreporter of local temperature (i.e., using NIR light for the excitation and getting red/NIR emission) was investigated in solution and on a biological substrate, by depositing a dispersion of TTMd-ONP on a slice of hydrated sclera from porcine eye. The sclera tissue was chosen as the suitable candidate to test the two-photon excited fluorescence (2PEF) of TTMd-ONPs due to its very low autofluorescence (Figure 5.13). As a first step, we performed one-photon excited fluorescence measurements, with λ_{exc} =380 nm, on a diluted water suspension of TTM-ONPs (ca., 0.002 mM) in a cryostat in the 5–35 °C temperature range. Fluorescence spectra (reported in Figure 5.14a, normalized at the short-wavelength emission maximum) are characterized by two bands that have been attributed to the monomer and excimer emissions (short and long wavelength, respectively).[60] The ratio between the green-shaded and the red-shaded area of emission spectra (Q = A_G/A_R) as a function of temperature during a heating and cooling cycle was calculated and is shown in Figure 5.14c. The ratio between these two areas was chosen as a metrics for the ratiometric output instead of using the intensities at the emission maxima of monomer and excimers. Despite the availability of the entire emission spectrum in the one-photon excited fluorescence measurements (Figure 5.14a), we chose to use the ratio between the green-shaded and the red-shaded area to be consistent with the ratio that we are forced to use in the two-photon excited experiment (Figure 5.14b, due to the limited accessible spectral range).

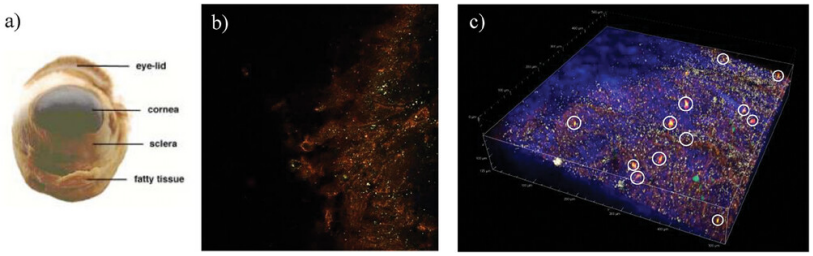

Figure 5.13: a) Porcine eye, indicating its main parts, among them the sclera tissue.[187] b) microscope image of a slice of porcine sclera tissue containing the TTMd-ONPs and c) 3D image of the sclera tissue showing the TTM-ONPs (white circles) penetration along the z-axis.

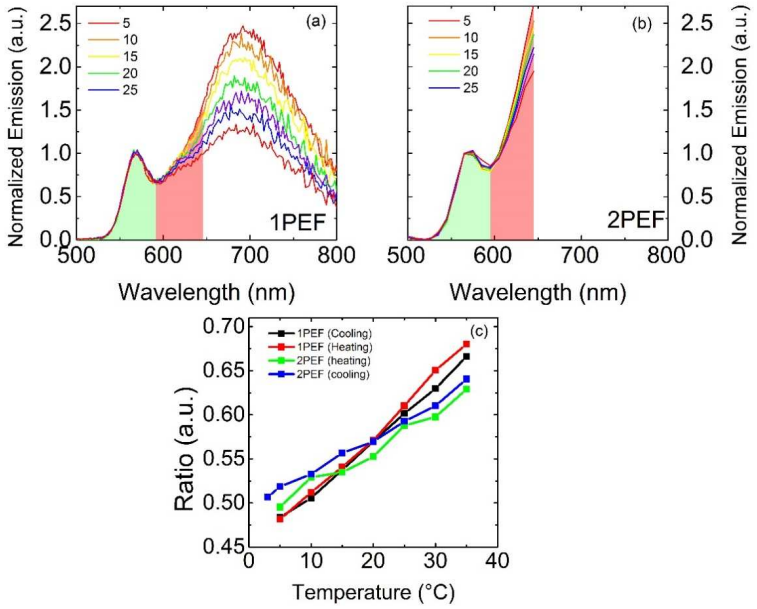

Figure 5.14: One-photon-excited (a) and two-photon-excited (b) emission spectra of TTM-ONPs water suspension as function of temperature (in C°). Evolution of the ratio between green-shaded and red-shaded area with the temperature (c).

The aim of such "one-photon-excitation" preliminary measurements was to obtain a reference correlation curve between the fluorescence monomer/excimer ratio and temperature to compare with the 2PEF measurement (Figure 5.14b). The results, reported in Figure 5.14c, show an almost linear correlation in the 5–35 °C temperature range from which a thermal absolute sensitivity S_a = 0.52-0.73 or mean 0.62 ± 0.06% K^{-1} and S_r= 1.080-1.095 or mean 1.088 ± 0.004% K^{-1} were obtained (see Equation 5.2 for the definition of S_r).

$$S_r = \frac{S_a}{Q} \times 100\%, [\%, K^{-1}] \tag{5.2}$$

2PEF measurements were conducted with a Nikon A1R MP+ Upright multiphoton microscope coupled with a femtosecond pulsed laser source (Coherent Chameleon-Discovery, 80 fs, 80 MHZ, 660–1320 nm). The microscope is equipped with a spectrograph (composed by a linear variable filter monochromator,[188] as dispersing element, and a photomultiplier tube as a detector) capable of acquiring the spectrum of the fluorescence emitted by the sample with a resolution of 10 nm within the 435–645 nm spectral range (more details can be found in chapter 10.4). Unfortunately, due to limitations of our equipment, the spectral range cannot be expanded up to 800 nm. To measure the spectrum, the microscope records a series of images (in this case a low spatial resolution, 64 × 64 pixels, is enough) each one at a different emission wavelength: 22 images to cover the 435–645 nm spectral range with 10 nm steps. Then,

each point of the spectral profile is obtained by integrating (over all the pixels) the signal from each image. The measurements on the TTM-ONPs suspension were performed on a 1 mm thick cuvette in contact with a base plate whose temperature was controlled owing to a thermostat with an external circulator and monitored with an external thermo-couple. 2PEF spectra are reported in Figure 5.14b and the areas ratios were calculated as well (Figure 5.14c), showing Sa = 0.24-0.64 or mean 0.41 ± 0.1% K^{-1} and S_r = 0.48-0.99 or mean 0.7 ± 0.1% K^{-1} that are in a very nice agreement with the one-photon-excited results, demonstrating the potential of TTM-ONPs as NIR-to-red/NIR nanothermometers for bio applications. In the second phase of our work, we investigated, with the help of the apparatus described before, the 2PEF response of the TTM-ONPs dispersed on a few mm thick slice of hydrated sclera tissue from porcine eye. The sclera tissue, previously hydrated, was treated with a water suspension containing TTM-ONPs for half an hour before the measurement session. The same suspension of TTM-ONPs was used as contact medium between the objective (25× Nikon CFI APO LWD Objective, 420-1400 nm, 1.10 NA, 2.0 mm WD) and the tissue surface. Since fluorescence is excited by exploiting a TPA process, it will occur with appreciable probability only where the photon density is maximum, i.e., in the focus produced by the objective. This allows to eliminate any interference due to the presence of TTM-ONPs in the contact solution between the focal plane and the objective surface, as well as to gain the typical 3D spatial resolution intrinsic of nonlinear optical techniques.

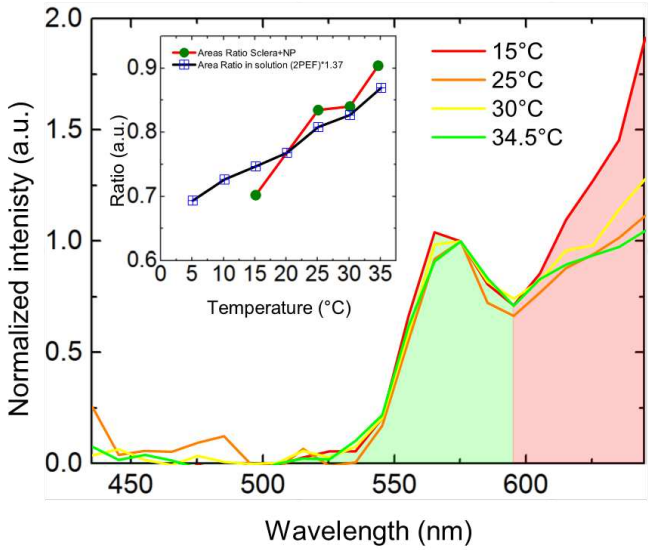

Figure 5.15: Two-photon-excited emission spectra of TTM-ONPs dispersed on a slice of porcine sclera tissue. Inset: Area Ratio as a function of temperature of TTM-ONPs on sclera tissue (green dots and red line) in comparison with TTM-ONPs suspension of Figure 5.14c) multiplied by a scaling factor (1 .37).

In these conditions, we measured the emission spectrum of TTM-ONPs on the sclera surface following the procedure described before. The procedure has been repeated for various temperatures and the results are displayed in Figure 5.15. Following the same approach formerly adopted, the ratio between the green-shaded and the red-shaded area of the emission spectra as a function of temperature has been obtained (Figure 5.15, inset). A slightly different response of the TTM-ONPs as a function of temperature was observed from water suspension and sclera surface. Nevertheless, the temperature trend is still linear and the two

sets of measurements can be correlated by using a simple scaling factor. Therefore, the outcomes obtained for this sclera tissue model demonstrated that TTMd-ONPs are excellent NIR-to-NIR nanothermometers with promising capabilities for bio applications.

5.3 Conclusions

Polychlorinated trityl radicals TTM and PTM can be one- and two-photon excited in solution exhibiting acceptable two-photon absorption (TPA) cross-sections of 17 and 6 GM, respectively. This result provides the possibility to prepare NIR-based ratiometric nanothermometers made of organic nanoparticles (ONPs) doped with radical molecules, exploiting the formation of dimeric excimers. The emission intensity of ONPs doped with a small portion of TTM and PTM radicals (i.e., isolated radical species), is independent of temperature. In contrast, the excimer emission intensity decays with the temperature increase, allowing to monitor temperature changes by a ratiometric approach. The intensity changes exhibited by TTM radical-doped ONPs are more pronounced than those of ONPs doped with PTM, in line with the theoretical simulations. Accordingly, TTMd-ONPs show an excellent temperature absolute sensitivity of 0.6–3.7 $\%\cdot K^{-1}$ in the 278 – 328 K temperature range. This excellent property, together with the acceptable TPA cross sections in the NIR, made TTM-ONPs excellent candidates for NIR-to-NIR temperature sensing. This was confirmed by measuring the emission spectra of a water suspension of TTM radical-based ONPs in the 5–35 °C temperature range with TPA (using an excitation wavelength of 810 nm): the ratiometric output signals were similar to those obtained with 1PA at 380 nm and similar thermal absolute sensitivities of S_a = 0.24–0.64 $\% \ K^{-1}$ were obtained. Finally, as a proof of concept, the use of TTMd-ONPs as ratiometric NIR-nanothermometers with 2-photon excitation were tested on enucleated pig eye sclera, as a real tissue model, obtaining a similar temperature relative sensitivity as in aqueous suspensions, demonstrating their potential as NIR-to-NIR nanothermometers for bio applications.

Introduction to chirality and optical activity

6

6.1 Chirality in molecules

We define "chiral" (from Greek $\chi\epsilon\iota\rho$, which means "hand") an object which is not superimposable with its mirror image. The mirror images of a chiral object are called enantiomers.[189]

Chirality is ubiquitous in nature,[190, 191] with most biomolecules such as aminoacids and nucleic acids being chiral[192] and usually present only in one enantiomer (homochirality).[193, 194]

Enantiomers exhibit identical physical and chemical properties—such as melting point, optical spectra, and reactivity—when in a non-chiral environment. However, these properties change significantly when they interact with a chiral environment or substance.[159, 195] A classic example of enantiospecific process is given by thalidomide, a chiral sedative for which only one enantiomer is teratogenic.[196]

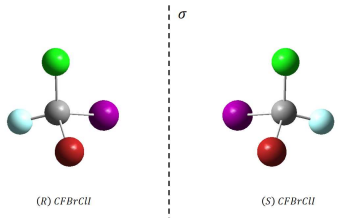

Figure 6.1: Two enantiomers of CFClBrI. σ indicates a plane of reflection.

Everyday world is full of chiral objects (hand, screws, shells...), but the simplest chiral object a chemist can think of is a stereogenic carbon. A sp^3 hybridized carbon with four different substituents is not superimposable to its mirror image (Fig. 6.1)[159]. The enantiomers of a stereogenic carbon can be attributed an absolute configuration, *S* or *R*, according to Cahn-Ingold-Prelog (CIP) rules.[197] This kind of chirality is usually referred to as point chirality. The presence of more than one stereogenic carbon on the same molecule implies the existence of more diastereoisomers, i.e. molecules in which the absolute configuration of stereogenic centers is different, but not totally opposite.

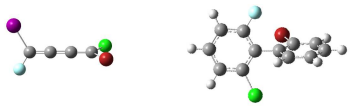

Figure 6.2: An allene (left panel) and a biaryl (right panel) displaying axial chirality.

Other atoms such as nitrogen and phosphorus can show point chirality,[198] but the interconversion between enantiomers is usually rapid, and quickly yielding to a racemate, i.e. a 50-50 mixture of both enantiomers. Point chirality is just one possible source of chirality in molecular systems. Axial chirality is present when a molecule contains two pairs of chemical groups in a non planar arrangement around a molecular axis, termed *chiral axis*.[199] This is the case of allenes and substituted biaryls (Fig. 6.2).

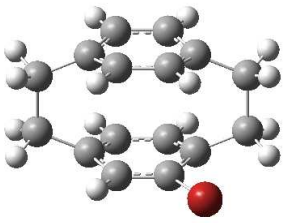

Figure 6.3: A chiral bromine-substituted paracyclophane.

Free rotation around a chiral axis leads to complete racemization. In order to have definite axial chirality it is therefore fundamental to block the rotation around the chiral axis. Usually this is attained by steric hindrance of the substituents, a phenomenon which is called atropoisomerism.[200] Substituted biaryls are typical examples of atropisomers. In the case of allenes free rotation is instead prevented by the rigidity of cumulated double bonds.

Planar chirality (which formally originates from a *chiral plane*) is typical of paracyclophanes (Fig. 6.3).[201] Racemization is possible if the aromatic rings are free to flip, which happens if alkyl chains joining them are longer than four carbon atoms.

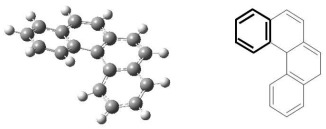

Figure 6.4: Left panel: side view of a P[4]-helicene; right panel: top view as depicted from Lewis formula.

Last there is helical chirality, which is typical of helicenes (Fig. 6.4). Helical chirality usually stems from steric repulsion between hydrogens of condensed aromatic rings, which is avoided by imposing a screw sense to the whole molecule. The right-handed and left-handed helices are respectively indicated as P and M.

6.2 Chiroptical properties

A spectroscopist is interested in the interaction between molecules and light, which is an electromagnetic radiation.

Electromagnetic radiation is formed by a beam of waves each having a magnetic field and an electric field oscillating on planes perpendicular to each other and perpendicular to the direction of propagation, identified by the wave vector $\vec{k}$. By convention, only the direction of oscillation of the electric field (the $\vec{E}$ vector) is considered, which together with the direction of propagation of the wave outlines the polarization plane of the radiation.[202] An electromagnetic radiation is non-polarized when it is made up of waves that have a polarization plane oriented in a random direction around the propagation axis. If all the waves all have the same orientation of the polarization plane, the radiation is linearly polarized. An electromagnetic radiation is circularly polarized when its propagation is accompanied by the rotation of the electric field vector around the wave vector: observing from the point of view of the radiation source, if the rotation of the electric field vector occurs clockwise, the wave has a right circular polarization; if, however, the rotation of the electric field vector around the axis of propagation occurs counterclockwise, the wave is said to be left circularly polarized.[203]

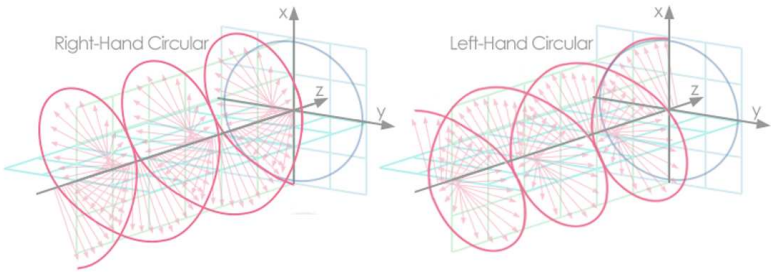

Figure 6.5: Left panel: Right Handed circularly polarized light. Right panel: Left Handed circularly polarized light (image adapted from JEM Engineering).

Linearly polarized radiation can be considered as formed by two waves with the same amplitude and frequency, having opposite circular polarization. The phase difference between the two waves determines the orientation of the polarization plane of the electromagnetic radiation.

The simplest observation of optical activity is given by the rotation of the plane of linearly polarized light which passes through a chiral medium. The RH and LH components of linearly polarized light have different refractive index in the medium ($\eta_L \neq \eta_R$) and therefore different speeds. This induces a phase difference between the two components and, as a consequence, the plan of polarization is rotated by an angle α in respect to the incident polarization.[204–206]

The angle α is called optical rotatory power. For diluted solutions, α linearly depends on the chiral molecule concentration according to Eq. 6.1:

$$\alpha = [\alpha]_D^{293} lc \tag{6.1}$$

where $[\alpha]_D^{20}$ is the specific rotatory power at 293 K and for an incident wavelength of 589 nm (line D of sodium), l is the optical path and c the concentration in g/mL. The specific rotatory power of a medium is related to the difference $\eta_L - \eta_R$ by the Fresnel equation:[207]

$$[\alpha] = 1800(\eta_L - \eta_r)\frac{l}{\lambda_0} \tag{6.2}$$

where l is the optical path in dm, λ_0 the light wavelength in cm and $[\alpha]$ is expressed in degrees.

As evident from Eq. 6.2, the rotatory optical power is a function of the wavelength of the incident light. The whole curve plotting $[\alpha]$ against the energy or wavelength of the incident radiation is called optical rotatory dispersion (ORD).[205, 207]

In proximity of the absportion frequencies of chiral molecules, RH and LH radiations are absorbed with different efficiencies. Electronic circular dichroism (ECD, or simply CD) measures the differential absorption (or proportional quantities) of the two polarizations as function of wavelength in the UV-Vis.[208, 209] The analogous effect for IR frequencies is called vibrational circular dichroism (VCD).[210–212]

If the incident radiation is linearly polarized, not only the two circular components will have a different phase when coming out of the sample, but their relative amplitudes will also change. As a result, the polarization of light coming out of the sample is not linear anymore, but elliptical.[207] The ratio between the axes of the ellipsis is related to the difference between extinction coefficients for LH and RH light ($\epsilon_L - \epsilon_R$). In particular, the ellipticity θ is defined as:

$$\theta = arctan(\frac{M}{m})$$

where m and M are respectively the minor and major axes of the ellipses described by the electric field. Ellipicticity is usually measured in millidegrees (mdeg).

Experimentally, CD is more often measured as the difference in absorbance between a LH and a RH radiation, as:

$$\Delta A = A_L - A_R$$

In the limit of weak signals ΔA is related to θ as $\theta = 32.98\Delta A$.[207, 213]

We can exploit Lambert Beer's law to write $\Delta A = cl\Delta\epsilon$, where c and l are respectively the sample concentration and the optical path. $\Delta\epsilon = \epsilon_L - \epsilon_R$ is independent from sample concentration.

Since the wavelength of incident light is much bigger than the dimension of chiral molecules (hundreds of nm vs some Å) the molecules feel very little curvature of the incident electric field, that's why ORD and CD signals are weak.[214] A measure of CD strength in relation to normal absorption is offered by the dissymmetry factor g_{abs}:

$$g_{abs} = \frac{\Delta\epsilon}{\epsilon} \tag{6.3}$$

g_{abs} for organic molecules are usually around $10^{-4} - 10^{-3}$.[214]

It can be shown that CD and ORD are interrelated by Kramers-Kronig relations, i.e. one can be calculated if the other is known.[215] Enantiomers have equal absolute value, but opposite sign, of CD and ORD. Therefore both CD and ORD can be used to assess the enantiomeric excess, or optical purity, of a mixture.[159]

At a quantum mechanical level, CD comes from a mixed interaction of the system with the electric and magnetic fields of the incident light. CD requires the presence of transitions with both an electric ($\vec{\mu}$) and a magnetic ($\vec{m}$) transition dipole moment. This means charge must both translate (thus generating $\vec{\mu}$) and rotate (thus generating $\vec{m}$) during the transition. Moreover, $\vec{\mu}$ and $\vec{m}$ should have common components.[205, 216]

In analogy to absorption, whose strength is proportional to the squared electric transition dipole moment (or line strength, $|\vec{\mu}|^2$), the strength of a CD peak is quantified by the rotational strength:[205]

$$R = Im(\vec{\mu} \cdot \vec{m}) \tag{6.4}$$

where Im means the imaginary part of the argument must be taken (the magnetic dipole moment is imaginary).

Eq. 6.4 involves the scalar product between a polar vector, $\vec{\mu}$, and an axial vector, $\vec{m}$. Only one of them changes sign when reflected through a mirror, and this is the reason why enantiomers have opposite sign of CD spectrum. For this reason, a molecule possessing reflection planes, inversion center or more in general improper rotation axes, can not show optical activity.

Since for electric dipole allowed transitions $|\mu| >> |m|$ we can rewrite the g_{abs} of Eq. 6.3:

$$g_{abs} = 4\frac{|m|}{|\mu|}cos(\chi) \tag{6.5}$$

where χ is the angle between $\vec{\mu}$ and $\vec{m}$.

The phenomenon analogous to CD, but regarding emission, is called circularly polarized luminescence (CPL).[217–219] Upon excitation with non-polarized light, a chiral molecule can emit RH and LH light with different intensities. CPL is defined as $\Delta I = I_L - I_R$. In analogy with Eq. 6.3 we can define a dissymmetry factor in emission, the g_{lum}, as $g_{lum} = 2\frac{I_L - I_R}{I_L + I_R}$.

Emission in molecules usually takes place from the lowest excited state, Kasha state. If there are no major rearrangements when the molecule is excited, the g_{lum} is expected to be equal to the g_{abs} relative to the transition from the ground state to Kasha state.[214, 220]

For application in OLEDs, it is crucial to maximize the g_{lum}, which can be theoretically as high as 2. The delicate conundrum chemists are facing is that g_{lum} grows with decreasing $|\vec{\mu}|$ (this is the case of dipole-forbidden transitions in lanthanide complexes)[221], but this basically means the molecule emission becomes weaker. The challenge is to obtain emitters with both high emissivity and high g_{lum}. The parameter of Eq. 6.5 to which most synthetic efforts are addressed is χ: molecules are designed in order to have the most collinear (or anti-collinear for the enantiomer) $\vec{\mu}$ and $\vec{m}$.[219, 222]

6.3 Supramolecular chirality

Non chiral molecules can be arranged in a chiral fashion in order to form chiral supramolecular aggregates, usually making use of chiral templating agents.[223] Supramolecular chirality is often seen as a way to enhance the chiroptical properties of organic molecules, typically through an exciton coupling mechanism.[57, 224] The CD characteristics of supramolecular chirality can rationalized within the framework of the exciton model, which we introduced in chapter 1.[205] Let's consider again a dimer of molecules, each one possessing an electric dipole allowed state, but now the molecules are oriented to form a chiral dimer, meaning their transition electric dipole moments form a θ angle, with $\theta \neq 0, 90, 180°$.

Eigenstates and eigenvalues are exactly the same we obtained in chapter 1. However, if the dimer is chiral, both exciton state are optically allowed, at least partially. As a consequence, two bands can be noticed in the absorption spectrum, one of them at higher energies and the other at lower in respect to the monomer absorption maximum (Fig. 6.6).

The relative intensity of the bands depends both on the θ angle (which defines the aggregate handedness) and the sign of electrostatic interaction J (cfr. chapter 1). For any θ angle, the absorption is stronger for the in-phase combination of basis states, therefore the dimer can still be labeled as a H-dimer ($J > 0$, in-phase combination has higher energy) or J-dimer ($J < 0$, in-phase combination has lower energy).

The most interesting observation, however, is that each of the exciton states is now associated to a rotational strength from the ground state, and the sign of rotational strengths is opposite for the two states, leading to the appearance of a characteristic doublet in the CD spectrum.

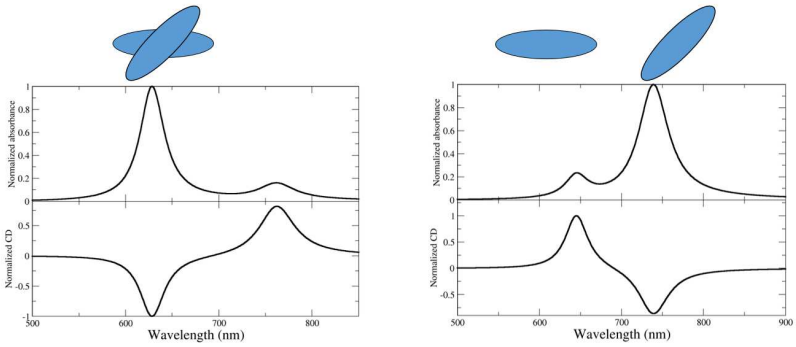

Figure 6.6: Normalized absorption (upper panels) and CD (lower panels) of chiral H-dimer (left panel) and J-dimer (right panel).

The rotational strength of both states is proportional to the triple product $r_{21} \cdot (\vec{\mu}_1 \times \vec{\mu}_2)$, where r_{21} is the vector joining the two molecules, and $\vec{\mu}_{1/2}$ the transition dipole moments of the two molecules. The in-phase combination has a positive (negative) rotational strength for a left (right) handed dimer. This allows to attribute the helicity of the dimer based on the sign of the lower energy CD peak and constitutes the so-called chirality rule.[208]

It must be stressed than the sign of CD spectrum does not only depend on handedness, but also on the sign of electrostatic interactions, therefore the chirality rule should be applied only if the dimer is known *a priori* to be a H or a J-dimer.[57]

Moreover the use of chirality rule could be thwarted by conformational mobility within the aggregate, or in presence of strong magnetic transition dipole moments.[225, 226]

A scheme of the dependence of CD sign on handedness and electrostatic interactions is reported in Fig. 6.7.

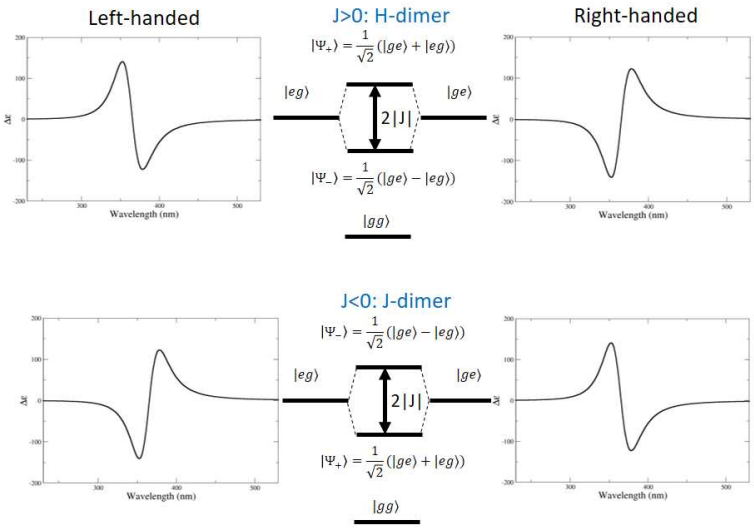

Figure 6.7: Exciton levels and CD spectra in the case of right-handed (right panel) and left-handed (left panel) dimers, with attractive (lower panel) or repulsive (upper panel) electrostatic interactions.

6.4 Outline

Chapter 7 will explore and quantitatively assess the chiroptical properties of a series of helicene-based compounds. CPL, stemming from their

intrinsic chirality, will be the specific focus of the chapter. Chapter 8 will derive the chiroptical properties of a chiral supramolecular aggregate, using different approaches which converge to the same results. Chapter 9 will highlight the role magnetic transition dipole moments in determining the chiroptical response of chiral supramolecular aggregates.

Last, in Chapter 10, the notions of intrinsic and supramolecular chirality will be joined together in order to rationalize the peculiar chiroptical behaviour of tubular cyanine aggregates.

Chiroptical activity of a series of π-Extended double heterohelicenes

7

7.1 Introduction

Heterohelicenes belong to the class of ortho-fused aromatics containing at least one heteroatom incorporated into the helix backbone.[227] One of the factors drawing scientists attention is their unique molecular 3D architecture, making them an ideal scaffold used in complex stereodynamics studies.[228–231] Their chirality allows for effective implementation as auxiliaries in asymmetric synthesis.[232] Proper functionalization of the helical structure leads to two photon absorbers[233] and "turn-on" fluorescence sensing materials,[234, 235] while π-expansion offers remarkable supramolecular behavior.[236] Moreover, some of them can be effectively applied in cell imaging[237] and recent reports also shed light on the bioactivity of heterohelicenes, which can be used as selective drugs in the treatment of renal cell carcinoma.[238] It should also be mentioned that helicenes, like other aromatic systems, found application in optoelectronics, e.g. organic light emitting devices (OLED),[239, 240] organic field effect transistors (OFET)[241] and organic photovoltaics (OPV).[242, 243] Despite these numerous applications, the most dynamically developing application field of helicenes are technologies directly utilizing their chiral optical activity, e.g. circular dichroism (CD),[244] circularly polarized luminescence (CPL)[245] and chirality-induced spin selectivity (CISS).[246] However, relatively small helicenes exhibit rather low Φ_f and the observed absorption dissymmetry factor (g_{abs}) as well as the luminescence dissymmetry factor (g_{lum}) are in the range of $10^{-4} - 10^{-2}$, leaving much space for improvements.[247] Indeed, the appropriate design of heterohelicenes leads to enhancements of their chiral optical responses. For instance, the peripheral decoration of the helicene scaffold via naphthalimide subunits, results in a rise of Φ_f from 0.04 up to 0.7.[248] Likewise, it was also shown that heteroatom doping or distinct π-electron system expansion increase the dissymmetry factors.[249–251] Furthermore, appropriate molecular design governs long-lived circular polarization of phosphorescence.[252, 253] Undoubtedly, the main obstacle standing in the way of further practical applications of the most promising extended heterohelicenes is their multistep synthesis, which often requires nontrivial reagents, conditions, or catalysts. The group of Prof. D. Gryko synthesized expanded, electron rich double heterohelicenes, exhibiting fluorescence in the visible range with good quantum yields.

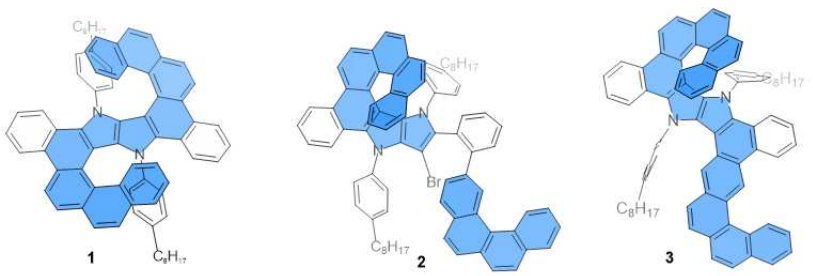

Figure 7.1: Chemical structures of the π-Extended double heterohelicenes

7.2 Experimental methods

7.2.1 CD measurements

CD spectra were measured on a JASCO J-815 spectrometer equipped with a JASCO Peltier cell holder PTC-423 to maintain the temperature at 25.0 ± 0.2°C. A CD quartz cell of 1 mm optical pathlength was used. The CD spectrometer was purged with nitrogen before recording each spectrum. The baseline was acquired by measuring the pure solvent and the spectral range was cut at the cut-off wavelength of the relevant solvent (233 nm for dichloromethane, 284 nm for toluene).

7.2.2 CPL measurements

A FLS1000 Edinburgh Instruments Fluorimeter, equipped with a photoelastic modulator (PEM), a lock-in amplifier and an emission polarizer at 135°, was employed to acquire CPL spectra and obtain the corresponding dissymmetry factors (g_{lum}) in DCM (Fig. 7.9) and in toluene (Fig. 7.11). The solutions were diluted as to have absorbance lower than 0.1, in order to minimize inner-filter effects. The absence of linearly polarized components in emission was confirmed by verifying that the CPL spectra did not change when excited through a horizontal polarizer[219]. Moreover, fluorescence excitation anisotropies were acquired in order to confirm the complete depolarization of emission due to the molecular rotation during the lifetime of the excited state.

7.3 Results and discussion

7.3.1 Synthesis

All the syntheses and NMR experiments were carried out by Dr. D Kusy and Dr. K. Górski in the laboratory of Prof. D. Gryko.

The syntheses of **1-3** (Fig. 7.1) were achieved by procedures developed by the group of Prof. D. Gryko. The most important step of this strategy is 6π-electrocyclization. The synthesis of compound **1** started from Suzuki-Miyaura coupling reaction of 3-bromophenanthrene and (2-formylphenyl)boronic acid using Pd(PPh3)4 as the catalyst and K_2CO_3 as the base, which afforded 2-(phenanthren-3-yl)benzaldehyde **4** in a very good yield of 80%. Next step was one-pot multicomponent condensation between **4**, 4-octylaniline and butane-2,3-dione catalyzed by iron(III) perchlorate, which gave TAPP **6** in 70% yield. Intermediate **6** was brominated using N-bromosuccinimide, smoothly leading to **8** in 77% yield (Scheme 7.2). In the last key step, compound **8** was subjected to 6π-electrocyclization, which allowed us to obtain the desired double helicene **1** in 10% yield. We used the same methodology to synthesize compounds **2** and **3**. In the first stage of the Suzuki reaction, we used 2-bromobenzo[c]phenanthrene obtained according to the procedure of Jakubec et al.[254]

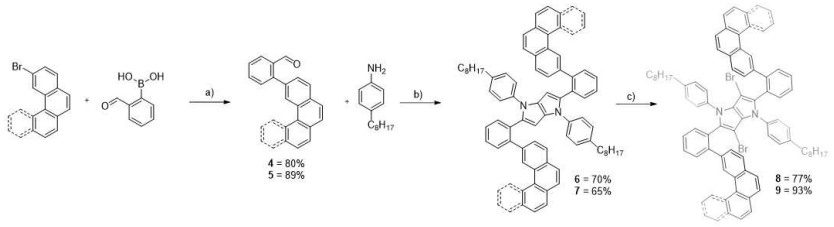

Figure 7.2: Synthetic route to compound 1-3. Reagents and conditions: a)$Pd(PPh_3)_4$ (0.0075 eq), K_2CO_3 (3 equiv.), THF:H_2O, 60 °C, 4 h, b) $Fe(ClO_4)_3$ x H_2O (6 mol%), AcOH/-toluene, 50 °C, 16, $CHCl_3$, NBS (N-Bromosuccinimide)

The next steps were synthesis of TAPP **7** followed by a bromination reaction to obtain **9**. The goal of the project was to obtain a double seven helicene. However, unfortunately it was not possible to obtain compound **10** (Scheme 7.3).

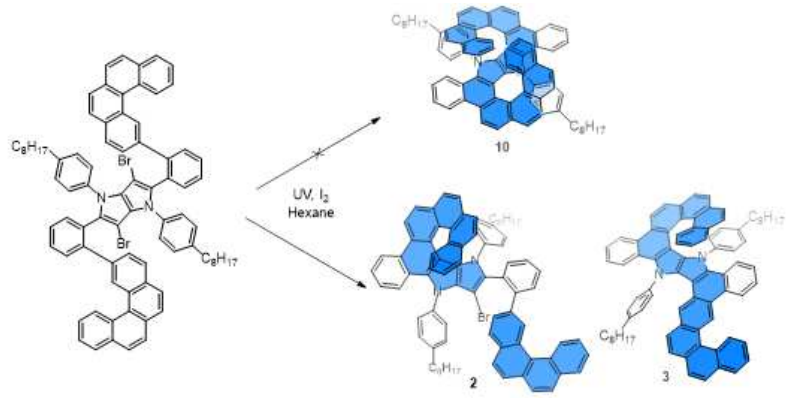

Figure 7.3: Photocyclization of **9** leads to compounds **2** and **3** instead of compound **10**.

The unexpected course of **9** photocyclization can be explained via analysis of electron density distribution at LUMO level of **2**. Firstly, the symmetry of wave function within the 6π-electrocyclization center indicates that upon excitation the bonding interaction between helical arm and PP core can be achieved, leading to **3** (dark red. Fig. 7.4).

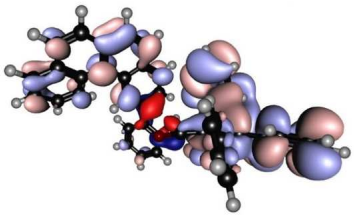

Figure 7.4: LUMO of **2** for contour value 0.008, dark red and blue represent electron density involved in 6π-electrocyclization process

Secondly, a clear bonding character of orbital, between [4]helicene and benzene ring as well as benzene ring and PP subunit, are stabilizing the presented conformation.(Fig. 7.4) These two factors are directly responsible for the observed regiospecificity of the photocyclization process. On the other hand, the steric hindrance induced by [4]helicene moiety, as well as relatively small electron density within the 6π-electrocyclization center (orbital contour value = 0.008), makes the discussed interaction not efficient, which stands in line with small reaction yield of **3** (4%). Moreover, the photocyclization time leading to 3 was elongated up to 32h, more than **10** times longer in comparison to **1**, for which electrocyclization process takes place in around 3h.

The structure of **1** and **3** was verified by variable-temperature nuclear magnetic resonance (NMR) analysis and high-resolution mass spectra. For molecules **1** and **3**, owing to the rotation of the p-octyl benzene rings, we observed coalescence of the peaks of the protons of the p-octyl benzene rings at room temperature, while at low temperature (233 K) we observed four peaks (Figure 7.5, and 7.6). These results indicate that the p-octyl benzene rings can interconvert rapidly on the NMR timescale.[255, 256]

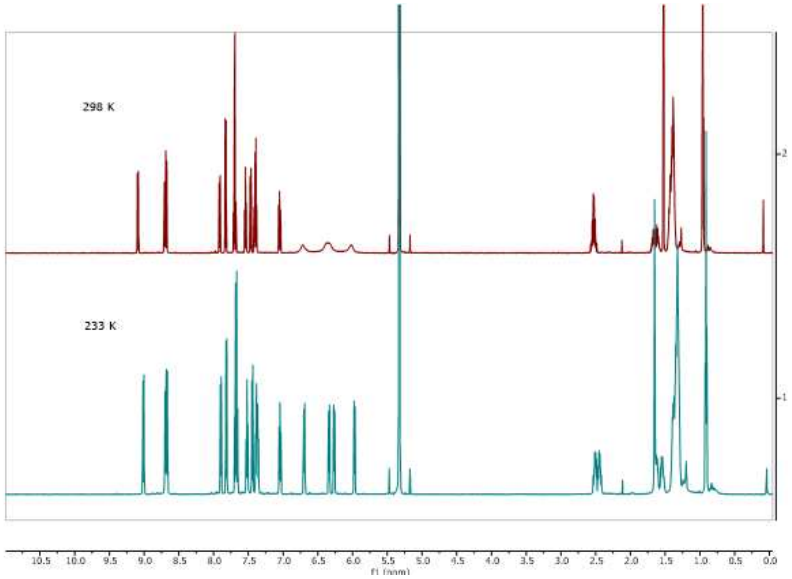

Figure 7.5: Variable-temperature ^{1}H NMR spectra of **1** (600 MHz, CD_2Cl_2). The temperature 298 and 233 K.

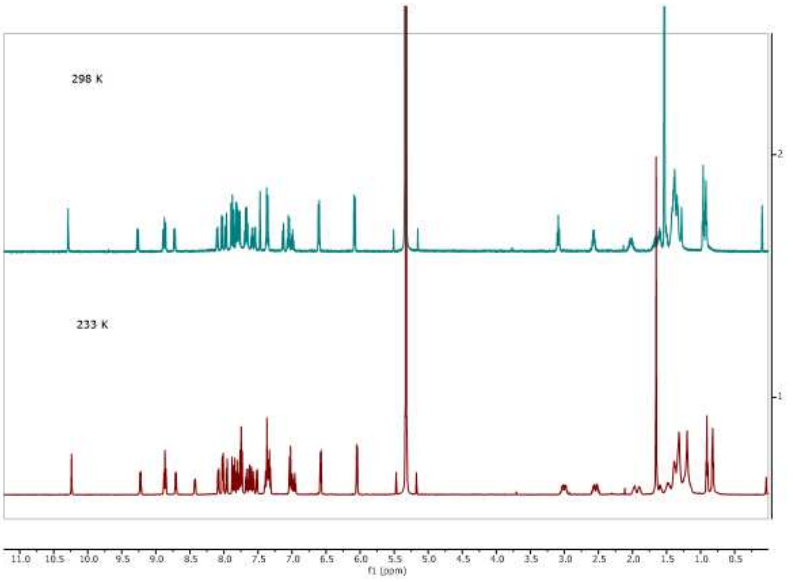

Figure 7.6: Variable-temperature ^{1}H NMR spectra of **3** (600 MHz, CD_2Cl_2). The temperature 298 and 233 K.

All compounds **1-3** showed high stability under ambient light in air at room temperature, as well as good solubility in various solvents such as methylene chloride (DCM), toluene and dimethyl sulfoxide (DMSO).

7.3.2 TD-DFT calculations of molecular orbitals

The following computational calculations were run at DFT/TD-DFT level of theory, employing B3LYP as functional and 6-31G(d,p) as basis set.

Depending on degree of annulation, the obtained helicenes can be divided into two groups: fully fused (**1** and **3**) and semi-fused (**2**). Due to semi-fused structure, **2** possesses the largest energy gap between frontiers orbitals, ΔE = 3.42 eV. (Fig. 7.7) On the other hand, annulation results in distinct destabilization of HOMO level up to -4.64 eV and -4.61 eV and stabilization of LUMO to -1.44 eV and -1.43 eV, respectively, for **1** and **3**. Interestingly the presence of two additional benzene rings in **3** comparing

to **1**, as well as different molecular structure and symmetry, only slightly affects the energy of frontier orbitals, thus the HOMO-LUMO barely changes. (Fig. 7.7)

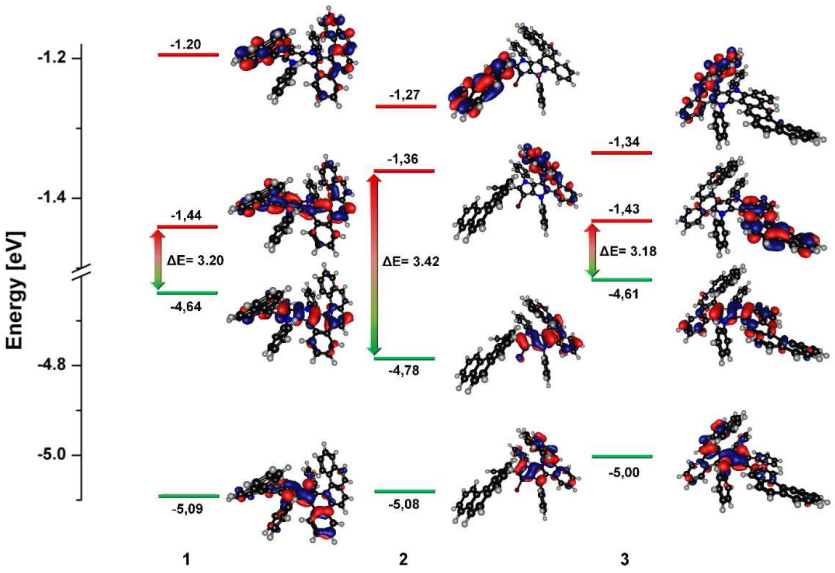

Figure 7.7: LUMO of 2 for contour value 0.008, dark red and blue represent electron density involved in 6π-electrocyclization process

Despite the differences in molecular architecture, helicenes **1**-**3** share some common spectroscopic features, e.g. weak to moderate absorption of main part of visible light (400-450 nm) and strong absorption in the violet spectral region and in UV region (Fig. 7.8, Table 7.2). Computational studies underline the similarities between the helicenes. First of all, the electron density at HOMO as well as HOMO-1 is mostly localized on the electron rich PP core and partially on the helical arm (Fig. 7.7). On the other hand, LUMO of **1** is primarily placed at the molecule's center, while in the case of **2** and **3** it is distinctly shifted to one of the helical arms. A similar displacement of the electron density toward the molecular periphery is observed for the LUMO+1 level of all the investigated systems. TDDFT calculations indicate that, for all systems, HOMO→LUMO is the main contribution to the in $S_0 \rightarrow S_1$ transition. It is worth mentioning that the contribution of HOMO→LUMO+1 cannot be omitted for **3** (Table 7.1).

Table 7.1: TD DFT results for helicenes **1-3**, Showed MOs contributions more than 5%.

	1			2			3		
transition	MOs cont (%)	$f(S_0 \rightarrow S_n)$	$E_{0-0}[eV/nm]$	MOs cont (%)	$f(S_0 \rightarrow S_n)$	$E_{0-0}[eV/nm]$	MOs cont (%)	$f(S_0 \rightarrow S_n)$	$E_{0-0}[eV/nm]$
$S_0 \rightarrow S_1$	$H \rightarrow$L (96.9)	0.5405	2.81/442	$H \rightarrow L$ (91.6)	0.0473	2.86/434	$H \rightarrow L$ (60.4) $H \rightarrow L_{+1}$ (34.5)	0.1003	2.73/456
$S_0 \rightarrow S_2$	$H \rightarrow L_{+1}$ (79.3) $H_{-1} \rightarrow L$ (16.5)	0.0091	2.90/428	$H \rightarrow L_{+2}$ (47.4) $H_{-1} \rightarrow L$ (25.6) $H \rightarrow L_{+1}$ (22.2)	0.0401	3.06/405	$H \rightarrow L_{+1}$ (59.0) $H \rightarrow L$ (34.7)	0.0303	2.79/444
$S_0 \rightarrow S_3$	$H \rightarrow L_{+2}$ (90.2) $H_{-2} \rightarrow L$ (5.6)	0.0128	2.94/422	H$\rightarrow L_{+1}$ (68.1) $H \rightarrow L_{+2}$ (18.8)	0.0861	3.11/398	$H \rightarrow L_{+2}$ (85.3) $H_{-1} \rightarrow L_{+1}$ (8.9)	0.0310	2.96/419
$S_0 \rightarrow S_4$	$H_{-1} \rightarrow L$ (77.0) $H_{-2} \rightarrow L$ (15.6)	0.1147	3.20/387	$H_{-1} \rightarrow L$ (63.2) $H \rightarrow L_{+2}$ (18.7) $H \rightarrow L_{+4}$ (5.2)	0.0633	3.25/382	$H_{-1} \rightarrow L$ (57.1) $H \rightarrow L_{+3}$ (28.7) $H_{-3} \rightarrow L$ (5.9)	0.0549	3.06/405
$S_0 \rightarrow S_5$	$H \rightarrow L_{+3}$ (73.2) $H_{-1} \rightarrow L_{+2}$ (22.1)	0.0033	3.27/379	$H_{-1} \rightarrow L_{+2}$ (60.1) $H_{-1} \rightarrow L_{+1}$ (11.6) $H_{-3} \rightarrow L$ (8.9)	0.0826	3.31/375	$H_{-1} \rightarrow L_{+1}$ (36.0) $H \rightarrow L_{+4}$ (11.9) $H \rightarrow L_{+2}$ (6.4)	0.0235	3.16/392
$S_0 \rightarrow S_6$	$H_{-1} \rightarrow L_{+1}$ (95.0)	0.1347	3.37/368	$H \rightarrow L_{+3}$ (86.1)	0.0160	3.41/364	$H_{-1} \rightarrow L_{+2}$ (36.0) $H \rightarrow L_{+4}$ (17.2) $H \rightarrow L_{+3}$ (11.5) $H_{-1} \rightarrow L$ (9.2)	0.2626	3.19/389
$S_0 \rightarrow S_7$	$H_{-1} \rightarrow L_{+2}$ (72.4) $H \rightarrow L_{+3}$ (21.2)	0.0276	3.43/362	$H_{-1} \rightarrow L_{+1}$ (77.3) $H_{-1} \rightarrow L_{+2}$ (7.2)	0.0345	3.44/360	$H \rightarrow L_{+3}$ (34.2) $H \rightarrow L_{+4}$ (29.6) $H_{-1} \rightarrow L$ (17.1)	0.0912	3.24/383

7.3.3 Absorption and fluorescence properties

The observed experimental molar absorption coefficients (ϵ) are ~2500 $M^{-1}cm^{-1}$ (~(@ 437 nm), ~3000 $M^{-1}cm^{-1}$ (@ 446 nm) and 10000 $M^{-1}cm^{-1}$ (@ 456 nm) for **1**, **2** and **3**, respectively (Table 7.2). TDDFT results suggest that the longest-wavelenght band in the experimental absorption spectra is actually due to the superposition of many peaks near to each other ($S_0 \rightarrow S_{1-7}$). The electron density separation between occupied (HOMO) and unoccupied orbitals (LUMO, LUMO+1) involved in the first electronic transition leads to relatively small oscillator strengths, explaining the weak absorption in most part of the visible region. Strong absorption in the violet and UV region is due to transitions in the range $S_0 \rightarrow S_{8-12}$.

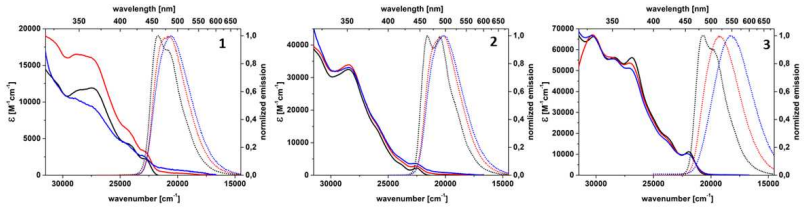

Figure 7.8: Absorption (solid) and emission spectra (dot) of 1-3 in toluene (black), dichloromethane (red) and dimethyl sulfoxide (blue)

Table 7.2: Spectroscopic data in toluene, dichloromethane, and dimethyl sulfoxide for helicenes **1-3**. λ_{abs} / λ_{em} – absorption / emission wavelength, ϵ – molar absorption coefficient, Φ_f – fluorescence quantum yield, $\Delta\nu$ – Stokes shift, τ – fluorescence lifetime, k_r / k_{nr} – radiative/nonradiative constant

Compound	Solvent	λ_{abs} [nm] ($\epsilon \cdot 10^{-3}$ [cm^{-1} M^{-1}])	λ_{em} [nm]	$\Delta\nu$ [cm^{-1}]	Φ_f	τ [ns]	$k_r \cdot 10^{-7}$ [s^{-1}]	$k_{nr} \cdot 10^{-7}$ [s^{-1}]
1	Tol	350 (11.6), 364 (11.9), 410 (4.4), 438 (2.2)	460, 481	1100	0.27	4.32	6.3	17
	DCM	350 (16.5), 364 (16.0), 412 (6.1), 437 (3.3)	481	2100	0.25	4.63	5.4	16
	DMSO	350 (10.1), 364 (9.4), 407 (4.4), 435 (2.6)	486	2400	0.29	–	–	–
2	Tol	350 (32.5), 446 (2.1)	463, 488	800	0.045	1.80	2.5	53
	DCM	350 (33.9), 446 (2.9)	495	2200	0.033	1.72	1.9	56
	DMSO	350 (33.1), 446 (3.5)	495	2200	0.031	–	–	–
3	Tol	330 (66.2), 350 (56.2), 372 (56.2), 456 (11.2)	483, 505	1200	0.32	4.62	7.0	15
	DCM	330 (66.2), 350 (56.2), 369 (53.6), 456 (10.0)	520	2700	0.26	6.68	3.8	11
	DMSO	330 (66.2), 350 (56.2), 369 (51.1), 456 (10.0)	546	3600	0.43	–	–	–

In emission spectra of **1-3** in toluene, a clear vibronic progression is observed. However, upon increasing solvent polarity, the vibronic structure is smeared out by inhomogeneous broadening (Fig. 7.8). This is consistent with emission from a charge-transfer state, in agreement with the differences in electron density distribution over HOMO and LUMO (Fig. 7.7). The charge-transfer nature of the S_1 state is particularly pronounced for **3**, causing a noticeable solvatofluorochromism (the emission wavelength moves from 483 nm in toluene to 546 nm in dimethyl sulfoxide, Fig. 7.7, Table 7.2). Analysis of radiative and nonradiative decay constants (k_r and k_{nr}) gives more insight into the nature of the emitting excited state. For systems **1** and **2**, k_r and k_{nr} values are slightly affected by solvent polarity, thus fluorescence quantum yields (Φ_f) are also barely affected (Table 7.2). The nonradiative decay constant of **2** is more than three times larger than for **1** or **3**. This observation is directly associated to the presence of the bromine atom that enhances the spin-orbit coupling. As a result of effective nonradiative deactivation of the S_1 state through intersystem crossing, the fluorescence quantum yield of **2** is nearly ten times smaller compared to **1** or **3** (Table 7.2). Increased solvent polarity distinctly affects the nature of the S1 state for **3**, as shown by nearly two-times drop in the radiative constant when passing from toluene to dichloromethane.

7.3.4 Chiroptical properties

CD spectra of the pairs of enantiomers of **1**, **2** and **3** in DCM (Fig. 7.9) show multiple peaks, as many transitions underlie their absorption spectra (Tab. 7.1).

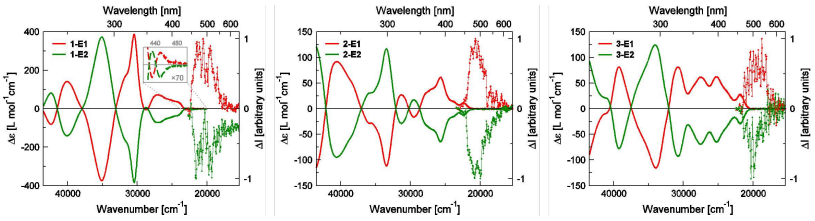

Figure 7.9: CD (full lines) and CPL (lines with dots) spectra of the enantiomers of 1, 2 and 3 in DCM.

The dissymmetry factors, g_{abs}, are lower than 10^{-2} in the whole UV-Vis range (Fig. The intensity of the longest-wavelength peak in the CD spectra (located at 449, 446 and 457 nm for **1**, **2** and **3**, respectively) is very weak for **1**, more than twice and seven times higher for **2** and **3**, respectively. Since the longest-wavelength transition is related to the Kasha state, we expect the same ranking in the CPL activity.[217, 218] 7.10).

Fig. 7.9 shows CPL of helicenes **1-3** in DCM as dotted lines. For all the helicenes, the sign of CPL is consistent with the sign of the lowest energy CD peak. CPL spectra of helicenes **1-3** were also acquired in toluene (Fig. 7.11)

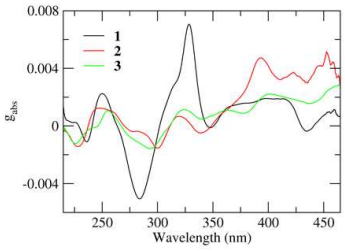

Figure 7.10: Dissymmetry factors in absorption (g_{abs}) for **1-3** in DCM.

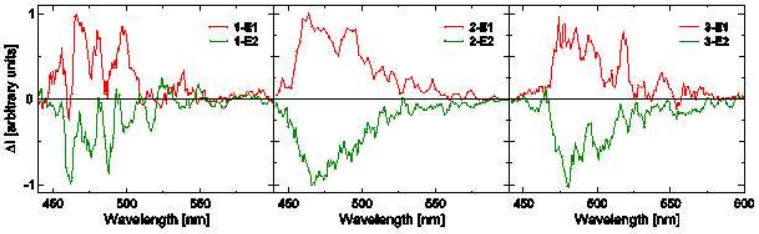

Figure 7.11: CPL spectra of **1-3** in toluene.

The g_{lum} values reported in Table 7.3 were obtained as the average of the values measured in the wavelength range falling inside the FWHM (full width at half maximum) of the corresponding emission band. The luminescence dissymmetry factors of the pairs of enantiomers are in good agreement, with mean $|g_{lum}|$ on the order of 10^{-3} for **1** and **3**, and approaching 10^{-2} for **2**, in both solvents. The $|g_{lum}|$ values are very similar to the g_{abs} values relevant to the lowest-energy CD bands, suggesting that minimal geometrical rearrangements take place in the excited state prior to emission. As anticipated by the CD spectra, **1** has the lowest $|g_{lum}|$ factor. In general we observe that higher radiative decay constants (typically associated with high luminescence quantum yields, Tab. 7.2) correspond to lower $|g_{lum}|$ values, since it can be shown that $g_{lum} \propto \frac{1}{\sqrt{k_r}}$[214]. To take into account the overall CPL performance of a sample, in addition to its dissymmetry factor, the CPL brightness (BCPL) was introduced[257]. The values of BCPL for our compounds are reported in Tab. 7.2, showing that the enantiomers of compound **3** have the highest CPL brightness, comparable with other S-shaped helicenes reported in the literature[257].

Table 7.3: Helicene-based emitters **1-3** and their g_{lum}, fluorescence quantum yield (Φ_f), absorption coefficient (ε) at 350 nm, and CPL brightness (BCPL). Solvent: toluene (black), methylene chloride (red).

	g_{lum} (E1 / E2)	Φ_f	ε [M^{-1} cm^{-1}] @ 350 nm	BCPL
1	$+1.20\times10^{-3}$ / -1.33×10^{-3}	0.27	11600	2.0
	$+1.89\times10^{-3}$ / -1.95×10^{-3}	0.25	16500	4.0
2	$+5.60\times10^{-3}$ / -6.11×10^{-3}	0.045	32500	4.3
	$+6.64\times10^{-3}$ / -7.22×10^{-3}	0.033	33900	3.9
3	$+3.20\times10^{-3}$ / -3.25×10^{-3}	0.32	56200	29.3
	$+2.60\times10^{-3}$ / -2.33×10^{-3}	0.26	56200	17.7

In order to assign the right absolute configuration to each eluted fraction of **1-3**, we performed TD-DFT calculations following the procedure described in ref. [258], just skipping the molecular dynamics simulations sampling, not needed because of the high structural rigidity of the chiral chromophoric cores. Gaussian 16 suite[259] was used for calculations. Each structure was optimized to a minimum for the ground state at a DFT level of theory, using B3LYP as functional and 6-31G(d) as basis set, in gas phase (optimized geometries are reported in Fig. 7.12). TD-DFT calculations were performed on the optimized structure using three different functionals (B3LYP, CAM-B3LYP, M062X) in order to evaluate the stability of the results. Absorption and CD spectra were calculated using 30 excited states, assigning to each of them a Gaussian band. The comparison of the calculated and experimental CD spectrum (mainly the sign of the different peaks) allowed to assign the absolute configuration. The comparison is reported in Fig. 7.12 (for the M062X functional) and shows good agreement in the spectral shape and energies for both

absorption and CD of **1**-**3**. In general, enantiomers showing a positive rotational strength for the lowest energy CD peak were found to be P (or P,P in the case of **1**) helixes. The sign of the lowest energy CD peak of the calculated spectrum was in agreement with the experimental one for **2** and **3**, while for **1** the calculated sign was the opposite. This inconsistency does not surprise, since **1** has an extremely low rotational strength relative to the Kasha state, therefore even tiny geometry variations can alter its sign. In particular, the sign is highly sensitive to the precise orientation of the phenyl groups linked to the bi-pyrrole nitrogens, which are spatially close to the two helixes. Moreover, the right sign of the lowest energy CD peak is recovered if the phenyl groups are substituted with methyl groups, while the rest of the CD spectrum is not significantly affected.

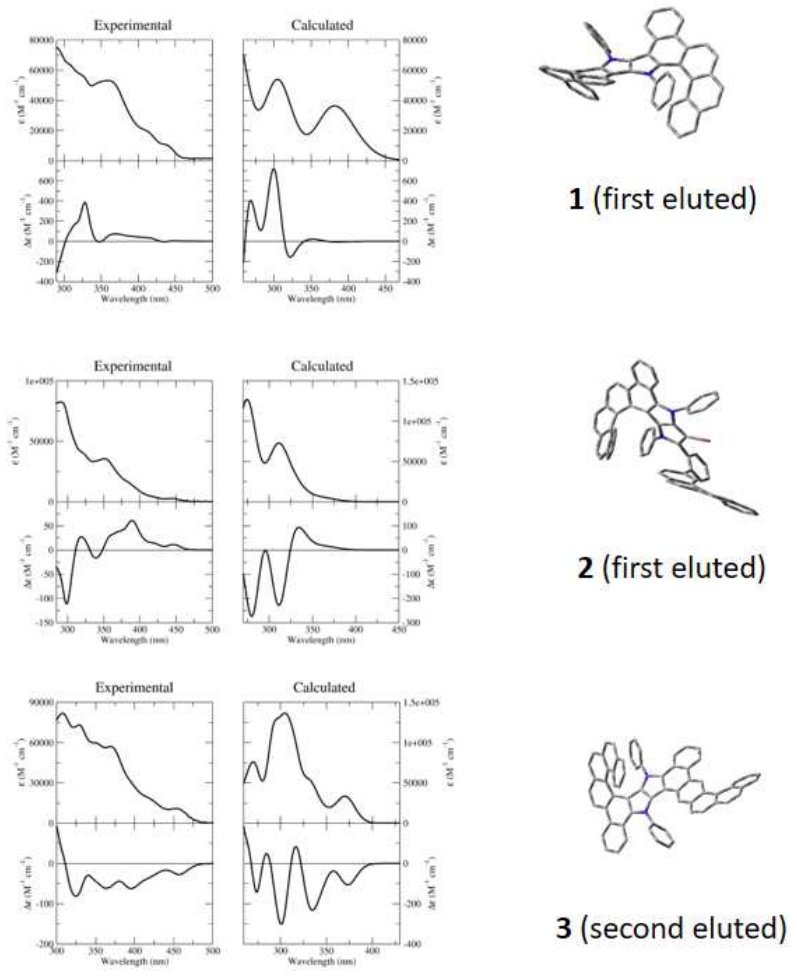

Figure 7.12: Comparison between experimental (left panels) and calculated (right panels) absorption and CD spectra of **1**-**3**.

7.4 Conclusions

The first binary helicenes incorporating the pyrrolo[3,2-b]pyrrolo (PP) moiety were designed and synthesized. Our four-step synthesis involved Suzuki-Miyaura coupling, pyrrolo[3,2-b]pyrrolo synthesis, bromination, and 6π-electrocyclization.

The synthesis yielded a mixture of enantiomers, which we successfully separated using chiral high-performance liquid chromatography (HPLC).

Analysis of the enantiopure fractions of compounds **1**-**3** confirmed their helical structures. Notably, compound **3** exhibited moderate molar extinction coefficients for the $S_0 \rightarrow S_1$ transition, high molar extinction coefficients in the violet spectral region, excellent fluorescence quantum yields of 0.32, and circularly polarized luminescence brightness (BCPL) up to 30 $M^{-1} \cdot cm^{-1}$. These findings demonstrate the potential of our synthesized helicenes for advanced optoelectronic applications and underscore the success of our novel synthetic approach.

Circular dichroism of molecular aggregates: a tutorial on the calculation of spectra

8

8.1 Introduction

When non-chiral objects (molecules, nanoparticles, etc) are arranged to form a chiral super-structure, large chiral responses may emerge in a spectral region where the isolated species do not show absorption bands [260–262]. This so-called supramolecular chirality, induced by intermolecular interactions, will be the topic of this chapter. The first model to explain supramolecular chirality, proposed by Condon [205] and Kirkwood [216] in 1937, was later reconsidered in the classical book by Craig and Thirunamachandran [203]. The model describes the supramolecular structure as a collection of oscillating dipoles, interacting via electrostatic forces, thus relying on the same physical picture that was later introduced to describe molecular aggregates [54] and molecular crystals [263, 264]. A different approach was proposed by DeVoe, who in two very elegant papers [213, 265], described the supramolecular structure as a collection of interacting polarizable objects. More recently, a similar approach to the one proposed by DeVoe was adopted by Govorov to describe the chiral responses of chiral assemblies of plasmonic nanoparticles [266]. While apparently very different, the two approaches, that will be referred to in the following as the oscillating dipole approach, ODA, and the polarizable object approach, POA, rely on the same approximations. Specifically, both consider the electrons as fully localized on each individual structure so that only electrostatic intermolecular interactions are accounted for. Moreover, both rely on the dipole approximation. Here we will review the two approaches to assess their equivalence. In the next Section we will derive explicit expressions for CD spectra of a molecular dimer, demonstrating the formal equivalence of ODA and POA for this system. The final Section will extend relevant expressions to an aggregate of N molecules, showing again that spectra obtained in the ODA and POA approaches are equivalent.

8.2 Results and discussion

8.2.1 The molecular dimer

We consider a molecular dimer, where, on each molecule, we account for the ground state $|g\rangle$ and a single excited state $|e\rangle$, in the hypothesis that all other excitations fall in a spectral region outside the window of interest. This approximation can be released [267], but for the sake of clarity we limit the discussion to the simplest case. The frequency and the amplitude of the transition dipole moment of the relevant excitation are ω_0 and μ_0, respectively. Fig. 8.1 schematically shows the structures of a dimer, with the transition dipole moment of each molecule represented as a double-sided arrow. In the same figure, $\vec{e}_1$ and $\vec{e}_2$ are the unit vectors associated to the two transition dipoles, while $\vec{e}_{21} = (\vec{r}_2 - \vec{r}_1)/r$ is the unit

vector that defines the direction connecting the two molecules, r being the relevant distance. In the same figure, X, Y, Z define the laboratory reference frame. The light wavevector, $\vec{k}$, is parallel to Z. To describe molecular dimers in solution, we will assume random orientation of the dimers in the laboratory frame. In the following all quantities are expressed in cgs units.

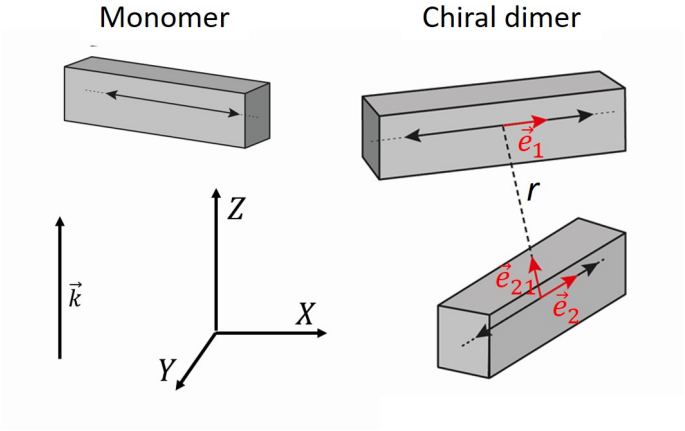

Figure 8.1: Top left: a generic molecule, whose transition dipole moment is represented by a double-sided arrow. Bottom left: X, Y, Z axis define the laboratory frame, $\vec{k}$ is the light wavevector parallel to Z. Right: a generic chiral dimer. Red arrows $\vec{e}_1$ and $\vec{e}_2$ define the unit vectors associated with the transition dipole moments of the two molecules. Finally, r is the distance between the center of mass of the two molecules, $\vec{e}_{21}$ being the unit vector that defines the relevant direction.

Linear absorption To start with, we consider a single isolated molecule (say molecule 1) interacting with a light beam propagating along the Z direction (laboratory frame, see Fig. 8.1). We consider linearly polarized light, with the electric field $\vec{E}(\vec{r}, t)$ oscillating along X with frequency ω and amplitude E_0 [266]:

$$\vec{E}(\vec{r}, t) = Re[E_0 \vec{X} e^{i\vec{k}\cdot\vec{r}} e^{-i\omega t}] \tag{8.1}$$

where $\vec{k}$ is the light wavevector, aligned along the propagation direction with magnitude $2\pi/\lambda_0$, λ_0 being the light wavelength in vacuum, $\vec{X}$ is the unit vector directed along the X axis, and $Re[...]$ indicates the real part of the expression in parenthesis. The first exponential in the above equation can be developed in series:

$$e^{i\vec{k}\cdot\vec{r}} = 1 + i\vec{k}\cdot\vec{r} + ... \tag{8.2}$$

In the long wavelength approximation (also called the dipolar approximation), the series is truncated to the zeroth order term, a good approximation since the wavelength of UV-Vis light is several order of magnitudes larger than the molecular dimension (the approximation is weaker when applied to plasmonic nanoparticles).

Exploiting linear response theory [268], the molecular polarizability tensor relevant to absorption phenomena has a single non-vanishing component (the diagonal component along the $\vec{e}_1$ direction):

$$\alpha(\omega) = \frac{1}{\pi\hbar} \frac{\mu_0^2}{(\omega_0 - \omega) - i\gamma} \tag{8.3}$$

where γ, in frequency units, is proportional to the inverse lifetime of the excited state. In the presence of the field, an oscillating dipole is generated at the molecular location, aligned along the $\vec{e}_1$ direction and

with magnitude, μ_1, proportional to the relevant component of the electric field:

$$\mu_1(\omega) = \alpha(\omega)\vec{e}_1 \cdot \vec{E}$$

The molar extinction coefficient, $L/(mol * cm)$ units, for a collection of molecules in solution is [265, 266]:

$$\epsilon(\omega) = \frac{4\pi\omega N_A}{\ln(10)E_0^2 c} 10^{-3} \langle Im(\mu_1(\omega) \cdot \vec{E}^*) \rangle = \frac{4\pi\omega N_A}{3\ln(10)c} 10^{-3} Im(\alpha(\omega)) \quad (8.4)$$

where c is the light velocity in vacuum, $\vec{E}^*$ is the complex conjugate of the field (equal to $\vec{E}$ in the long-wavelength approximation), N_A is Avogadro's number and $\langle ... \rangle$ stands for orientational averaging, leading to the $\frac{1}{3}$ factor.

Eq. 8.4 regains a well known result: the imaginary part of the complex polarizability defines the absorption spectrum as a Lorentzian band, centered at ω_0, with 2γ measuring the full width at half maximum. The intensity of the transition, i.e. the area below the absorption band, is proportional to μ_0^2. In an alternative approach, relying on the Fermi golden rule for transition probabilities [269], the same expression for the extinction coefficient in Eq. 8.4 could be obtained assigning the transition at frequency ω_0 a Lorentzian bandshape with linewidth γ and intensity proportional to μ_0^2 [205].

We can now address the dimer. In ODA a microscopic picture is adopted that relies on the calculation of the dimer eigenstates and of the relevant transition probabilities. Specifically, the Hamiltonian for a dimer of molecules, each one showing a single dipole-allowed electronic transition in the region of interest, can be written on the basis obtained as the direct product of the molecular states, $|gg\rangle$, $|ge\rangle$, $|eg\rangle$, $|ee\rangle$, as follows:

$$\begin{bmatrix} \langle gg|\hat{H}|gg\rangle & \langle gg|\hat{H}|ge\rangle & \langle gg|\hat{H}|eg\rangle & \langle gg|\hat{H}|ee\rangle \\ \langle ge|\hat{H}|gg\rangle & \langle ge|\hat{H}|ge\rangle & \langle ge|\hat{H}|eg\rangle & \langle ge|\hat{H}|ee\rangle \\ \langle eg|\hat{H}|gg\rangle & \langle eg|\hat{H}|ge\rangle & \langle eg|\hat{H}|eg\rangle & \langle eg|\hat{H}|ee\rangle \\ \langle ee|\hat{H}|gg\rangle & \langle ee|\hat{H}|ge\rangle & \langle ee|\hat{H}|eg\rangle & \langle ee|\hat{H}|ee\rangle \end{bmatrix} = \begin{bmatrix} 0 & 0 & 0 & J \\ 0 & \hbar\omega_0 & J & 0 \\ 0 & J & \hbar\omega_0 & 0 \\ J & 0 & 0 & 2\hbar\omega_0 \end{bmatrix} \quad (8.5)$$

Perturbation theory tells us that the mixing between states with different energies decreases with increasing the energy difference. Therefore, in the exciton model one only accounts for the interaction between states having the same energy, and specifically $|ge\rangle$ and $|eg\rangle$, so that we must diagonalize just the two dimensional Hamiltonian matrix 8.6, written on the basis of the two degenerate $|ge\rangle$ and $|eg\rangle$ states:

$$H = \begin{bmatrix} \hbar\omega_0 & J \\ J & \hbar\omega_0 \end{bmatrix} \quad (8.6)$$

where $J = \langle ge|\hat{H}|eg\rangle$ can be expressed in the point-dipole approximation as follows:

$$J = \frac{1}{4\pi\epsilon_0}\mu_0^2 \frac{\vec{e}_1 \cdot \vec{e}_2 - 3(\vec{e}_1 \cdot \vec{e}_{21})(\vec{e}_2 \cdot \vec{e}_{21})}{r^3} = \mu_0^2 \mathcal{G} \quad (8.7)$$

where ϵ_0 is the vacuum dielectric constant and

$$\mathcal{G} = \frac{1}{4\pi\epsilon_0}\frac{\vec{e}_1\cdot\vec{e}_2 - 3(\vec{e}_1\cdot\vec{e}_{21})(\vec{e}_2\cdot\vec{e}_{21})}{r^3} \tag{8.8}$$

only depends of the dimer geometry.

We now turn attention to the dipole moment operator. We consider non-polar molecules, so that all diagonal matrix elements of the dipole moment operator vanish. We call μ_0 the magnitude of the transition dipole moment of each monomer: $\mu_0 = |\langle g|\hat{\mu}|e\rangle|$. With these definitions, the matrix that defines the dipole moment operator is

$$\begin{bmatrix} \langle gg|\hat{\mu}|gg\rangle & \langle gg|\hat{\mu}|ge\rangle & \langle gg|\hat{\mu}|eg\rangle & \langle gg|\hat{\mu}|ee\rangle \\ \langle ge|\hat{\mu}|gg\rangle & \langle ge|\hat{\mu}|ge\rangle & \langle ge|\hat{\mu}|eg\rangle & \langle ge|\hat{\mu}|ee\rangle \\ \langle eg|\hat{\mu}|gg\rangle & \langle eg|\hat{\mu}|ge\rangle & \langle eg|\hat{\mu}|eg\rangle & \langle eg|\hat{\mu}|ee\rangle \\ \langle ee|\hat{\mu}|gg\rangle & \langle ee|\hat{\mu}|ge\rangle & \langle ee|\hat{\mu}|eg\rangle & \langle ee|\hat{mu}|ee\rangle \end{bmatrix} = \mu_0 \begin{bmatrix} 0 & \vec{e}_2 & \vec{e}_1 & 0 \\ \vec{e}_2 & 0 & 0 & \vec{e}_1 \\ \vec{e}_1 & 0 & 0 & \vec{e}_2 \\ 0 & \vec{e}_1 & \vec{e}_2 & 0 \end{bmatrix} \tag{8.9}$$

Diagonalizing the Hamiltonian 8.6, two eigenstates are found for the dimer, corresponding to the in-phase ($|\Psi_+\rangle = |ge\rangle + |eg\rangle)/\sqrt{2}$) and out-of-phase ($|\Psi_-\rangle = (|ge\rangle - |eg\rangle)/\sqrt{2}$) combinations of the singly excited states, with energies $\hbar\omega_0 + J$ and $\hbar\omega_0 - J$, respectively. The splitting $2J$ between the levels is called the Davydov splitting [270]. As illustrated in Fig. 8.2, for repulsive intermolecular interactions ($J > 0$), the lowest energy state corresponds to the out of phase combination of the two monomer states, the opposite being true for attractive interactions ($J < 0$).

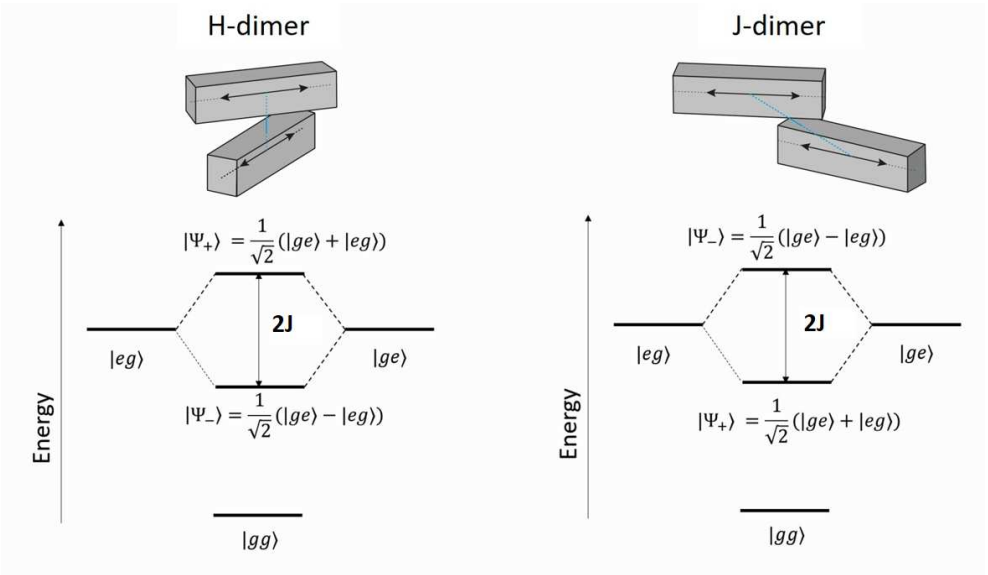

Figure 8.2: Energy levels for the dimer in the exciton model. Left, H-aggregate case: repulsive intermolecular interactions ($J > 0$). Right, J-aggregate case, attractive intermolecular interactions ($J < 0$).

To address absorption spectra, the transition dipole moments are calculated as follows:

$$\begin{aligned} \langle gg|\hat{\vec{\mu}}|\Psi_+\rangle &= \frac{1}{\sqrt{2}}(\langle gg|\hat{\vec{\mu}}|ge\rangle + \langle gg|\hat{\vec{\mu}}|eg\rangle) = \frac{\mu_0}{\sqrt{2}}(\vec{e}_1 + \vec{e}_2) \\ \langle gg|\hat{\vec{\mu}}|\Psi_-\rangle &= \frac{1}{\sqrt{2}}(\langle gg|\hat{\vec{\mu}}|ge\rangle - \langle gg|\hat{\vec{\mu}}|eg\rangle) = \frac{\mu_0}{\sqrt{2}}(\vec{e}_1 - \vec{e}_2) \end{aligned} \tag{8.10}$$

The absorption spectrum of the dimer then describes two transitions, at energy $\hbar\omega_0 \pm J$, with intensity proportional to $\frac{1}{3}\mu_0^2(1 \pm \vec{e}_1\cdot\vec{e}_2)$ where

the 1/3 factor comes from orientational averaging [205, 265, 271]. For aligned dipoles, only $|\Psi_+\rangle$ has a finite transition dipole moment from the ground state and a single band is observed to the blue of the monomer band for $J > 0$, the so-called H-exciton case, while for $J < 0$ the exciton band is red-shifted, in the so-called J-exciton case. Of course, for generic geometries, both transitions are optically allowed, with relative intensities dictated by the square of the transition dipole moments in Eq. 8.10. To get the absorption profile a bandshape is assigned to each transition. In the following (to match with the POA approach below,) we adopt Lorentzian bandshapes with width γ, but other choices, typically Gaussian bandshapes, are possible.

The POA relies on a macroscopic description of the light-matter interaction. When two molecules come close, each molecule feels an electric field that is the sum of the external field, $\vec{E}(\omega)$, and the field generated by the induced dipole in the other molecule. We adopt the dipolar approximation for intermolecular interactions and, calling $\mu_2(\omega)$ the amplitude of the induced dipole at molecule 2, the component of the induced field $\vec{E}_{ind}$ along $\vec{e}_1$ at the location of molecule 1 due to the presence of molecule 2 is:

$$\vec{e}_1 \cdot \vec{E}_{ind} = -\mathcal{G}\mu_2(\omega) \tag{8.11}$$

where $\mathcal{G}$ is defined in Eq. 8.8. The magnitude of the induced dipoles is in turn calculated as the product of the molecular polarizability times the total electric field at the molecular location:

$$\begin{aligned} \mu_1(\omega) &= \alpha(\omega)[\vec{e}_1 \cdot \vec{E} - \mathcal{G}\mu_2(\omega)] \\ \mu_2(\omega) &= \alpha(\omega)[\vec{e}_2 \cdot \vec{E} - \mathcal{G}\mu_1(\omega)] \end{aligned} \tag{8.12}$$

The system

$$\begin{cases} \mu_1(\omega) = \alpha(\omega)[\vec{e}_1 \cdot \vec{E} - \mathcal{G}\mu_2(\omega)] \\ \mu_2(\omega) = \alpha(\omega)[\vec{e}_2 \cdot \vec{E} - \mathcal{G}\mu_1(\omega)] \end{cases} \tag{8.13}$$

can be rewritten as:

$$\begin{bmatrix} \frac{1}{\alpha(\omega)} & \mathcal{G} \\ \mathcal{G} & \frac{1}{\alpha(\omega)} \end{bmatrix} \begin{bmatrix} \mu_1 \\ \mu_2 \end{bmatrix} = \begin{bmatrix} \vec{e}_1 \cdot \vec{E} \\ \vec{e}_2 \cdot \vec{E} \end{bmatrix} \tag{8.14}$$

and can be solved for the dipole moments:

$$\begin{bmatrix} \mu_1 \\ \mu_2 \end{bmatrix} = \begin{bmatrix} \frac{1}{\alpha(\omega)} & \mathcal{G} \\ \mathcal{G} & \frac{1}{\alpha(\omega)} \end{bmatrix}^{-1} \begin{bmatrix} \vec{e}_1 \cdot \vec{E} \\ \vec{e}_2 \cdot \vec{E} \end{bmatrix} \tag{8.15}$$

Inverting the matrix of the coefficients:

$$\hat{A} = \begin{bmatrix} \frac{1}{\alpha(\omega)} & \mathcal{G} \\ \mathcal{G} & \frac{1}{\alpha(\omega)} \end{bmatrix}^{-1} = \begin{bmatrix} \frac{\alpha(\omega)}{(1-\alpha^2(\omega)\mathcal{G}^2)} & \frac{\alpha^2(\omega)\mathcal{G}}{(\alpha^2(\omega)\mathcal{G}^2-1)} \\ \frac{\alpha^2(\omega)\mathcal{G}}{(\alpha^2(\omega)\mathcal{G}^2-1)} & \frac{\alpha(\omega)}{(1-\alpha^2(\omega)\mathcal{G}^2)} \end{bmatrix} \tag{8.16}$$

the induced dipole moments on each monomer are readily obtained as:

$$\begin{aligned}\mu_1(\omega) &= \frac{\alpha(\omega)}{1-\alpha^2(\omega)\mathcal{G}^2}\vec{e}_1\cdot\vec{E}+\frac{\alpha^2(\omega)\mathcal{G}}{\alpha^2(\omega)\mathcal{G}^2-1}\vec{e}_2\cdot\vec{E}\\ \mu_2(\omega) &= \frac{\alpha^2(\omega)\mathcal{G}}{\alpha^2(\omega)\mathcal{G}^2-1}\vec{e}_1\cdot\vec{E}+\frac{\alpha(\omega)}{1-\alpha^2(\omega)\mathcal{G}^2}\vec{e}_2\cdot\vec{E}\end{aligned} \tag{8.17}$$

The identities:

$$\begin{aligned}\frac{\alpha(\omega)}{1-\alpha^2(\omega)\mathcal{G}^2} &= \frac{1}{2(\frac{1}{\alpha(\omega)}+\mathcal{G})}+\frac{1}{2(\frac{1}{\alpha(\omega)}-\mathcal{G})}\\ \frac{\alpha^2(\omega)\mathcal{G}}{\alpha^2(\omega)\mathcal{G}^2-1} &= \frac{1}{2(\frac{1}{\alpha(\omega)}+\mathcal{G})}-\frac{1}{2(\frac{1}{\alpha(\omega)}-\mathcal{G})}\end{aligned} \tag{8.18}$$

are substituted into the expression for the averaged induced dipole moment of the dimer[265]:

$$\vec{\mu}_t(\omega)=\mu_1(\omega)\vec{e}_1+\mu_2(\omega)\vec{e}_2 \tag{8.19}$$

The substution leads to:

$$\begin{aligned}\vec{\mu}_t(\omega) &= \frac{1}{2(\frac{1}{\alpha}(\omega)+\mathcal{G})}\Big((\vec{e}_1\cdot\vec{E})\vec{e}_1+(\vec{e}_2\cdot\vec{E})\vec{e}_1+(\vec{e}_1\cdot\vec{E})\vec{e}_2+(\vec{e}_2\cdot\vec{E})\vec{e}_2\Big)\\ &+ \frac{1}{2(\frac{1}{\alpha}(\omega)-\mathcal{G})}\Big((\vec{e}_1\cdot\vec{E})\vec{e}_1-(\vec{e}_2\cdot\vec{E})\vec{e}_1-(\vec{e}_1\cdot\vec{E})\vec{e}_2+(\vec{e}_2\cdot\vec{E})\vec{e}_2\Big)\end{aligned}$$

To calculate orientational averages we use the general expression:

$$\langle(\vec{e}_i\cdot\vec{E})\vec{e}_j\rangle=\frac{1}{3}(\vec{e}_i\cdot\vec{e}_j)\vec{E} \tag{8.20}$$

to get

$$\langle\vec{\mu}_t(\omega)\rangle=\frac{1}{(\frac{1}{\alpha}(\omega)+\mathcal{G})}\frac{1}{3}(\vec{E}+(\vec{e}_1\cdot\vec{e}_2)\vec{E})+\frac{1}{(\frac{1}{\alpha}(\omega)-\mathcal{G})}\frac{1}{3}(\vec{E}-(\vec{e}_1\cdot\vec{e}_2)\vec{E}) \tag{8.21}$$

As before, the absorption spectrum is calculated as the imaginary part of $\langle\vec{\mu}_t(\omega)\cdot\vec{E}^*\rangle$ and, setting all needed prefactors, the extinction coefficient reads:

$$\begin{aligned}\epsilon(\omega) &= \frac{N_A 4\omega}{3\hbar c\ln(10)}10^{-3}\left[\frac{\gamma\mu_0^2}{(\omega_0-\omega+\mathcal{G}\mu_0^2/\hbar)^2+\gamma^2}(1+\vec{e}_1\cdot\vec{e}_2)\right.\\ &\left.+\frac{\gamma\mu_0^2}{(\omega_0-\omega-\mathcal{G}\mu_0^2/\hbar)^2+\gamma^2}(1-\vec{e}_1\cdot\vec{e}_2)\right]\end{aligned} \tag{8.22}$$

According to the above equation, the absorption band, described for the isolated molecule by a Lorentzian peak at frequency ω_0 (Eq. 8.4), splits in the dimer in two Lorentzian bands centered at $\omega_0+\mathcal{G}\mu_0^2/\hbar$ and $\omega_0-\mathcal{G}\mu_0^2/\hbar$. The relative intensities of the two Lorentzian bands depends on the dimer geometry. For parallel molecules ($\vec{e}_1\cdot\vec{e}_2=1$) one of the two bands is silent and the whole intensity, $\propto 2\mu_0^2$, is associated to the other band. For perpendicular arrangement, the dipolar interaction vanishes

[56] and the spectrum reduces to the sum of two monomer spectra. For generic orientation of the monomers, both bands are partially allowed with intensities $\propto \mu_0^2(1 \pm \cos\theta)$ where θ is the angle between the two transition dipole moments. The resonance frequency of the two bands depends again on the geometry and specifically on the sign of $\mathcal{G}$. If $\mathcal{G} > 0$ (repulsive interactions) the in-phase mode resonates at energies higher than the monomer in a so-called H-aggregate. If $\mathcal{G} < 0$ (attractive interactions) the in-phase mode resonates at lower energy, in the so-called J-aggregate. Overall, the POA describes the same absorption spectrum as ODA.

Circular dichroism Circular dichroism (CD) is defined as the differential absorption of left-handed (anticlockwise) and right-handed (clockwise) polarized light [203, 208]. Specifically, it measures

$$\Delta\epsilon = \epsilon_+ - \epsilon_- \tag{8.23}$$

where ϵ_+ and ϵ_- are the extinction coefficients for the left and right-handed polarized light. In the long-wavelength approximation the left and right circularly polarized fields are [266]:

$$\vec{E}_\pm = E_0 \frac{\vec{X} \pm i\vec{Y}}{\sqrt{2}} \tag{8.24}$$

$\vec{X}$ and $\vec{Y}$ being unit vectors aligned along the X and Y axes of Fig. 8.1. In the long-wavelength approximation, $\vec{E}_+ = \vec{E}_-^*$. The components along X and Y are out of phase by $\frac{\pi}{2}$ and the sum of $\vec{E}_+$ with $\vec{E}_-$ gives a linearly polarized field. In close analogy with Eq. 8.12, we calculate the magnitude of induced dipole moments on each molecule in response to a circularly polarized field $\vec{E}_+$:

$$\begin{aligned} \mu_1^+(\omega) &= \alpha(\omega)[\vec{e}_1 \cdot \vec{E}_+ - \mathcal{G}\mu_2^+(\omega)] \\ \mu_2^+(\omega) &= \alpha(\omega)[\vec{e}_2 \cdot \vec{E}_+ - \mathcal{G}\mu_1^+(\omega)] \end{aligned} \tag{8.25}$$

The system of equations can be solved as before:

$$\begin{aligned} \mu_1^+(\omega) &= \frac{\alpha(\omega)}{1-\alpha^2(\omega)\mathcal{G}^2}\vec{e}_1 \cdot \vec{E}_+ + \frac{\alpha^2(\omega)\mathcal{G}}{\alpha^2(\omega)\mathcal{G}^2-1}\vec{e}_2 \cdot \vec{E}_+ \\ \mu_2^+(\omega) &= \frac{\alpha^2(\omega)\mathcal{G}}{\alpha^2(\omega)\mathcal{G}^2-1}\vec{e}_1 \cdot \vec{E}_+ + \frac{\alpha(\omega)}{1-\alpha^2(\omega)\mathcal{G}^2}\vec{e}_2 \cdot \vec{E}_+ \end{aligned} \tag{8.26}$$

Along the same lines as described previously, we get the total dipole moment induced by left-handed light:

$$\begin{aligned} \vec{\mu}_t^+(\omega) &= \frac{1}{2(\frac{1}{\alpha(\omega)}+\mathcal{G})}\Big((\vec{e}_1 \cdot \vec{E}_+)\vec{e}_1 + (\vec{e}_2 \cdot \vec{E}_+)\vec{e}_1 + (\vec{e}_1 \cdot \vec{E}_+)\vec{e}_2 + (\vec{e}_2 \cdot \vec{E}_+)\vec{e}_2\Big) \\ &+ \frac{1}{2(\frac{1}{\alpha(\omega)}-\mathcal{G})}\Big((\vec{e}_1 \cdot \vec{E}_+)\vec{e}_1 - (\vec{e}_2 \cdot \vec{E}_+)\vec{e}_1 - (\vec{e}_1 \cdot \vec{E}_+)\vec{e}_2 + (\vec{e}_2 \cdot \vec{E}_+)\vec{e}_2\Big) \end{aligned} \tag{8.27}$$

The orientational average of $< \vec{\mu}_t^+(\omega) \cdot \vec{E}_+^* >$ is

$$\begin{aligned}
\langle \vec{\mu}_t^+(\omega) \cdot \vec{E}_+^* \rangle &= \langle \frac{1}{2(\frac{1}{\alpha(\omega)} + \mathcal{G})} \Big((\vec{e}_1 \cdot \vec{E}_+)(\vec{e}_1 \cdot \vec{E}_+^*) + (\vec{e}_2 \cdot \vec{E}_+)(\vec{e}_2 \cdot \vec{E}_+^*) \\
&+ (\vec{e}_2 \cdot \vec{E}_+)(\vec{e}_1 \cdot \vec{E}_+^*) + (\vec{e}_1 \cdot \vec{E}_+)(\vec{e}_2 \cdot \vec{E}_+^*) \Big) \\
&+ \frac{1}{2(\frac{1}{\alpha(\omega)} - \mathcal{G})} \Big((\vec{e}_1 \cdot \vec{E}_+)(\vec{e}_1 \cdot \vec{E}_+^*) + (\vec{e}_2 \cdot \vec{E}_+)(\vec{e}_2 \cdot \vec{E}_+^*) \\
&- (\vec{e}_2 \cdot \vec{E}_+)(\vec{e}_1 \cdot \vec{E}_+^*) - (\vec{e}_1 \cdot \vec{E}_+)(\vec{e}_2 \cdot \vec{E}_+^*) \Big) \rangle \qquad (8.28)
\end{aligned}$$

Since in the long wavelength approximation $\vec{E}_+^* = \vec{E}_-$, we get:

$$\begin{aligned}
\langle \vec{\mu}_t^+(\omega) \cdot \vec{E}_+^* \rangle &= \langle \frac{1}{2(\frac{1}{\alpha(\omega)} + \mathcal{G})} \Big((\vec{e}_1 \cdot \vec{E}_+)(\vec{e}_1 \cdot \vec{E}_-) + (\vec{e}_2 \cdot \vec{E}_+)(\vec{e}_2 \cdot \vec{E}_-) \\
&+ (\vec{e}_2 \cdot \vec{E}_+)(\vec{e}_1 \cdot \vec{E}_-) + (\vec{e}_1 \cdot \vec{E}_+)(\vec{e}_2 \cdot \vec{E}_-) \Big) \\
&+ \frac{1}{2(\frac{1}{\alpha(\omega)} - \mathcal{G})} \Big((\vec{e}_1 \cdot \vec{E}_+)(\vec{e}_1 \cdot \vec{E}_-) + (\vec{e}_2 \cdot \vec{E}_+)(\vec{e}_2 \cdot \vec{E}_-) \\
&- (\vec{e}_2 \cdot \vec{E}_+)(\vec{e}_1 \cdot \vec{E}_-) - (\vec{e}_1 \cdot \vec{E}_+)(\vec{e}_2 \cdot \vec{E}_-) \Big) \rangle \qquad (8.29) \\
&= \langle \vec{\mu}_t^-(\omega) \cdot \vec{E}_-^* \rangle \qquad (8.30)
\end{aligned}$$

leading to the disappointing result of vanishing CD signal.

Indeed, chiral responses are only obtained if the the long wavelength approximation is relaxed, i.e. accounting for the first order term in the expansion in of Eq. 8.2. Since $\vec{k} \cdot \vec{r}$ is small in molecular systems, chiral responses are tiny[203, 224], or, in other terms, molecular systems are too small to efficiently match the field curvature[214]. Relaxing the long wavelength approximation the left and right circularly polarized fields are no more mutually conjugated:

$$\begin{aligned}
\vec{E}_+ &= \frac{E_0}{\sqrt{2}} (\vec{X} + i\vec{Y} + i(\vec{k} \cdot \vec{r})(\vec{X} + i\vec{Y})) \\
\vec{E}_- &= \frac{E_0}{\sqrt{2}} (\vec{X} - i\vec{Y} + i(\vec{k} \cdot \vec{r})(\vec{X} - i\vec{Y})) \qquad (8.31)
\end{aligned}$$

The amplitude of the two molecular dipole moments generated in response to $\vec{E}_\pm$ is calculated along the same lines as described in the previous section to obtain the total orientationally averaged dipole moments generated by the two fields [213]. The averaged total dipole moment for the left circularly polarized field is:

$$\begin{aligned}
< \vec{\mu}_t^+(\omega) > &= \frac{1}{2(\frac{1}{\alpha(\omega)} + \mathcal{G})} \Big(< (\vec{e}_1 \cdot \vec{E}_+)\vec{e}_1 > + < (\vec{e}_2 \cdot \vec{E}_+)\vec{e}_2 > \\
&+ < (\vec{e}_2 \cdot \vec{E}_+)\vec{e}_1 > + < (\vec{e}_1 \cdot \vec{E}_+)\vec{e}_2 > \Big) \\
&+ \frac{1}{2(\frac{1}{\alpha(\omega)} - \mathcal{G})} (< (\vec{e}_1 \cdot \vec{E}_+)\vec{e}_1 > + < (\vec{e}_2 \cdot \vec{E}_+)\vec{e}_2 > + \\
&- < (\vec{e}_2 \cdot \vec{E}_+)\vec{e}_1 > - < (\vec{e}_1 \cdot \vec{E}_+)\vec{e}_2 >)
\end{aligned}$$

we relax the long wavelength approximation including the first term in

$\vec{k}\cdot\vec{r}$ in the series development in $\vec{E}_+$ to get:

$$\begin{aligned}
<\vec{\mu}_t^+(\omega)> \;=\; & \frac{1}{2(\frac{1}{\alpha(\omega)}+\mathcal{G})}\frac{E_0}{\sqrt{2}}\Big(\langle(\vec{e}_1\cdot(\vec{X}+i\vec{Y}))(1+i\vec{k}\cdot(\vec{r}_1-\vec{r}_1))\vec{e}_1\rangle \\
& +\langle(\vec{e}_2\cdot(\vec{X}+i\vec{Y}))(1+i\vec{k}\cdot(\vec{r}_2-\vec{r}_2))\vec{e}_2\rangle + \\
& \langle(\vec{e}_2\cdot(\vec{X}+i\vec{Y}))(1+i\vec{k}\cdot(\vec{r}_2-\vec{r}_1))\vec{e}_1\rangle \\
& +\langle(\vec{e}_1\cdot(\vec{X}+i\vec{Y}))(1+i\vec{k}\cdot(\vec{r}_1-\vec{r}_2))\vec{e}_2\rangle\Big) \\
& +\frac{1}{2(\frac{1}{\alpha(\omega)}-\mathcal{G})}\frac{E_0}{\sqrt{2}}\Big(\langle(\vec{e}_1\cdot(\vec{X}+i\vec{Y}))(1+i\vec{k}\cdot(\vec{r}_1-\vec{r}_1))\vec{e}_1\rangle \\
& +\langle(\vec{e}_2\cdot(\vec{X}+i\vec{Y}))(1+i\vec{k}\cdot(\vec{r}_2-\vec{r}_2))\vec{e}_2\rangle \\
& -\langle(\vec{e}_2\cdot(\vec{X}+i\vec{Y}))(1+i\vec{k}\cdot(\vec{r}_2-\vec{r}_1))\vec{e}_1\rangle \\
& -\langle(\vec{e}_1\cdot(\vec{X}+i\vec{Y}))(1+i\vec{k}\cdot(\vec{r}_1-\vec{r}_2))\vec{e}_2\rangle\Big)
\end{aligned} \tag{8.32}$$

To calculate orientational averages we exploit the relation:

$$<\vec{e}_i(\vec{e}_j\cdot\vec{V})(\vec{e}_k\cdot\vec{k})>=\frac{1}{6}[\vec{e}_i\cdot(\vec{e}_k\times\vec{e}_j)](\vec{k}\times\vec{V}) \tag{8.33}$$

valid if $\vec{V}$ and $\vec{k}$ are orthogonal vectors. The relevant elements for CD spectra, linearly dependent upon $\vec{k}\cdot\vec{r}$, are:

$$\begin{aligned}
\langle(\vec{e}_j\cdot(\vec{X}+i\vec{Y}))(i\vec{k}\cdot(\vec{r}_j-\vec{r}_i))\vec{e}_i\rangle &= \langle(\vec{e}_j\cdot\vec{X})(i\vec{k}\cdot\vec{r}_{ji})\vec{e}_i\rangle-\langle(\vec{e}_j\cdot\vec{Y})(\vec{k}\cdot\vec{r}_{ji})\vec{e}_i\rangle \\
&= \frac{i}{6}[\vec{e}_i\cdot(\vec{r}_{ji}\times\vec{e}_j)](\vec{k}\times\vec{X})-\frac{1}{6}[\vec{e}_i\cdot(\vec{r}_{ji}\times\vec{e}_j)](\vec{k}\times\vec{Y})
\end{aligned} \tag{8.34}$$

The wavevector $\vec{k}$ is perpendicular to both $\vec{X}$ and $\vec{Y}$, therefore:

$$\begin{aligned}
\vec{k}\times\vec{X} &= |k|\vec{Y} \\
\vec{k}\times\vec{Y} &= -|k|\vec{X}
\end{aligned} \tag{8.35}$$

Moreover, the triple product $[\vec{e}_i\cdot(\vec{r}_{ji}\times\vec{e}_j)]$ can be rearranged into $[\vec{r}_{ji}\cdot(\vec{e}_j\times\vec{e}_i)]$. Defining $\vec{r}_{21}=r\vec{e}_{21}$ we finally get the induced dipole moment as:

$$\begin{aligned}
&<\vec{\mu}_t^+(\omega)>= \\
&=\frac{1}{2(\frac{1}{\alpha(\omega)}+\mathcal{G})}\frac{E_0}{\sqrt{2}}\Big(\frac{2}{3}\vec{X}+\frac{2i}{3}\vec{Y}+\frac{2}{3}(\vec{e}_1\cdot\vec{e}_2)\vec{X}+\frac{2i}{3}(\vec{e}_1\cdot\vec{e}_2)\vec{Y}+\frac{ikr}{3}\vec{e}_{21}\cdot(\vec{e}_2\times\vec{e}_1)\vec{Y}+\frac{kr}{3}\vec{e}_{21}\cdot(\vec{e}_2\times\vec{e}_1)\vec{X}\Big) \\
&+\frac{1}{2(\frac{1}{\alpha(\omega)}-\mathcal{G})}\frac{E_0}{\sqrt{2}}\Big(\frac{2}{3}\vec{X}+\frac{2i}{3}\vec{Y}-\frac{2}{3}(\vec{e}_1\cdot\vec{e}_2)\vec{X}-\frac{2i}{3}(\vec{e}_1\cdot\vec{e}_2)\vec{Y}-\frac{ikr}{3}\vec{e}_{21}\cdot(\vec{e}_2\times\vec{e}_1)\vec{Y}-\frac{kr}{3}\vec{e}_{21}\cdot(\vec{e}_2\times\vec{e}_1)\vec{X}\Big)
\end{aligned}$$

$<\vec{\mu}_t^-(\omega)>$ is derived in the same way:

$$\begin{aligned}
&<\vec{\mu}_t^-(\omega)>= \\
&=\frac{1}{2(\frac{1}{\alpha(\omega)}+\mathcal{G})}\frac{E_0}{\sqrt{2}}(\frac{2}{3}\vec{X}-\frac{2i}{3}\vec{Y}+\frac{2}{3}(\vec{e}_1\cdot\vec{e}_2)\vec{X}-\frac{2i}{3}(\vec{e}_1\cdot\vec{e}_2)\vec{Y}-\frac{ikr}{3}\vec{e}_{21}\cdot(\vec{e}_2\times\vec{e}_1)\vec{Y}-\frac{kr}{3}\vec{e}_{21}\cdot(\vec{e}_2\times\vec{e}_1)\vec{X}) \\
&+\frac{1}{2(\frac{1}{\alpha(\omega)}-\mathcal{G})}\frac{E_0}{\sqrt{2}}(\frac{2}{3}\vec{X}-\frac{2i}{3}\vec{Y}-\frac{2}{3}(\vec{e}_1\cdot\vec{e}_2)\vec{X}-\frac{2i}{3}(\vec{e}_1\cdot\vec{e}_2)\vec{Y}+\frac{ikr}{3}\vec{e}_{21}\cdot(\vec{e}_2\times\vec{e}_1)\vec{Y}+\frac{kr}{3}\vec{e}_{21}\cdot(\vec{e}_2\times\vec{e}_1)\vec{X})
\end{aligned}$$

We reorganize the above expressions to write:

$$\begin{aligned} < \vec{\mu}_t^+(\omega) > &= \frac{1}{2(\frac{1}{\alpha(\omega)} + \mathcal{G})} \frac{E_0}{\sqrt{2}} \left\{ \left[\frac{2}{3}(1 + \vec{e}_1 \cdot \vec{e}_2)(\vec{X} + i\vec{Y}) \right] \right. \\ &\quad \left. - \frac{kr}{3} \left[\vec{e}_{21} \cdot (\vec{e}_1 \times \vec{e}_2)(\vec{X} + i\vec{Y}) \right] \right\} \\ &+ \frac{1}{2(\frac{1}{\alpha(\omega)} - \mathcal{G})} \frac{E_0}{\sqrt{2}} \left\{ \left[\frac{2}{3}(1 - \vec{e}_1 \cdot \vec{e}_2)(\vec{X} + i\vec{Y}) \right] \right. \\ &\quad \left. + \frac{kr}{3} \left[\vec{e}_{21} \cdot (\vec{e}_1 \times \vec{e}_2)(\vec{X} + i\vec{Y}) \right] \right\} \quad (8.36) \end{aligned}$$

$$\begin{aligned} < \vec{\mu}_t^-(\omega) > &= \frac{1}{2(\frac{1}{\alpha(\omega)} + \mathcal{G})} \frac{E_0}{\sqrt{2}} \left\{ \left[\frac{2}{3}(1 + \vec{e}_1 \cdot \vec{e}_2)(\vec{X} - i\vec{Y}) \right] \right. \\ &\quad \left. + \frac{\vec{k}\vec{r}}{3} \left[\vec{e}_{21} \cdot (\vec{e}_1 \times \vec{e}_2)(\vec{X} - i\vec{Y}) \right] \right\} \\ &+ \frac{1}{2(\frac{1}{\alpha(\omega)} - \mathcal{G})} \frac{E_0}{\sqrt{2}} \left\{ \left[\frac{2}{3}(1 - \vec{e}_1 \cdot \vec{e}_2)(\vec{X} - i\vec{Y}) \right] \right. \\ &\quad \left. - \frac{\vec{k}\vec{r}}{3} \left[\vec{e}_{21} \cdot (\vec{e}_1 \times \vec{e}_2)(\vec{X} - i\vec{Y}) \right] \right\} \quad (8.37) \end{aligned}$$

We calculate the molar extinction coefficient for both circular polarizations as:

$$\begin{aligned} < \vec{\mu}_t^+(\omega) \cdot \vec{E}_+^* > &= \frac{|\vec{E}_0|^2}{(\frac{1}{\alpha}(\omega) + \mathcal{G})} (\frac{1}{3} + \frac{1}{3}\vec{e}_1 \cdot \vec{e}_2 + \frac{kr}{6}\vec{e}_{21} \cdot (\vec{e}_2 \times \vec{e}_1)) \\ &+ \frac{|\vec{E}_0|^2}{(\frac{1}{\alpha}(\omega) - \mathcal{G})} (\frac{1}{3} - \frac{1}{3}\vec{e}_1 \cdot \vec{e}_2 - \frac{kr}{6}\vec{e}_{21} \cdot (\vec{e}_2 \times \vec{e}_1)) \end{aligned}$$

and

$$\begin{aligned} < \vec{\mu}_t^-(\omega) \cdot \vec{E}_-^* > &= \frac{|\vec{E}_0|^2}{(\frac{1}{\alpha}(\omega) + \mathcal{G})} (\frac{1}{3} + \frac{1}{3}\vec{e}_1 \cdot \vec{e}_1 - \frac{kr}{6}\vec{e}_{21} \cdot (\vec{e}_2 \times \vec{e}_1)) \\ &+ \frac{|\vec{E}_0|^2}{(\frac{1}{\alpha}(\omega) - \mathcal{G})} (\frac{1}{3} - \frac{1}{3}\vec{e}_1 \cdot \vec{e}_2 + \frac{kr}{6}\vec{e}_{21} \cdot (\vec{e}_2 \times \vec{e}_1)) \end{aligned}$$

Molar extinction coefficients can therefore be obtained as:

$$\begin{aligned} \epsilon_+(\omega) = &\frac{1}{3} \frac{N_A}{2303} \frac{4\pi}{|E_0^2|} \frac{\omega}{\hbar c} \frac{\gamma \mu_0^2}{(\omega_0 - \omega + \mathcal{G}\mu_0^2/\hbar)^2 + \gamma^2} (1 + \vec{e}_1 \cdot \vec{e}_2 + kr\vec{e}_{21} \cdot (\vec{e}_2 \times \vec{e}_1)) \\ &\frac{1}{3} \frac{N_A}{2303} \frac{4\pi}{|E_0^2|} \frac{\omega}{\hbar c} \frac{\gamma \mu_0^2}{(\omega_0 - \omega - \mathcal{G}\mu_0^2/\hbar)^2 + \gamma^2} (1 - \vec{e}_1 \cdot \vec{e}_2 - kr\vec{e}_{21} \cdot (\vec{e}_2 \times \vec{e}_1)) \end{aligned}$$

and

$$\epsilon_{-}(\omega) = \frac{1}{3}\frac{N_A}{2303}\frac{4\pi}{|E_0^2|}\frac{\omega}{\hbar c}\frac{\gamma\mu_0^2}{(\omega_0-\omega+\mathcal{G}\mu_0^2/\hbar)^2+\gamma^2}(1+\vec{e}_1\cdot\vec{e}_2-kr\vec{e}_{21}\cdot(\vec{e}_2\times\vec{e}_1))$$
$$\frac{1}{3}\frac{N_A}{2303}\frac{4\pi}{|E_0^2|}\frac{\omega}{\hbar c}\frac{\gamma\mu_0^2}{(\omega_0-\omega-\mathcal{G}\mu_0^2/\hbar)^2+\gamma^2}(1-\vec{e}_1\cdot\vec{e}_2+kr\vec{e}_{21}\cdot(\vec{e}_2\times\vec{e}_1))$$

Finally, the CD spectrum is obtained as the difference of the two extinction coefficients:

$$\Delta\epsilon(\omega) = -\frac{N_A 4\pi\omega^2}{3\ln(10)\hbar c^2}10^{-3}\left[\frac{r\gamma\mu_0^2}{(\omega_0-\omega+\mathcal{G}\mu_0^2/\hbar)^2+\gamma^2}\vec{e}_{21}\cdot(\vec{e}_1\times\vec{e}_2)\right.$$
$$\left.+\frac{r\gamma\mu_0^2}{(\omega_0-\omega-\mathcal{G}\mu_0^2/\hbar)^2+\gamma^2}\vec{e}_{21}\cdot(\vec{e}_1\times\vec{e}_2)\right] \tag{8.38}$$

where r is the intermolecular distance and all unit vectors are defined in Fig. 8.1. The CD spectrum features a doublet: the band at $\omega_0+\mathcal{G}\mu_0^2/\hbar$ has intensity $\propto -r\vec{e}_{21}\cdot(\vec{e}_1\times\vec{e}_2)$ and the band at $\omega_0-\mathcal{G}\mu_0^2/\hbar$ has intensity $\propto r\vec{e}_{21}\cdot(\vec{e}_1\times\vec{e}_2)$. The sign of the two peaks depends on the sine of the angle θ between $\vec{e}_1$ and $\vec{e}_2$, thus ensuring that enantiomers have opposite CD spectra. Since, irrespective of θ, the energy order of the two resonances depends on the sign of $\mathcal{G}$, for fixed handedness of the dimer, the sign of the CD spectrum depends on the sign of $\mathcal{G}$ [57, 208, 226].

The POA derivation of the CD spectrum is very elegant and applies quite naturally to describe plasmonic gold nanoparticles as object having a sizable polarizability in more than one dimension [266]. However, when applied to molecular systems, and in the specific case to a molecule having a single excited state (in the relevant spectral region) and hence a one-dimensional polarizability, the POA approach is expected to lead to the same results as the older ODA method. To demonstrate this result, following Condon [205], the two dimer eigenstates $|\Psi_{\pm}\rangle$ are assigned a chiroptical response proportional to the rotational strength $R_{\pm}$

$$R_{\pm} = Im\left\{\langle gg|\hat{\vec{\mu}}|\Psi_{\pm}\rangle\cdot\langle\Psi_{\pm}|\hat{\vec{M}}|gg\rangle\right\} \tag{8.39}$$

where $Im\{...\}$ takes the imaginary part of the term inside the parenthesis, $\hat{\vec{\mu}}$ and $\hat{\vec{M}}$ are the electric and magnetic dipole moment operators, respectively. This expression is very useful as it allows to immediately recognize the fundamental symmetry requirement for chirality. The electric dipole moment is related to the position of charges, it is therefore a polar vector (basically the typical vector we are used to deal with) and changes its sign upon reflection on a plane perpendicular to the vector itself, while it maintains its sign for any reflection on planes that contain the vector itself. The magnetic dipole moment is different, technically it is an axial vector. Magnetic dipoles are generated by rotating charges, so that, to address their symmetry, we must consider a charge rotating in a circular loop: the magnetic dipole is a vector orthogonal to the plane that contains the loop and its sign is defined by the right hand rule. A reflection on the plane that contains the loop (hence perpendicular to the vector) leaves the rotational motion and hence vector unaffected, while the reflection

on a plane perpendicular to the loop (and hence a plane that contains the vector) inverts the rotation direction and hence inverts the sign of the vector.[224] Eq. 8.39, imposes that, in order to have a finite chiral response, at least one component of the electric and magnetic dipoles must have the same symmetry properties and this is only possible in molecules whose symmetry group does not contain improper axis (including of course inversion point and symmetry planes).

In the hypothesis of non-chiral molecular units, the magnetic dipole moment relevant to each monomer vanishes and the magnetic dipole moment operator of the dimer reads:

$$\hat{\vec{M}} = \frac{e}{2m_e c}\sum_{k=1}^{2}\hat{\vec{r}}_k \times \hat{\vec{p}}_k \tag{8.40}$$

where k runs on the two molecules, $\hat{\vec{p}}_k$ is the linear momentum operator as relevant to molecule k (sum of the linear momentums of its electrons), $\hat{\vec{r}}_k$ is the position vector of the k-th molecule, m_e and e are the electron mass and charge.

The diagonalization of the exciton Hamiltonian (Eq. 8.6) defines the two dimer eigenstates, $|\Psi_\pm\rangle$. Their rotational strengths are:

$$\begin{aligned}
R_\pm &= Im(\langle gg|\,\vec{\mu}\,|\Psi_\pm\rangle \cdot \langle\Psi_\pm|\,\vec{M}\,|gg\rangle) = \\
&= Im(\langle gg|\,\vec{\mu}_1 + \vec{\mu}_2\,|\Psi_\pm\rangle \cdot \langle\Psi_\pm|\,\vec{M}_1 + \vec{M}_2\,|gg\rangle) = \\
&= \langle gg|\,\vec{\mu}_1\,|\Psi_\pm\rangle \cdot \langle\Psi_\pm|\,\vec{M}_1\,|gg\rangle + \langle gg|\,\vec{\mu}_2\,|\Psi_\pm\rangle \cdot \langle\Psi_\pm|\,\vec{M}_2\,|gg\rangle \\
&+ \langle gg|\,\vec{\mu}_1\,|\Psi_\pm\rangle \cdot \langle\Psi_\pm|\,\vec{M}_2\,|gg\rangle + \langle gg|\,\vec{\mu}_2\,|\Psi_\pm\rangle \cdot \langle\Psi_\pm|\,\vec{M}_1\,|gg\rangle
\end{aligned}$$

In the hypothesis that the isolated molecules do not show chiral behavior in the spectral region of interest the terms describing the intrinsic rotational strength of each monomer, $\langle gg|\,\vec{\mu}_1\,|\Psi_\pm\rangle \cdot \langle\Psi_\pm|\,\vec{M}_1\,|gg\rangle$ and $\langle gg|\,\vec{\mu}_2\,|\Psi_\pm\rangle \cdot \langle\Psi_\pm|\,\vec{M}_2\,|gg\rangle$ will be null, so we keep only the crossed terms of the above expression. Making use of the the expression of Equation 8.40, we get:

$$R_\pm = \frac{e}{2m_e c}\langle gg|\,\vec{\mu}_1\,|\Psi_\pm\rangle\cdot\vec{r}_2\times\langle\Psi_\pm|\,\vec{p}_2\,|gg\rangle + \frac{e}{2m_e c}\langle gg|\,\vec{\mu}_2\,|\Psi_\pm\rangle\cdot\vec{r}_1\times\langle\Psi_\pm|\,\vec{p}_1\,|gg\rangle \tag{8.41}$$

And, setting the origin of the reference system on the first monomer, $\vec{r}_1$=0:

$$R_+ = Im(\frac{e}{2m_e c}\langle gg|\,\vec{\mu}_1\,|\Psi_+\rangle \cdot \vec{r}_2 \times \langle\Psi_+|\,\vec{p}_2\,|gg\rangle) \tag{8.42}$$

Remembering that [205]:

$$\hat{\vec{p}}_k = \frac{im_e}{\hbar}[H_k, \hat{\vec{r}}_k] \tag{8.43}$$

where i is the imaginary unit and H is the system Hamiltonian, and $\hat{\vec{\mu}}_k = e\hat{\vec{r}}_k$, where e is the electron charge, we rewrite Equation 8.43 as:

$$\hat{\vec{p}}_k = \frac{im_e}{e\hbar}[\hat{H}, \hat{\vec{\mu}}_k] \tag{8.44}$$

Summing on the electrons of the second monomer in the aggregate, we

get:

$$\hat{\vec{p}}_2 = \frac{im_e}{e\hbar}[\hat{H}, \hat{\vec{\mu}}_2] \tag{8.45}$$

Substituting Eq. 8.45 in Equation 8.41, we get:

$$\begin{aligned} R_\pm &= Im(\frac{i}{2c\hbar}\left\langle gg\right|\vec{\mu}_1\left|\Psi_\pm\right\rangle \cdot \vec{r}_2 \times \left\langle \Psi_\pm\right|[H, \vec{\mu}_2]\left|gg\right\rangle) \\ &= Im(\frac{i}{2c\hbar}\left\langle gg\right|\vec{\mu}_1\left|\Psi_\pm\right\rangle \cdot \vec{r}_2 \times \left\langle \Psi_\pm\right|H\vec{\mu}_2 - \vec{\mu}_2 H\left|gg\right\rangle) \\ &= Im(\frac{i}{2c\hbar}\left\langle gg\right|\vec{\mu}_1\left|\Psi_\pm\right\rangle \cdot \vec{r}_2 \times (\left\langle \Psi_\pm\right|H\vec{\mu}_2\left|gg\right\rangle - \left\langle \Psi_\pm\right|\vec{\mu}_2 H\left|gg\right\rangle)) \\ &= Re(\frac{1}{2c\hbar}\left\langle gg\right|\vec{\mu}_1\left|\Psi_\pm\right\rangle \cdot \vec{r}_2 \times \hbar\omega_\pm \left\langle \Psi_\pm\right|\vec{\mu}_2\left|gg\right\rangle) \end{aligned} \tag{8.46}$$

Substituting $|\Psi_\pm\rangle = \frac{1}{\sqrt{2}}(\left|ge\right\rangle \pm \left|eg\right\rangle)$:

$$\begin{aligned} \left\langle gg\right|\vec{\mu}_1\left|\Psi_\pm\right\rangle &= \frac{1}{\sqrt{2}}\left\langle gg\right|\vec{\mu}_1(\left|ge\right\rangle \pm \left|eg\right\rangle) = \pm\frac{1}{\sqrt{2}}\left\langle gg\right|\vec{\mu}_1\left|eg\right\rangle = \pm\frac{1}{\sqrt{2}}\vec{\mu}_1 \\ \left\langle gg\right|\vec{\mu}_2\left|\Psi_\pm\right\rangle &= \frac{1}{\sqrt{2}}\left\langle gg\right|\vec{\mu}_2(\left|ge\right\rangle \pm \left|eg\right\rangle) = \frac{1}{\sqrt{2}}\left\langle gg\right|\vec{\mu}_2\left|ge\right\rangle = \frac{1}{\sqrt{2}}\vec{\mu}_2 \end{aligned} \tag{8.47}$$

so that:

$$R_\pm = \pm Re\big(\frac{1}{4c}(\omega_0 \pm \mathcal{G}\mu_0^2/\hbar)(\vec{\mu}_1 \cdot \vec{r}_2 \times \vec{\mu}_2)\big) \tag{8.48}$$

Finally, the general relation $\vec{\mu}_1 \cdot \vec{r}_2 \times \vec{\mu}_2 = \vec{r}_2 \cdot \vec{\mu}_2 \times \vec{\mu}_1$ leads us to the well known expression for rotational strength:

$$R_\pm = \pm Re\big(\frac{1}{4c}(\omega_0 \pm \mathcal{G}\mu_0^2/\hbar)(\vec{r}_2 \cdot \vec{\mu}_2 \times \vec{\mu}_1)\big) \tag{8.49}$$

The two rotational strengths have opposite sign, but slightly different modulus. This is an annoying result, since it constrasts with the basic rule of circular dichroism [205], that imposes that the sum of all rotational strengths vanishes, $\sum_f R_{gf} = 0$. As discussed in [57], this inconsistency is resolved if the exciton approximation is relaxed.

In the limit of weak signals, the rotational strength is linked to ellipticity per unit length ϕ' as:

$$\phi' = \frac{8\pi N}{6}\frac{\omega}{\hbar c}\sum_k \frac{R_k \gamma}{(\omega_k - \omega)^2 + \gamma^2} \tag{8.50}$$

where N is the number of absorbing molecules per cm^3 and the k index runs over the system eigenstates (two for a dimer of course). $\Delta\epsilon$ in $L/(mol * cm)$ can be obtained as:

$$\Delta\epsilon = \frac{N_A}{2303}\frac{1}{N}4\phi' \tag{8.51}$$

Assigning a Lorentzian lineshape of width γ the CD spectrum in units

of $L/mol * cm$ is given by [205]:

$$\Delta\epsilon(\omega) = \frac{N_A 16\omega}{3\ln(10)\hbar c} 10^{-3} \left(\frac{\gamma R_+}{(\omega_0 + G\mu_0^2/\hbar - \omega)^2 + \gamma^2} + \frac{\gamma R_-}{(\omega_0 - G\mu_0^2/\hbar - \omega)^2 + \gamma^2}\right) \tag{8.52}$$

This expression is equivalent to Eq. 8.38, apart from a marginal difference. Eq. 8.52 is derived accounting for a system that resonates at specific transition frequencies, $\omega_\pm$, so that $\Delta\epsilon$ is proportional to $\omega\omega_\pm$. Eq. 8.38, instead, is derived accounting for a continuous response of the system in the frequency domain, leading to a $\Delta\epsilon$ that depends on ω^2. The two approaches converge if the spectral bandwidth γ is narrow.

8.2.2 Larger aggregates

In the previous chapter, working with a dimer, we proved the formal equivalence of POA and ODA approaches for the calculation of absorption and CD spectra. The more general case of N molecules cannot be attacked analytically, since it requires the diagonalization or the inversion of large matrices, which is only possible numerically. We therefore demonstrate the equivalence of the two approaches via the explicit calculation of the spectra for a finite size aggregate. To such an aim we must generalize the equations obtained in the previous Section to a general aggregate of N molecules.

The POA approach is readily extended to treat larger molecular aggregates. Specifically, since each molecule responds to the electric field given by the sum of the applied field plus the field generated by all surrounding molecules, a system of N equation is written as follows:

$$\mu_i(\omega) = \alpha(\omega)[\vec{e}_i \cdot \vec{E} - \sum_{j=1, j\neq i}^{N} \mathcal{G}_{ij}\mu_j(\omega)] \tag{8.53}$$

where i runs from 1 to N and $\vec{e}_i$ is the unit vector aligned with the transition dipole moment in molecule i. Moreover,

$$\mathcal{G}_{ij} = \frac{1}{4\pi\epsilon_0} \frac{\vec{e}_i \cdot \vec{e}_j - 3(\vec{e}_i \cdot \vec{e}_{ij})(\vec{e}_j \cdot \vec{e}_{ij})}{r_{ij}^3} \tag{8.54}$$

with r_{ij} mesuring the distance between molecules i and j. The system of equations in Eq. 8.53 is solved for the amplitudes of the induced dipoles:

$$\begin{bmatrix} \mu_1 \\ \dots \\ \mu_N \end{bmatrix} = \begin{bmatrix} \frac{1}{\alpha(\omega)} & \dots & \mathcal{G}_{ij} & \dots & \mathcal{G}_{1N} \\ \dots & \dots & \dots & \dots & \dots \\ \mathcal{G}_{N1} & \dots & \mathcal{G}_{ji} & \dots & \frac{1}{\alpha(\omega)} \end{bmatrix}^{-1} \begin{bmatrix} \vec{e}_1 \cdot \vec{E} \\ \dots \\ \vec{e}_N \cdot \vec{E} \end{bmatrix} \tag{8.55}$$

The total dipole moment of the aggregate

$$\vec{\mu}_t(\omega) = \sum_{i=1}^{N} \vec{e}_i \mu_i(\omega) \tag{8.56}$$

finally enters Equation 8.22 to calculate the extinction coefficient $\epsilon(\omega)$. In order to calculate the CD spectrum two linear equation systems, one relevant to E_+, the other to E_-, must be set up, taking care to account for

the first order term in the expansion in Eq. 8.2. The two equation systems are solved to get the molecular dipole moments that are summed up to give the total induced dipole moment which finally enters the expression for the extinction coefficient as needed to calculate the CD spectrum.

In ODA, the first step is the diagonalization of the exciton Hamiltonian written on the basis formed by the states $|i\rangle$, defined as the states where all molecules are in the ground state, but the i-th molecule that is in the excited state. The exciton Hamiltonian reads:

$$\hat{H} = \begin{bmatrix} \hbar\omega_0 & J_{12} & \dots & J_{1j} & \dots & J_{1N} \\ J_{21} & \hbar\omega_0 & \dots & \dots & \dots & \dots \\ \dots & \dots & \hbar\omega_0 & \dots & \dots & \dots \\ J_{j1} & \dots & \dots & \hbar\omega_0 & \dots & \dots \\ \dots & \dots & \dots & \dots & \hbar\omega_0 & \dots \\ J_{N1} & \dots & \dots & \dots & \dots & \hbar\omega_0 \end{bmatrix} \tag{8.57}$$

where, in the dipolar approximation:

$$J_{ij} = \mu_0^2 \mathcal{G}_{ij} \tag{8.58}$$

The diagonalization of the Hamiltonian in Eq. 8.57 gives the eigenstates as a linear combinations of the basis states:

$$|\Psi_k\rangle = \sum_i c_{ik} |i\rangle \tag{8.59}$$

The transition dipole moment from the ground state $|G\rangle$ (the state where all molecules are in the ground state) to Ψ_k reads:

$$\langle G| \hat{\vec{\mu}} |\Psi_k\rangle = \sum_i c_{ik} \vec{\mu}_i \tag{8.60}$$

The absorption spectrum is calculated assigning a Lorentzian lineshape to each transition:

$$\epsilon(\omega) = \frac{N_A 4\omega}{3\ln(10)\hbar c} 10^{-3} \sum_k \frac{|\langle G| \hat{\vec{\mu}} |\Psi_k\rangle|^2 \gamma}{(\omega_k - \omega)^2 + \gamma^2} \tag{8.61}$$

where ω_k is the frequency of the transition from the ground state to Ψ_k. The rotational strength associated to Ψ_k reads:

$$R_k = \frac{\omega_k}{4c} \sum_{i,j}^{N} c_{ik} c_{jk} \vec{r}_{ij} \cdot \vec{\mu}_j \times \vec{\mu}_i \tag{8.62}$$

where $\vec{r}_{ij}$ is the vector joining the i-th and j-th molecules. To obtain consistency with POA approach ω_k is replaced by ω in the following and the CD spectrum is calculated as:

$$\Delta\epsilon(\omega) = \frac{N_A 16\omega}{3\ln(10)\hbar c} 10^{-3} \sum_k \frac{R_k \gamma}{(\omega_k - \omega)^2 + \gamma^2} \tag{8.63}$$

To compare ODA and POA results we consider two right-handed aggregates arranged in a helix geometry or in a creeper geometry, as schematically illustrated in Fig. 8.3. Specifically, we consider aggregates of 5 molecules, with each molecule characterized by a single excited state

with excitation energy $\hbar\omega_0$=3.4 eV (365 nm) and with a transition dipole moment from the ground state of 7 Debye. To construct the helix we set in both cases the origin of the reference system on the first monomer ($\vec{r}_1 = (0,0,0)$), which is oriented along the x axis, so that $\vec{e}_1 = (1,0,0)$. Since in both geometries every molecule is rotated of 30° with respect to the previous one, constituting a right-handed screw, and all molecules are perpendicular to z, the unit vector that describes the i-th molecule orientation within the reference system is

$$\vec{e}_i = \left(cos\left((i-1)\frac{\pi}{6}\right), sin\left((i-1)\frac{\pi}{6}\right), 0\right) \tag{8.64}$$

In the "helix" geometry the centroids of the molecules are all stacked along z with intermolecular distance set to 7 Å, so that

$$\vec{r}_i = \left(0, 0, 7(i-1)\right) \tag{8.65}$$

In the "creeper" geometry the distance along z is reduced to 5 Å and each molecule is shifted by 5 Å on the xy plane with respect to the previous one, so that the centroid of the i-th molecule is defined by

$$\vec{r}_i = \left(\sum_{j=1}^{i} 5cos((j-2)\frac{\pi}{6}), \sum_{j=1}^{i} 5sin((j-2)\frac{\pi}{6}), 5(i-1)\right) \tag{8.66}$$

so that, in the creeper geometry, the intermolecular distance is $5\sqrt{2}$ Å. In either case the molecular dipole moments are lay in a plane perpendicular to the helical axis. In the simple helix the center of mass of each molecule is on the helical axis. On the opposite, in the creeper geometry, each dipole is tangentially located around a cylinder of finite radius whose axis coincides with the helical axis (you may visualize the molecules winding around the cylinder much as an ivy creeper grows around a tree trunk). In our case, the radius of the cylinder around which the creeper winds is 9.7 Å. While in the helix geometry the $\mathcal{G}$ parameter is always positive (H aggregate case), in the creeper geometry negative $\mathcal{G}$ (J aggregate case) are possible.

Fig. 8.4 shows the spectra calculated for the two geometries. We explicitly verified that the spectra are not affected by the choice of the reference system. ODA and POA spectra are exactly equivalent, demonstrating that the formal equivalence of the two methods, discussed in the previous Section for a dimer, also applies to larger aggregates.

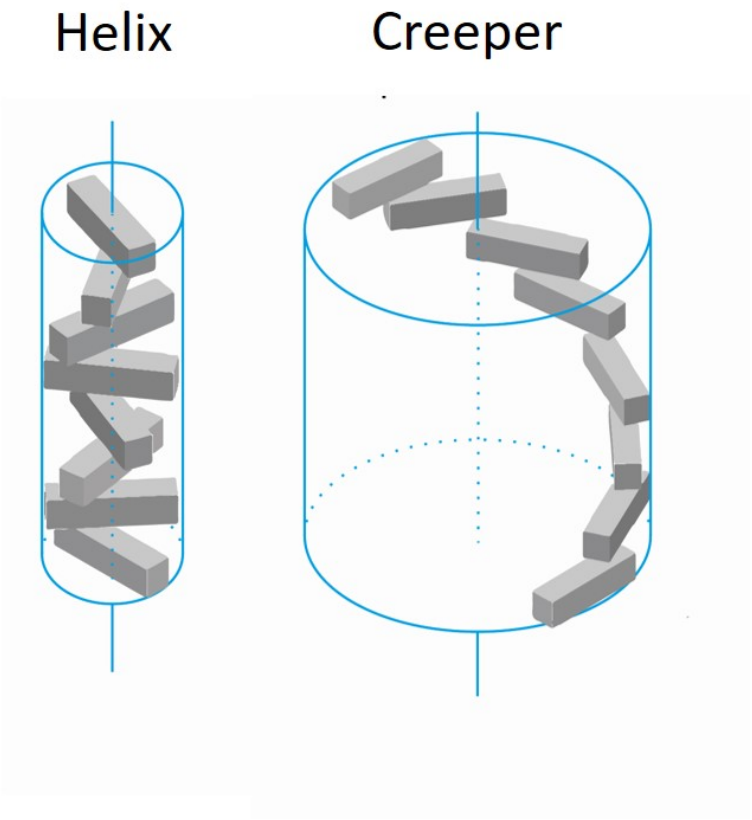

Figure 8.3: Sketch of the supramolecular geometries employed in the following calculations. Left panel: helix geometry, right panel: creeper geometry. For both geometries side views (upper panel) and top views (lower panel) are shown.

We notice that for the helix geometry, the absorption spectrum is shifted to the blue vs the monomer and the sign of the longest wavelength feature in the CD spectrum has a positive sign, while the shortest wavelength feature has a negative sign (positive Cotton effect). For the creeper geometry, the absorption spectrum is shifted to the red vs the monomer (signalling negative $\mathcal{G}$) and the sign of the CD couplet is reversed if compared to the "helix" geometry, despite both aggregates being right-handed[57, 272].

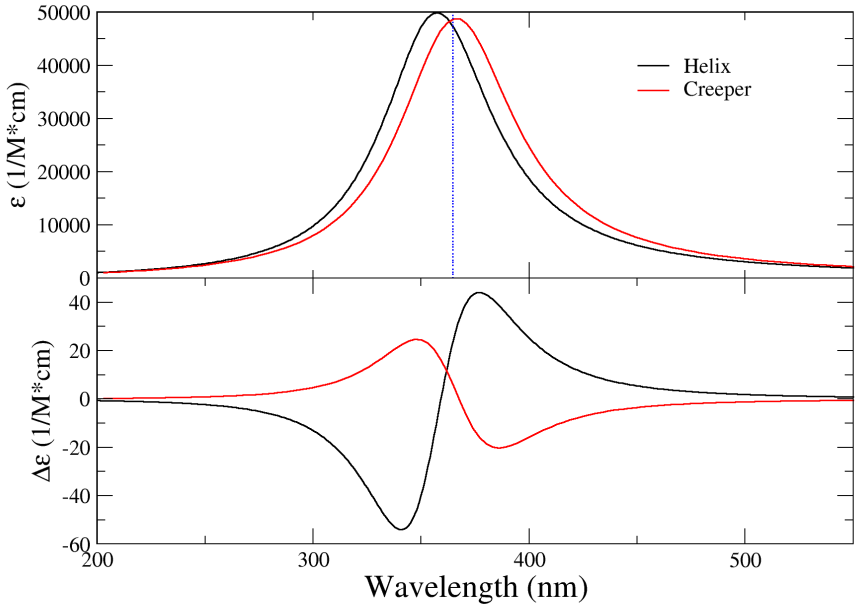

Figure 8.4: Left panel: absorption and CD spectra calculated for a right-handed aggregate of 5 molecules in the helix (black line) and creeper (red line) geometries. ODA and POA results are perfectly superimposed. The blue vertical line show the monomer absorption frequency.

8.2.3 Mixed systems of molecules and plasmonic nanoparticles

Nanoparticles of metals such as silver and gold can absorb visible light, which induces collective oscillations of their electrons, the plasmons.[273–275] The frequency and amplitude of the plasmon depends on the dimension and shape of the nanoparticle.[276] Here we limit the discussion to spherical nanoparticles. For the optical polarizability of spherical plasmonic nanoparticles there is an analytical solution:

$$\alpha(\omega) = r^3 \epsilon_m \frac{\epsilon(\omega) - \epsilon_m}{2\epsilon_m + \epsilon(\omega)} \tag{8.67}$$

where $\epsilon(\omega)$ is the dielectric constant of bulk metal (gold in our case) and ϵ_m is the medium dielectric constant. In the following calculations we use a bulk dielectric constant taken from Ref. [277] and ϵ_m is set to 1, a value corresponding to vacuum.[266]

Plasmonic polarizabilities are $10^2 - 10^3$ times higher than molecular polarizabilities, as the number of electrons involved in the plasmonic modes is quite large. Plasmonic nanoparticles can be organized in chiral supraplasmonic assemblies which give rise to intense CD signals in the visible due to the Coulomb couplings between plasmonic modes. The dimensions of these aggregates are in the order of tens of nanometres, matching the wavelength of incident light much better than supramolecular aggregates.[214] This brings the possibility to have intense chiroptical response in the visible and exploit the optical activity of NPs to enhance the signal of molecules.

The POA approach we illustrated before can be easily extended to treat supraplasmonic chiral aggregates[266] and chiral aggregates comprising both plasmonic and molecular entities. This allows to evaluate the transfer of chirality between molecules and plasmonic NPs.

The whole procedure still involves writing down a system of linear equations, which is solved for right and left handed polarizations in order to calculate the induced dipole moments and the relevant properties. For spherical nanoparticles the polarizability is isotropic, meaning that the plasmonic dipole moment is always generated in the direction along which the external field is applied.

Let's first consider a right-handed chiral dimer of linear molecules, which absorb at 365 nm (3.4 eV) and have an electric transition dipole moment μ_0 of 15 D. As for the helix case in the section 8.2.2, the mass centers of the molecules are stacked along an axis we define as z, the distance along the stacking direction being now 16 nm. The second molecule is rotated of 72° in the xy plane in respect to the first. At this distance the J interaction between molecules is extremely weak, leading to a very low intensity CD doublet (dashed line in Fig. 8.5). The γ bandwidth of molecular absorption is 0.4 eV. The CD spectrum features a positive first Cotton effect, as typical for right handed helixes.[272]

We now insert a plasmonic gold nanoparticle with a 14 nm diametre between the molecules, in order to observe how the CD spectrum changes (Fig. 8.5).

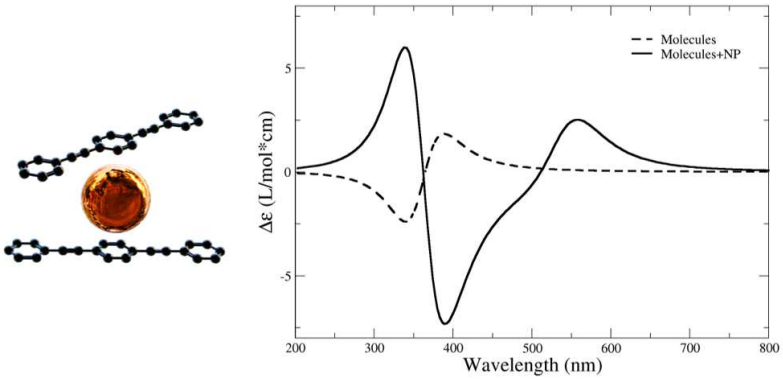

Figure 8.5: Schematic representation (left) and CD spectrum (right) of the assembly described in the text.

We notice the CD signal in the region where the dimer of molecules absorbs is increased by approximately a three fold factor upon electrostatic interaction with the plasmonic nanoparticle. In fact each molecule now feels the induced field generated by the nanoparticle in addition to the external field, leading to an increased transition dipole moment[278]. The enhancement in local electromagnetic field, which influences the chiroptical response, depends on the nanoparticle polarizability, hence on its diametre as shown in Eq. 8.67. Quite interestingly, the sign of the molecular CD doublet is reversed in respect to the dimer without the nanoparticle.

Moreover, a CD signal arises in the region corresponding to the absorption peak of the gold nanoparticle (~ 540 nm), due to its presence within a

chiral environment, even without a specific interaction with the molecules other than spatial proximity. Although the spectral overlap between CD of isolated molecular dimer and the induced CD on gold nanoparticle is virtually null, CD can be induced by molecular ORD[278], as the real part of molecular polarizability is significant even at low frequencies.

As the chiroptical interation between the molecules and the nanoparticle can take place even for low spectral overlaps, we obtain a result analogous to that of Fig. 8.5 when the molecule absorbs at 1.6 eV (776 nm, Fig. 8.6). As spectral resolution is worse at higher wavelengths, we restricted the molecular bandwidth to 0.1 eV in order to have well defined peaks.

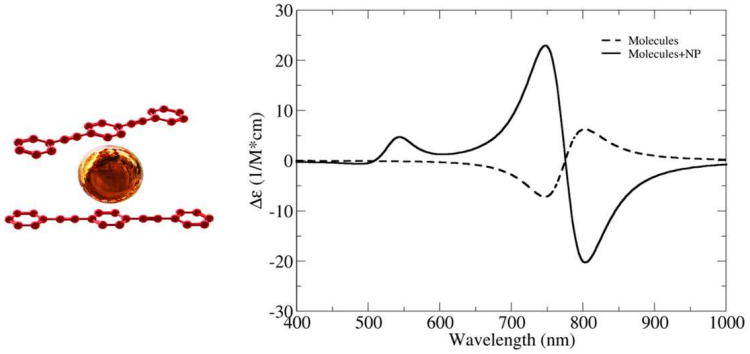

Figure 8.6: Schematic representation (left) and CD spectrum (right) of the assembly described in the text.

The case of Fig. 8.6 is interesting as the lowest energy excited state of the system, i.e. the Kasha state, mostly derives from the molecules and could possibly be fluorescent, whereas plasmonic nanoparticles are generally scarcely emissive. This opens to the possibility of enhancing the efficiency of Circularly Polarized Luminescence (CPL) as expressed by the dissymmmetry factor for CPL[219].

We showed how a chiral arrangement of molecules can induce a chiroptical response where a spherical nanoparticle absorbs and in turn have their own chiroptical response amplified. Now we instead consider a linear molecule placed near a chiral arrangement of spherical gold nanoparticles, in particular a helix with four gold nanoparticles, which is, in a point dipole approximation, the smallest number of nanoparticles able to form a chiral helix[266].

The supraplasmonic helix gives rise to a typical intense doublet in the visible, in this case around the plasmonic frequency of nanoparticles (2.4 eV, or 540 nm, see black line in Fig. 8.7). We put a linear molecule which absorbs at 3.4 eV (365 nm) inside the helix, at first perpendicular to the helix axis. In this case there is no apparent variation of the CD spectrum and no transfer of chirality from the gold NPs assembly to the molecule (Fig. 8.7).

However, if the molecule is placed with its transition dipole moment aligned with the helix axis, a strong, single CD peak appears in correspondence of the molecule absorption peak (Fig. 8.7). A right handed gold helix induces a negative molecular CD peak, while a left handed helix would induce a positive CD peak.

We can explain this dependence on the molecule position by thinking about the helix as (an approximate) solenoid: the solenoid magnetic field

is directed alongside its axis, therefore the induced magnetic field in the molecule will be sizeable only if the molecule is aligned to the axis. In this case in fact both electric transition dipole moment and induced magnetic dipole moment due to the assembly will be directed alongside the helix axis, giving rise to the highest possible rotational strength from the molecule. Otherwise if the molecule is perpendicular to the axis the induced magnetic dipole moment will be perpendicular to the electronic transition dipole moment, and induced chiroptical response will be null.

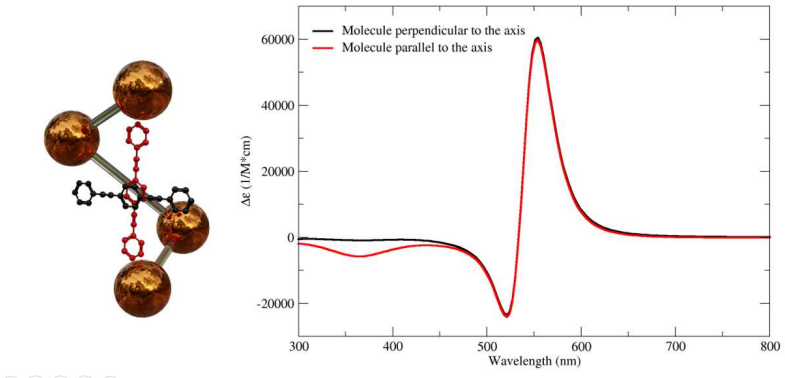

Figure 8.7: Schematic representation (left) and CD spectrum (right) of the assembly described in the text. Black line indicates the CD spectrum of the helic of nanoparticles without the molecule.

The induced molecular CD response in Fig. 8.7 is particularly high for a single molecule, being in the order of thousands of 1/(M*cm). The interaction between achiral molecules and chiral assemblies of plasmonic nanoparticles can be seen as a way to induce or enhance chiroptical responses of molecules. In particular if the molecule is fluorescent and its absorption is red shifted in comparison to the gold nanoparticle, there is hope to obtain efficient CPL. In fact we can consider a molecule absorbing at 1.76 eV (705 nm), inserted in the chiral helix we described above, and repeat the calculation of Fig. 8.7 we get a single red-shifted peak as in Fig. 8.8.

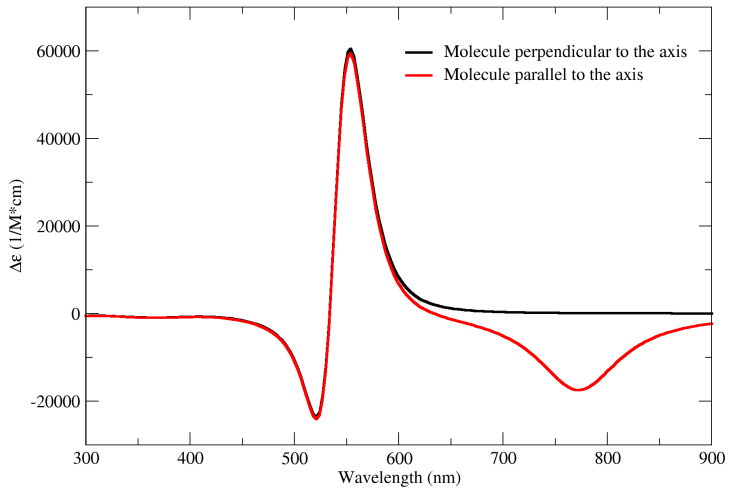

Figure 8.8: Same calculation of 8.7, but molecule absorbs at 1.76 eV. Black line indicates the CD spectrum of the helic of nanoparticles without the molecule.

8.3 Conclusions

In this chapter we overviewed two approaches adopted in the literature to address supramolecular chirality. While seemingly different, the two approaches rely on the same approximations and we proved the analytical equivalence of the two methods for the simplest dimeric case, where closed expressions are obtained. The equivalence is then numerically demonstrated for bigger aggregates. We underline that both approaches rely on a semiclassical description of the light-matter interaction, with the radiating field described classically and the matter describe quantum-mechanically. The link between the two approaches can be found in Eq. 8.3 where the molecular polarizability (entering the POA approach) is expressed in terms of the transition dipole moment μ_0 and the transition frequency ω_0, the two quantities that enter the ODA model.

The last section extended the treatment to chiral aggregates comprising both plasmonic and molecular species. Transfer of chirality is evaluated both in the case of a chiral supramolecular aggregate interacting with a spherical nanoparticle and in the case of a chiral supraplasmonic assembly interacting with a single molecule. In both cases the CD signal of molecules is vastly enhanced upon interaction with plasmonic nanoparticles.

Circular dichroism of molecular aggregates: the role of magnetic dipole moments

9

9.1 Introduction

Circular Dichroism (CD) spectroscopy has provided valuable insights into the structural and electronic characteristics of supramolecular aggregates[118, 208, 209, 260, 279]. Traditionally, chiroptical response at the supramolecular level has been ascribed to the interaction between asymmetrically arranged molecular electric transition dipole moments (which we will refer to as ETDMs for brevity), with exciton coupling theories forming the bedrock of our understanding[55, 57].

However molecules can possess, in addition to ETDMs, magnetic transition dipole moments (which we will refer to as MTDMs)[280–282], whose role in determining the chiroptical response of a supramolecular aggregate has often been overlooked. We can visualize ETDMs as charge translating back and forth through the molecular structure at the transition frequency, while MTDMs can be ascribed to charge rotating at the transition frequency, with the molecule behaving as a current-carrying coil[203, 283].

When molecules are assembled together in a chiral fashion, the interaction between ETDMs gives a substantial contribution to the CD spectrum of the assembly. The resulting shape of CD is usually a doublet (exciton doublet), deriving from the lifting of degeneracy of the levels of interacting molecules. The sign of the CD doublet can allow, with some caveats[57, 284], to assign the handedness of a supramolecular aggregate[208], as underlined in chapters 6 and 8. However, if monomers posses sizeable MTDMs, their role in determining the chiroptical response of a supramolecular assembly cannot be neglected.

The role of MTDMs was underlined in the original works of Kirkwood[216] and Condon[205], but only recently it has been rediscovered and subjected to experimental validation[225]. Neglecting MTDMs when assessing the chiroptical response of an aggregate can lead to severe mistakes, even in assigning the handedness of the aggregate itself[226].

This chapter aims to shed light on the significance of accounting for magnetic dipole moments alongside their electric counterparts when calculating CD spectra of supramolecular aggregates.

As in chapter 8, we adopt the exciton model framework[55, 132], first deriving general relationships for the chiroptical responses of aggregates of N molecules, then moving on to analyze how MTDMs can influence the response of a molecular dimer, obtaining closed analytical expressions. Last, numerical simulations are carried out on a few significant geometries of a dimer, in order to illustrate the theoretical concepts.

9.2 Results and discussion

9.2.1 General theory

We consider a molecular aggregate consisting of N molecules, where, for each molecule, we account for the ground state $|g\rangle$ and a single electronic excited state $|e\rangle$, in the hypothesis that all other excitations fall in a spectral region outside the window of interest (cfr. chapter 8). The relevant excitation is characterized by a frequency ω_0, an ETDM $\vec{\mu}$ of amplitude μ_0 and a MTDM $\vec{m}$ of amplitude m_0. $\vec{\mu}$ and $\vec{m}$ form a generic angle χ within the molecular frame. Of course, the chromophore is optically active if $\chi \neq 90°$, i.e. $\vec{\mu}$ and $\vec{m}$ have components in common directions[203, 205].

In the exciton model framework, we write the Hamiltonian of the assembly on the basis on single excitations, meaning that in the $|i\rangle$ basis state the i-th molecule is in its $|e\rangle$ state, while all the others are in the $|g\rangle$ state[54]. The system Hamiltonian has NxN dimension and can be written as:

$$H = \hbar\omega_0 \sum_i^N |i\rangle\langle i| + \sum_{i,j}^N J(i,j)\,|i\rangle\langle j| \tag{9.1}$$

where $J(i,j)$, the interaction energy between two different molecules within the assembly, can be expressed in the point-dipole approximation as follows:

$$J(i,j) = \frac{1}{4\pi\epsilon_0}\frac{\vec{\mu}_i\cdot\vec{\mu}_j - 3(\vec{\mu}_i\cdot\hat{\vec{r}}_{ji})(\vec{\mu}_j\cdot\hat{\vec{r}}_{ji})}{r_{ji}^3} \tag{9.2}$$

where ϵ_0 is the vacuum dielectric constant, r_{ji} is the distance between the i and j molecules and $\hat{\vec{r}}_{ji}$ is the unit vector joining them ($\hat{\vec{r}}_{ji} = \frac{\vec{r}_j - \vec{r}_i}{r_{ji}}$).

A first question may arise spontaneous: why aren't we considering interactions between MTDMs in Eq. 9.2?

To answer, we shall compare the orders of magnitude of μ_0 and m_0 in a typical molecular system. These two amplitudes have the same measurement units in c.g.s. units, while in SI units μ_0 is measured in C·m and m_0 in $\frac{J}{T}$, which converts to $\frac{C\cdot m^2}{s}$, making it apparent one should divide m_0 by the light velocity in vacuum c in order to have it in the same measurement units as μ_0[205]. From now on we refer to m_0 and μ_0 having comparable measurement units. Typical values for bright molecular transitions are $\mu_0 \sim 5 - 10$ D and $m_0 \sim 0.01 - 0.1$ D. We immediately understand the average MTDM is order of magnitudes smaller than the average ETDM. Since the dipolar interaction between magnetic dipole moments goes with m_0^2[285] it is further order of magnitudes smaller than the interaction between electric dipole moments, making it completely negligible when calculating $J(i,j)$. The interactions between MTDMs may come into play for dipole-forbidden transitions, like the ones observed in lanthanide complexes[286].

The diagonalization of Hamiltonian 9.1 gives eigenstates as a linear combinations of the basis states:

$$|\Psi_k\rangle = \sum_i c_{ik}\,|i\rangle \tag{9.3}$$

where $c_{ik} = \langle i|\Psi_k\rangle$. The electric transition dipole moment from the aggregate ground state $|G\rangle$ (the state where all molecules are in their $|g\rangle$ state) to Ψ_k reads:

$$\langle G|\,\hat{\vec{\mu}}\,|\Psi_k\rangle = \sum_i c_{ik}\vec{\mu}_i \tag{9.4}$$

we can also define a magnetic transition dipole moment from $|G\rangle$ to $|\Psi_k\rangle$ as:

$$\langle G|\,\hat{\vec{m}}\,|\Psi_k\rangle = \sum_i c_{ik}\vec{m}_i \tag{9.5}$$

The absorption spectrum is calculated assigning a Lorentzian (or Gaussian) lineshape of γ width to each transition, whose intensity is proportional to the squared ETDM:

$$\epsilon(\omega) = \frac{N_A 4\omega}{3\ln(10)\hbar c}10^{-3}\sum_k \frac{|\,\langle G|\,\hat{\vec{\mu}}\,|\Psi_k\rangle\,|^2\gamma}{(\omega_k-\omega)^2+\gamma^2} \tag{9.6}$$

where ω_k is the frequency of the transition from the ground state to $|\Psi_k\rangle$. It should be noticed that the full oscillator strength for the $|G\rangle$ to $|\Psi_k\rangle$ transition is given by $|\,\langle G|\,\hat{\vec{\mu}}+\hat{\vec{m}}\,|\Psi_k\rangle\,|^2$[214], but we can forget the magnetic dipole contribution to oscillator strength for the same reason we neglected magnetic dipole couplings in Eq. 9.2. Again, this does not hold true for forbidden transition, like in lanthanides, for which μ_0 and m_0 become comparable. From now on we will refer to the squared ETDM of Eq. 9.6 as the "line strength" D_k relative to the $|G\rangle$ to $|\Psi_k\rangle$ transition[205].

The intensity of the CD peak relative to the same transition is instead associated with the rotational strength R_k, which is defined as:

$$R_k = Im(\langle G|\,\hat{\vec{\mu}}\,|\Psi_k\rangle\cdot\langle\Psi_k|\,\hat{\vec{m}}\,|G\rangle) = Im(\langle G|\sum_{i=1}^{N}\hat{\vec{\mu}}_i\,|\Psi_k\rangle\cdot\langle\Psi_k|\sum_{j=1}^{N}\hat{\vec{M}}_j\,|G\rangle+\langle G|\sum_{i=1}^{N}\hat{\vec{\mu}}_i\,|\Psi_k\rangle\cdot\langle\Psi_k|\sum_{j=1}^{N}\hat{\vec{m}}_j\,|G\rangle) \tag{9.7}$$

The indices j and i run over the N molecules in the system. The term $\hat{\vec{\mu}}_i$ represents the ETDM operator for the i-th molecule. For the j-th molecule, $\hat{\vec{m}}_j$ and $\hat{\vec{M}}_j$ correspond to two different components of the MTDM operator.

$\hat{\vec{m}}_j$ refers to the intrinsic magnetic transition dipole moment of the j-th molecule [225], while $\hat{\vec{M}}_j$ represents the contribution of the j-th molecule's electrons to the total magnetic transition dipole moment of the aggregate, measured relative to the system's center of mass [205, 225].This last contributions arises when molecules are inside an assembly. $\hat{\vec{M}}_j$ is defined as:

$$\hat{\vec{M}}_j = \frac{e}{2m_e c}(\vec{\mathcal{R}}_j\times\hat{\vec{p}}_j) \tag{9.8}$$

where $\hat{\vec{p}}_j$ is the linear momentum operator as relevant to j-th molecule (sum of the linear momentums of its electrons), $\vec{\mathcal{R}}_j$ is the position vector of the j-th molecule, m_e and e are the electron mass and charge. The procedure to simplify the rotational strength expression closely parallels chapter 8. Substituting Eq. 9.8 into Eq. 9.7 we get:

$$R_k = Im(\langle G|\sum_{i=1}^{N}\hat{\vec{\mu}}_i|\Psi_k\rangle\cdot\frac{e}{2m_e c}\langle\Psi_k|\sum_{j=1}^{N}\vec{\mathcal{R}}_j\times\hat{\vec{p}}_j|G\rangle+\langle G|\sum_{i=1}^{N}\hat{\vec{\mu}}_i|\Psi_k\rangle\cdot\langle\Psi_k|\sum_{j=1}^{N}\hat{\vec{m}}_j|G\rangle) \tag{9.9}$$

Remembering that:

$$\hat{\vec{p}}_j = \frac{im_e}{e\hbar}[H,\hat{\vec{\mu}}_j] \tag{9.10}$$

where i is the imaginary unit and H is the system Hamiltonian, we substitute Eq. 9.10 into the relevant term of Eq. 9.9:

$$\frac{e}{2m_e c}Im(\langle\Psi_k|\sum_{j=1}^{N}\vec{\mathcal{R}}_j\times\hat{\vec{p}}_j|G\rangle) = \frac{e}{2m_e c}Im(\langle\Psi_k|\sum_{j=1}^{N}\vec{\mathcal{R}}_j\times\frac{im_e}{e\hbar}[\hat{H},\hat{\vec{\mu}}_j]|G\rangle) = \frac{\omega_k}{2c}\sum_{j=1}^{N}\vec{\mathcal{R}}_j\times\langle\Psi_k|\hat{\vec{\mu}}_j|G\rangle \tag{9.11}$$

Substituting Eqs. 9.4, 9.5 and 9.11 into Eq. 9.9,and exploiting triple product circular shift, gives the final expression for R_k as:

$$R_k = \sum_{i,j}^{N} c_{i,k}^* c_{j,k}(\frac{\omega_k}{4c}\vec{r}_{j,i}\cdot\vec{\mu}_j\times\vec{\mu}_i + \vec{\mu}_i\cdot\vec{m}_j) \tag{9.12}$$

where $\vec{r}_{j,i}$ is the vector joining the i-th and j-th molecules ($\vec{r}_{j,i} = \vec{\mathcal{R}}_j - \vec{\mathcal{R}}_i$). The CD spectrum is calculated assigning a Lorentzian bandshape of width γ to each transition, as:

$$\Delta\epsilon(\omega) = \frac{N_A 16\omega}{3\ln(10)\hbar c}10^{-3}\sum_k\frac{R_k\gamma}{(\omega_k-\omega)^2+\gamma^2} \tag{9.13}$$

We now proceed to analyze in details the various terms of Eq. 9.12. The first term in brackets of Eq. 9.12 is called $\mu-\mu$ coupling and originates when the ETDMs of molecules within the assembly are ordered in a chiral fashion. Commonly considered the leading term in CD of supramolecular aggregates[57, 226], its contribution to the CD spectrum decreases with the square intermolecular distance $\frac{1}{r_{j,i}^2}$, resulting from the balance between electrostatic interactions (Eq. 9.2) which decrease with $\frac{1}{r_{j,i}^3}$[225] and the contribution to rotational strength, which increases linearly with $r_{j,i}$.

We separate the second term in brackets of Eq. 9.12 as:

$$\sum_{i,j}^{N} c_{i,k}^* c_{j,k}(\vec{\mu}_i\cdot\vec{m}_j) = \sum_{i}^{N} c_{i,k}^* c_{i,k}(\vec{\mu}_i\cdot\vec{m}_i) + \sum_{i,j,i\neq j}^{N} c_{j,k}^* c_{i,k}(\vec{\mu}_i\cdot\vec{m}_j) \tag{9.14}$$

The firs term of Eq. 9.14 refers to optical activity shown by the isolated monomers, therefore we label it as "intrinsic chirality", or intramolecular $\mu - m$ coupling. We instead refer to the second term as intermolecular $\mu - m$ coupling, that is the coupling between the MTDM of a molecule and the ETDM of a different molecule of the assembly. The contributions of this intermolecular term to the CD spectra goes with $\frac{1}{r_{ij}^3}$, exactly as the electrostatic interaction of Eq. 9.2, making it a shorter range term in comparison to $\mu - \mu$ coupling[225].

We now proceed to show some physical properties of the terms of Eq. 9.14. It can be shown that, for assemblies of identical chiral chromophores, the intrinsic rotational strength is equipartite between the exciton Hamiltonian eigenstates of Eq. 9.4. In fact if monomers are identical we can write:

$$(\vec{\mu}_i \cdot \vec{m}_i) = \mu_0 m_0 cos(\chi) \quad \forall i$$

where χ is the angle between the ETDM and MTDM in the monomer frame. Since the $|\Psi_k\rangle$ eigenstate is normalized, meaning that $\sum_i^N c_{i,k}^* c_{i,k} = 1$, we can write:

$$\sum_i^N c_{i,k}^* c_{i,k} (\vec{\mu}_i \cdot \vec{m}_i) = \mu_0 m_0 cos(\chi) \tag{9.15}$$

According to Eq. 9.15 every exciton state gets the same rotational strength contribution from intrinsic chirality, and this contribution is equal to the rotational strength of a single monomer. In the case of a racemate mixture the equipartition of rotational strengths assures this contribution is null for every $|\Psi_k\rangle$ state.

We now consider the second term in Eq. 9.14, which we labelled as intermolecular $\mu - m$ coupling. If we sum this contribution all over the N excited states we get:

$$Im(\sum_k \sum_{i \neq j} c_{j,k}^* c_{i,k} \vec{\mu}_i \cdot \vec{m}_j) = Im(\sum_{i \neq j} \sum_k \langle i|\Psi_k\rangle \langle \Psi_k|j\rangle \vec{\mu}_i \cdot \vec{m}_j \tag{9.16}$$

but $|\Psi_k\rangle$ are the eigenstates of the exciton Hamiltonian, therefore due to completeness $\sum_k |\Psi_k\rangle \langle \Psi_k| = 1$, and:

$$Im(\sum_{i \neq j} \sum_k \langle i|\Psi_k\rangle \langle \Psi_k|j\rangle \vec{\mu}_i \cdot \vec{m}_j = Im \sum_{i \neq j} \langle i|j\rangle \vec{\mu}_i \cdot \vec{m}_j = Im \sum_{i \neq j} \delta_{ij} \vec{\mu}_i \cdot \vec{m}_j = 0 \tag{9.17}$$

Eq. 9.17 shows that the sum of intermolecular $\mu - m$ coupling contributions to the rotational strengths over the exciton manifold is zero, implying this term gives positive and negative CD peaks in equal measure. It should always be remembered that the sum of rotational strengths over the whole range of energies, independently on their physical origin, must be

equal to zero[205]; eq. 9.17 shows that the intermolecular $\mu - m$ coupling contribution *over the exciton manifold* amounts to zero.

9.2.2 Calculations for a dimer

The dimer Hamiltonian is a 2×2 matrix, written on basis states $|1\rangle$ and $|2\rangle$, which represent the excitations localized on either monomer.

$$H = \begin{bmatrix} \hbar\omega_0 & J \\ J & \hbar\omega_0 \end{bmatrix} \tag{9.18}$$

By diagonalizing Hamiltonian 9.18 and exploiting Eq. 9.3, we get two eigenstates, $|\Psi_+\rangle$ and $|\Psi_-\rangle$, at energies $\hbar\omega_0 + J$ and $\hbar\omega_0 - J$, respectively representing the in-phase and out-of-phase combinations of monomers excitations:

$$\begin{aligned} |\Psi_+\rangle &= \frac{1}{\sqrt{2}}(|1\rangle + |2\rangle) \\ |\Psi_-\rangle &= \frac{1}{\sqrt{2}}(|1\rangle - |2\rangle) \end{aligned} \tag{9.19}$$

According to Eq. 9.4 we esteem the ETDM from the ground state to the excited states:

$$\begin{aligned} \vec{\mu}_+ &= \frac{1}{\sqrt{2}}(\vec{\mu}_1 + \vec{\mu}_2) \\ \vec{\mu}_- &= \frac{1}{\sqrt{2}}(\vec{\mu}_1 - \vec{\mu}_2) \end{aligned} \tag{9.20}$$

and the respective line strengths (see above and ref. [205] for the definition) as:

$$\begin{aligned} D_+ &= \frac{1}{2}(\vec{\mu}_1 \cdot \vec{\mu}_1 + \vec{\mu}_2 \cdot \vec{\mu}_2) + \vec{\mu}_1 \cdot \vec{\mu}_2 \\ D_- &= \frac{1}{2}(\vec{\mu}_1 \cdot \vec{\mu}_1 + \vec{\mu}_2 \cdot \vec{\mu}_2) - \vec{\mu}_1 \cdot \vec{\mu}_2 \end{aligned} \tag{9.21}$$

The energy order of the in-phase and out-of-phase combinations is determined by the sign of the electrostatic interaction J[57]. From Eqs. 9.21 it emerges how the transition toward the in-phase excited state is always more intense than the out-of-phase by a $2\vec{\mu}_1 \cdot \vec{\mu}_2$ quantity[55]. If $\vec{\mu}_1$ and $\vec{\mu}_2$ are parallel the out-of-phase combination has vanishing line strength, while the in-phase combination gets twice the monomer line strength, $2\mu_0^2$.

We now turn our attention to the rotational strengths relative to the transitions from the ground state $|G\rangle$ to $|\Psi_{+/-}\rangle$. According to Eq. 9.12 we calculate:

$$R_+ = \frac{\omega_0 + \frac{J}{\hbar}}{4c}[\vec{r}_{21} \cdot \vec{\mu}_1 \times \vec{\mu}_2] + \frac{1}{2}(\vec{\mu}_1 \cdot \vec{m}_1 + \vec{\mu}_2 \cdot \vec{m}_2) + \frac{1}{2}(\vec{\mu}_1 \cdot \vec{m}_2 + \vec{\mu}_2 \cdot \vec{m}_1)$$
$$R_- = -\frac{\omega_0 - \frac{J}{\hbar}}{4c}[\vec{r}_{21} \cdot \vec{\mu}_1 \times \vec{\mu}_2] + \frac{1}{2}(\vec{\mu}_1 \cdot \vec{m}_1 + \vec{\mu}_2 \cdot \vec{m}_2) - \frac{1}{2}(\vec{\mu}_1 \cdot \vec{m}_2 + \vec{\mu}_2 \cdot \vec{m}_1) \quad (9.22)$$

Eqs. 9.22 offer a concrete proof of the general relationships introduced in the previous section:

- the $\mu - \mu$ coupling contribution has opposite sign for the $|\Psi_+\rangle$ and $|\Psi_-\rangle$ eigenstates, but the absolute value is not exactly the same as it is proportional to the transition frequency[55, 57]
- the intrinsic chirality contribution is the same for both states and equal to the monomer rotational strength, as shown in Eq. 9.15
- the intermolecular $\mu - m$ coupling contribution has opposite sign for the $|G\rangle$ to $|\Psi_+\rangle$ and $|\Psi_-\rangle$ transitions, and is equal in absolute value, as shown in Eq. 9.17

The sign of each contribution strictly depends on the angles between electric and/or magnetic transition dipole moments, making it hard if not impossible to assign absolute configuration to a chiral assembly upon visual inspection when MTDM contribution is sizeable[226]. Moreover, in the case of strong intrinsic chirality, all CD peaks could in principle have the same sign.

The cofacial dimer of chiral molecules We consider a dimer of chiral molecules whose ETDMs are parallel, leading to a vanishing $\mu - \mu$ coupling contribution to the CD spectrum. $\vec{\mu}_1$ and $\vec{\mu}_2$ are oriented along the x axis, so that their unit vectors are $\hat{\mu}_1 = \hat{\mu}_2 = (1, 0, 0)$. The molecules are identical so that their MTDMs are parallel too and oriented along the unit vector $(cos(\chi), sin(\chi), 0)$. The distance between the two molecules is described by the unit vector $\hat{r}_{21} = (0, 0, 1)$ which is orthogonal to all ETDMs and MTDMs. We indicate with r the absolute value of the distance between the molecules. We evaluate line strengths from Eq. 9.21 and rotational strengths from Eq. 9.22.

$$D_+ = \frac{1}{2}(\vec{\mu}_1 \cdot \vec{\mu}_1 + \vec{\mu}_2 \cdot \vec{\mu}_2) + \vec{\mu}_1 \cdot \vec{\mu}_2 = 2\mu_0^2$$
$$D_- = \frac{1}{2}(\vec{\mu}_1 \cdot \vec{\mu}_1 + \vec{\mu}_2 \cdot \vec{\mu}_2) - \vec{\mu}_1 \cdot \vec{\mu}_2 = 0 \quad (9.23)$$

Eqs. 9.23 shows how the in-phase combination is dipole allowed, with twice the monomer line strength, and the out-of-phase combination is totally forbidden. As for the rotational strengths:

$$R_+ = \frac{\omega_0 + \frac{J}{\hbar}}{4c}[\vec{r}_{21} \cdot \vec{\mu}_1 \times \vec{\mu}_2] + \frac{1}{2}(\vec{\mu}_1 \cdot \vec{m}_1 + \vec{\mu}_2 \cdot \vec{m}_2) + \frac{1}{2}(\vec{\mu}_1 \cdot \vec{m}_2 + \vec{\mu}_2 \cdot \vec{m}_1) \quad (9.24)$$
$$= \mu_0 m_0 cos(\chi) + \mu_0 m_0 cos(\chi) = 2\mu_0 m_0 cos(\chi)$$
$$R_- = -\frac{\omega_0 - \frac{J}{\hbar}}{4c}[\vec{r}_{21} \cdot \vec{\mu}_1 \times \vec{\mu}_2] + \frac{1}{2}(\vec{\mu}_1 \cdot \vec{m}_1 + \vec{\mu}_2 \cdot \vec{m}_2) - \frac{1}{2}(\vec{\mu}_1 \cdot \vec{m}_2 + \vec{\mu}_2 \cdot \vec{m}_1)$$
$$= \mu_0 m_0 cos(\chi) - \mu_0 m_0 cos(\chi) = 0$$

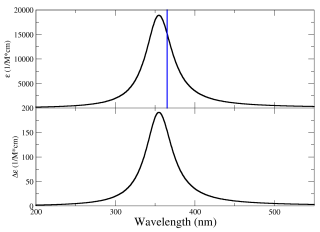

Figure 9.1: Upper panel: calculated absorption spectrum for a cofacial H-

μ_0 (D)	7
m_0 (a.u.)	1.5
$\hbar\omega_0$ (eV)	3.4
γ (eV)	0.04
r Å	7
χ (°)	45

Table 9.1: Molecular and geometrical paramaters relative to the H-dimer described in the text.

Eqs. 9.24 show the in-phase combination has twice the rotational strength of the monomer, while the out-of-phase combination has no rotational strength. While this could seem trivial, it should be underlined that the correct result can be obtained only if both intrinsic chirality and intermolecular $\mu - m$ contributions are accounted for. We calculate various contributions to the CD spectrum for a dimer with molecular and geometrical parameters reported in Tab. 9.1. The resulting absorption and CD spectrum are plotted in Fig. 9.1.

Fig. 9.2 shows that intrinsic chirality and intermolecular $\mu - m$ coupling contributions cancel out for the lower energy transition, while they sum for the higher energy transition, which has twice the monomer's rotational strength. Intermolecular μ-m coupling was deemed as not important in the original work by Kirkwood[216], while Condon recognized the need to go into detail with it[205], without further elaborating on the matter. The caveat is that, at least in the exciton model framework, intramolecular and intermolecular $\mu - m$ couplings should always be considered together in order to avoid unphysical results, i.e. getting a finite rotational strength for a completely dipole-forbidden band.

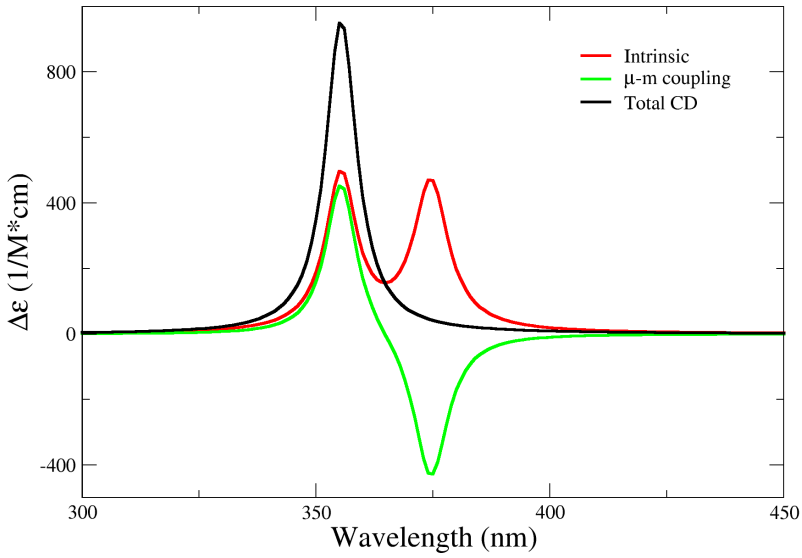

Figure 9.2: The various contribution to the CD spectrum of a cofacial H-dimer of chiral molecules.

For the spectra of Fig. 9.3 we employed the same geometrical and molecular parameters of Tab. 9.1, only with an additional shift of 5 Å between the molecules along the x direction. In order to have a sizeable splitting between exciton states even with increased distance, we additionally reduce r to 5 Å. With these geometrical parameters $J < 0$ and the dimer is classified as a J-dimer.

The $\mu - m$ and intrinsic chirality contributions strenghten each other for the lowest energy state, which is now the in-phase combination of basis states, $|\Psi_+\rangle$, while they cancel out exactly for the dipole-forbidden higher energy state $|\Psi_-\rangle$.

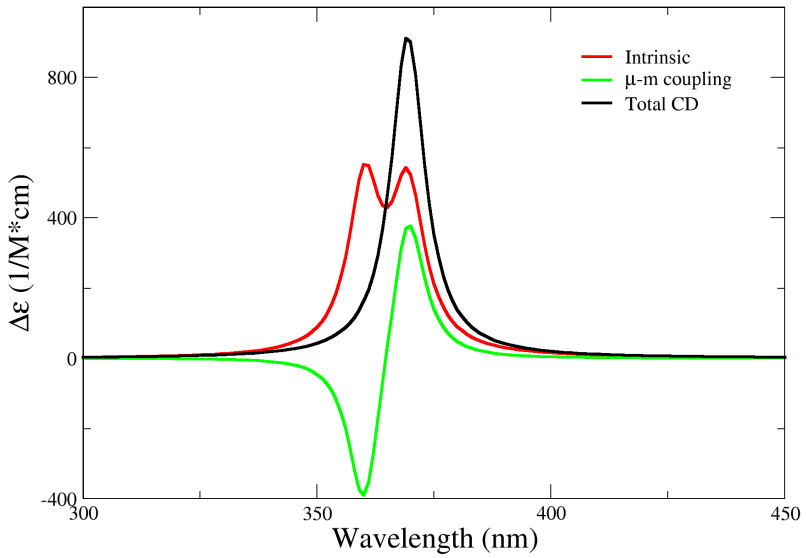

Figure 9.3: The various contribution to the CD spectrum of a J-dimer of chiral molecules.

Chiral dimer of non-chiral molecules Isolated molecules do not show optical activity if their ETDM and MTDM, even if sizeable, are orthogonal. A chiral dimer of non-chiral molecules can show anyway both $\mu - \mu$ and intermolecular $\mu - m$ coupling contributions to the CD spectrum. These contributions can have the same sign, therefore enhancing each other, or different signs[225]. To illustrate the concept, we build a dimer in which $\vec{\mu}_1$ lies along $(1,0,0)$ and $\vec{m}_1$ lies along the orthogonal direction $(0, cos(\phi), sin(\phi))$. $\vec{\mu}_2$ and $\vec{m}_2$ lie respectively along the $(cos(\theta), sin(\theta), 0)$ and $(-sin(\theta)cos(\xi), cos(\theta)cos(\xi), sin(\xi))$ mutually orthogonal directions. $\vec{r}_{21}$ is directed along the z axis as before, and the employed parameters are the same of Tab. 9.1. We calculate line and rotational strengths for the $|G\rangle$ to $|\Psi_+\rangle$ and $|\Psi_-\rangle$ transitions as:

$$
\begin{aligned}
D_+ &= \frac{1}{2}(\vec{\mu}_1 \cdot \vec{\mu}_1 + \vec{\mu}_2 \cdot \vec{\mu}_2) + \vec{\mu}_1 \cdot \vec{\mu}_2 = \mu_0^2(1 + cos(\theta)) \\
D_- &= \frac{1}{2}(\vec{\mu}_1 \cdot \vec{\mu}_1 + \vec{\mu}_2 \cdot \vec{\mu}_2) - \vec{\mu}_1 \cdot \vec{\mu}_2 = \mu_0^2(1 - cos(\theta))
\end{aligned} \tag{9.25}
$$

Eqs. 9.25 show that both states become partially allowed for $\theta \neq 0$. We then proceed to calculate rotational strengths for the two transitions as:

$$
\begin{aligned}
R_+ &= \frac{\omega_0 + \frac{J}{\hbar}}{4c}[\vec{r}_{21} \cdot \vec{\mu}_1 \times \vec{\mu}_2] + \frac{1}{2}(\vec{\mu}_1 \cdot \vec{m}_1 + \vec{\mu}_2 \cdot \vec{m}_2) + \frac{1}{2}(\vec{\mu}_1 \cdot \vec{m}_2 + \vec{\mu}_2 \cdot \vec{m}_1) = \\
&= \frac{\omega_0 + \frac{J}{\hbar}}{4c} r\mu_0^2 sin(\theta) + \frac{1}{2}\mu_0 m_0 sin(\theta)(cos(\phi) - cos(\xi)) \\
R_- &= \frac{\omega_0 + \frac{J}{\hbar}}{4c}[\vec{r}_{21} \cdot \vec{\mu}_1 \times \vec{\mu}_2] + \frac{1}{2}(\vec{\mu}_1 \cdot \vec{m}_1 + \vec{\mu}_2 \cdot \vec{m}_2) + \frac{1}{2}(\vec{\mu}_1 \cdot \vec{m}_2 + \vec{\mu}_2 \cdot \vec{m}_1) = \\
&= -\frac{\omega_0 - \frac{J}{\hbar}}{4c} r\mu_0^2 sin(\theta) - \frac{1}{2}\mu_0 m_0 sin(\theta)(cos(\phi) - cos(\xi))
\end{aligned} \tag{9.26}
$$

Eqs. 9.26 shows that the $\mu-\mu$ coupling and intermolecular $\mu-m$ coupling contribution have the same sign if $cos(\phi) > cos(\xi)$, have opposite sign if $cos(\phi) < cos(\xi)$ and the intermolecular $\mu - m$ coupling contribution vanishes for $cos(\xi) = cos(\phi)$. Fig. 9.4 shows calculations for a dimer with θ=45°, ϕ=30° and ξ=60°. In this case the μ-m coupling and μ-μ coupling contributions have the same sign and strengthen each other, as previously observed in literature[225].

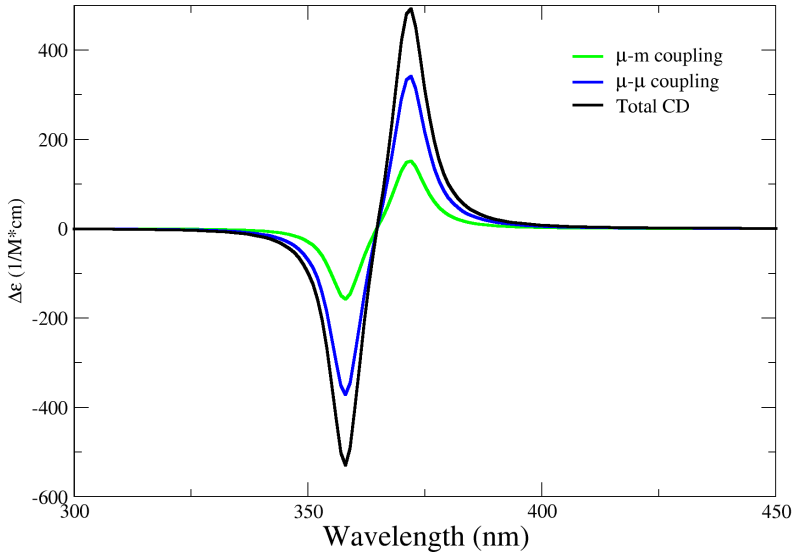

Figure 9.4: $\mu - m$, μ-μ contributions and total CD spectrum for the dimer described in the text, in the case the contributions have the same sign.

If ξ=30° and ϕ=60° the contributions have opposite sign and tend to cancel each other, as shown in Fig. 9.5.

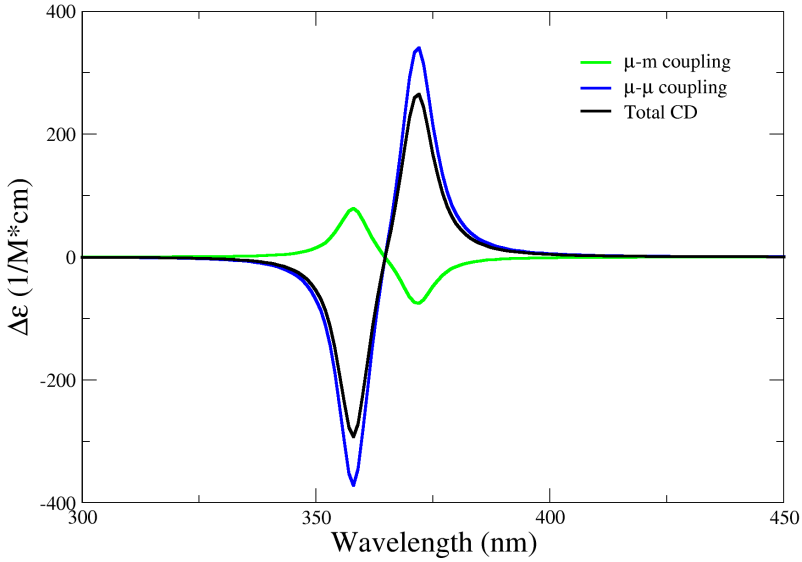

Figure 9.5: $\mu - m$, μ-μ contributions and total CD spectrum for the dimer described in the text, in the case the contributions have opposite sign.

If $\mu-\mu$ and intermolecular $\mu-m$ coupling contributions are opposite, the CD sign (i.e. the sign of the lowest energy CD peak) can be determined by the strongest one between them. In our particular case, we get that the contributions are equal when

$$\frac{\mu_0}{m_0} = \frac{|(cos(\phi) - cos(\xi))|2c}{r(\omega_0 - \frac{J}{\hbar})} \tag{9.27}$$

The $\frac{\mu_0}{m_0}$ ratio at which condition 9.27 is achieved depends:

- on the intermolecular distance r. As shown in section 9.2.1 the $\mu - m$ coupling contribution becomes more important at short distances.
- on the angles ξ and ϕ, i.e. the specific geometry of the dimer
- on the monomer absorption frequency ω_0 and the interaction energy J. Usually $J << \hbar\omega_0$, leading to the consideration that ω_0 plays the pivotal role. If ω_0 is higher the μ-μ coupling contribution is favoured.

We repeat the calculation of Fig. 9.5, but with m_0=3.8 a.u. and μ_0=4 D. The results in Fig. 9.6 show that the CD sign is now determined by $\mu - m$ coupling rather than μ-μ coupling. This could be a common occurrence for nominally forbidden transitions like $n \rightarrow \pi^*$ in systems presenting heteroatoms such as carbonyls and BODIPYs[225]. The application of the chirality rule, commonly used to assign the handedness of supramolecular aggregates, can be thwarted by the presence of sizeable MTDMs at the molecular level[226].

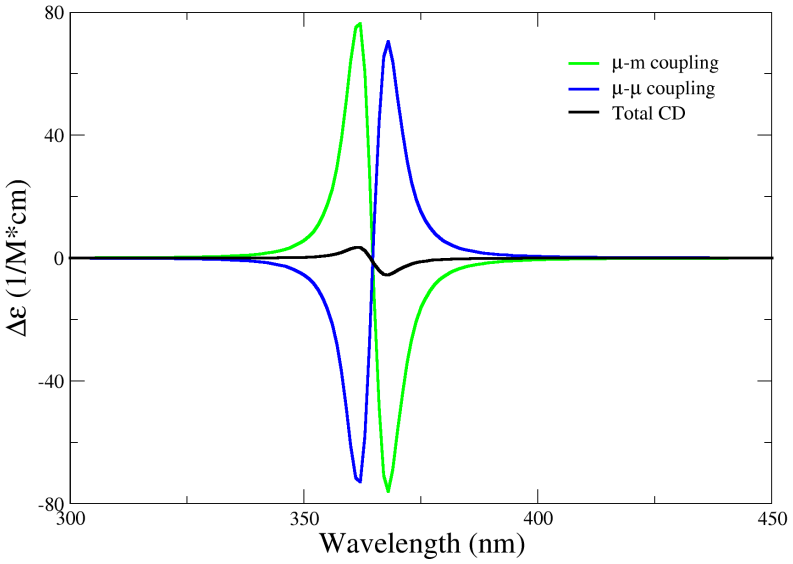

Figure 9.6: $\mu - m$, μ-μ contributions and total CD spectrum for the dimer described in the text, in the case the contributions have opposite sign and $\mu - m$ is the prevalent contribution.

9.3 Conclusion

In section 9.2.1 the general expressions for every contribution to the CD spectrum of a N-molecules aggregate were derived within an exciton model. We identify three possible contributions, namely $\mu - \mu$ coupling, intermolecular $\mu - m$ coupling and intramolecular $\mu - m$ coupling, the latter also referred to as "intrinsic chirality". Fundamental physical properties were derived for each contribution. In section 9.2.2 analytical closed expressions for a generic molecular dimer are obtained, and CD spectra are calculated for specific dimer geometries. The foremost conclusion is that all contributions are important to determine the aggregate overall CD spectrum and arbitrarily neglecting one of them leads to unphysical results. Furthermore, the role of MTDMs is shown to be important to determine the sign of the first Cotton effect of a molecular dimer, sending a strong warning about the applicability of chirality rule in systems with sizeable MTDMs.

Hierarchical Chiroptics in C8O3 Cyanine Aggregates

10

10.1 Introduction

Cyanines are a large family of dyes with remarkable aggregation behavior.[25, 55, 82, 83, 88] Among them, 3,3′-bis(2-sulfopropyl)-5,5′,6,6′-tetrachloro-1,1′-dioctylbenzimidacarbocyanine (C8S3) and 3,3′-bis(3-carboxy-n-propyl)-3,3′-di-n-octyl- 5,5′,6,6′-tetrachlorobenzimidacarbocyanine (C8O3) cyanines show an impressive propensity to form strongly coupled supramolecular aggregates in polar environments and in thin films.[287–290] In 1996, the spontaneous aggregation of C8O3 molecules into non-racemic chiral aggregates was observed, an astonishing result since the chromophoric core of the monomer, in its equilibrium geometry, is planar and non chiral.[291] The aggregation of C8O3 is hierarchical, with different structural features appearing in successive size scales:[292] monomers assemble into J-aggregates in the shapes of tubes, which in turn interweave to form bundles.[293–295] In each aggregation step, notable spectroscopic features appear, ascribed to a strong exciton coupling among the constituent units. Previous study from Thomas et al. revealed robust chiroptical responses through hierarchical aggregation of C8O3 in solution,[261] and a perfectly correlated g_{abs} and g_{lum}, for C8O3 bundles in films reaching an impressive g_{lum} of 0.08.[220] Moreover, several uncommon chiroptical features were uncovered. Specifically, individual C8O3 tubes displayed a single CD peak instead of the typical doublet indicative of exciton coupling,[57, 296, 297] leading to an apparent violation of the "sum rule". This rule, first enunciated by Condon,[205] states that the integrated area beneath a CD spectrum vanishes. Adding complexity to the problem, a CD doublet pattern appears for bundled aggregates, which also show a remarkable bisignate CPL, indicative of uncommon double emission at room temperature and anti-Kasha behaviour. Given their importance, these features need to be analyzed and understood.

Here we clarify the distinctive spectral characteristics exhibited by C8O3 aggregates and rationalize the chiroptical features present at each tier of the hierarchical structure in C8O3 aggregates. A bottom-up modeling approach is adopted,[54, 105, 115] as illustrated in the bottom panels of Fig.10.1. A joint analysis of experimental data and TD-DFT computational results leads to a reliable description and parametrization of a model for the C8O3 monomer. This model sets a reliable basis to construct a model for the aggregates in the tubular form and then the bundles as hierarchical assemblies of tubes. The multiscale theoretical protocol proposed in this work enables the investigation of the complex aggregation phenomena observed in C8O3 at different aggregation stages. The unusual spectral features observed in experimental spectra are addressed, providing a complete picture of the physical origin of these results.

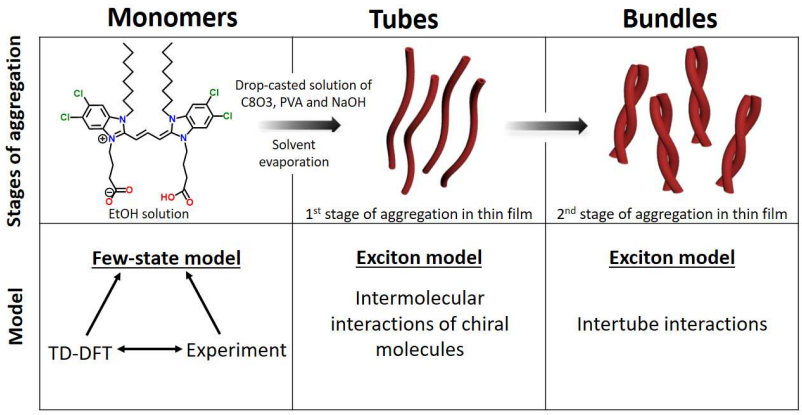

Figure 10.1: Upper panels: various stages of aggregation and relevant experimental conditions. Lower panels: theoretical models employed to describe each stage of aggregation.

10.2 Technical section

10.2.1 Geometries of C8O3 single tubes

Due to the cylindrical shape of the tubes,[293, 294] it is convenient to work with cylindrical coordinates. They define the position of the center of mass of each molecule in terms of the radial distance from the tube axis, ρ; the angle θ, which defines the position of the molecule in the XY plane perpendicular to the tube axis Z; the quota z, which is the position of the molecule along the tube axis. This set of coordinates is related to cartesian coordinates x, y, z by simple transformations as reported in Eqs. 10.1:

$$\begin{aligned} x &= \rho cos(\theta) \\ y &= \rho sin(\theta) \\ z &= z \end{aligned} \tag{10.1}$$

The center of mass of each cyanine is located in a point $\vec{r}$ on the surface of a tube of diameter d, so that $\rho = \frac{d}{2}$. The relevant cylindrical coordinates are:

$$\vec{r} = (\frac{d}{2}cos(\theta), \frac{d}{2}sin(\theta), z) \tag{10.2}$$

Cyanines are arranged in rings with the angular distance between two adjacent cyanines in each ring defined by θ'. Rings are stacked along the Z axis with spacing s and are mutually rotated around the Z axis by a twist angle ϕ.

Accordingly, setting the coordinates of the first cyanine as $(\frac{d}{2}, \frac{d}{2}, 0)$, the coordinates of the i-th cyanine in the j-th ring, $\vec{r}_{i,j}$ are:

$$\vec{r}_{i,j} = \left(\frac{d}{2}cos\big((i-1)\theta' + (j-1)\phi\big), \frac{d}{2}sin\big((i-1)\theta' + (j-1)\phi\big), (j-1)s\right) \tag{10.3}$$

The electric transition dipole moment, $\vec{\mu}$, oriented along the cyanine polymethine bridge, is tangent to the cylinder wall, forming a χ angle with the tube axis. In order to ensure orthogonality with the radius, $\vec{\mu}$ should lie along one of the unit vectors $(-\sin(\theta)\sin(\beta), \cos(\theta)\sin(\beta), \cos(\beta))$, with χ determining its component along the tube axis. This guarantees

the scalar product with the radius to be null, implying the dipole moment is tangent to the surface.

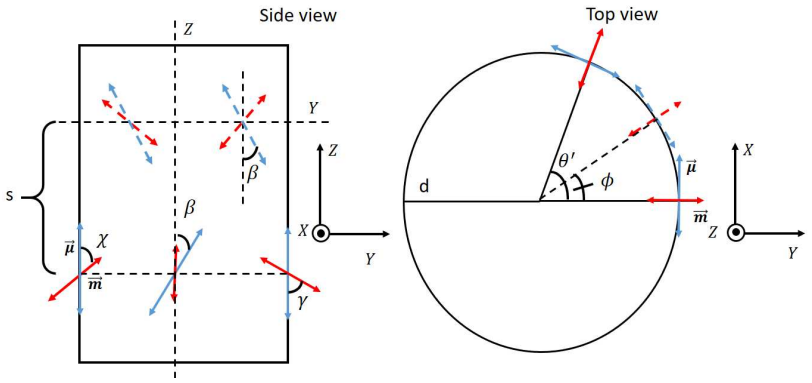

Figure 10.2: Side (left panel) and top (right panel) views of the tubular aggregate geometry, illustrating the various parameters. The electric and magnetic transition dipole moments are represented as blue and red double-headed arrows, respectively. The dipole moments of the upper row are represented as dashed lines in order to distinguish the rows in the top view.

In the "herringbone-like" tube geometry the electric dipole moments of the cyanines in the j-th circle form a β angle with positive direction of the tube axis, Z, while the electric dipole moments of cyanines in the $(j+1)$-th circle form the same angle with the opposite direction of the tube axis, and the ϕ rotation between stacked circles is equal to $\frac{\theta'}{2}$.

The direction of the magnetic transition dipole moment $\vec{m}$ is $(cos(\theta)sin(\gamma), sin(\theta)sin(\gamma), cos(\gamma))$, so that the scalar product between magnetic and electric transition dipole moments of each cyanine is proportional to $cos(\beta)cos(\gamma)$ and the angle between them, α, is $\alpha = arccos(cos(\chi)cos(\gamma))$. It should be noticed that the projections of $\vec{\mu}$ and $\vec{m}$ on the XY plane are orthogonal, thus ensuring the molecular chiroptical response is coupled to longitudinal modes only. We keep the α value close to that obtained by TD-DFT results (Tab. 10.3). All geometrical parameters employed to build the single tube are reported in Tab. 10.1 and illustrated in Fig. 10.2.

Parameter	Value
d	20 Å
θ'	30°
β	50°
γ	90.8°
α	90.5°
ϕ	15°
s	14 Å
N	240

Table 10.1: Geometrical parameters employed for C8O3 calculations.

10.2.2 Exciton Hamiltonian and calculation of spectra

To address optical spectra of the tube, we rely on the exciton model, where only states with a single excited molecule are considered. Specifically, $|n,i\rangle$ represents a state where the i-th molecule in the n-th unit cell (the unit cell consists of two adjacent molecules in consecutive rows, having opposite orientation with respect to the Z axis) is excited. The exciton Hamiltonian accounts for the electrostatic interactions between transition dipole moments: [297, 298]

$$H = E_0 \sum_{n,i} |n,i\rangle\langle n,i| + \sum_{n,m,i,j} J(n,i;m,j)|n,i\rangle\langle m,j| \qquad (10.4)$$

where E_0 is the monomer excitation energy and $J(n,i;m,j)$ is the electrostatic interaction between the electric transition dipole moments of the i-th and j-th molecules in the n-th and m-th unit cells, whose explicit form is given in Eq. 10.6. The aggregate Hamiltonian is written on the basis formed by the states $|n,i\rangle$, defined as the states where all molecules are in the ground state, but the i-th molecule in the n-th unit cell that is in the excited state. The exciton approximation neglects interactions

between states having different energies,[54, 105, 115] so that for an aggregate of N identical molecules the $N \times N$ Hamiltonian matrix is:

$$\hat{H} = \begin{bmatrix} E_0 & \dots & \dots & \dots & \dots & \dots \\ \dots & E_0 & \dots & J(n,i;m,j) & \dots & \dots \\ \dots & \dots & E_0 & \dots & \dots & \dots \\ \dots & J(m,j;n,i) & \dots & E_0 & \dots & \dots \\ \dots & \dots & \dots & \dots & E_0 & \dots \\ \dots & \dots & \dots & \dots & \dots & E_0 \end{bmatrix} \tag{10.5}$$

where E_0 is the monomer transition energy and the interaction energy $J(n,i;m,j) = \langle n,i|\,\hat{H}\,|m,j\rangle$ is expressed in the dipolar approximation as follows:

$$J(n,i;m,j) = \frac{1}{4\pi\epsilon_0\eta^2}\frac{\vec{\mu}_{n,i}\cdot\vec{\mu}_{m,j} - 3(\vec{\mu}_{n,i}\cdot\vec{n}_{m,j;n,i})(\vec{\mu}_{m,j}\cdot\vec{n}_{m,j;n,i})}{r^3_{m,j;n,i}} \tag{10.6}$$

where ϵ_0 is the vacuum dielectric constant, η is the medium refractive index at optical frequencies, $\vec{\mu}_{n,i}$ is the electric transition dipole moment vector of molecule i in the n unit cell, and $\vec{n}_{m,j;n,i}$ is the unit vector defining the distance between molecules i and j in unit cells n and m, its length being $r_{m,j;n,i}$. We set $\eta = 1.6$, as relevant for organic films[299].

The diagonalization of the Hamiltonian in Eq. 10.5 gives the eigenstates as a linear combination of the basis states:

$$|\Psi_k\rangle = \sum_{i,n} c_{n,i;k}\,|n,i\rangle$$

with $c_{n,i;k} = \langle n,i|\Psi_k\rangle$.

The electric transition dipole moment from the ground state $|G\rangle$ (the state where all molecules are in the ground state) to $|\Psi_k\rangle$ reads:

$$\langle G|\,\hat{\vec{\mu}}\,|\Psi_k\rangle = \sum_{n,i} c_{n,i;k}\vec{\mu}_{n,i} \tag{10.7}$$

The absorption spectrum is calculated assigning a Gaussian lineshape of appropriate bandwidth σ to each transition:

$$\epsilon(\omega) = \frac{N_A 4\pi\omega}{3\ln(10)\hbar c}10^{-3}\sum_k \frac{|\langle G|\,\hat{\vec{\mu}}\,|\Psi_k\rangle|^2 e^{-\frac{(\omega-\omega_k)^2}{2\sigma^2}}}{\sigma\sqrt{2\pi}} \tag{10.8}$$

where ω_k is the frequency of the transition from the ground state to $|\Psi_k\rangle$, c is the light velocity in vacuum and N_A is Avogadro's number.

As the tube axis is aligned along the Z direction, the longitudinal contribution to absorption can be calculated by considering the Z component of the electric dipole moment operator, as:

$$\epsilon_l(\omega) = \frac{N_A 4\pi\omega}{3\ln(10)\hbar c}10^{-3}\sum_k \frac{|\langle G|\,\hat{\mu}_Z\,|\Psi_k\rangle|^2 e^{-\frac{(\omega-\omega_k)^2}{2\sigma^2}}}{\sigma\sqrt{2\pi}} \tag{10.9}$$

The transverse contribution to absorption can be obtained by considering the components of the electric transition dipole moments perpendicular

to the Z direction. In particular:

$$\epsilon_t(\omega) = \frac{N_A 4\pi\omega}{3\ln(10)\hbar c} 10^{-3} \sum_k \frac{(|\langle G|\hat{\mu}_X|\Psi_k\rangle|^2 + |\langle G|\hat{\mu}_Y|\Psi_k\rangle|^2) e^{-\frac{(\omega-\omega_k)^2}{2\sigma^2}}}{\sigma\sqrt{2\pi}} \tag{10.10}$$

The magnetic transition dipole moment from the ground state $|G\rangle$ to $|\Psi_k\rangle$ is:

$$\langle G|\hat{\vec{m}}|\Psi_k\rangle = \sum_{n,i} c_{n,i;k}\vec{m}_{n,i} \tag{10.11}$$

The rotational strength associated to the $|G\rangle$ to $|\Psi_k\rangle$ transition reads:

$$R_k = \sum_{n,m,i,j} c_{n,i;k}c_{m,j;k}\left(\frac{\omega_k}{4c}(\vec{r}_{m,j;n,i}\cdot\vec{\mu}_{m,j}\times\vec{\mu}_{n,i}) + \vec{m}_{m,j}\cdot\vec{\mu}_{n,i}\right) \tag{10.12}$$

where the first term in brackets accounts for μ-μ coupling and the second for μ-m coupling and intrinsic chirality. The CD spectrum is finally calculated as[297]:

$$\Delta\epsilon(\omega) = \frac{N_A 16\pi\omega}{3\ln(10)\hbar c} 10^{-3} \sum_k \frac{R_k e^{-\frac{(\omega-\omega_k)^2}{2\sigma^2}}}{\sigma\sqrt{2\pi}} \tag{10.13}$$

In order to facilitate comparison with the experiment, the longitudinal mode has been assigned a bandwidth $\sigma = 0.014eV$ and the transversal mode a bandwidth $\sigma = 0.045eV$[298]. The exciton Hamiltonian can be diagonalized for very large systems (here we consider up to 240 molecules), to obtain relevant eigenstates, as entering the calculation of polarized absorption spectra.

10.3 Results and discussion

In section 10.3.1 we shortly summarize relevant experimental data, addressing the evolution of chiroptical data of C8O3 when going from solution to tubular aggregates and finally bundles.[220] The theoretical analysis begins in section 10.3.2 where a minimal model for the C8O3 dye is proposed and parametrized, relying on TD-DFT calculations on the distorted chromophoric core, as extracted from the crystal structure. The dyes are then assembled to form a tubular aggregate (section 10.3.3) whose spectral properties are analyzed relying on an exciton model for intermolecular electrostatic interactions. Finally, in section 10.3.4 a model is proposed for the bundle that quantitatively accounts for CD spectra and even more interestingly for the observation of a bisignated CPL feature.

10.3.1 Experimental data analysis

Our analysis mainly relies on experimental data collected in a previous study by Thomas et al. and Li et al.[220, 261] The preparation of a film of C8O3 aggregates begins by mixing a monomeric C8O3 solution (0.25 mM in ethanol) with an aqueous polyvinyl alcohol (PVA)/NaOH solution at a 1:1 volume ratio. The PVA/NaOH solution is made by combining

6 wt % PVA and 10 mM NaOH aqueous solutions, also in a 1:1 volume ratio. After dropcasting the resulting C8O3/PVA/NaOH mixture onto a glass substrate, solvent evaporation triggers a hierarchical aggregation process. This process initially forms tubular structures that subsequently intertwine to create bundles. (cf Fig.10.1). A comprehensive analysis of thin films of C8O3 aggregates exploiting Mueller polarimetry[261, 300] allowed for the artefact-free acquisition of absorption, emission, Circular Dichroism (CD), and Circularly Polarized Luminescence (CPL) spectra of the aggregates. Using a microscope objective within the Mueller setup, light could be focused on specific sample regions containing either individual tubes or bundles. Fig. 10.3 summarizes experimental (chiro)optical spectra obtained for the monomer in solution and for single tubes and bundles in thin films.

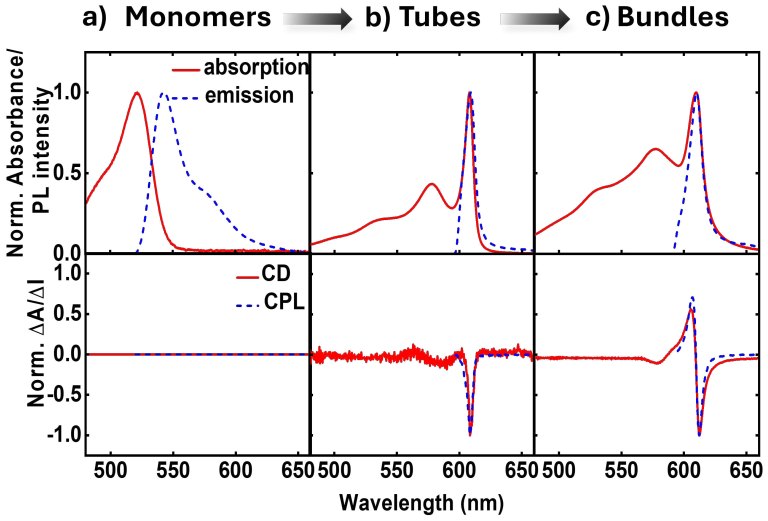

Figure 10.3: Experimental spectra of C8O3 monomer in ethanol (a), and of tubes (b) and bundles (c) in thin film. Top panels show normalized absorbance and emission spectra; bottom panels show normalized CD and CPL spectra. $\Delta A = A_L - A_R$ and $\Delta I = I_L - I_R$, where A is absorbance, I is emission intensity and the $L(R)$ subscript refers to left(right) circular polarization of incident light.

The main absorption peak shows a large red shift when going from solution (~ 520 nm) to the aggregates (~ 610 nm), indicative of strong J-aggregation, as further supported by the intense emission observed in the aggregates with negligible Stokes shift.[55, 77, 111] The narrowing of J-aggregates absorption is ascribed to the reduced electron-vibration coupling as due to exciton delocalization.[111] The absorption spectra of tubes and bundles show, besides the prominent sharp peak at 610 nm, a secondary less intense, broad peak at shorter wavelength (~ 575 nm). Linear dichroism measurements on oriented samples of tubular aggregates demonstrate that the main peak at 610 nm is polarized along the tube axis and is therefore termed the "longitudinal mode," while the 575 nm peak is attributed to a "transverse mode" with polarization perpendicular to the tube axis.[261, 301, 302]

Tubes and bundles have similar absorption and emission spectra, but qualitatively different chiroptical responses. Tubes exhibit monosignate CD and CPL spectra, peaking at the same wavelength as the longitudinal absorption peak. A very weak, bisignate signal can be noticed in the region of the transverse absorption band. On the opposite, bundles display an intense doublet both in CD and CPL spectra in the region of the longitudinal absorption maximum.

The monosignate feature observed in CD spectra of tubular aggregates is a notable chiroptical anomaly. Just as the intensity of an absorption

peak is quantified by its oscillator strength (proportional to the transition frequency times the squared electric transition dipole moment), the intensity of a CD peak is quantified by the associated rotational strength.[205] For a transition between the ground state $|g\rangle$ and an excited state $|f\rangle$, the rotational strength, R_{gf}, is

$$R_{gf} = Im(\langle g|\,\hat{\vec{\mu}}\,|f\rangle \cdot \langle f|\,\hat{\vec{m}}\,|g\rangle) \tag{10.14}$$

where Im takes the imaginary part of the argument and $\hat{\vec{\mu}}$ and $\hat{\vec{m}}$ are the electric and magnetic dipole moment operators, respectively. A theorem, originally derived by Condon[205], proves that the sum of the rotational strengths for all transitions and hence the integrated area beneath a CD spectrum (plotted against transition energies) must vanish. The sum of the rotational strengths on all the excited states is:

$$\sum_f R_{gf} = \sum_f \mathrm{Im}(\langle g|\,\hat{\vec{\mu}}\,|f\rangle \cdot \langle f|\,\hat{\vec{m}}\,|g\rangle) = \mathrm{Im}(\langle g|\,\hat{\vec{\mu}} \sum_f |f\rangle\langle f|\,\hat{\vec{m}}\,|g\rangle)$$

where $|g\rangle$ is the ground states and f runs on the excited states of the Hamiltonian. The sum can be extended to the ground state, since for any non-degenerate state $\langle g|\,\hat{\vec{m}}\,|g\rangle = 0$. The eigenstates of an Hamiltonian constitute a complete and orthonormal basis, so that, applying closure, eq. 10.3.1 becomes:

$$\sum_f R_{gf} = \mathrm{Im}(\langle g|\,\hat{\vec{\mu}} \cdot \hat{\vec{m}}\,|g\rangle) = 0$$

The above expression vanishes since the diagonal element of the Hermitian operator $\hat{\vec{\mu}} \cdot \hat{\vec{m}}$) is real.

Supramolecular chirality nicely illustrates this principle. Chiral aggregates usually show CD doublets attributed to an asymmetric arrangement of electric transition dipole moments, which leads to the CD contribution noted as μ-μ coupling.[205, 216, 225] The asymmetric arrangement of electric transition dipole moments within a chiral aggregate can be associated with an effective magnetic dipole moment so that the chiroptical effect can be described in terms of the rotational strength of Eq. 10.14. [203, 225] For a chiral dimer of interacting molecules, the $\mu - \mu$ coupling contribution to the rotational strength produces two peaks of opposite sign centered around the monomer absorption frequency, ω_0. [205, 297] The intensity of the two peaks approximately goes as $\pm\omega_0 \vec{r}_{12} \cdot (\vec{\mu}_1 \times \vec{\mu}_2)$, where $\vec{r}_{12}$ is the vector joining molecules 1 and 2, and $\vec{\mu}_{1/2}$ denotes the electric transition dipole moments of the molecules, confirming the sum rule at least in the limit of weak exciton coupling.* Even in larger aggregates, $\mu - \mu$ coupling results in CD doublets which approximately obey the sum rule.[57]

If the relevant transition of the monomer is characterized by a sizeable transition magnetic dipole moment besides the electric dipole moment,

* As discussed in Ref.[57], the intensity of the two CD peaks should read $\pm\omega_\pm \vec{r}_{12} \cdot (\vec{\mu}_1 \times \vec{\mu}_2)$, where $\omega_\pm$ defines the frequencies of the two exciton states. In the very weak coupling limit, the exciton splitting is tiny and the two frequencies can be approximated by ω_0, recovering the sum rule. More generally, it can be proved that, if the exciton model is extended to account for doubly excited states, i.e. relaxing the Heitler-London approximation, the sum rule is recovered without imposing any approximation on transition frequencies.[57]

additional contributions, due to $\mu - m$ coupling, appear that are particularly significant for weakly allowed transitions.[225] The $\mu - m$ coupling is defined intramolecular or intermolecular when it involves dipoles centered on the same or different molecules, respectively.[225] Intramolecular $\mu - m$ coupling implies sizeable electric and magnetic transition dipole moments on the same molecule, having components in common directions, and is only possible in inherently chiral molecules. Intramolecular $\mu - m$ coupling offers a possible explanation for the single CD peak in the spectrum of individual tubes.[205, 303] CD spectra of inherently chiral molecules are often characterized by a monosignated peak, the sum rule being satisfied by CD peaks located at high energies, outside the conventional spectral window of analysis.[304]

C8O3 molecules can exist in twisted conformations due to the formation of intramolecular hydrogen bond between carboxylic groups,[293] but the absence of optical activity in solution indicates rapid interconversion processes between enantiomers. On the other hand, when a twisted C8O3 molecule is stuck within an aggregate, steric constraints may prevent the interconversion, giving rise to a neat chiroptical response, consistent with our recent experimental results.[261] Support for this hypothesis comes from spectra collected from aggregates in thin film upon heating at 388 K to disrupt the supramolecular organization. In these conditions, the absorption spectrum closely resembles the monomer spectrum in ethanol (Fig. 10.3), supporting the disaggregation of the tube, but a faint monosignated CD peak emerges near the monomer absorption region (Fig. 10.4), suggesting that chiral monomers are freed upon the disassembly of bundles and tubes, allowing for the acquisition of their chiroptical response prior to racemization.The absorption and CD spectra of Fig. 10.4 closely resemble those reported in Fig. 3(B) and (G) of Ref.[261], acquired in the early stages of C8O3 aggregation.

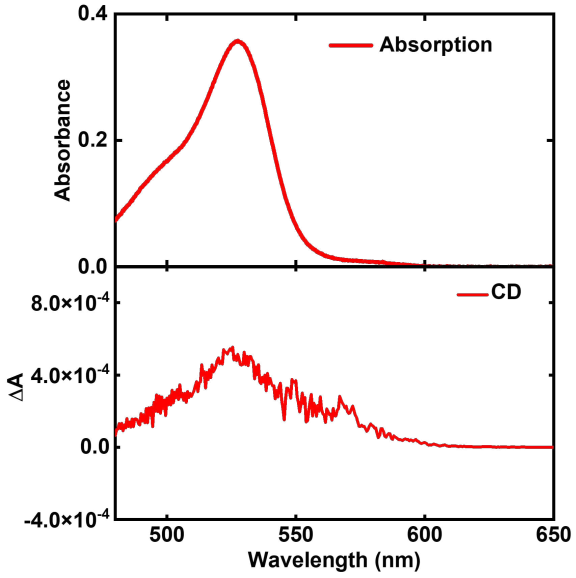

Figure 10.4: Absorption (upper panel) and CD spectrum (lower panel) of C8O3 aggregates in thin film, after they have been heated progressively to 388 K until the aggregates are disassembled.

While the CD signal of Fig. 10.4 could be due to the presence of small clusters of poorly interacting chiral C8O3 molecules, we point out that the racemization process of isolated C8O3 molecules can be slower in the film than in ethanol solution, since ethanol competes with the formation of

intramolecular hydrogen bonds[40, 41], speeding up the interconversion between enantiomers. In any case, the monosignate CD spectrum of Fig. 10.4 can only derive from intrinsic chirality of C8O3 molecules.

As demonstrated by the statistical analysis in Ref. [220], the sign of CD spectra for C8O3 aggregates can differ among different samples and even in different zones of the same sample. This suggests that the chirality of monomers, released upon disrupting the aggregates, also varies within the sample, depending on the chirality of the original aggregates.

10.3.2 C8O3 monomer: the model

C8O3 (Fig. 10.3a) is an amphiphilic cyanine dye with a positively charged Cy3 polymethinic bridge, long alkylic C8 chains linked to one nitrogen of the benzimidazolium rings, and C3 chains ending with carboxylic groups linked to the opposite nitrogen atom. In the crystal structure,[293] two distinct configurations of C8O3 chromophoric cores, planar and twisted, are observed. The side carboxylic groups of C8O3 are prone to form intra and intermolecular hydrogen bonds, affecting the geometry of the chromophoric core. Specifically, molecules forming intermolecular hydrogen bonds show planar cores, while those forming intramolecular hydrogen bonds show a twisted core, with an 18° dihedral angle between the cyanines' benzimidazolium rings (D in Fig. 10.5). While the whole crystal is a racemate, the distorted monomers in the crystal structure of C8O3, exhibit the axial chirality typical of biaryls.[159] TD-DFT calculations are carried out for the S-axial (S_a) enantiomer of chiral C8O3 core, sketched in Fig. 10.5.

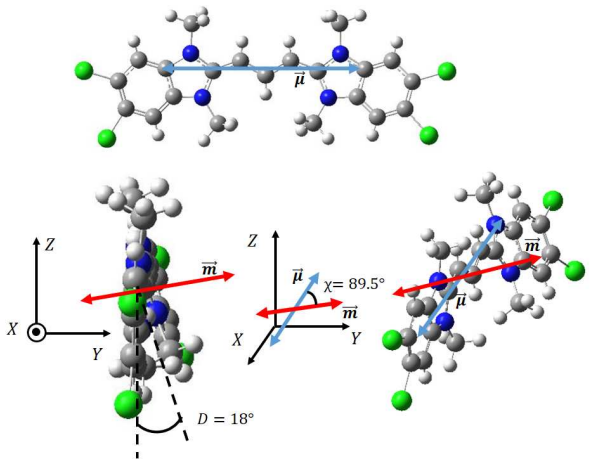

Figure 10.5: Upper panel: front view of C8O3 chromophoric core, where the electric transition dipole moment $\vec{\mu}$ is visible as a double headed blue arrow. Left lower panel: side view of twisted C8O3 chromophoric core, where the magnetic transition dipole moment $\vec{m}$ is visible as a double-headed red arrow. Right lower panel: the molecular reference system is rotated to showcase the orientation of both the electric and magnetic transition dipole moments.

According to TD-DFT calculations (B3LYP, 6-31G(d), Gaussian 16 suite[259]) on the twisted chromophoric core, in the geometry extracted from the crystal structure, the lowest energy transition has sizable and non-orthogonal electric and magnetic dipole moment (angle $\chi = 89.5°$, right lower panel of Fig. 10.5)), resulting in a rotational strength of 12.95 (10^{-40} c.g.s. units) associated with a monosignate positive peak in the CD spectrum. Of course, the enantiomer has the opposite sign with a $\mu - m$ angle of 90.5°. Additional details, including results for the higher energy excited states and a comparison with the planar chromophoric core, can be found in Tabs. 10.2 and 10.3. The rotational strength associated with the

second excited state (Tab. 10.3) is negligible, suggesting the absence of an opposite sign CD peak within the spectral window of interest.

We run TD-DFT calculations (B3LYP,6-31G(d)) on (a)the twisted chromophore structure as extracted from crystallographic data and (b) a planar chromophoric core whose geometry was optimized at the DFT level (same functional and basis set). In both geometries the first excitation at $\sim$ 2.87 eV is a bright HOMO-LUMO transition.(Fig. 10.6), with a transition electric dipole moment $\mu \sim 13$ D, polarized along the polymethinic bridge, and a sizeable transition magnetic dipole moment $m \sim 1.4$ and 1.5 atomic units, for the twisted and planar geometries respectively.

The magnetic dipole moment is perpendicular to the cyanine π-conjugated system for the planar non-chiral core, while the magnetic and electric dipoles form a 89.5° angle in the twisted chiral system (Tab. 10.3 and lower panel of Fig. 3). The second excited state is dark and is located much higher in energy, at 3.83 eV[55, 94, 96]. More information about excited states of the planar C8O3 are reported in Tab. 10.2.

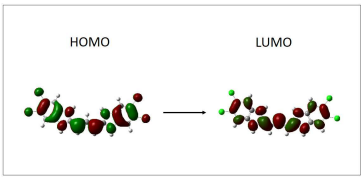

Figure 10.6: Orbitals involved in the lowest lying (HOMO-LUMO) transition for the planar chromophoric core of C8O3. Orbital contribution does not significantly vary for the twisted C8O3.

Table 10.2: TD-DFT results for the first two excited states of planar C803. f and R indicate the oscillator and rotational strengths, respectively.

State	Transition energy (eV)	μ (D)	m (atomic units)	μ-m angle	f	R (10^{-40} c.g.s.)
1	2.87	13	1.5	90°	2	0
2	3.85	0	0	/	0	0

Table 10.3: TD-DFT results for the first two excited states of twisted C803. f and R indicate the oscillator and rotational strengths, respectively.

State	Transition energy (eV)	μ (D)	m (atomic unit)	μ-m angle	f	R (10^{-40} c.g.s.)
1	2.88	13	1.4	89.5°	2	12.95
2	3.85	0	0	/	0	0

In order to build the exciton model for the aggregates, as described in subsections 10.3.3 and 10.3.4, we parametrize the lowest energy transition of the C8O3 dye. Specifically, from the energy and integrated area[305] of the absorption spectrum of Fig. 10.3 we estimate the monomer transition energy as 2.37 eV and the transition electric dipole moment as 9.6 D (molar extinction coefficient was taken from Ref. [294]). The magnetic transition dipole moment is estimated from TD-DFT as 1.4 a.u. (that is $2.6 * 10^{-23} J/T$ in SI) with a μ-m angle of 90.5°. With this information, absorption and CD spectra of the distorted monomer (as extracted from the crystal structure) are calculated as shown in Fig. 10.7.

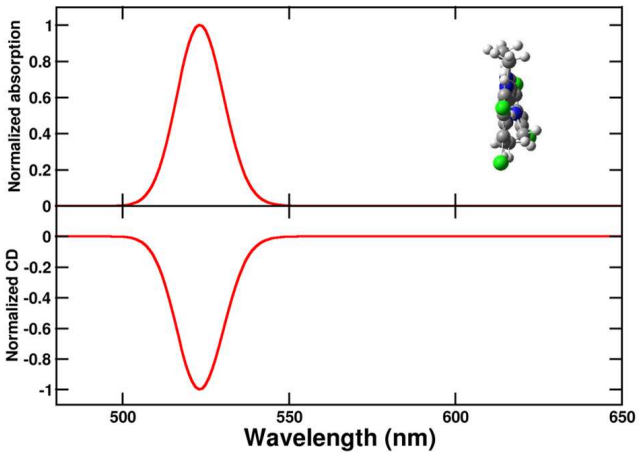

Figure 10.7: Normalized absorption (upper panel) and circular dichroism (CD, lower panel) spectra of the distorted C8O3 chromophoric core. A single transition is considered for the monomeric unit (see text), with a Gaussian bandshape and a width $\sigma = 0.045$ eV (cf Eq. (10.8).

Calculated spectra of Fig. 10.7 are in qualitative agreement with the high-temperature experimental spectra of Fig. 10.4. The spectra calculated for a planar chromophoric core are shown in Fig. 10.8 for comparison.

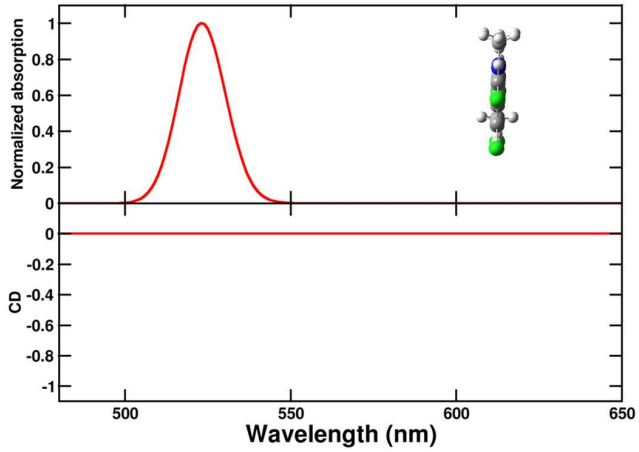

Figure 10.8: Normalized absorption (upper panel) and circular dichroism (CD, lower panel) spectra of the planar C8O3 chromophoric core. Spectra are broadened using a gaussian bandwidth σ = 0.045 eV, according to Eq. (10.8).

While the absorption spectrum does not significantly depend on the chromophoric core conformation, the CD spectrum vanishes for the planar core.

10.3.3 The C8O3 single tube

Having parametrized the monomeric unit, we use it as a building block to construct a plausible supramolecular structure for the C8O3 single tube. The tubes of C8O3 are made of two concentric bilayers, separated by the interpenetrated C8 alkyl chains.[293] The interaction between the cylindric walls was shown to be negligible in similar aggregates,[298] the overall spectrum being the sum of the spectra of each wall. Accordingly, to simulate the spectra, we consider a single cylindric wall, with a diameter d=2 nm, close to the experimental value of the diameter of the inner wall.[295] The "bricklayer" structure proposed in previous works to rationalize the (chiro)optical properties of C8O3 aggregates[287, 306–308] would result in an overall chiral arrangement of the transition electric dipole moments and hence in a strong μ-μ coupling contribution[306] whose characteristic bisignate CD feature is not observed for C8O3 tubular aggregates (cfr Fig. 10.3). Moreover, the bricklayer structure does not account for the presence of absorption bands with different polarization.[298] Quite interestingly, in Ref. [298] a herringbone structure was proposed for tubular aggregates of a similar cyanine dye, C8S3, where *two molecules per unit cell* are considered, as needed to account for the presence of absorption bands with different polarization. Here we adopt the same arrangement for the C8O3 chromophores inside the walls, further extending the model to describe the chiroptical properties of the supramolecular assembly.

The tube is constructed from a planar herringbone lattice with two molecules per unit cell (the unit cell is highlighted in red in Fig. 10.9) that is then folded along vector $\vec{a}$, to obtain a non-chiral cylinder (see Fig. 10.9), in close analogy with the arrangement of "zigzag" carbon nanotubes[309]. Within the tube, cyanines are arranged in rows (from bottom to top in

Fig. 10.9). Cyanines in the r-th row are oriented in such a way that their long axis makes an angle β with respect to the tube axis (z), cyanines in the $(r+1)$-th row form the same angle with $-z$. The transition electric dipole moment of each molecule (aligned with the polymethine bridge) is tangent to the cylinder surface. The magnetic transition dipole moments form an angle of 90.5° with the electric dipole moments, hence making the molecules chiral, as discussed in section 10.3.2.

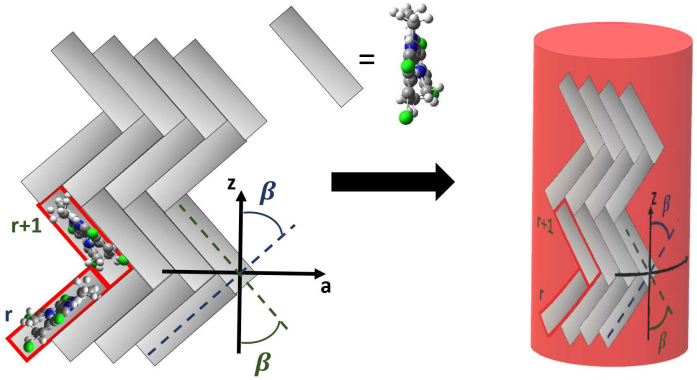

Figure 10.9: The herringbone 2D-lattice of C8O3, where cyanines in the r-th row form a β angle with the positive direction of the Z axis and cyanines in the $r+1$-th row form the same angle with the opposite direction of the Z axis (left), is folded to obtain a tube, with Z becoming the tube axis (right).

While C8O3 solutions do not show optical activity due to rapid interconversion between enantiomers,[220] sterical constraints within the tubes may prevent interconversion, keeping the molecules in a fixed conformation and leading to a neat chiroptical response. Moreover, the presence of a distorted C8O3 unit can induce distortions in neighboring monomers, in the so-called *sergeant and soldiers* chirality amplification mechanism[310]. Specifically, a distorted monomer may induce similar distortion in adjacent monomers, without necessarily transferring chirality to the supramolecular level, i.e. maintaining a non-chiral supramolecular organization.

To address optical the spectra of the tube, we rely on the exciton model, where only states with a single excited molecule are considered. Specifically, $|n,i\rangle$ represents a state where the i-th molecule in the n-th unit cell is excited. The exciton Hamiltonian accounts for the electrostatic interactions between transition dipole moments: [297, 298]

$$H = E_0 \sum_{n,i} |n,i\rangle\langle n,i| + \sum_{n,m,i,j} J(n,i;m,j)|n,i\rangle\langle m,j| \tag{10.15}$$

where E_0 is the monomer excitation energy and $J(n,i;m,j)$ is the electrostatic interaction between the electric transition dipole moments of the i-th and j-th molecules in the n-th and m-th unit cells, whose explicit form is given in Eq. 9.2. As discussed in section 10.2.2, the exciton Hamiltonian can be diagonalized for very large systems (here we consider up to 240 molecules), to obtain relevant eigenstates, as entering the calculation of optical spectra.

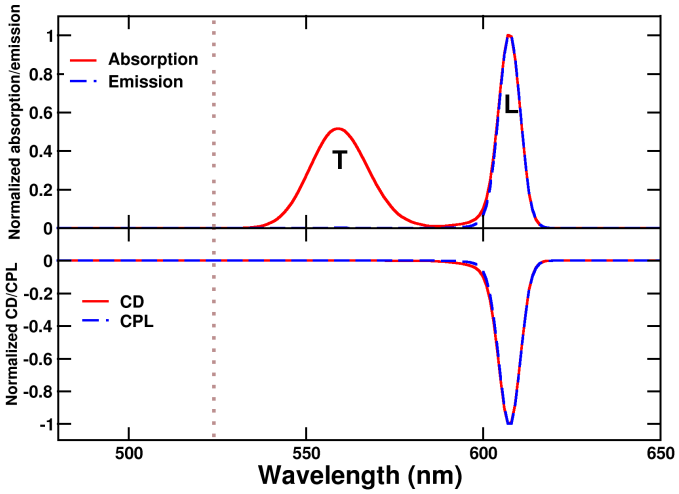

Figure 10.10: Spectra calculated for a single C8O3 tube. Upper panel: Normalized absorption and emission spectra, L and T respectively stand for "transverse" and "longitudinal". Lower panel: calculated CD and CPL spectra.

The absorption spectrum of the tube features two bands, both red-shifted with respect to the monomer. The more intense and red-shifted band ($\lambda_{max} \sim 607$ nm) is longitudinally polarized, while the higher energy band ($\lambda_{max} \sim 560$ nm) has transverse polarization. The presence of two molecules per unit cell allows for two absorption bands with different energies and polarization. In contrast, a "bricklayer" model with one molecule per unit cell would results in all bands sharing the same polarization.[298]

As the overall arrangement of electric transition dipole moments within the herringbone structure is symmetric, the μ-μ coupling contribution vanishes, and the CD spectrum features a single peak in the region of the longitudinal absorption band, well in line with experimental data of Fig. 10.3. Emission and CPL signals occur at the same frequency as the lowest transition observed in absorption and CD spectra, in line with the Kasha's rule. For these aggregates, the absorption and emission dissymetry factors are very similar, pointing to negligible geometrical rearrangement upon excitation.[220] Accordingly, we estimate the two dissimetry factors for the Kasha's state as[311, 312] $g_{abs/lum} = 4\frac{R}{D}$, where R and D are the rotational strength and squared electric transition dipole moment, respectively, associated with the transition from the ground state to the Kasha state. Our estimate of the dissymmetry factor amounts to $\sim 2 \times 10^{-4}$, much smaller than the experimental value ($\sim 10^{-2}$). This important discrepancy suggests that monomers could have a much more distorted structure inside the tubes than in the crystals.[261] Interestingly, small chiral distortions of the herringbone geometry lead to small $\mu - \mu$ coupling contributions, and tiny doublets appear in the CD spectrum in the region of the transverse mode (Fig. 10.11), in fairly good agreement with experimental observation (Fig. 10.3).

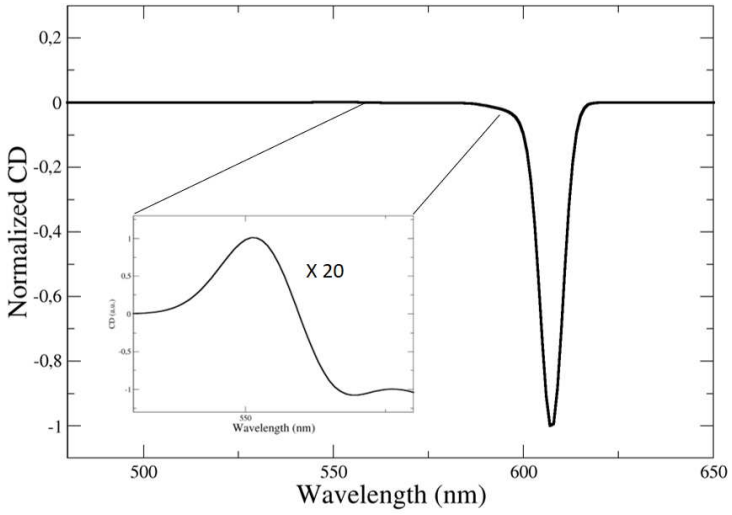

Figure 10.11: CD spectra of a single tube calculated for a distorted herringbone with ϕ=23°. The $\mu - \mu$ coupling contribution which appears at lower wavelengths is amplified in the inset.

10.3.4 The C8O3 bundle

Bundles, which are made out of two or more interwoven weakly interacting tubes,[261, 295] represent a further tier in the hierarchical aggregation of C8O3. The simplest model for a bundle accounts for a pair of tubes, each parametrized as described in Section 10.3.3. The two tubes, at distance l, are arranged with their axes both perpendicular to the vector that joins them and are mutually rotated by an angle Φ, as shown in Fig. 10.12. The bundle is chiral for $0° < \Phi < 90°$, with the corresponding enantiomeric structures having $-90° < \Phi < 0°$. Calculations were performed for a bundle with inter-tube distance $l = 40$ Å and rotation angle Φ=50° (representing a left-handed screw as in Fig. 10.12). These values were chosen in order to reproduce the energies and relative intensities of the CD and CPL peaks measured experimentally [220]. Absorption, emission, CD, and CPL spectra of the bundle are shown in Fig. 10.13. In order to account for the thermal population of the first two excited states, emission ($I(\omega)$) and CPL ($\Delta I(\omega)$)spectra are calculated as follows:

$$I(\omega) \propto \omega^3 \sum_k e^{-\frac{E_k - E_1}{k_b T}} \frac{|\vec{\mu}_k|^2 e^{-\frac{(\omega-\omega_k)^2}{2\sigma^2}}}{\sigma\sqrt{2\pi}} \tag{10.16}$$

$$\Delta I(\omega) \propto \omega^3 \sum_k e^{-\frac{E_k - E_1}{k_b T}} \frac{R_k e^{-\frac{(\omega-\omega_k)^2}{2\sigma^2}}}{\sigma\sqrt{2\pi}} \tag{10.17}$$

where k_b is Boltzmann constant and $T = 300$ K. k runs on the excited states, E_k, $|\vec{\mu}_k|^2$ and R_k (see definition in Eq. 10.12) are respectively the energy, squared electric transition dipole moment and rotational strength associated to the transition from the ground state to the k-th excited state. Finally, E_1 is the energy of the Kasha state. The dependence of both spectra upon ω^3 is a consequence of the isotropic character of the emission.

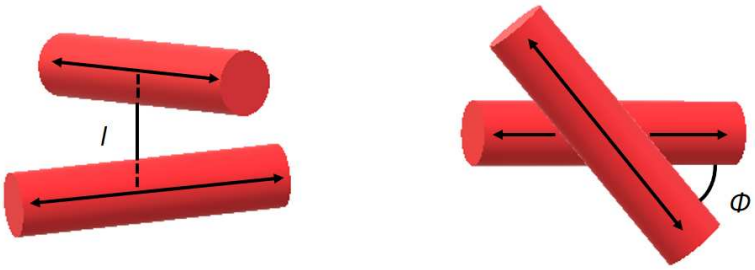

Figure 10.12: Side view (left panel) and top view (right panel) of the geometry for the bundle model, where each tube is represented by a red cylinder.

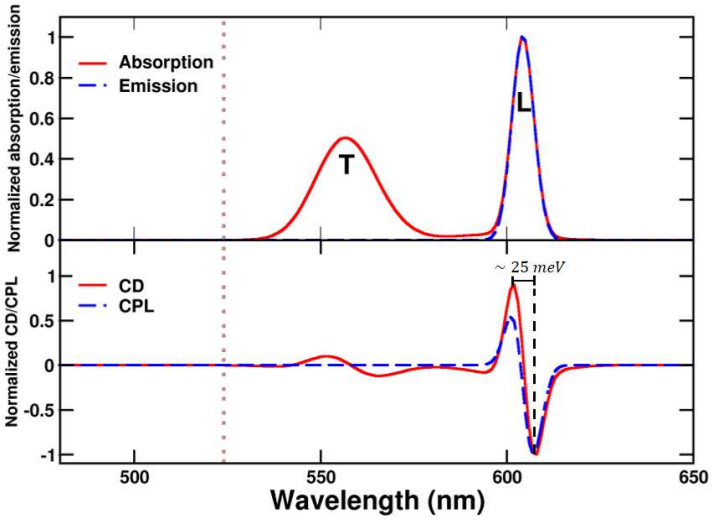

Figure 10.13: Spectra calculated for the bundle of C8O3. Upper panel: Normalized absorption and emission, L and T indicate bands that stem respectively from the coupling between longitudinal and transverse modes of the tubes. Lower panel: CD and CPL. Spectra are calculated for a left-handed bundle, with l=40 Å and $\Phi = 50°$. CD and CPL spectra are computed according to Eqs. (10.13) and 10.17. Of course, calculations for the corresponding right-handed bundle give CD and CPL spectra of opposite signs.

While absorption and emission spectra show no significant deviation from those of a single tube (Fig. 10.10), the CD spectrum of the bundle exhibits two doublets arising from the longitudinal (L) and transverse (T) modes of the tubes, with the longitudinal doublet largely dominating the overall spectrum. The appearance of doublets in the CD spectrum of the bundle is ascribed to μ-μ coupling between the modes of the two interwoven tubes that form a left-handed screw.[296] The μ-μ coupling contribution becomes predominant with respect to the intrinsic chirality present at the molecular level. These features are in very good agreement with the intense CD doublet, centered around the single tube CD peak, in the experimental spectrum of the bundle (Fig. 10.3).

The anomalous observation of a bisignate CPL feature in Fig. 10.3 deserves some discussion. As already mentioned in Ref. [220] a plausible explanation relies on a significant thermal population of an additional state besides the Kasha state, as expected if the energy difference between the two states is comparable to the thermal energy. Upon optical excitation, the system undergoes internal conversion eventually reaching the Kasha state, where it stays long enough to reach thermal equilibrium.[313] If excited states lie close to the Kasha state, their thermal population is responsible for the observation of anomalous (non-Kasha) emission .[314] In the case of the bundle geometry defined above, the calculated interaction between longitudinal modes results in a very small exciton splitting (~ 1 meV), smaller than thermal energy at room temperature (~ 25 meV). Accordingly, both exciton states are sizably populated, leading to the bisignated CPL observed experimentally.[220] We emphasize that the energy gap between the two exciton states is significantly smaller

than the gap estimated from the difference between the energies of the positive and negative peaks in the CPL (or CD) spectra (amounting in this case to ~ 25 meV). Indeed, when the separation between the two exciton states is tiny, positive and negative signals cancel each other, widening the apparent gap. The calculated dissymmetry factor g_{lum} is approximately 0.08, closely matching the experimental factor.

The $\mu - \mu$ coupling contribution arising from the interaction between the longitudinal modes of the tubes results in highly intense CD and CPL signals, despite the partial cancellation of peaks due to the low exciton gap. Notably, the rotational strength per monomer in the bundle increases by a 50-fold factor compared to that in the tube, where chirality is solely attributed to the monomer distortion.

10.4 Conclusions

In this work a bottom-up theoretical approach is presented to elucidate the chiroptical properties of C8O3 aggregates, tracking their evolution across different stages of hierarchical aggregation, from monomers to tubular aggregates and from tubular aggregates to bundles.

The C8O3 chromophoric core is planar in its equilibrium geometry, but it can be twisted following the formation of intramolecular hydrogen bonds between the side carboxylic groups, inducing axial chirality. While a distinct CD signal is not observed in solution, due to the rapid interconversion between enantiomers, the conformational constraints in the tubular aggregates result in a neat chiroptical response. Within the walls of tubular aggregates, C8O3 dyes adopt a herringbone-like arrangement, leading to the emergence of two distinct absorption bands with orthogonal polarization, namely the longitudinal and transversal modes. The singular CD peak exhibited by C8O3 tubular aggregates directly reflects the intrinsic chirality of the monomers, whereas the herringbone arrangement within the tube is non-chiral, leading to a vanishingly small $\mu - \mu$ coupling contribution, thus explaining the monosignate CD spectral feature.

The C8O3 bundle is modeled as a chiral dimer of tubular aggregates, wherein the restoration of a CD doublet shape arises from $\mu - \mu$ coupling interactions between the excitations of constituent tubes. The weak electrostatic interaction between the tubes results in an exciton splitting smaller than thermal energy at room temperature. As a consequence, two excited states can be significantly populated according to a Boltzmann probability distribution, yielding the distinctive anti-Kasha bisignated CPL shown by the bundles. The large CD and CPL signals are attributed to the remarkably large transition dipole moments of the tubes within the bundle, and to the narrow bandwidth that reduces their partial cancellation. Our analysis explains the origin of the remarkably high g_{lum} value ($\sim 10^{-1}$) measured for the bundles. Indeed, we are able to reproduce it accounting for the electrostatic interaction between tubular aggregates that are organized in a chiral fashion. The tubes themselves are aggregates and, more specifically, J-aggregates and their enormous transition dipole moments explain the amplified dissymmetry factors of

the bundles. In other terms, the bundles are aggregates of J-aggregates, which leads to large chiroptical responses.

The availability of a large set of reliable experimental data on aggregates of C8O3 at various stages of the aggregation process offers a solid basis to develop detailed models for supramolecular chirality, a challenging but extremely rewarding endeavor. Specific information on the aggregate geometry can indeed be extracted from the analysis of experimental spectra and solid structure-property relationships can be extracted at the supramolecular level with the potential to offer reliable guidelines towards the design of novel nanostructured materials with amplified CD and CPL responses.

General conclusions

This thesis demonstrates how supramolecular aggregation profoundly influences the optical and chiroptical properties of molecular systems, presenting pathways for their use in advanced functional applications, including sensing and CPL. The integration of theoretical modeling with experimental validation has proven to be a robust approach to rationalizing material properties and potentially predicting the behavior of new materials. Designing aggregates with targeted optical and functional properties, such as sensing or stimuli-responsive behaviors, can be achieved through rationally controlled ground-state interactions, including electrostatic forces and hydrogen bonding. By tailoring these interactions, one can influence the equilibrium geometry of aggregates, thus guiding their optical responses and enhancing their functionality. A key contribution of this work is the demonstration of the general applicability of the exciton model framework, which reliably describes and predicts optical and chiroptical properties across a wide variety of supramolecular aggregates, if properly applied. This broad applicability offers a solid theoretical foundation to investigate similar behaviorin other molecular systems, guiding synthetic efforts toward the rational design of aggregates with specific, sought properties. This thesis also deals with chirality at both molecular and supramolecular levels. A central focus for the scientific community remains the design of materials with maximal CPL efficiency. Here, we propose two promising approaches: at the molecular level, extending π-conjugated systems to enhance and favorably align electric and magnetic transition dipole moments; at the supramolecular level, fostering hierarchical chiral aggregation to yield larger, chiral superstructures with amplified chiroptical properties. Together, these findings underline the potential of supramolecular design, guided by proper modeling, as a powerful tool for engineering responsive, optically active materials with applications spanning advanced sensors, chiral photonics, and next-generation CPL emitters.

Experimental Part

Dynamic Light Scattering (DLS)

Dynamic light scattering (DLS) is a technique used to analyze colloidal systems and particles ranging in size from a few nanometers to several micrometers. It works by measuring the time-dependent fluctuations in the light scattered by particles in Brownian motion, which occurs due to collisions with solvent molecules. The data collected is processed through autocorrelation analysis to determine the particles' diffusion coefficient (D) by fitting the autocorrelation function to a mathematical model. Using the Stokes-Einstein equation, the particle size is then calculated as the hydrodynamic diameter d_h:[315]

$$D = \frac{k_b T}{3\pi d_h \eta}$$

where T is the temperature, k_b is the Boltzmann constant, and η is the medium viscosity. The hydrodynamic diameter (d_h) represents the diameter of a sphere that has the same translational diffusion coefficient as the particle being measured. This effective size parameter reflects how the particle diffuses in a fluid, considering its translational motion and interactions with surrounding solvent molecules. As a result, DLS measurements capture not only the particle's actual size but also factors such as its hydration shell and the medium's composition, including the presence of ions and surface structures.

DLS measurements were performed at 25 °C with a Malvern Zetasizer Nano ZSP apparatus equipped with a 633 nm HeNe laser (Malvern Instruments, Malvern, UK). The backscattering mode (scattered light is collected at an angle of 173°) was employed for all the analyzed samples.

In the case of samples that absorb light at 633 nm the Malvern Zetasizer Nano ZSP equipment cannot be employed, especially if they are fluorescent.

Absorption and fluorescence measurements

Solutions for spectroscopic measurements were prepared using spectrophotometric or HPLC-grade solvents. UV-vis absorption measurements were performed with a PerkinElmer Lambda650 double beam spectrophotometer, while emission/excitation spectra were recorded with an FLS1000 Edinburgh fluorometer
All fluorescence spectra were obtained from diluted solutions (absorbance < 0.1) and duly corrected for the excitation intensity and detector sensitivity.

Fluorescence quantum yields (ϕ) were measured employing quartz cuvettes (1 cm optical path) and fluorescein in $NaOH_{aq}$ 0.1 M (ϕ = 0.90) as reference, using the following equation:

$$\phi = \phi_{ref} \frac{A_{ref}}{A} \frac{E}{E_{ref}} \frac{\eta}{\eta_{ref}}$$

where A is the absorbance, E is the integrated corrected emission intensity, and η is the refractive index of the solvent. The subscript "ref" is related to the properties of the reference, while all the others terms refer to the sample. For fluorescence quantum yield, an error of ±10% is assumed.[316]

Two-Photon Microscopy setup

All TPA and TPEF measurements were carried out using a Two-Photon Microscope Nikon A1R MP+ Upright equipped with a femtosecond pulsed laser Coherent Chameleon Discovery (~100 fs pulse duration with 80 MHz repetition rate, tunable excitation range 700–1300 nm). A 25× water dipping objective with numerical aperture (NA) 1.2 and 2 mm working distance was employed for focusing the excitation beam and for collecting the TPEF signal.
TPEF signal was detected by four non-descanned detectors (NDDs) and a spectral detector (descanned, DD) connected to the microscope through an optical fiber. The series of NDDs is composed of three high sensitivity Gallium Arsenide Phosphide (GaAsP) and a Multi- Alkali photomultiplier tubes (PMTs), each one preceded by a specific filter cube in order to detect different spectral regions simultaneously: blue channel (415–485 nm), green channel (506–593 nm), red channel (604–679 nm) for the GaAsP's PMTs and far-red (698-750 nm) for the Multi-Alkali PMT. The spectral detector consists of a GaAsP PMT preceded by a dispersive element that allows to collect emission spectra in the 400-650 nm region with a 10 nm resolution. When using the NDDs, the associated dichroic filter allows for excitation in between 820 and 1300 nm, while the descanned spectral detector is associated with a dichroic mirror allowing for excitation in the 700-1080 nm region. A simplified scheme of the two-photon microscope setup is reported in Figure 10.14.

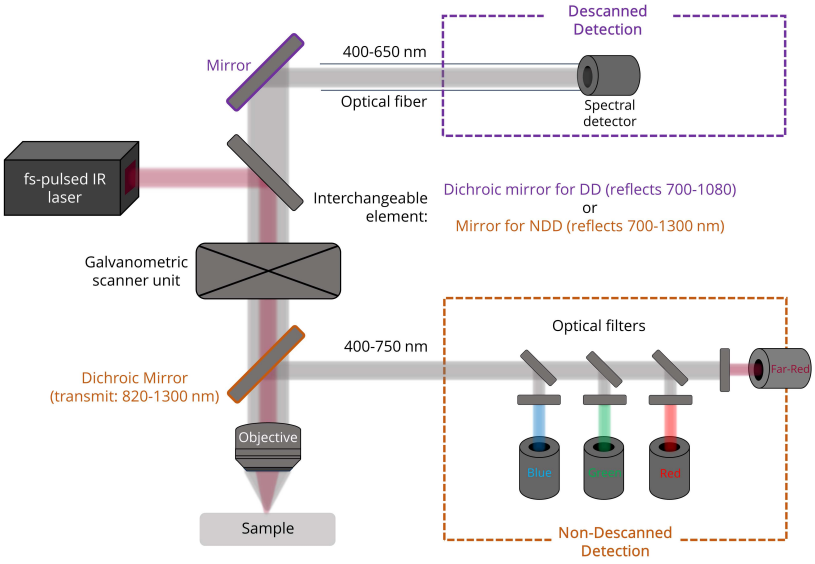

Figure 10.14: Simplified scheme of the two-photon microscope employed in this research work.

Bibliography

Here are the references in citation order.

[1] Belinda Heyne. 'Self-assembly of organic dyes in supramolecular aggregates'. In: *Photochem. Photobiol. Sci.* 15 (9 2016), pp. 1103–1114. DOI: 10.1039/C6PP00221H (cited on page 3).

[2] George M. Whitesides, John P. Mathias, and Christopher T. Seto. 'Molecular Self-Assembly and Nanochemistry: a Chemical Strategy for the Synthesis of Nanostructures'. In: *Science* 254.5036 (1991), pp. 1312–1319. DOI: 10.1126/science.1962191 (cited on page 3).

[3] George Whitesides and Mila Boncheva. 'Beyond molecules: Self-assembly of mesoscopic and macroscopic components'. In: *Proceedings of the National Academy of Sciences of the United States of America* 99 (May 2002), pp. 4769–74. DOI: 10.1073/pnas.082065899 (cited on page 3).

[4] Ronit Freeman et al. 'Reversible self-assembly of superstructured networks'. In: *Science* 362.6416 (2018), pp. 808–813. DOI: 10.1126/science.aat6141 (cited on page 3).

[5] Zi-Kui Liu, John Ågren, and Mats Hillert. 'Application of the Le Chatelier principle on gas reactions'. In: *Fluid Phase Equilibria* 121.1 (1996), pp. 167–177. DOI: https://doi.org/10.1016/0378-3812(96)02994-9 (cited on page 3).

[6] Dudley H. Williams, Dominic P. O'Brien, and Ben Bardsley. 'Enthalpy/Entropy Compensation as a Competition between Dynamics and Bonding: The Relevance to Melting of Crystals and Biological Aggregates'. In: *Journal of the American Chemical Society* 123.4 (2001), pp. 737–738. DOI: 10.1021/ja0029230 (cited on page 3).

[7] I.M. Klotz. 'Enthalpy, Enthalpy of Reaction, and Heat Capacity'. In: *Chemical Thermodynamics*. John Wiley & Sons, Ltd, 2008. Chap. 4, pp. 43–79. DOI: https://doi.org/10.1002/9780470285237.ch4 (cited on page 3).

[8] Pavel Hobza and Klaus Muller-Dethlefs. *Non-covalent Interactions: Theory and Experiment*. The Royal Society of Chemistry, Nov. 2009 (cited on pages 3, 4).

[9] D. F. Bartlett, P. E. Goldhagen, and E. A. Phillips. 'Experimental Test of Coulomb's Law'. In: *Phys. Rev. D* 2 (3 Aug. 1970), pp. 483–487. DOI: 10.1103/PhysRevD.2.483 (cited on page 4).

[10] R. F. W. Bader and W. H. Henneker. 'The Ionic Bond'. In: *Journal of the American Chemical Society* 87.14 (1965), pp. 3063–3068. DOI: 10.1021/ja01092a008 (cited on page 4).

[11] Katherine H. Sippel and Florante A. Quiocho. 'Ion–dipole interactions and their functions in proteins'. In: *Protein Science* 24.7 (2015), pp. 1040–1046. DOI: https://doi.org/10.1002/pro.2685 (cited on page 4).

[12] Francesca Terenziani et al. 'Effects of Dipolar Interactions on Linear and Nonlinear Optical Properties of Multichromophore Assemblies: A Case Study'. In: *Chemistry – A European Journal* 12.11 (2006), pp. 3089–3102. DOI: https://doi.org/10.1002/chem.200500910 (cited on page 5).

[13] Cristina Sissa et al. 'The effectiveness of essential-state models in the description of optical properties of branched push–pull chromophores'. In: *Phys. Chem. Chem. Phys. : PCCP* 12 (Oct. 2010), pp. 11715–27. DOI: 10.1039/c003563g (cited on page 5).

[14] J. M. Luttinger and L. Tisza. 'Theory of Dipole Interaction in Crystals'. In: *Phys. Rev.* 70 (11-12 Dec. 1946), pp. 954–964. DOI: 10.1103/PhysRev.70.954 (cited on page 5).

[15] Kenneth J. Miller. 'Calculation of the molecular polarizability tensor'. In: *Journal of the American Chemical Society* 112.23 (1990), pp. 8543–8551. DOI: 10.1021/ja00179a045 (cited on page 6).

[16] H. Margenau. 'Van der waals forces'. In: *Rev. Mod. Phys.* 11 (1 Jan. 1939), pp. 1–35. DOI: 10.1103/RevModPhys.11.1 (cited on page 6).

[17] F. London. 'The general theory of molecular forces'. In: *Trans. Faraday Soc.* 33 (0 1937), 8b–26. DOI: 10.1039/TF937330008B (cited on page 6).

[18] A. Subha Mahadevi and G. Narahari Sastry. 'Cooperativity in Noncovalent Interactions'. In: *Chemical Reviews* 116.5 (2016). PMID: 26840650, pp. 2775–2825. DOI: 10.1021/cr500344e (cited on page 6).

[19] Michele Vendruscolo and Monika Fuxreiter. 'Towards sequence-based principles for protein phase separation predictions'. In: *Current Opinion in Chemical Biology* 75 (2023), p. 102317. DOI: https://doi.org/10.1016/j.cbpa.2023.102317 (cited on page 6).

[20] Konrad Meister et al. 'Observation of ice-like water layers at an aqueous protein surface'. In: *Proceedings of the National Academy of Sciences* 111.50 (2014), pp. 17732–17736. DOI: 10.1073/pnas.1414188111 (cited on page 7).

[21] José Manuel del Río and Malcolm N. Jones. 'Thermodynamics of the Hydrophobic Effect'. In: *The Journal of Physical Chemistry B* 105.6 (2001), pp. 1200–1211. DOI: 10.1021/jp002097h (cited on page 7).

[22] B. Widom, P. Bhimalapuram, and Kenichiro Koga. 'The hydrophobic effect'. In: *Phys. Chem. Chem. Phys.* 5 (15 2003), pp. 3085–3093. DOI: 10.1039/B304038K (cited on page 7).

[23] Bengt Kronberg. 'The hydrophobic effect'. In: *Current Opinion in Colloid & Interface Science* 22 (2016), pp. 14–22. DOI: https://doi.org/10.1016/j.cocis.2016.02.001 (cited on page 7).

[24] Frank Biedermann, Werner M. Nau, and Hans-Jörg Schneider. 'The Hydrophobic Effect Revisited—Studies with Supramolecular Complexes Imply High-Energy Water as a Noncovalent Driving Force'. In: *Angewandte Chemie International Edition* 53.42 (2014), pp. 11158–11171. DOI: https://doi.org/10.1002/anie.201310958 (cited on page 7).

[25] A. Delledonne et al. 'Increasing resonance energy transfer upon dilution: a counterintuitive observation in CTAB micelles'. In: *J. Mater. Chem. C* 9 (2021), pp. 10952–10964 (cited on pages 7, 20, 42, 129).

[26] Julian Vrbancich and Geoffrey L. D. Ritchie. 'Quadrupole moments of benzene, hexafluorobenzene and other non-dipolar aromatic molecules'. In: *J. Chem. Soc., Faraday Trans. 2* 76 (0 1980), pp. 648–659. DOI: 10.1039/F29807600648 (cited on page 7).

[27] J. L. Petersen. 'The pi pi Interaction'. In: (Feb. 1977). DOI: 10.5170/CERN-1977-004 (cited on page 7).

[28] Christopher A. Hunter and Jeremy K. M. Sanders. 'The nature of .pi.-.pi. interactions'. In: *Journal of the American Chemical Society* 112.14 (1990), pp. 5525–5534. DOI: 10.1021/ja00170a016 (cited on pages 7, 8).

[29] Blagoje P. Dimitrijević, Sunčica Z. Borozan, and Srđan Đ. Stojanović. 'π–π and cation–π interactions in protein–porphyrin complex crystal structures'. In: *RSC Adv.* 2 (33 2012), pp. 12963–12972. DOI: 10.1039/C2RA21937A (cited on page 8).

[30] Manisha Bajpai et al. 'Role of reduced pi-pi stacking in the charge transport in polyfluorene'. In: *Materials Science and Engineering: B* 212 (2016), pp. 62–70. DOI: https://doi.org/10.1016/j.mseb.2016.07.012 (cited on page 8).

[31] S Mecozzi, A P West, and D A Dougherty. 'Cation-pi interactions in aromatics of biological and medicinal interest: electrostatic potential surfaces as a useful qualitative guide.' In: *Proceedings of the National Academy of Sciences* 93.20 (1996), pp. 10566–10571. DOI: 10.1073/pnas.93.20.10566 (cited on page 8).

[32] Brandi L. Schottel, Helen T. Chifotides, and Kim R. Dunbar. 'Anion-π interactions'. In: *Chem. Soc. Rev.* 37 (1 2008), pp. 68–83. DOI: 10.1039/B614208G (cited on page 8).

[33] Seiji Tsuzuki. 'CH/π interactions'. In: *Annu. Rep. Prog. Chem., Sect. C: Phys. Chem.* 108 (1 2012), pp. 69–95. DOI: 10.1039/C2PC90003C (cited on page 8).

[34] Peter A. Kollman and Leland C. Allen. 'Theory of the hydrogen bond'. In: *Chemical Reviews* 72.3 (1972), pp. 283–303. DOI: 10.1021/cr60277a004 (cited on page 8).

[35] A.D. Buckingham, J.E. Del Bene, and S.A.C. McDowell. 'The hydrogen bond'. In: *Chemical Physics Letters* 463.1 (2008), pp. 1–10. DOI: https://doi.org/10.1016/j.cplett.2008.06.060 (cited on page 8).

[36] Peter W. Kenny. 'Hydrogen Bonding, Electrostatic Potential, and Molecular Design'. In: *Journal of Chemical Information and Modeling* 49.5 (2009). PMID: 19382744, pp. 1234–1244. DOI: 10.1021/ci9000234 (cited on page 8).

[37] Norman D. Coggeshall. 'Electrostatic Interaction in Hydrogen Bonding'. In: *The Journal of Chemical Physics* 18.7 (July 1950), pp. 978–983. DOI: 10.1063/1.1747822 (cited on page 8).

[38] Thomas Steiner. 'The Hydrogen Bond in the Solid State'. In: *Angewandte Chemie International Edition* 41.1 (2002), pp. 48–76. DOI: https://doi.org/10.1002/1521-3773(20020104)41:1<48::AID-ANIE48>3.0.CO;2-U (cited on page 8).

[39] Christer B. Aakeröy and Kenneth R. Seddon. 'The hydrogen bond and crystal engineering'. In: *Chem. Soc. Rev.* 22 (6 1993), pp. 397–407. DOI: 10.1039/CS9932200397 (cited on page 8).

[40] Francesco Bertocchi et al. 'Tuning the Optical Properties Through Hydrogen Bond-assisted H-aggregate Formation: The ODIN Case'. In: *Chemistry – A European Journal* 30.1 (2024), e202302619. DOI: https://doi.org/10.1002/chem.202302619 (cited on pages 8, 137).

[41] Adélia J. A. Aquino et al. 'Solvent Effects on Hydrogen BondsA Theoretical Study'. In: *The Journal of Physical Chemistry A* 106.9 (2002), pp. 1862–1871. DOI: 10.1021/jp013677x (cited on pages 8, 137).

[42] Nicole Y. Meredith et al. 'Dissecting Solvent Effects on Hydrogen Bonding'. In: *Angewandte Chemie International Edition* 61.30 (2022), e202206604. DOI: https://doi.org/10.1002/anie.202206604 (cited on page 8).

[43] Charles H. Langley and Norman L. Allinger. 'Molecular Mechanics (MM4) and ab Initio Study of Amide-Amide and Amide-Water Dimers'. In: *The Journal of Physical Chemistry A* 107.26 (2003), pp. 5208–5216. DOI: 10.1021/jp021764z (cited on page 9).

[44] Gastone Gilli et al. 'Evidence for resonance-assisted hydrogen bonding from crystal-structure correlations on the enol form of the .beta.-diketone fragment'. In: *Journal of the American Chemical Society* 111.3 (1989), pp. 1023–1028. DOI: 10.1021/ja00185a035 (cited on page 9).

[45] Kamran T. Mahmudov and Armando J. L. Pombeiro. 'Resonance-Assisted Hydrogen Bonding as a Driving Force in Synthesis and a Synthon in the Design of Materials'. In: *Chemistry – A European Journal* 22.46 (2016), pp. 16356–16398. DOI: https://doi.org/10.1002/chem.201601766 (cited on page 9).

[46] Célia Fonseca Guerra et al. 'Hydrogen Bonding in DNA Base Pairs: Reconciliation of Theory and Experiment'. In: *Journal of the American Chemical Society* 122.17 (2000), pp. 4117–4128. DOI: 10.1021/ja993262d (cited on page 9).

[47] Lucas J. Karas et al. 'Hydrogen bond design principles'. In: *WIREs Computational Molecular Science* 10.6 (2020), e1477. DOI: https://doi.org/10.1002/wcms.1477 (cited on page 9).

[48] Peter Politzer and Jane S. Murray. 'Halogen Bonding: An Interim Discussion'. In: *ChemPhysChem* 14.2 (2013), pp. 278–294. DOI: https://doi.org/10.1002/cphc.201200799 (cited on page 9).

[49] Gabriella Cavallo et al. 'The Halogen Bond'. In: *Chemical Reviews* 116.4 (2016). PMID: 26812185, pp. 2478–2601. DOI: 10.1021/acs.chemrev.5b00484 (cited on page 9).

[50] Jason Y.C. Lim and Paul D. Beer. 'Sigma-Hole Interactions in Anion Recognition'. In: *Chem* 4.4 (2018), pp. 731–783. DOI: https://doi.org/10.1016/j.chempr.2018.02.022 (cited on page 9).

[51] Kelling J. Donald, Nam Pham, and Pranav Ravichandran. 'Sigma Hole Potentials as Tools: Quantifying and Partitioning Substituent Effects'. In: *The Journal of Physical Chemistry A* 127.48 (2023). PMID: 38058158, pp. 10147–10158. DOI: 10.1021/acs.jpca.3c05797 (cited on page 9).

[52] Siwei Zhao et al. 'E2/SN2 Selectivity Driven by Reaction Dynamics. Insight into Halogen Bonding'. In: *Precision Chemistry* 1.8 (2023), pp. 507–515. DOI: 10.1021/prechem.3c00053 (cited on page 10).

[53] Nicholas Hestand and Francis Spano. 'Expanded Theory of H- and J-Molecular Aggregates: The Effects of Vibronic Coupling and Intermolecular Charge Transfer'. In: *Chem. Rev.* 118 (Apr. 2018), pp. 7069–7163. DOI: 10.1021/acs.chemrev.7b00581 (cited on pages 10, 11, 22, 51, 57).

[54] Kasha, M. 'Energy Transfer Mechanism and the Molecular Exciton Model for Molecular Aggregates'. In: *Radiat. Res.* 3 (1964), pp. 317–331 (cited on pages 10, 53, 95, 118, 129, 132).

[55] F. Bertocchi et al. 'Aggregates of Cyanine Dyes: When Molecular Vibrations and Electrostatic Screening Make the Difference'. In: *J. Phys. Chem. C* (2023). DOI: 10.1021/acs.jpcc.3c01253 (cited on pages 10, 11, 42, 117, 122, 123, 129, 134, 138).

[56] Ebin Sebastian et al. 'Null Exciton Splitting in Chromophoric Greek Cross (+) Aggregate'. In: *Angewandte Chemie International Edition* 57.48 (2018), pp. 15696–15701. DOI: https://doi.org/10.1002/anie.201810209 (cited on pages 11, 101).

[57] K. Swathi et al. 'Supramolecular chirality: A caveat in assigning the handedness of chiral aggregates'. In: *Chemical Communications* 56 (June 2020). DOI: 10.1039/D0CC01922D (cited on pages 11, 81, 82, 105, 107, 111, 117, 120, 122, 123, 129, 135).

[58] Joachim Vollbrecht. 'Excimers in organic electronics'. In: *New J. Chem.* 42 (14 2018), pp. 11249–11254. DOI: 10.1039/C8NJ02135J (cited on page 11).

[59] Nerea Gonzalez-Pato et al. 'Nanothermometer Based on Polychlorinated Trityl Radicals Showing Two-Photon Excitation and Emission in the Biological Transparency Window: Temperature Monitoring of Biological Tissues'. In: *Small Methods* 8.3 (2024), p. 2301060. DOI: https://doi.org/10.1002/smtd.202301060 (cited on page 12).

[60] D Blasi et al. 'Excimers from stable and persistent supramolecular radical-pairs in red/NIR-emitting organic nanoparticles and polymeric films'. In: *Physical Chemistry Chemical Physics* 19.13 (2017), pp. 9313–9319. DOI: 10.1039/C7CP00623C (cited on pages 12, 62, 64, 65, 67, 68, 71, 72).

[61] Ahsan U Khan and Michael Kasha. 'Mechanism of four-level laser action in solution excimer and excited-state proton-transfer cases'. In: *Proceedings of the National Academy of Sciences* 80.6 (1983), pp. 1767–1770 (cited on page 12).

[62] J. B. Birks et al. ''Excimer' fluorescence V. Influence of solvent viscosity and temperature'. In: *Proceedings of the Royal Society of London. Series A. Mathematical and Physical Sciences* 280.1381 (1964), pp. 289–297. DOI: 10.1098/rspa.1964.0146 (cited on page 12).

[63] M Reyes Vigil et al. 'Non-diffusion-controlled excimer formation with indane and acenaphthene.: Kinetics and thermodynamics from picosecond-time-resolved fluorescence'. In: *Chemical Physics Letters* 287.3 (1998), pp. 379–387. DOI: https://doi.org/10.1016/S0009-2614(98)00147-X (cited on page 12).

[64] Amaresh Mishra et al. 'Cyanines during the 1990s: A Review'. In: *Chem. Rev.* 100.6 (2000), pp. 1973–2012. DOI: 10.1021/cr990402t (cited on page 16).

[65] G.S. Gopika et al. 'Chemistry of cyanine dyes-A review'. In: *Mater. Today:. Proc.* 46 (2021). International Conference on Advances in Material Science and Chemistry – 2020 (ICAMSC-2020), pp. 3102–3108. DOI: https://doi.org/10.1016/j.matpr.2021.02.622 (cited on page 16).

[66] Hui Zhang et al. 'Semitransparent organic photovoltaics using a near-infrared absorbing cyanine dye'. In: *Sol. Energy Mater. Sol. Cells* 118 (2013), pp. 157–164. DOI: https://doi.org/10.1016/j.solmat.2013.08.011 (cited on page 16).

[67] Vikram J. Pansare et al. 'Review of Long-Wavelength Optical and NIR Imaging Materials: Contrast Agents, Fluorophores, and Multifunctional Nano Carriers'. In: *Chem. Mater.* 24.5 (2012), pp. 812–827. DOI: 10.1021/cm2028367 (cited on page 16).

[68] Guangjin Li et al. 'Cyanine-based fluorescent indicator for mercury ion and bioimaging application in living cells'. In: *Spectrochim. Acta, Part A* 239 (2020), p. 118465. DOI: https://doi.org/10.1016/j.saa.2020.118465 (cited on page 16).

[69] Yang Li et al. 'Cyanine Conjugate-Based Biomedical Imaging Probes'. In: *Adv. Healthcare Mater.* 9 (Oct. 2020), p. 2001327. DOI: 10.1002/adhm.202001327 (cited on page 16).

[70] Judit Morla-Folch et al. 'Ultrabright Föster Resonance Energy Transfer Nanovesicles: The Role of Dye Diffusion'. In: *Chem. Mater.* 34 (July 2022), pp. 8517–8527. DOI: 10.1021/acs.chemmater.2c00384 (cited on page 16).

[71] Kubra Onbasli et al. 'Recent Advances in Cyanine-Based Phototherapy Agents'. In: *Front. Chem.* 9 (June 2021), p. 707876. DOI: 10.3389/fchem.2021.707876 (cited on page 16).

[72] Jie Cao et al. 'Iodinated Cyanine Dyes for Fast Near-Infrared-Guided Deep Tissue Synergistic Phototherapy'. In: *ACS Appl. Mater. Interfaces* 11.29 (2019), pp. 25720–25729. DOI: 10.1021/acsami.9b07694 (cited on page 16).

[73] Syed Muhammad Usama, Sopida Thavornpradit, and Kevin Burgess. 'Optimized Heptamethine Cyanines for Photodynamic Therapy'. In: *ACS Appl. Bio Mater.* 1.4 (2018), pp. 1195–1205. DOI: 10.1021/acsabm.8b00414 (cited on page 16).

[74] Joel M. Hales et al. 'Design of Organic Chromophores for All-Optical Signal Process. Applications'. In: *Chem. Mater.* 26.1 (2014), pp. 549–560. DOI: 10.1021/cm402893s (cited on page 16).

[75] Mike Heilemann et al. 'Carbocyanine Dyes as Efficient Reversible Single-Molecule Optical Switch'. In: *J. Am. Chem. Soc.* 127.11 (2005), pp. 3801–3806. DOI: 10.1021/ja044686x (cited on page 16).

[76] Wen Sun et al. 'Recent Development of Chemosensors Based on Cyanine Platforms'. In: *Chem. Rev.* 116.14 (2016), pp. 7768–7817. DOI: 10.1021/acs.chemrev.6b00001 (cited on page 16).

[77] E.E. Jelley. 'Molecular, Nematic and Crystal States of I: I-Diethyl–Cyanine Chloride'. In: *Nature* 139 (1937), p. 631. DOI: 10.1038/139631b0 (cited on pages 16, 35, 51, 134).

[78] G. Scheibe. 'Über die Veränderlichkeit der Absorptionsspektren in Lösungen und die Nebenvalenzen als ihre Ursache'. In: *Angew. Chem.* 50.11 (1937), pp. 212–219. DOI: https://doi.org/10.1002/ange.19370501103 (cited on pages 16, 35).

[79] Cătălin Didraga et al. 'Structure, Spectroscopy, and Microscopic Model of Tubular Carbocyanine Dye Aggregates'. In: *J. Phys. Chem. B* 108.39 (2004), pp. 14976–14985. DOI: 10.1021/jp048288s (cited on page 16).

[80] Oh-Kil Kim et al. 'Super-Helix Formation Induced by Cyanine J-Aggregates onto Random-Coil Carboxymethyl Amylose as Template'. In: *J. Am. Chem. Soc.* 128.2 (2006), pp. 510–516. DOI: 10.1021/ja0533141 (cited on page 16).

[81] Suresh Gadde et al. 'Control of H- and J-Aggregate Formation via Host-Guest Complexation using Cucurbituril Hosts'. In: *J. Am. Chem. Soc.* 130.50 (2008), pp. 17114–17119. DOI: 10.1021/ja807197c (cited on page 16).

[82] Yutaka Kawabe and Sho Kato. 'Spectroscopic study of cyanine dyes interacting with the biopolymer, DNA'. In: *Dyes Pigm.* 95.3 (2012), pp. 614–618. DOI: https://doi.org/10.1016/j.dyepig.2012.07.002 (cited on pages 16, 36, 129).

[83] Julia Bricks et al. 'Fluorescent J-aggregates of cyanine dyes: basic research and applications Review'. In: *Method. Appl. Fluoresc.* 6 (2018), p. 012001. DOI: 10.1088/2050-6120/aa8d0d (cited on pages 16, 129).

[84] Austin D. Bailey et al. 'Exploring the design of superradiant J-aggregates from amphiphilic monomer units'. In: *Nanoscale* 15 (8 2023), pp. 3841–3849. DOI: 10.1039/D2NR05747F (cited on page 16).

[85] Katie A. Clark, Emma L. Krueger, and David A. Vanden Bout. 'Direct Measurement of Energy Migration in Supramolecular Carbocyanine Dye Nanotubes'. In: *J. Phys. Chem. Lett.* 5.13 (2014), pp. 2274–2282. DOI: 10.1021/jz500634f (cited on page 16).

[86] Chao Wang and Yizhong Yuan. 'The Influence of the Aggregation on the Third-order Nonlinear Optical Property of the π-Conjugated Chromophores: the Case of Cyanine Dyes'. In: *Phys. Chem. Chem. Phys.* 20 (2018), pp. 16777–16785. DOI: 10.1039/c8cp00770e (cited on page 16).

[87] Die Chen et al. 'A Supramolecular Counter Circuit Based on Cyanine Dye Assembly'. In: *Chemistry* 26 (Apr. 2020), pp. 13235–13240. DOI: 10.1002/chem.202001240 (cited on page 16).

[88] Xiaomeng Guo et al. 'A cyanine dye supramolecular FRET switch driven by G-quadruplex to monitor mitophagy'. In: *Dyes Pigm.* 192 (2021), p. 109429. DOI: https://doi.org/10.1016/j.dyepig.2021.109429 (cited on pages 16, 129).

[89] Ilya O. Aparin et al. 'Fluorogenic Dimers as Bright Switchable Probes for Enhanced Super-Resolution Imaging of Cell Membranes'. In: *J. Am. Chem. Soc.* 144.39 (2022), pp. 18043–18053. DOI: 10.1021/jacs.2c07542 (cited on page 16).

[90] Alice Cuzzocrea et al. 'Reference Excitation Energies of Increasingly Large Molecules: A QMC Study of Cyanine Dyes'. In: *J. Chem. Theory Comput.* 18 (Jan. 2022), pp. 1089–1095. DOI: 10.1021/acs.jctc.1c01162 (cited on page 16).

[91] Robert Send, Omar Valsson, and Claudia Filippi. 'Electronic Excitations of Simple Cyanine Dyes: Reconciling Density Functional and Wave Function Methods'. In: *J. Chem. Theory Comput.* 7.2 (2011), pp. 444–455. DOI: 10.1021/ct1006295 (cited on page 16).

[92] Paul Boulanger et al. 'Fast and Accurate Electronic Excitations in Cyanines with the Many-Body Bethe–Salpeter Approach'. In: *J. Chem. Theory Comput.* 10 (Feb. 2014), pp. 1212–1218. DOI: 10.1021/ct401101u (cited on page 16).

[93] Boris Le Guennic and Denis Jacquemin. 'Taking Up the Cyanine Challenge with Quantum Tools'. In: *Acc. Chem. Res.* 48 (Feb. 2015), pp. 530–537. DOI: 10.1021/ar500447q (cited on page 16).

[94] Francesca Terenziani et al. 'Charge Instability in Quadrupolar Chromophores: Symmetry Breaking and Solvatochromism'. In: *J. Am. Chem. Soc.* 128 (Jan. 2006), pp. 15742–15755. DOI: 10.1021/ja064521j (cited on pages 16, 25, 27, 35, 138).

[95] Daniel Timmer et al. 'Charge Delocalization and Vibronic Couplings in Quadrupolar Squaraine Dyes'. In: *J. Am. Chem. Soc.* 144.41 (2022), pp. 19150–19162. DOI: 10.1021/jacs.2c08682 (cited on page 16).

[96] Francesca Terenziani et al. 'Essential-State Model for Polymethine Dyes: Symmetry Breaking and Optical Spectra'. In: *J. Phys. Chem. Lett.* 1 (May 2010), pp. 1800–1804. DOI: 10.1021/jz100430x (cited on pages 16, 25, 35, 138).

[97] Honghua Hu et al. 'Two-photon absorption spectra of a near-infrared 2-azaazulene polymethine dye: solvation and ground-state symmetry breaking'. In: *Phys. Chem. Chem. Phys.* 15 (20 2013), pp. 7666–7678. DOI: 10.1039/C3CP50811K (cited on pages 16, 25, 27, 35).

[98] Francesca Terenziani and Anna Painelli. 'Collective and cooperative phenomena in molecular materials: dimers of polar chromophores'. In: *J. Lumin.* 112.1 (2005), pp. 474–478. DOI: https://doi.org/10.1016/j.jlumin.2004.09.079 (cited on page 17).

[99] Francesca Terenziani, Gabriele D'Avino, and Anna Painelli. 'Multichromophores for Nonlinear Optics: Designing the Material Properties by Electrostatic Interactions'. In: *ChemPhysChem* 8 (Dec. 2007), pp. 2433–2444. DOI: 10.1002/cphc.200700368 (cited on pages 17, 29).

[100] Brunella Bardi et al. 'Spectroscopic Investigation and Theoretical Modeling of Benzothiadiazole-Based Charge-Transfer Chromophores: From Solution to Nanoaggregates'. In: *J. Phys. Chem. C* 121.32 (2017), pp. 17466–17478. DOI: 10.1021/acs.jpcc.7b04647 (cited on pages 17, 29, 32).

[101] David Bialas et al. 'Essential States Model for Merocyanine Dye Stacks: Bridging Electronic and Optical Absorption Properties'. In: *J. Phys. Chem. C* 123 (July 2019), pp. 18654–18664. DOI: 10.1021/acs.jpcc.9b04430 (cited on pages 17, 29).

[102] Chia-An Shen et al. 'Polymorphism in Squaraine Dye Aggregates by Self-Assembly Pathway Differentiation: Panchromatic Tubular Dye Nanorods versus J-Aggregate Nanosheets'. In: *Angew. Chem. Int. Ed.* 60.21 (2021), pp. 11949–11958. DOI: https://doi.org/10.1002/anie.202102183 (cited on pages 17, 51).

[103] Xin Chang, Mohammad Balooch Qarai, and Frank C. Spano. 'Intermolecular Charge Transfer in H- and J-Aggregates of Donor–Acceptor–Donor Chromophores: The Curious Case of Bithiophene-DPP'. In: *J. Phys. Chem. C* 126.44 (2022), pp. 18784–18795. DOI: 10.1021/acs.jpcc.2c05910 (cited on page 17).

[104] Mattia Anzola, Francesco Di Maiolo, and Anna Painelli. 'Optical spectra of molecular aggregates and crystals: testing approximation schemes'. In: *Phys. Chem. Chem. Phys.* 21 (Aug. 2019), pp. 19816–19824. DOI: 10.1039/C9CP03122G (cited on pages 17, 22, 24, 29, 35).

[105] Mattia Anzola and Anna Painelli. 'Aggregates of polar dyes: beyond the exciton model'. In: *Phys. Chem. Chem. Phys.* 23 (Mar. 2021), pp. 8282–8291. DOI: 10.1039/D1CP00335F (cited on pages 17, 29, 30, 32, 129, 132).

[106] Cristina Sissa et al. 'Dimers of Quadrupolar Chromophores in Solution: Electrostatic Interactions and Optical Spectra'. In: *J. Phys. Chem. B* 114 (Jan. 2010), pp. 882–93. DOI: 10.1021/jp909475d (cited on pages 17, 29, 30).

[107] Judit Morla-Folch et al. 'Dye-Loaded Quatsomes Exhibiting FRET as Nanoprobes for Bioimaging'. In: *ACS Appl. Mater. Interfaces* 12 (Apr. 2020), p. 20253. DOI: 10.1021/acsami.0c03040 (cited on pages 18, 20, 21).

[108] Knut Rurack and Monika Spieles. 'Fluorescence Quantum Yields of a Series of Red and Near-Infrared Dyes Emitting at 600-1000 nm'. In: *Anal. Chem.* 83 (Feb. 2011), pp. 1232–1242. DOI: 10.1021/ac101329h (cited on page 18).

[109] Sophie Gronlier de Reguardati et al. 'High-accuracy reference standards for two-photon absorption in the 680–1050 nm wavelength range'. In: *Opt. Express* 24 (Apr. 2016), p. 9053. DOI: 10.1364/OE.24.009053 (cited on page 18).

[110] Marius Albota, Chris Xu, and Watt Webb. 'Two-Photon Fluorescence Excitation Cross Sections of Biomolecular Probes from 690 to 960 nm'. In: *Appl. Opt.* 37 (Dec. 1998), pp. 7352–7356. DOI: 10.1364/AO.37.007352 (cited on page 18).

[111] Francis Spano. 'The Spectral Signatures of Frenkel Polarons in H- and J-Aggregates'. In: *Acc. Chem. Res.* 43 (Dec. 2009), pp. 429–439. DOI: 10.1021/ar900233v (cited on pages 22, 134).

[112] Alexei Cravcenco et al. 'Exciton Delocalization Counteracts the Energy Gap: A New Pathway toward NIR-Emissive Dyes'. In: *J. Am. Chem. Soc.* 143.45 (Nov. 2021), pp. 19232–19239. DOI: 10.1021/jacs.1c10654 (cited on page 22).

[113] Brian Orr and J. Ward. 'Perturbation theory of the non-linear optical polarization of an isolated system'. In: *Mol. Phys. - MOL PHYS* 20 (Mar. 1971), pp. 513–526. DOI: 10.1080/00268977100100481 (cited on page 27).

[114] Cristina Sissa et al. 'Essential State Model for Two-Photon Absorption Spectra of Polymethine Dyes'. In: *ChemPhysChem* 13.11 (2012), pp. 2795–2800. DOI: https://doi.org/10.1002/cphc.201200021 (cited on page 27).

[115] Francesca Terenziani and Anna Painelli. 'Supramolecular interactions in clusters of polar and polarizable molecules'. In: *Phys. Rev. B* 68 (2003), p. 165405 (cited on pages 29, 30, 129, 132).

[116] Anna Painelli and Francesca Terenziani. 'Multielectron Transfer in Clusters of Polar-Polarizable Chromophores'. In: *J. Am. Chem. Soc.* 125.19 (2003), pp. 5624–5625. DOI: 10.1021/ja034155t (cited on page 29).

[117] Brunella Bardi et al. 'Multistimuli-Responsive Materials from Benzothiadiazole-Based Charge-Transfer Chromophores: Interdependence of Optical Properties and Aggregation'. In: *ChemPhotoChem* 2.12 (2018), pp. 1027–1037. DOI: 10.1002/cptc.201800145 (cited on pages 29, 32).

[118] D. Giavazzi et al. 'A Comprehensive Approach to Exciton Delocalization and Energy Transfer'. In: *J. Chem. Theory Comput.* 19.2 (2023), pp. 436–447. DOI: 10.1021/acs.jctc.2c00980 (cited on pages 29, 30, 117).

[119] Francesca Terenziani et al. 'Linear and Two-Photon Absorption Properties of Interacting Polar Chromophores: Standard and Unconventional Effects'. In: *ChemPhysChem* 7.3 (2006), pp. 685–696. DOI: https://doi.org/10.1002/cphc.200500536 (cited on page 32).

[120] C. Zheng et al. 'Non-Kasha Behavior in Quadrupolar Dye Aggregates: The Red-Shifted H-Aggregate'. In: *J. Phys. Chem. C* 123 (2019), pp. 3203–3215 (cited on page 32).

[121] Chuwei Zhong, David Bialas, and Frank C. Spano. 'Unusual Non-Kasha Photophysical Behavior of Aggregates of Push–Pull Donor–Acceptor Chromophores'. In: *J. Phys. Chem. C* 124.3 (2020), pp. 2146–2159. DOI: 10.1021/acs.jpcc.9b09368 (cited on page 32).

[122] Anna Painelli, Luca Del Freo, and Francesca Terenziani. 'Vibronic contributions to resonant NLO responses: two-photon absorption in push–pull chromophores'. In: *Chem. Phys. Lett.* 346.5-6 (2001), pp. 470–478 (cited on page 36).

[123] A. Datta and S. K. Pati. 'Dipolar interactions and hydrogen bonding in supramolecular aggregates: understanding cooperative phenomena for 1st hyperpolarizability'. In: *Chem. Soc. Rev.* 35 (2006), pp. 1305–1323 (cited on page 38).

[124] C. Liu et al. 'Tuning the Dynamic Fragility of Acrylic Polymers by Small Molecules: The Interplay of Hydrogen Bonding Strength'. In: *Macromolecules* 48 (2015), pp. 4196–4206 (cited on page 38).

[125] J. X. Chen et al. 'Optimizing Intermolecular Interactions and Energy Level Alignments of Red TADF Emitters for High-Performance Organic Light-Emitting Diodes'. In: *Small* 18 (2022). DOI: 10.1002/smll.202201548 (cited on page 38).

[126] Y. Tang et al. 'Manipulating Förster and Dexter interactions between a thermally activated delayed fluorescence host and a phosphorescent dopant for highly efficient solution-processed red and white OLEDs'. In: *J. Mater. Chem. C* 10 (2022), pp. 4637–4645 (cited on page 38).

[127] U. Ray, Z. Pang, and T. Li. 'Programming material properties by tuning intermolecular bonding'. In: *J. Appl. Phys.* 132 (2022). DOI: 10.1063/5.0123058 (cited on page 38).

[128] Libin Liang, KimNgan Burrill, and Madalina Furis. 'Transition Dipole Moments of One-Dimensional Excitons in Soluble Phthalocyanine Thin Films'. In: *J. Phys. Chem. C* (Dec. 2021), pp. 27966–27974. DOI: 10.1021/acs.jpcc.1c08253 (cited on page 38).

[129] N. R. Ávila-Rovelo and A. Ruiz-Carretero. 'Recent Progress in Hydrogen-Bonded π-Conjugated Systems Displaying J-Type Aggregates'. In: *Org. Mater.* 02 (2020), pp. 047–063 (cited on page 38).

[130] J. Heo et al. 'Recent trends in molecular aggregates: An exploration of biomedicine'. In: *Aggregate* 3 (2022). DOI: 10.1002/agt2.159 (cited on page 38).

[131] N. J. Hestand and F. C. Spano. 'Expanded Theory of H- and J-Molecular Aggregates: The Effects of Vibronic Coupling and Intermolecular Charge Transfer'. In: *Chem. Rev.* 118 (2018), pp. 7069–7163 (cited on page 38).

[132] D. M. Eisele et al. 'Utilizing redox-chemistry to elucidate the nature of exciton transitions in supramolecular dye nanotubes'. In: *Nat. Chem.* 4 (2012), pp. 655–662 (cited on pages 38, 117).

[133] C. D. Bösch, S. M. Langenegger, and R. Häner. 'Light-Harvesting Nanotubes Formed by Supramolecular Assembly of Aromatic Oligophosphates'. In: *Angew. Chem.* 128 (2016), pp. 10115–10118 (cited on page 38).

[134] S. Doria et al. 'Vibronic coherences in light harvesting nanotubes: unravelling the role of dark states'. In: *J. Mater. Chem. C* (2022). DOI: 10.1039/d2tc00203e (cited on page 38).

[135] D. M. Eisele et al. 'Robust excitons inhabit soft supramolecular nanotubes'. In: *Proc. Natl. Acad. Sci. U.S.A.* 111 (2014), E3367–E3375 (cited on page 38).

[136] L. Jiang et al. 'Tuning intermolecular non-covalent interactions for nanowires of organic semiconductors'. In: *Nanoscale* 2 (2010), pp. 2652–2656 (cited on page 38).

[137] M. Shirakawa et al. 'Hydrogen-Bond-Assisted Control of H versus J Aggregation Mode of Porphyrins Stacks in an Organogel System'. In: *J. Org. Chem.* 68 (2003), pp. 5037–5044 (cited on page 38).

[138] C. A. Hunter and H. L. Anderson. 'What is Cooperativity?' In: *Angew. Chem. Int. Ed.* 48 (2009), pp. 7488–7499 (cited on page 38).

[139] L. L. Parker, A. R. Houk, and J. H. Jensen. 'Cooperative Hydrogen Bonding Effects Are Key Determinants of Backbone Amide Proton Chemical Shifts in Proteins'. In: *J. Am. Chem. Soc.* 128 (2006), pp. 9863–9872 (cited on page 38).

[140] Y. Zhou et al. 'Evidences for Cooperative Resonance-Assisted Hydrogen Bonds in Protein Secondary Structure Analogs'. In: *Sci. Rep.* 6 (2016). DOI: 10.1038/srep36932 (cited on page 38).

[141] B. A. Blight et al. 'An AAAA–DDDD quadruple hydrogen-bond array'. In: *Nat. Chem.* 3 (2011), pp. 244–248 (cited on page 38).

[142] W. L. Jorgensen and J. Pranata. 'Importance of secondary interactions in triply hydrogen bonded complexes: guanine-cytosine vs uracil-2,6-diaminopyridine'. In: *J. Am. Chem. Soc.* 112 (1990), pp. 2008–2010 (cited on page 38).

[143] J. Tellers et al. 'Dynamic Cross-Linking of Polyethylene via Sextuple Hydrogen Bonding Array'. In: *Macromolecules* 51 (2018), pp. 7680–7691 (cited on pages 38–42).

[144] M. Golkaram et al. 'Supramolecular Mimic for Bottlebrush Polymers in Bulk'. In: *ACS Omega* 4 (2019), pp. 16481–16492 (cited on pages 38, 42, 43).

[145] M. Gemmi et al. '3D Electron Diffraction: The Nanocrystallography Revolution'. In: *ACS Cent. Sci.* 5 (2019), pp. 1315–1329 (cited on pages 39, 40).

[146] M. Gemmi and A. E. Lanza. '3D electron diffraction techniques'. In: *Acta Crystallogr. B Struct. Sci. Cryst. Eng. Mater.* 75 (2019), pp. 495–504 (cited on pages 39, 40).

[147] I. Nederlof et al. 'A Medipix quantum area detector allows rotation electron diffraction data collection from submicrometre three-dimensional protein crystals'. In: *Acta Crystallogr. D Biol. Crystallogr.* 69 (2013), pp. 1223–1230 (cited on page 40).

[148] T. Yang et al. 'Improving data quality for three-dimensional electron diffraction by a post-column energy filter and a new crystal tracking method'. In: *J. Appl. Crystallogr.* 55 (2022), pp. 1583–1591 (cited on page 41).

[149] A. E. Clark, C. Qin, and A. D. Q. Li. 'Beyond Exciton Theory: A Time-Dependent DFT and Franck-Condon Study of Perylene Diimide and Its Chromophoric Dimer'. In: *J. Am. Chem. Soc.* 129 (2007), pp. 7586–7595 (cited on page 49).

[150] J. M. Giaimo et al. 'Excited Singlet States of Covalently Bound, Cofacial Dimers and Trimers of Perylene-3,4:9,10-bis(dicarboximide)s'. In: *J. Phys. Chem. A* 112 (2008), pp. 2322–2330 (cited on page 49).

[151] K. E. Brown et al. 'Direct Observation of Ultrafast Excimer Formation in Covalent Perylenediimide Dimers Using Near-Infrared Transient Absorption Spectroscopy'. In: *J. Phys. Chem. Lett.* 5 (2014), pp. 2588–2593 (cited on page 49).

[152] P. B. Walczak, A. Eisfeld, and J. S. Briggs. 'Exchange narrowing of the J band of molecular dye aggregates'. In: *The Journal of Chemical Physics* 128.4 (Jan. 2008), p. 044505. DOI: 10.1063/1.2823730 (cited on page 51).

[153] Lukas J. Patalag et al. 'Transforming Dyes into Fluorophores: Exciton-Induced Emission with Chain-like Oligo-BODIPY Superstructures'. In: *Angewandte Chemie International Edition* 61.22 (2022), e202116834. DOI: https://doi.org/10.1002/anie.202116834 (cited on pages 51, 52, 54–56).

[154] Mikhail A. Filatov. 'Heavy-atom-free BODIPY photosensitizers with intersystem crossing mediated by intramolecular photoinduced electron transfer'. In: *Org. Biomol. Chem.* 18 (1 2020), pp. 10–27. DOI: 10.1039/C9OB02170A (cited on page 51).

[155] Wenwu Qin et al. 'Photophysical Properties of Borondipyrromethene Analogues in Solution'. In: *The Journal of Physical Chemistry A* 109.33 (2005). PMID: 16834104, pp. 7371–7384. DOI: 10.1021/jp052626n (cited on page 51).

[156] Hisato Sunahara et al. 'Design and Synthesis of a Library of BODIPY-Based Environmental Polarity Sensors Utilizing Photoinduced Electron-Transfer-Controlled Fluorescence ON/OFF Switching'. In: *Journal of the American Chemical Society* 129.17 (2007). PMID: 17425310, pp. 5597–5604. DOI: 10.1021/ja068551y (cited on page 51).

[157] Daniel Escudero. 'Revising Intramolecular Photoinduced Electron Transfer (PET) from First-Principles'. In: *Accounts of Chemical Research* 49.9 (2016), pp. 1816–1824. DOI: 10.1021/acs.accounts.6b00299 (cited on page 51).

[158] Donald J. Metz and Althea Glines. 'Density, viscosity, and dielectric constant of tetrahydrofuran between -78 and 30.degree.' In: *The Journal of Physical Chemistry* 71.4 (1967), pp. 1158–1158. DOI: 10.1021/j100863a067 (cited on pages 52, 54).

[159] Ernest Eliel, Samuel H. Wilen, and Lewis N. Mander. *Stereochemistry of organic compounds*. Wiley, 1994 (cited on pages 52, 77, 80, 137).

[160] Rama Dhali et al. 'Understanding TADF: a joint experimental and theoretical study of DMAC-TRZ'. In: *Phys. Chem. Chem. Phys.* 23 (1 2021), pp. 378–387. DOI: 10.1039/D0CP05982J (cited on pages 52–55).

[161] Barbara Boldrini et al. 'Polar Dyes in Solution: A Joint Experimental and Theoretical Study of Absorption and Emission Band Shapes'. In: *The Journal of Physical Chemistry A* 106.26 (2002), pp. 6286–6294. DOI: 10.1021/jp020031b (cited on pages 53–55).

[162] Brunella Bardi et al. 'Solid state solvation: a fresh view'. In: *Mater. Horiz.* 10 (10 2023), pp. 4172–4182. DOI: 10.1039/D3MH00988B (cited on pages 54, 55).

[163] Andrii Obolda et al. 'Up to 100% formation ratio of doublet exciton in deep-red organic light-emitting diodes based on neutral π-radical'. In: *ACS applied materials & interfaces* 8.51 (2016), pp. 35472–35478. DOI: 10.1021/acsami.6b12338 (cited on page 62).

[164] Qiling Peng et al. 'Organic light-emitting diodes using a neutral π radical as emitter: the emission from a doublet'. In: *Angewandte Chemie International Edition* 54.24 (2015), pp. 7091–7095. DOI: 10.1002/anie.201500242 (cited on page 62).

[165] Yijun Tao et al. 'Thermally activated delayed fluorescence materials towards the breakthrough of organoelectronics'. In: *Advanced Materials* 26.47 (2014), pp. 7931–7958. DOI: 10.1002/adma.201402532 (cited on page 62).

[166] Andrii Obolda, Meng Zhang, and Feng Li. 'Evolution of emission manners of organic light-emitting diodes: from emission of singlet exciton to emission of doublet exciton'. In: *Chinese Chemical Letters* 27.8 (2016), pp. 1345–1349. DOI: 10.1016/j.cclet.2016.06.030 (cited on page 62).

[167] Giovanni M Farinola and R Ragni. 'Electroluminescent materials for white organic light emitting diodes'. In: *Chemical Society Reviews* 40.7 (2011), pp. 3467–3482. DOI: 10.1039/c0cs00204f (cited on page 62).

[168] Chi Fan and Chuluo Yang. 'Yellow/orange emissive heavy-metal complexes as phosphors in monochromatic and white organic light-emitting devices'. In: *Chemical Society Reviews* 43.17 (2014), pp. 6439–6469. DOI: 10.1039/C4CS00110A (cited on page 62).

[169] Xuemei Bai et al. 'Stable red nanoparticles loaded neutral luminescent radicals for fluorescence imaging'. In: *Dyes and Pigments* 202 (2022), p. 110260. DOI: https://doi.org/10.1016/j.dyepig.2022.110260 (cited on page 62).

[170] Lisa Chen et al. 'Red-Fluorescing Paramagnetic Conjugated Polymer Nanoparticles – Triphenyl Methyl Radicals as Monomers in C–C Cross-Coupling Dispersion Polymerization'. In: *Macromolecules* 56.5 (2023), pp. 2104–2112 (cited on page 62).

[171] T. Li Chu and S. I. Weissman. 'Symmetry Classification of the Energy Levels of Some Triarylmethyl Free Radicals and Their Cations'. In: *Journal of Chemical Physics* 22.1 (1954), pp. 21–25. DOI: 10.1063/1.1739848 (cited on page 62).

[172] T Okamura, K Obi, and I Tanaka. 'The fluorescence lifetime of the methyl-substituted benzyl, triphenylmethyl and diphenylmethyl radicals'. In: *Chemical Physics Letters* 30 (1973), pp. 90–91 (cited on page 62).

[173] A Bromberg and D Meisel. 'Photophysics of arylmethyl radicals at 77 K. Structure-photoreactivity correlation'. In: *The Journal of Physical Chemistry* 89.12 (1985), pp. 2507–2513. DOI: 10.1021/j100258a017 (cited on pages 62, 64).

[174] A Bromberg, K H Schmidt, and D Meisel. 'Photophysics and photochemistry of arylmethyl radicals in liquids'. In: *Journal of the American Chemical Society* 107.1 (1985), pp. 83–91. DOI: 10.1021/ja00287a016 (cited on pages 62, 64).

[175] Y Hattori, T Kusamoto, and H Nishihara. 'Luminescence, stability, and proton response of an open-shell (3, 5-dichloro-4-pyridyl) bis (2, 4, 6-trichlorophenyl) methyl radical'. In: *Angewandte Chemie International Edition* 53.44 (2014), pp. 11845–11848. DOI: 10.1002/anie.201407362 (cited on pages 62, 64).

[176] D Blasi et al. 'Ratiometric nanothermometer based on a radical excimer for in vivo sensing'. In: *Small* (2023). DOI: 10.1002/smll.202207806 (cited on page 62).

[177] David J Naczynski et al. 'Rare-earth-doped biological composites as in vivo shortwave infrared reporters'. In: *Nature Communications* 4.1 (2013), pp. 1–9. DOI: 10.1038/ncomms3199 (cited on page 63).

[178] I Martinić, Svetlana V Eliseeva, and Stéphane Petoud. 'Near-infrared emitting probes for biological imaging: organic fluorophores, quantum dots, fluorescent proteins, lanthanide (III) complexes and nanomaterials'. In: *Journal of Luminescence* 189 (2017), pp. 19–43. DOI: 10.1016/j.jlumin.2016.09.058 (cited on page 63).

[179] Xiaojin Wu et al. 'Push–Pull-Type Polychlorotriphenylmethyl Radicals: New Two-Photon Absorbers and Dyes for Generation of Photo-Charges'. In: *Chemistry–A European Journal* 23.32 (2017), pp. 7698–7702 (cited on pages 63, 64).

[180] Yohei Hattori et al. 'Luminescent Mono-, Di-, and Triradicals: Bridging Polychlorinated Triarylmethyl Radicals by Triarylamines and Triarylboranes'. In: *Chemistry – A European Journal* 25.68 (2019), pp. 15463–15471. DOI: https://doi.org/10.1002/chem.201903007 (cited on page 63).

[181] Bernard Valeur. *Molecular fluorescence: principles and applications*. Wiley-VCH Verlag GmbH, 2001 (cited on page 64).

[182] Jaume Guasch et al. 'The perchlorotriphenylmethyl (PTM) radical'. In: *Acta Crystallographica Section C: Crystal Structure Communications* 69.3 (2013), pp. 255–257. DOI: 10.1107/S0108270113002072 (cited on pages 65, 68).

[183] O Armet et al. In: *The Journal of Physical Chemistry* 91.22 (1987), pp. 5608–5657. DOI: 10.1021/j100306a (cited on page 68).

[184] David Casanova. 'Theoretical investigations of the perylene electronic structure: monomer, dimers, and excimers'. In: *International Journal of Quantum Chemistry* 115.7 (2015), pp. 442–452. DOI: 10.1002/qua.24869 (cited on page 68).

[185] Yong Joon Bae et al. 'Balancing charge transfer and Frenkel exciton coupling leads to excimer formation in molecular dimers: Implications for singlet fission'. In: *The Journal of Physical Chemistry A* 124.41 (2020), pp. 8478–8487. DOI: 10.1021/acs.jpca.0c07646 (cited on page 68).

[186] Anna L Bialas and Frank C Spano. 'A Holstein–Peierls approach to excimer spectra: the evolution from vibronically structured to unstructured emission'. In: *The Journal of Physical Chemistry C* 126.8 (2022), pp. 4067–4081. DOI: 10.1021/acs.jpcc.1c10255 (cited on pages 68, 70).

[187] M. Ghezzi et al. 'Symmetry Classification of the Energy Levels of Some Triarylmethyl Free Radicals and Their Cations'. In: *Journal of Controlled Release* 349 (2022), p. 744 (cited on page 73).

[188] URL: https://www.bmglabtech.com/en/lvf-monochromators/ (cited on page 73).

[189] William Thomson Baron Kelvin. *Baltimore Lectures on Molecular Dynamics and the Wave Theory of Light*. Cambridge Library Collection - Physical Sciences. Cambridge University Press, 1904 (cited on page 77).

[190] Stephen Mason. 'The origin of chirality in nature'. In: *Trends in Pharmacological Sciences* 7 (1986), pp. 20–23. DOI: https://doi.org/10.1016/0165-6147(86)90235-X (cited on page 77).

[191] Martin Schaferling. 'Chirality in Nature and Science'. In: *Chiral Nanophotonics: Chiral Optical Properties of Plasmonic Systems*. Cham: Springer International Publishing, 2017, pp. 5–42. DOI: 10.1007/978-3-319-42264-0_2 (cited on page 77).

[192] Robert N. Compton and Richard M. Pagni. In: *The Chirality of Biomolecules*. Ed. by Benjamin Bederson and Herbert Walther. Vol. 48. Advances In Atomic, Molecular, and Optical Physics. Academic Press, 2002, pp. 219–261. DOI: https://doi.org/10.1016/S1049-250X(02)80010-6 (cited on page 77).

[193] L. Keszthelyi. 'Origin of the homochirality of biomolecules'. In: *Quarterly Reviews of Biophysics* 28.4 (1995), pp. 473–507. DOI: 10.1017/S0033583500003309 (cited on page 77).

[194] Noemie Globus and Roger Blandford. 'The Chiral Puzzle of Life'. In: *The Astrophysical Journal* 895 (May 2020), p. L11. DOI: 10.3847/2041-8213/ab8dc6 (cited on page 77).

[195] E.M. Carreira and H. Yamamoto. *Comprehensive Chirality*. Sept. 2012, pp. 1–5215 (cited on page 77).

[196] Neil Vargesson. 'Thalidomide-induced teratogenesis: History and mechanisms'. In: *Birth Defects Research Part C: Embryo Today: Reviews* 105.2 (2015), pp. 140–156. DOI: https://doi.org/10.1002/bdrc.21096 (cited on page 77).

[197] R. S. Cahn, Christopher Ingold, and V. Prelog. 'Specification of Molecular Chirality'. In: *Angewandte Chemie International Edition in English* 5.4 (1966), pp. 385–415. DOI: https://doi.org/10.1002/anie.196603851 (cited on page 77).

[198] Sherry Chemler. 'The enantioselective intramolecular aminative functionalization of unactivated alkenes, dienes, allenes and alkynes for the synthesis of chiral nitrogen heterocycles'. In: *Organic & biomolecular chemistry* 7 (July 2009), pp. 3009–3019. DOI: 10.1039/B907743J (cited on page 77).

[199] Juntao Ye and Shengming Ma. 'Conquering Three-Carbon Axial Chirality of Allenes'. In: *Org. Chem. Front.* 1 (Sept. 2014). DOI: 10.1039/C4QO00208C (cited on page 77).

[200] Sean T Toenjes and Jeffrey L Gustafson. 'Atropisomerism in medicinal chemistry: challenges and opportunities'. In: *Future medicinal chemistry* 10.4 (2018), pp. 409–422 (cited on page 77).

[201] A Papakostas et al. 'Optical manifestations of planar chirality'. In: *Physical review letters* 90.10 (2003), p. 107404 (cited on page 77).

[202] Minh Tran. 'An Introduction to Classical Electromagnetic Radiation'. In: *Nuclear Fusion* 38 (May 2002), p. 775. DOI: 10.1088/0029-5515/38/5/701 (cited on page 78).

[203] D. P. Craig and T Thirunamachandran. *Molecular Quantum Electrodynamics*. Academic Press, 1984 (cited on pages 78, 95, 101, 102, 117, 118, 135).

[204] Werner Kuhn. 'The physical significance of optical rotatory power'. In: *Trans. Faraday Soc.* 26 (0 1930), pp. 293–308. DOI: 10.1039/TF9302600293 (cited on page 78).

[205] E. U. Condon. 'Theories of Optical Rotatory Power'. In: *Rev. Mod. Phys.* 9 (4 Oct. 1937), pp. 432–457. DOI: 10.1103/RevModPhys.9.432 (cited on pages 78–81, 95, 97, 99, 105–108, 117–119, 122, 124, 129, 135, 136).

[206] S. F. Mason. 'Optical rotatory power'. In: *Q. Rev. Chem. Soc.* 17 (1 1963), pp. 20–66. DOI: 10.1039/QR9631700020 (cited on page 78).

[207] Henry. Eyring, Han-Chung. Liu, and Dennis. Caldwell. 'Optical rotatory dispersion and circular dichroism'. In: *Chemical Reviews* 68.5 (1968), pp. 525–540. DOI: 10.1021/cr60255a001 (cited on page 79).

[208] N. Berova, K. Nakanishi, and Robert Woody. 'Circular Dichroism: Principles and Applications'. In: *Circular Dichroism: Principles and Applications* (Jan. 2000), pp. 337–395 (cited on pages 79, 82, 101, 105, 117).

[209] Nina Berova et al. *Comprehensive Chiroptical Spectroscopy : Volume 1 - Instrumentation, Methodologies, and Theoretical Simulations*. John Wiley & Sons, 2012 (cited on pages 79, 117).

[210] Sergio Abbate et al. 'Harmonic and anharmonic features of IR and NIR absorption and VCD spectra of chiral 4-X-[2.2] paracyclophanes'. In: *The Journal of Physical Chemistry A* 111.30 (2007), pp. 7031–7040 (cited on page 79).

[211] Sergio Abbate, Giovanna Longhi, Ettore Castiglioni, et al. 'Near-infrared vibrational circular dichroism: NIR-VCD'. In: *Comprehensive Chiroptical Spectroscopy: Instrumentation, Methodologies, and Theoretical Simulations* 1 (2012), pp. 247–273 (cited on page 79).

[212] Marco Fusè et al. 'Pushing measurements and interpretation of VCD spectra in the IR, NIR and visible ranges to the detectability and computational complexity limits'. In: *Spectrochimica Acta Part A: Molecular and Biomolecular Spectroscopy* 305 (2024), p. 123496 (cited on page 79).

[213] Howard Devoe. 'Optical Properties of Molecular Aggregates. II. Classical Theory of the Refraction, Absorption, and Optical Activity of Solutions and Crystals'. In: *The Journal of Chemical Physics* 43 (Nov. 1965), pp. 3199–3208. DOI: 10.1063/1.1697294 (cited on pages 79, 95, 102).

[214] Jake L. Greenfield et al. 'Pathways to increase the dissymmetry in the interaction of chiral light and chiral molecules'. In: *Chem. Sci.* 12 (25 2021), pp. 8589–8602. DOI: 10.1039/D1SC02335G (cited on pages 80, 81, 92, 102, 112, 119).

[215] Prasad L. Polavarapu. 'Kramers-Kronig Transformation for Optical Rotatory Dispersion Studies'. In: *The Journal of Physical Chemistry A* 109.32 (2005). PMID: 16834064, pp. 7013–7023. DOI: 10.1021/jp0524328 (cited on page 80).

[216] John G. Kirkwood. 'On the Theory of Optical Rotatory Power'. In: *The Journal of Chemical Physics* 5.6 (1937), pp. 479–491. DOI: 10.1063/1.1750060 (cited on pages 80, 95, 117, 124, 135).

[217] Frederick S. Richardson and James P. Riehl. 'Circularly polarized luminescence spectroscopy'. In: *Chemical Reviews* 77.6 (1977), pp. 773–792. DOI: 10.1021/cr60310a001 (cited on pages 80, 91).

[218] James P. Riehl and Frederick S. Richardson. 'Circularly polarized luminescence spectroscopy'. In: *Chemical Reviews* 86.1 (1986), pp. 1–16. DOI: 10.1021/cr00071a001 (cited on pages 80, 91).

[219] Giovanna Longhi et al. 'Circularly Polarized Luminescence: A Review of Experimental and Theoretical Aspects'. In: *Chirality* 28.10 (2016), pp. 696–707. DOI: https://doi.org/10.1002/chir.22647 (cited on pages 80, 81, 86, 114).

[220] Minghao Li et al. 'Strong Coupling of Chiral Frenkel Exciton for Intense, Bisignate Circularly Polarized Luminescence'. In: *Angewandte Chemie International Edition* 62.6 (2023), e202212724. DOI: https://doi.org/10.1002/anie.202212724 (cited on pages 81, 129, 133, 137, 140–143).

[221] Yoshinori Okayasu and Junpei Yuasa. 'Evaluation of circularly polarized luminescence in a chiral lanthanide ensemble'. In: *Molecular Systems Design & Engineering* 3.1 (2018), pp. 66–72 (cited on page 81).

[222] Ciro A. Guido, Francesco Zinna, and Gennaro Pescitelli. 'CPL calculations of [7]helicenes with alleged exceptional emission dissymmetry values'. In: *J. Mater. Chem. C* 11 (31 2023), pp. 10474–10482. DOI: 10.1039/D3TC01532G (cited on page 81).

[223] Minghua Liu, Li Zhang, and Tianyu Wang. 'Supramolecular Chirality in Self-Assembled Systems'. In: *Chemical Reviews* 115.15 (2015). PMID: 26189453, pp. 7304–7397. DOI: 10.1021/cr500671p (cited on page 81).

[224] N. Nizar et al. 'Emergent chiroptical properties in supramolecular and plasmonic assemblies'. In: *Chemical Society Reviews* 50 (Sept. 2021). DOI: 10.1039/D0CS01583K (cited on pages 81, 102, 106).

[225] Torsten Bruhn et al. 'Axially Chiral BODIPY DYEmers: An Apparent Exception to the Exciton Chirality Rule'. In: *Angewandte Chemie International Edition* 53.52 (2014), pp. 14592–14595. DOI: https://doi.org/10.1002/anie.201408398 (cited on pages 82, 117, 119–121, 125–127, 135, 136).

[226] Gennaro Pescitelli. 'ECD exciton chirality method today: a modern tool for determining absolute configurations'. In: *Chirality* 34.2 (2021), pp. 333–363. DOI: 10.1002/chir.23393 (cited on pages 82, 105, 117, 120, 123, 127).

[227] D. Volland et al. 'Synthesis of a Blue-Emissive Azaborathia[9]helicene by Silicon-Boron Exchange from Unusual Atropisomeric Teraryls'. In: *Angew. Chemie* (2023). DOI: 10.1002/ange.202304291 (cited on page 85).

[228] M. Akiyama and K. Nozaki. 'Synthesis of Optically Pure Helicene Metallocenes'. In: *Angew. Chemie Int. Ed.* 56 (2017), pp. 2040–2044 (cited on page 85).

[229] C. Li, Y. Yang, and Q. Miao. 'Recent Progress in Chemistry of Multiple Helicenes'. In: *Chem. - An Asian J.* 13 (2018), pp. 884–894 (cited on page 85).

[230] W. Yang and J. Shen. 'Frontispiece: Multiple Heterohelicenes: Synthesis, Properties and Applications'. In: *Chem. – A Eur. J.* (2022). DOI: 10.1002/chem.202202069 (cited on page 85).

[231] Y. Wu et al. 'Sulfur-Doped Quintuple [9]Helicene with Azacorannulene as Core'. In: *Angew. Chemie* (2022). DOI: 10.1002/ange.202204334 (cited on page 85).

[232] P. Aillard, A. Voituriez, and A. Marinetti. 'Helicene-like chiral auxiliaries in asymmetric catalysis'. In: *Dalt. Trans.* 43 (2014), pp. 15263–15278 (cited on page 85).

[233] Z. Hu et al. 'Indole-Based Aza[n]helicenes (n=5, 6) with Violet-Blue Fluorescence and Two-Photon Absorption (TPA)'. In: *Chempluschem* 85 (2020), pp. 742–750 (cited on page 85).

[234] M. Hasan et al. 'Sui Generis Helicene-Based Supramolecular Chirogenic System: Enantioselective Sensing, Solvent Control, and Application in Chiral Group Transfer Reaction'. In: *ACS Omega* 2 (2017), pp. 592–598 (cited on page 85).

[235] A. Petdum et al. '"Turn-ON" [5]helicene-based fluorescence sensor with very large Stokes shift for highly selective detection of Ag+ and AgNPs'. In: *Sensors Actuators B Chem.* 259 (2018), pp. 862–870 (cited on page 85).

[236] G. R. Kiel et al. 'Expanded Helicenes: A General Synthetic Strategy and Remarkable Supramolecular and Solid-State Behavior'. In: *J. Am. Chem. Soc.* 139 (2017), pp. 18456–18459 (cited on page 85).

[237] M. Li et al. 'Tetrahydro[5]helicene-Based Nanoparticles for Structure-Dependent Cell Fluorescent Imaging'. In: *Adv. Funct. Mater.* 24 (2014), pp. 4405–4412 (cited on page 85).

[238] X. He et al. 'Nonplanar Helicene Benzo[4]Helicenium for the Precise Treatment of Renal cell Carcinoma'. In: *Small Methods* 5 (2021), p. 2100770 (cited on page 85).

[239] S. Jhulki et al. 'Helicenes as All-in-One Organic Materials for Application in OLEDs: Synthesis and Diverse Applications of Carbo- and Aza[5]helical Diamines'. In: *Chem. - A Eur. J.* 22 (2016), pp. 9375–9386 (cited on page 85).

[240] K. Yavari et al. 'Phosphahelicenes: From Chiroptical and Photophysical Properties to OLED Applications'. In: *Chem. – A Eur. J.* 25 (2019), pp. 5303–5310 (cited on page 85).

[241] Y. Yang et al. 'Circularly polarized light detection by a chiral organic semiconductor transistor'. In: *Nat. Photonics* 7 (2013), pp. 634–638 (cited on page 85).

[242] P. Josse et al. 'Enantiopure versus Racemic Naphthalimide End-Capped Helicenic Non-fullerene Electron Acceptors: Impact on Organic Photovoltaics Performance'. In: *Chem. - A Eur. J.* 23 (2017), pp. 6277–6281 (cited on page 85).

[243] J. Wang et al. 'Aza[5]helicene Rivals N-Annulated Perylene as π-Linker of D-π-D Typed Hole-Transporters for Perovskite Solar Cells'. In: *Adv. Funct. Mater.* 30 (2020), p. 2002114 (cited on page 85).

[244] Nina Berova, Lorenzo Di Bari, and Gennaro Pescitelli. 'Application of Electronic Circular Dichroism in Configurational and Conformational Analysis of Organic Compounds'. In: *Chemical Society Reviews* 36 (July 2007), pp. 914–31. DOI: 10.1039/b515476f (cited on page 85).

[245] J. Han et al. 'Recent Progress on Circularly Polarized Luminescent Materials for Organic Optoelectronic Devices'. In: *Adv. Opt. Mater.* 6 (2018), p. 1800538 (cited on page 85).

[246] R. Naaman and D. H. Waldeck. 'New Perspective on Electron Transfer through Molecules'. In: *J. Phys. Chem. Lett.* 3 (2012), pp. 2178–2187 (cited on page 85).

[247] T. Mori. 'Chiroptical properties of symmetric double, triple, and multiple helicenes'. In: *Chem. Rev.* 121 (2021), pp. 2373–2412 (cited on page 85).

[248] X. Tian et al. 'Naphthalimide-Annulated [n]Helicenes: Red Circularly Polarized Light Emitters'. In: *J. Am. Chem. Soc.* 145 (2023), pp. 9886–9894 (cited on page 85).

[249] Y. Shen et al. 'A π-Extended Pentadecabenzo[9]Helicene'. In: *Angew. Chemie* (2023). DOI: 10.1002/ange.202300840 (cited on page 85).

[250] J.-K. Li et al. 'B,N-Embedded Double Hetero[7]helicenes with Strong Chiroptical Responses in the Visible Light Region'. In: *J. Am. Chem. Soc.* 143 (2021), pp. 17958–17963 (cited on page 85).

[251] G. R. Kiel et al. 'Expanded [23]-Helicene with Exceptional Chiroptical Properties via an Iterative Ring-Fusion Strategy'. In: *J. Am. Chem. Soc.* 144 (2022), pp. 23421–23427 (cited on page 85).

[252] L. Norel et al. 'Metallahelicenes: easily accessible helicene derivatives with large and tunable chiroptical properties'. In: *Angew. Chemie* 122 (2010), pp. 103–106 (cited on page 85).

[253] E. S. Gauthier et al. 'Long-Lived Circularly Polarized Phosphorescence in Helicene-NHC Rhenium(I) Complexes: The Influence of Helicene, Halogen, and Stereochemistry on Emission Properties'. In: *Angew. Chemie Int. Ed.* 59 (2020), pp. 8394–8400 (cited on page 85).

[254] M. Jakubec et al. '2-Bromo [6] helicene as a key intermediate for [6] helicene functionalization'. In: *J. Org. Chem.* 83 (2018), pp. 3607–3616 (cited on page 86).

[255] Y. Yu et al. 'Intramolecular Alkyne Aromatization: Unexpected Synthesis of Expanded [9]Helicene and π-Extended Double [4]Helicene, and Their Molecular Geometry Effect on Transistor Memory'. In: *Small Sci.* (2023). DOI: 10.1002/smsc.202300040 (cited on page 87).

[256] J. Malinčík et al. 'Circularly polarized luminescence in a Möbius helicene carbon nanohoop'. In: *Angew. Chemie - Int. Ed.* 61 (2022), pp. 1–6 (cited on page 87).

[257] Lorenzo Arrico, Lorenzo Di Bari, and Francesco Zinna. 'Quantifying the Overall Efficiency of Circularly Polarized Emitters'. In: *Chemistry – A European Journal* 27.9 (2021), pp. 2920–2934. DOI: https://doi.org/10.1002/chem.202002791 (cited on page 92).

[258] Gennaro Pescitelli and Torsten Bruhn. 'Good Computational Practice in the Assignment of Absolute Configurations by TDDFT Calculations of ECD Spectra'. In: *Chirality* 28.6 (2016), pp. 466–474. DOI: https://doi.org/10.1002/chir.22600 (cited on page 92).

[259] M. J. Frisch et al. *Gaussian~16 Revision C.01*. Gaussian Inc. Wallingford CT. 2016 (cited on pages 92, 137).

[260] Gennaro Pescitelli, Lorenzo Di Bari, and Nina Berova. 'Application of electronic circular dichroism in the study of supramolecular systems'. In: *Chem. Soc. Rev.* 43.15 (2014), pp. 5211–5233. DOI: 10.1039/c4cs00104d (cited on pages 95, 117).

[261] Anoop Thomas et al. 'Mueller Polarimetry of Chiral Supramolecular Assembly'. In: *The Journal of Physical Chemistry C* 122.25 (2018), pp. 14205–14212. DOI: 10.1021/acs.jpcc.8b01867 (cited on pages 95, 129, 133, 134, 136, 141, 142).

[262] Minghao Li et al. 'Strong Coupling of Chiral Frenkel Exciton for Intense, Bisignate Circularly Polarized Luminescence'. In: *Angewandte Chemie International Edition* (2022). DOI: 10.1002/anie.202212724 (cited on page 95).

[263] Davidov, A. S. *Theory of Molecular Excitons*. Plenum Press, 1971 (cited on page 95).

[264] Agranovich, V. M. and Galanin, M. D. *Excitons in Molecular Crystals*. North-Holland, 1982 (cited on page 95).

[265] Howard Devoe. 'Optical Properties of Molecular Aggregates. I. Classical Model of Electronic Absorption and Refraction'. In: *The Journal of Chemical Physics* 41 (July 1964), pp. 393–400. DOI: 10.1063/1.1725879 (cited on pages 95, 97, 99, 100).

[266] Zhiyuan Fan and Alexander Govorov. 'Plasmonic Circular Dichroism of Chiral Metal Nanoparticle Assemblies'. In: *Nano letters* 10 (July 2010), pp. 2580–7. DOI: 10.1021/nl101231b (cited on pages 95–97, 101, 105, 112–114).

[267] Sabnam Kar et al. 'Emergence of Chiroptical Properties in Molecular Assemblies of Phenyleneethynylenes: The role of Quasi-Degenerate Excitations'. In: *The Journal of Physical Chemistry Letters* 9 (July 2018). DOI: 10.1021/acs.jpclett.8b01988 (cited on page 95).

[268] Abraham Nitzan. *Chemical dynamics in condensed phases : relaxation, transfer, and reactions in condensed molecular systems*. Oxford: Oxford University Press, 2013 (cited on page 96).

[269] George C. Schatz and Mark A. Ratner. *Quantum mechanics in chemistry*. Prentice Hall, 2002 (cited on page 97).

[270] A S Davydov. 'The theory of molecular excitons'. In: *Soviet Physics Uspekhi* 7.2 (1964), pp. 145–178. DOI: 10.1070/pu1964v007n02abeh003659 (cited on page 98).

[271] Steven Andrews. 'Using Rotational Averaging To Calculate the Bulk Response of Isotropic and Anisotropic Samples from Molecular Parameters'. In: *Journal of Chemical Education - J CHEM EDUC* 81 (June 2004). DOI: 10.1021/ed081p877 (cited on page 99).

[272] Nobuyuki Harada, Sow-Mei Lai Chen, and Koji Nakanishi. 'Quantitative definition of exciton chirality and the distant effect in the exciton chirality method'. In: *Journal of the American Chemical Society* 97.19 (1975), pp. 5345–5352. DOI: 10.1021/ja00852a005 (cited on pages 111, 113).

[273] AL González et al. 'Size, shape, stability, and color of plasmonic silver nanoparticles'. In: *The Journal of Physical Chemistry C* 118.17 (2014), pp. 9128–9136 (cited on page 112).

[274] Majid Sharifi et al. 'Plasmonic gold nanoparticles: Optical manipulation, imaging, drug delivery and therapy'. In: *Journal of Controlled Release* 311 (2019), pp. 170–189 (cited on page 112).

[275] Nafeesa Sarfraz and Ibrahim Khan. 'Plasmonic gold nanoparticles (AuNPs): properties, synthesis and their advanced energy, environmental and biomedical applications'. In: *Chemistry–An Asian Journal* 16.7 (2021), pp. 720–742 (cited on page 112).

[276] Yinhe Peng et al. 'Recent advances in optical imaging with anisotropic plasmonic nanoparticles'. In: *Analytical Chemistry* 87.1 (2015), pp. 200–215 (cited on page 112).

[277] Ali Attaran et al. 'Circuit Model of Fano Resonance on Tetramers, Pentamers, and Broken Symmetry Pentamers'. In: *Plasmonics* 9 (Dec. 2014), pp. 1303–1313. DOI: 10.1007/s11468-014-9743-y (cited on page 112).

[278] Alexander O. Govorov. 'Plasmon-Induced Circular Dichroism of a Chiral Molecule in the Vicinity of Metal Nanocrystals. Application to Various Geometries'. In: *The Journal of Physical Chemistry C* 115.16 (2011), pp. 7914–7923. DOI: 10.1021/jp1121432 (cited on pages 113, 114).

[279] Nina Berova, Lorenzo Di Bari, and Gennaro Pescitelli. 'Application of Electronic Circular Dichroism in Configurational and Conformational Analysis of Organic Compounds'. In: *Chemical Society reviews* 36 (July 2007), pp. 914–31. DOI: 10.1039/b515476f (cited on page 117).

[280] Sinan Karaveli and Rashid Zia. 'Optical Frequency Magnetic Dipole Transitions'. In: *Encyclopedia of Nanotechnology*. Ed. by Bharat Bhushan. Dordrecht: Springer Netherlands, 2012, pp. 1942–1950. DOI: 10.1007/978-90-481-9751-4_30 (cited on page 117).

[281] Hiromu Kubo et al. 'Tuning Transition Electric and Magnetic Dipole Moments: [7]Helicenes Showing Intense Circularly Polarized Luminescence'. In: *The Journal of Physical Chemistry Letters* 12.1 (2021). PMID: 33399471, pp. 686–695. DOI: 10.1021/acs.jpclett.0c03174 (cited on page 117).

[282] Rafael G. Uceda et al. 'Can Magnetic Dipole Transition Moment Be Engineered?' In: *Angewandte Chemie International Edition* 63.4 (2024), e202316696. DOI: https://doi.org/10.1002/anie.202316696 (cited on page 117).

[283] Steven S. Andrews and James Tretton. 'Physical Principles of Circular Dichroism'. In: *Journal of Chemical Education* 97.12 (2020), pp. 4370–4376. DOI: 10.1021/acs.jchemed.0c01061 (cited on page 117).

[284] Gennaro Pescitelli. 'ECD exciton chirality method today: a modern tool for determining absolute configurations'. In: *Chirality* 34.2 (2022), pp. 333–363. DOI: https://doi.org/10.1002/chir.23393 (cited on page 117).

[285] Malcolm Levitt and Frank Försterling. 'Spin dynamics: Basics of Nuclear Magnetic Resonance, Second Edition'. In: *Medical Physics - MED PHYS* 37 (Jan. 2010). DOI: 10.1118/1.3273534 (cited on page 118).

[286] Miki Hasegawa et al. 'Luminescence of lanthanide complexes: From fundamental to prospective approaches related to water- and molecular-stimuli'. In: *Journal of Photochemistry and Photobiology C: Photochemistry Reviews* 50 (2022), p. 100484. DOI: https://doi.org/10.1016/j.jphotochemrev.2022.100484 (cited on page 118).

[287] Cătălin Didraga et al. 'Structure, Spectroscopy, and Microscopic Model of Tubular Carbocyanine Dye Aggregates'. In: *The Journal of Physical Chemistry B* 108.39 (2004), pp. 14976–14985. DOI: 10.1021/jp048288s (cited on pages 129, 139).

[288] Jennifer L. Lyon et al. 'Spectroelectrochemical Investigation of Double-Walled Tubular J-Aggregates of Amphiphilic Cyanine Dyes'. In: *The Journal of Physical Chemistry C* 112.4 (2008), pp. 1260–1268. DOI: 10.1021/jp077412f (cited on page 129).

[289] Anna Bondarenko, Thomas Jansen, and Jasper Knoester. *Exciton localization in tubular molecular aggregates: size effects and optical response*. Mar. 2020 (cited on page 129).

[290] Sandra Doria et al. 'Vibronic coherences in light harvesting nanotubes: unravelling the role of dark states'. In: *J. Mater. Chem. C* 10 (18 2022), pp. 7216–7226. DOI: 10.1039/D2TC00203E (cited on page 129).

[291] Umberto De Rossi et al. 'Spontaneous Formation of Chirality in J-Aggregates Showing Davydov Splitting'. In: *Angewandte Chemie International Edition in English* 35.7 (1996), pp. 760–763. DOI: https://doi.org/10.1002/anie.199607601 (cited on page 129).

[292] Roderic Lakes. 'Materials With Structural Hierarchy'. In: *Nature* 361 (Mar. 1993). DOI: 10.1038/361511a0 (cited on page 129).

[293] Stefan Kirstein et al. 'Chiral J-Aggregates Formed by Achiral Cyanine Dyes'. In: *ChemPhysChem* 1.3 (2000), pp. 146–150. DOI: https://doi.org/10.1002/1439-7641(20001103)1:3<146::AID-CPHC146>3.0.CO;2-Y (cited on pages 129, 130, 136, 137, 139).

[294] H. von Berlepsch et al. 'Supramolecular Structures of J-Aggregates of Carbocyanine Dyes in Solution'. In: *The Journal of Physical Chemistry B* 104.22 (2000), pp. 5255–5262. DOI: 10.1021/jp000220z (cited on pages 129, 130, 138).

[295] Chistian Spitz et al. 'Proof of Chirality of J-Aggregates Spontaneously and Enantioselectively Generated from Achiral Dyes'. In: *The Journal of Physical Chemistry B* 104.36 (2000), pp. 8664–8669. DOI: 10.1021/jp001805w (cited on pages 129, 139, 142).

[296] N. Berova, K. Nakanishi, and Robert Woody. 'Circular Dichroism: Principles and Applications'. In: *Circular Dichroism: Principles and Applications* (Jan. 2000), pp. 337–395 (cited on pages 129, 143).

[297] Francesco Bertocchi, Cristina Sissa, and Anna Painelli. 'Circular dichroism of molecular aggregates: A tutorial'. In: *Chirality* 35.10 (2023), pp. 681–691. DOI: https://doi.org/10.1002/chir.23565 (cited on pages 129, 131, 133, 135, 140).

[298] D Eisele et al. 'Utilizing redox-chemistry to elucidate the nature of exciton transitions in supramolecular dye nanotubes'. In: *Nature chemistry* 4 (July 2012), pp. 655–662. DOI: 10.1038/nchem.1380 (cited on pages 131, 133, 139–141).

[299] Cesar Garcia et al. '3D Printing of Anisotropic Metamaterials'. In: *Progress In Electromagnetics Research Letters* 34 (July 2012), pp. 75–82. DOI: 10.2528/PIERL12070311 (cited on page 132).

[300] Oriol Arteaga and Razvigor Ossikovski. 'Complete Mueller matrix from a partial polarimetry experiment: The 12-element case'. In: *Journal of the Optical Society of America A* 36 (Mar. 2019), p. 416. DOI: 10.1364/JOSAA.36.000416 (cited on page 134).

[301] Pugzlys A et al. 'Cylindrical aggregates of 5,5′,6,6′-tetrachlorobenzimida-carbocyanine amphiphilic derivatives: Structure-related optical properties and exciton dynamics'. In: *International Journal of Photoenergy* 2006 (Oct. 2006). DOI: 10.1155/IJP/2006/29623 (cited on page 134).

[302] Hans von Berlepsch et al. 'Modification of the Nanoscale Structure of the J-Aggregate of a Sulfonate-Substituted Amphiphilic Carbocyanine Dye through Incorporation of Surface-Active Additives'. In: *The Journal of Physical Chemistry B* 111.7 (2007). PMID: 17261059, pp. 1701–1711. DOI: 10.1021/jp065826n (cited on page 134).

[303] Chuan-Feng Chen and Yun Shen. 'Introduction to Helicene Chemistry'. In: Springer, Nov. 2017. DOI: 10.1007/978-3-662-53168-6_1 (cited on page 136).

[304] Sanoop Mambully Somasundaran et al. 'Structurally Induced Chirality of an Achiral Chromophore on Self-Assembled Nanofibers: A Twist Makes It Chiral'. In: *ACS Nano* 17.11 (2023), pp. 11054–11069. DOI: 10.1021/acsnano.3c03892 (cited on page 136).

[305] Joseph Lakowicz. *Lakowicz JR (2006) Principles of fluorescence spectroscopy, 3rd edn. Springer, New York, 2006*. Springer, Jan. 2006 (cited on page 138).

[306] Christian Spitz et al. 'Polarized absorption and anomalous temperature dependence of fluorescence depolarization in cylindrical J-aggregates'. In: *Chemical Physics* 275.1 (2002). Photoprocesses in Multichromophoric Molecular Assemblies, pp. 271–284. DOI: https://doi.org/10.1016/S0301-0104(01)00521-3 (cited on page 139).

[307] Cătălin Didraga, Joost A. Klugkist, and Jasper Knoester. 'Optical Properties of Helical Cylindrical Molecular Aggregates: The Homogeneous Limit'. In: *The Journal of Physical Chemistry B* 106.44 (2002), pp. 11474–11486. DOI: 10.1021/jp026217s (cited on page 139).

[308] Cătălin Didraga and Jasper Knoester. 'Excitons in tubular molecular aggregates'. In: *Journal of Luminescence* 110.4 (2004). 325th Wilhelm and Else Heraeus Workshop. Organic Molecular Solids : Excited Electronic States and Optical Properties, pp. 239–245. DOI: https://doi.org/10.1016/j.jlumin.2004.08.015 (cited on page 139).

[309] Aravind Jagadeesan, T. Krithiga, and Venkatesan Dhananjeyan. *Carbon Nanotubes: Synthesis, Properties and Applications*. IntechOpen, July 2020 (cited on page 139).

[310] Mark Green et al. 'Macromolecular stereochemistry: the out-of-proportion influence of optically active comonomers on the conformational characteristics of polyisocyanates. The sergeants and soldiers experiment'. In: *Journal of The American Chemical Society - J AM CHEM SOC* 111 (Aug. 1989). DOI: 10.1021/ja00198a084 (cited on page 140).

[311] Jake L. Greenfield et al. 'Pathways to increase the dissymmetry in the interaction of chiral light and chiral molecules'. In: *Chem. Sci.* 12 (25 2021), pp. 8589–8602. DOI: 10.1039/D1SC02335G (cited on page 141).

[312] Lorenzo Arrico, Lorenzo Di Bari, and Francesco Zinna. 'Quantifying the Overall Efficiency of Circularly Polarized Emitters'. In: *Chemistry – A European Journal* 27.9 (2021), pp. 2920–2934. DOI: https://doi.org/10.1002/chem.202002791 (cited on page 141).

[313] D. Giavazzi, Francesco Di Maiolo, and Anna Painelli. 'The fate of molecular excited states: modeling donor–acceptor dyes'. In: *Physical Chemistry Chemical Physics* 24 (Feb. 2022). DOI: 10.1039/D1CP05971H (cited on page 143).

[314] Koen Veys and Daniel Escudero. 'Anti-Kasha Fluorescence in Molecular Entities: Central Role of Electron–Vibrational Coupling'. In: *Accounts of Chemical Research* 55.18 (2022). PMID: 36048561, pp. 2698–2707. DOI: 10.1021/acs.accounts.2c00453 (cited on page 143).

[315] PN Pusey. 'Photon correlation and light beating spectroscopy'. In: *Plenum Press, New York* (1974) (cited on page 149).

[316] URL: https://static.horiba.com/fileadmin/Horiba/Application/Materials/Material_Research/Quantum_Dots/quantumyieldstrad.pdf (cited on page 150).